



# FRIEDRICH-SCHILLER- UNIVERSITÄT JENA

**Late Quaternary climate and environmental reconstruction  
based on lake and peat sediments from the central southern  
Cape region of South Africa**

**Dissertation  
(kumulativ)**

zur Erlangung des akademischen Grades  
Dr. rer. nat. (doctor rerum naturalium)

vorgelegt dem Rat der Chemisch-Geowissenschaftlichen Fakultät der  
Friedrich-Schiller-Universität Jena

von Paul Strobel (M.Sc.)  
geboren am 23.03.1992 in Weimar

Gutachter:

1. Prof. Dr. Roland Zech, Friedrich-Schiller-Universität Jena
2. Prof. Dr. Torsten Haberzettl, Universität Greifswald
3. Prof. Dr. Eva Lehndorff, Universität Bayreuth

Tag der Verteidigung: 24.08.2022

# Table of contents

---

	Statement of authorship (Selbstständigkeitserklärung) .....	v
	Acknowledgements .....	vi
	Manuscript overview .....	vii
	Abstract .....	1
	Zusammenfassung .....	5
1	Introduction .....	11
1.1	Motivation .....	11
1.2	Regional setting and study area .....	12
1.2.1	Major circulation systems and related climate .....	12
1.2.2	Regional setting at the central southern Cape coast and the study sites ...	15
1.3	State of research .....	20
1.3.1	Paleoclimatic background .....	20
1.3.2	Molecular biomarkers and their potential for paleoenvironmental reconstructions .....	25
1.3.2.1	<i>n</i> -Alkanes and their compound-specific hydrogen isotope composition .....	26
1.3.2.2	Hemicellulose-derived sugars and their compound-specific oxygen isotope composition .....	28
1.3.2.3	Coupled $\delta^2\text{H}_{n\text{-alkane}}-\delta^{18}\text{O}_{\text{sugar}}$ approach .....	29
1.4	Thesis outline and objectives .....	32
	References .....	35
2	The potential of $\delta^2\text{H}_{n\text{-alkanes}}$ and $\delta^{18}\text{O}_{\text{sugar}}$ for paleoclimate reconstruction – A regional calibration study for South Africa .....	45
3	Holocene sea level and environmental change at the southern Cape – an 8.5 kyr multi-proxy paleoclimate record from lake Voëlvlei, South Africa .....	57
4	Reconstructing Late Quaternary precipitation and its source on the southern Cape coast of South Africa: A multi-proxy paleoenvironmental record from Vankervelsvlei .....	78

5	Synthesis and discussion .....	112
5.1	Regional evaluation of $\delta^2\text{H}_{n\text{-alkane}}$ , $\delta^{18}\text{O}_{\text{sugar}}$ and the coupled isotope approach for reconstructing precipitation and relative humidity in South Africa .....	114
5.2	Holocene paleoclimate evolution and drivers of environmental change along South Africa's southern Cape coast .....	121
5.2.1	Holocene paleoclimate evolution along South Africa's southern Cape coast	121
5.2.2	Drivers of Holocene paleoclimate dynamics along South Africa's southern Cape coast .....	125
5.3	Late Quaternary paleoclimate evolution and drivers of environmental change along South Africa's southern Cape coast .....	128
5.3.1	Late Quaternary paleoenvironmental and paleoclimate reconstruction along South Africa's southern Cape coast .....	129
5.3.2	Driver of Late Quaternary climate dynamics along South Africa's southern Cape coast .....	133
	References .....	135
6	Conclusions and Outlook .....	142
6.1	Conclusions .....	143
6.2	Outlook .....	145
	Appendix .....	147

## Statement of authorship (Selbstständigkeitserklärung)

---

I declare that I prepared this thesis independently and using the specified tools, personal communications and sources.

(Ich erkläre, dass ich die vorliegende Arbeit selbstständig und unter Verwendung der angegebenen Hilfsmittel, persönlichen Mitteilungen und Quellen angefertigt habe.)

---

Ort, Datum

---

Unterschrift des Verfassers

# Acknowledgements

---

I would like to thank my supervisors Prof. Dr. Torsten Haberzettl and Prof. Dr. Roland Zech who always supported me during the past years and gave me the chance to take up the position within this research project. I also want to give special thanks to my closest colleagues Marcel and Julian who made the past years unforgettable.

I would not have been able to write this dissertation without the help and support of the many kind people around me who contributed to the successful completion of this thesis. I will not list all their names here, as the likelihood of forgetting somebody is very high. Nevertheless, I thank all colleagues, technicians, lab staff, student helpers and secretaries of the department of Physical Geography at the Institute of Geography, Friedrich Schiller University Jena. Moreover, I would like to express my gratitude to colleagues at the University of Cape Town, Nelson Mandela University and the University of Greifswald and all my co-authors and colleagues from other institutions who all supported me personally and professionally. Additionally, I acknowledge the state of Thuringia as well as Friedrich Schiller University Jena for the support with a scholarship (Landesgraduiertenstipendium) and the Deutsche Forschungsgemeinschaft (DFG) for funding the research project "Late Quaternary climate and environmental reconstruction based on lake and peat sediments from the central southern Cape region of South Africa".

Above all, I am deeply grateful to my parents, grandparents and girlfriend as well as my friends for their great patience, support and trust at all times.

# Manuscript overview

---

## **Erklärung zu den Eigenanteilen der Promovendin/des Promovenden sowie der weiteren Doktorandinnen/Doktoranden als Co-Autorinnen/-Autoren an den Publikationen und Zweitpublikationsrechten bei einer kumulativen Dissertation**

Für alle in dieser kumulativen Dissertation verwendeten Manuskripte liegen die notwendigen Genehmigungen der Verlage („Reprint permissions“) für die Zweitpublikation vor.

Die Co-Autorinnen/-Autoren der in dieser kumulativen Dissertation verwendeten Manuskripte sind sowohl über die Nutzung, als auch über die oben angegebenen Eigenanteile der weiteren Doktorandinnen/Doktoranden als Co-Autorinnen/-Autoren an den Publikationen und Zweitpublikationsrechten bei einer kumulativen Dissertation informiert und stimmen dem zu.

Die Anteile der Promovendin/des Promovenden sowie der weiteren Doktorandinnen/Doktoranden als Co-Autorinnen/Co-Autoren an den Publikationen und Zweitpublikationsrechten bei einer kumulativen Dissertation sind in der Anlage aufgeführt.

_____	_____	_____	_____
Name des Promovenden	Datum	Ort	Unterschrift

Ich bin mit der Abfassung der Dissertation als publikationsbasierte Dissertation, d.h. kumulativ, einverstanden und bestätige die vorstehenden Angaben.

_____	_____	_____	_____
Name Betreuer	Datum	Ort	Unterschrift

- [1] **Strobel, P.**, Haberzettl, T., Bliedtner, M., Struck, J., Glaser, B., Zech, M., Zech, R. (2020): The potential of  $\delta^2\text{H}_{n\text{-alkanes}}$  and  $\delta^{18}\text{O}_{\text{sugar}}$  for paleoclimate reconstruction – A regional calibration study for South Africa. *Science of The Total Environment* 716: 137045. DOI: <https://doi.org/10.1016/j.scitotenv.2020.137045>.

Autoren	Konzeption des Forschungsansatzes	Planung der Untersuchungen	Datenerhebung	Datenanalyse und -interpretation	Schreiben des Manuskripts	Vorschlag Anrechnung Publikationsäquivalente
<b>Strobel</b>	<b>X</b>	<b>X</b>	<b>X</b>	<b>X</b>	<b>X</b>	<b>1.0</b>
Haberzettl	X	X		X	X	n.a.
Bliedtner				X	X	n.a.
Struck				X	X	n.a.
Glaser				X	X	n.a.
Zech, M.	X			X	X	n.a.
Zech, R.	X	X	X	X	X	n.a.



- [2] **Strobel, P.**, Bliedtner, M., Carr, A. S., Frenzel, P., Klaes, B., Salazar, G., Struck, J., Szidat, S., Zech, R., Haberzettl, T. (2020): Holocene sea level and environmental change at the southern Cape – an 8.5 kyr multi-proxy paleoclimate record from lake Voëlveij, South Africa. *Climate of the Past* 17: 1567-1586. DOI: <https://doi.org/10.5194/cp-17-1567-2021>.

Autoren	Konzeption des Forschungsansatzes	Planung der Untersuchungen	Datenerhebung	Datenanalyse und -interpretation	Schreiben des Manuskripts	Vorschlag Anrechnung Publikationsäquivalente
<b>Strobel</b>	<b>X</b>	<b>X</b>	<b>X</b>	<b>X</b>	<b>X</b>	<b>1.0</b>
Bliedtner				X	X	n.a.
Carr				X	X	n.a.
Struck				X	X	n.a.
Frenzel			X	X	X	n.a.
Klaes				X	X	n.a.
Salazar				X	X	n.a.
Szidat				X	X	n.a.
Zech, R.	X	X		X	X	n.a.
Haberzettl	X	X		X	X	n.a.

**[3] Strobel, P.,** Bliedtner, M., Carr, A. S., Struck, J., du Plessis, N., Glaser, B., Meadows, M.E., Quick, L. J., Zech, M., Zech, R., Haberzettl, T. (submitted): Reconstructing Late Quaternary precipitation and its source on the southern Cape coast of South Africa: A multi-proxy paleoenvironmental record from Vankervelsvlei.

Submitted to: Quaternary Science Reviews  
 Date of Submission: 16.12.2021  
 Manuscript ID: JQSR-D-21-00813

Autoren	Konzeption des Forschungsansatzes	Planung der Untersuchungen	Datenerhebung	Datenanalyse und -interpretation	Schreiben des Manuskripts	Vorschlag Anrechnung Publikationsäquivalente
<b>Strobel</b>	<b>X</b>	<b>X</b>	<b>X</b>	<b>X</b>	<b>X</b>	<b>1.0</b>
Bliedtner				X	X	n.a.
Carr			X	X	X	n.a.
Struck				X	X	n.a.
du Plessis				X	X	n.a.
Glaser				X	X	n.a.
Meadows				X	X	n.a.
Quick				X	X	n.a.
Zech, M.				X	X	n.a.
Zech, R.	X	X		X	X	n.a.
Haberzettl	X	X		X	X	n.a.

## Abstract

---

Climate change is one of the biggest challenges of our society within recent times and will become even more challenging in the near future. Already today, large parts of South Africa suffer from increasing temperatures and droughts, while increasing numbers of heavy rainfall events lead to massive floods in certain areas. These trends have enormous implications on all levels of biophysical and socio-economic processes. Future climate scenarios given by the Intergovernmental Panel on Climate Change (IPCC) predict an even further increase of temperatures, decreasing precipitation amounts and, as a result, increasing aridity for southern Africa in the upcoming years. This will additionally be accompanied by increasing numbers of hazardous events such as heats, droughts and floods. Moreover, water and its availability in sufficient amounts is a fundamental resource of life and a key aspect for future development in many regions of the world, such as southern Africa. However, to reliably predict future water availability and climate change in South Africa, a robust understanding of past climate variability and its underlying mechanisms is a crucial precondition, which is limited so far.

The modern climate of South Africa is driven by complex interactions of major atmospheric circulation systems, i.e., the temperate mid-latitude Westerlies and the monsoon-driven Easterlies, oceanic circulation systems and the local topography, leading to the presence of three precipitation seasons across the country. The eastern and central parts of the country receive most of its precipitation during austral summer (October to March); this area is called the summer rainfall zone (SRZ). There, precipitation is mainly contributed by the tropical Easterlies and is isotopically positive as it originates from the Indian Ocean. A narrow belt along the west coast receives the majority of the annual precipitation during austral winter (April to September); this area is called the winter rainfall zone (WRZ). There, precipitation is mainly contributed by the temperate mid-latitude Westerlies and is isotopically negative as it originates from the Atlantic Ocean. The area between WRZ and SRZ receives precipitation from both atmospheric circulation systems throughout the year and is called the year-round rainfall zone (YRZ). As a result, the isotopic composition of precipitation is more positive during summer compared to more negative winter precipitation.

During the past decades, some studies have aimed to reconstruct past spatial shifts of the three major rainfall zones covering South Africa. Existing studies used for example stalagmites and rock hyrax (*Procavia capensis*) middens as well as marine and terrestrial deposits to reconstruct past environmental and climatic conditions in South Africa. However, in South Africa, there is a general paucity of terrestrial paleoenvironmental records of Late Quaternary age, largely due to the country's essentially erosive Cenozoic landscape history, which has limited the potential for the accumulation of terrestrial sedimentary deposits. Despite this

## Abstract

overall scarcity of terrestrial archives in South Africa, most of the few existing paleoenvironmental studies are rather discontinuous, relate to specific periods, lack a precise chronological control or provide only coarse temporal resolution. Additionally, the use of various rather indirect paleohydrological proxies derived from methods such as palynology, paleontology as well as organic, inorganic and stable isotope geochemistry further complicates this situation for paleoclimate and paleohydrological reconstruction. All this leads to an incoherent picture of the South African moisture evolution during the Late Quaternary. To overcome this situation, it is necessary to identify suitable sediment archives. Moreover, it is crucial to establish reliable chronologies and develop and analyze direct hydrological proxies in high temporal resolution. Taken together, all this could likely contribute to an increased understanding of past environmental and climatic dynamics in South Africa.

Biomarkers and their isotopic composition have evolved into valuable proxies in paleoenvironmental research and can strongly contribute to our understanding of past climatic conditions and hydrological variations. For example, leaf wax-derived *n*-alkanes and hemicellulose-derived sugars show great potential for paleohydrological studies because they preserve well in soils and sediments. The hydrogen isotopic composition of *n*-alkanes ( $\delta^2\text{H}_{n\text{-alkane}}$ ) and the oxygen isotopic composition of hemicellulose-derived sugars ( $\delta^{18}\text{O}_{\text{sugar}}$ ) are mostly driven by the isotopic composition of precipitation ( $\delta^2\text{H}_p$ ,  $\delta^{18}\text{O}_p$ ), which makes both direct hydrological proxies. However, environmental factors such as evapotranspirative enrichment can bias the isotopic signal of  $\delta^2\text{H}_{n\text{-alkane}}$  and  $\delta^{18}\text{O}_{\text{sugar}}$ , potentially complicating their interpretation when used as single isotopes. To overcome this issue, coupling  $\delta^2\text{H}_{n\text{-alkane}}$  and  $\delta^{18}\text{O}_{\text{sugar}}$  into a so-called “paleohygrometer” enables quantitative reconstruction of the isotopic composition of precipitation and relative humidity, which are of great interest for understanding and modelling past and future climate scenarios. Therefore, biomarker analyzes have the potential to greatly advance our knowledge of Late Quaternary paleoenvironmental conditions in southern Africa.

This thesis focuses on the reconstruction of paleoenvironmental and paleoclimatic changes, and in particular paleohydrological variations, along South Africa’s southern Cape coast during the Late Quaternary, which today is located in the YRZ. Due to their nature as direct hydrological proxies,  $\delta^2\text{H}_{n\text{-alkane}}$  and  $\delta^{18}\text{O}_{\text{sugar}}$  as well as coupling both biomarkers in a coupled  $\delta^2\text{H}_{n\text{-alkane}}-\delta^{18}\text{O}_{\text{sugar}}$  approach are target of this thesis. In a first step, the proxy signals are regionally calibrated on modern reference material (i.e., topsoils).  $\delta^2\text{H}_{n\text{-alkane}}$  significantly correlates with  $\delta^2\text{H}_p$  while no correlation exists between  $\delta^{18}\text{O}_{\text{sugar}}$  and  $\delta^{18}\text{O}_p$ . To test both biomarkers for their environmental control, apparent fractionation ( $\epsilon_{\text{app } 2\text{H}}$  and  $\epsilon_{\text{app } 18\text{O}}$ ) was calculated, which is the difference between  $\delta^2\text{H}_{n\text{-alkane}}$  and  $\delta^2\text{H}_p$ , and  $\delta^{18}\text{O}_{\text{sugar}}$  and  $\delta^{18}\text{O}_p$ , respectively. Along the southern Cape coast,  $\epsilon_{\text{app } 2\text{H}}$  shows no climatic control while aridity and potential evapotranspiration modulate the proxy-signal in the arid regions of South Africa. In

contrast,  $\epsilon_{\text{app } 18\text{O}}$  is strongly driven by both aridity and evapotranspiration along the southern Cape coast while samples lack for other parts of the country. The plants growth form and photosynthetic mode potentially influence the proxy-signal. The results of the coupled  $\delta^2\text{H}_{n\text{-alkane}}-\delta^{18}\text{O}_{\text{sugar}}$  approach show great potential to robustly reconstruct the isotopic composition of the plants-source water and relative humidity in South Africa. The reconstructed isotopic composition of precipitation refers to the atmospheric source of moisture and thus enables to disentangle precipitation contributions from the major atmospheric circulation systems. Reconstructed relative humidity reflects local moisture availability. This highlights that compound-specific isotope analyzes and the application of the coupled  $\delta^2\text{H}_{n\text{-alkane}}-\delta^{18}\text{O}_{\text{sugar}}$  approach provide an enormous added value to paleoenvironmental, paleoclimatic and particularly paleohydrological studies, when applied in sediment archives. However, they should always be considered together with palynological analyzes.

Within this thesis, two sediment archives, i.e., Lake Voëlvlei and the peatland Vankervelsvlei, were identified as ideally suited for paleoenvironmental and paleoclimatic reconstruction. For both sites, robust chronologies were developed by dating different sediment compounds using radiocarbon and optical stimulated luminescence. Lake Voëlvlei provides sediments of Holocene age while Vankervelsvlei provides sediments of Holocene and Late Pleistocene age. Both sediment archives are located in the YRZ and thus allow reconstruction of past variations of the atmospheric circulation patterns contributing precipitation along the southern Cape coast of South Africa. With that in mind, biomarker isotopes ( $\delta^2\text{H}_{n\text{-alkane}}$  and  $\delta^{18}\text{O}_{\text{sugar}}$ ) and the coupled  $\delta^2\text{H}_{n\text{-alkane}}-\delta^{18}\text{O}_{\text{sugar}}$  approach were applied together with well-established sedimentological and geochemical proxies in a multi-proxy approach in high temporal resolution. For the first time in this region, this combination of proxies was used to draw a coherent picture of moisture availability and precipitation sources along South Africa's southern Cape coast. During the Holocene, hydroclimate variability was driven by contributions from Easterly- and locally-derived precipitation leading to moist conditions and a year-round precipitation regime from  $\sim 7.5$  to  $\sim 5.0$  ka cal BP and from  $\sim 3.0$  ka cal BP until present day. Drier conditions accompanied by a shift to a winter rainfall regime occurred from  $\sim 5.0$  to  $\sim 3.0$  ka cal BP. Comparisons with other regional records support these results. However, proposed driving forces behind climate variability such as the frequency of El Niño-Southern Oscillation, the Southern Annular Mode, sea surface temperatures or the extent of the Antarctic sea ice are still subject of considerable debate.

On Late Quaternary timescales, the identical multi-proxy approach was applied to sediments from Vankervelsvlei. During glacial periods, distinct sea level variations caused the coastline to migrate up to 100 km south of its present position. This led to increased continentality and dry conditions at Vankervelsvlei and the southern Cape coast. Conversely, during interglacial periods, the coastline was approximately where it is situated in recent times and more humid

## Abstract

conditions have been recorded at Vankervelsvlei. Sea-level changes are therefore a main driver for climate variability at the site on orbital time scales. The results are confirmed by previous investigations at Vankervelsvlei as well as stalagmite records from the surrounding area, therefore providing a coherent regional climate signal for the southern Cape coast of South Africa.

For the first time, the atmospheric source of precipitation and local moisture availability were reliably reconstructed along the southern Cape coast of South Africa. This was possible due the nature of compound-specific oxygen and hydrogen isotopes from plant-derived biomarkers as direct hydrological proxies. These were regionally calibrated and coupled in a  $\delta^2\text{H}_{n\text{-alkane}}-\delta^{18}\text{O}_{\text{sugar}}$  approach, which enables to disentangle the atmospheric sources of precipitation and provides local moisture availability along South Africa's southern Cape coast. In order to robustly reconstruct paleoenvironmental and paleoclimatic changes based on sediments, it was crucial to establish reliable chronologies and apply broad multi-proxy approaches in high temporal resolution at each study site. Future studies should focus on the analyzes of additional modern reference material from the SRZ and WRZ to more comprehensively evaluate potentials and limitations of compound-specific oxygen and hydrogen isotopic isotopes as well as the coupled  $\delta^2\text{H}_{n\text{-alkane}}-\delta^{18}\text{O}_{\text{sugar}}$  approach for paleoclimate reconstruction in South Africa. Moreover, sediment archives located in the SRZ and WRZ should be analyzed using these biomarkers and the coupled  $\delta^2\text{H}_{n\text{-alkane}}-\delta^{18}\text{O}_{\text{sugar}}$  approach to robustly reconstruct paleoclimatic dynamics in these areas and to better evaluate the latitudinal extent of the climate signal reconstructed along the southern Cape coast.

# Zusammenfassung

---

Der globale Klimawandel ist eine der größten gesellschaftlichen Herausforderungen der Gegenwart und wird es auch zukünftig sein. Große Teile Südafrikas sind bereits heute von steigenden Temperaturen und zunehmenden Dürreperioden betroffen, wohingegen in anderen Teilen des Landes vermehrt Starkniederschlagsereignisse und Überschwemmungen auftreten. Dies sind nur einige Beispiele für eine klimatische Entwicklung mit weitreichenden biophysikalischen und sozioökonomischen Folgen im Land. Die vom Weltklimarat IPCC (Intergovernmental Panel on Climate Change) zusammengetragenen Klimaszenarien prognostizieren zunehmende Aridität in Südafrika als Folge von weiter steigenden Temperaturen und abnehmenden Niederschlägen. Darüber hinaus werden katastrophale Umweltereignisse wie Hitzewellen, Dürren und Überschwemmungen deutlich häufiger auftreten. Für die zukünftige Entwicklung vieler Länder, darunter auch Südafrika, ist Wasser und dessen Verfügbarkeit in ausreichenden Mengen von essenzieller Bedeutung. Um Veränderungen der Wasserverfügbarkeit besser prognostizieren zu können, ist ein robustes Verständnis der spätquartären Klimadynamik und deren zugrundeliegenden klimatischen Mechanismen von essenzieller Bedeutung, welches zurzeit in Südafrika nur begrenzt vorhanden ist.

Das rezente Klima in Südafrika ist durch ein komplexes Zusammenspiel von atmosphärischen (den gemäßigten Westwinden und den tropischen Ostwinden) und ozeanischen Zirkulationssystemen sowie der Topographie des Landes gesteuert, die zur Ausprägung von drei Hauptniederschlagszonen führen. Die östlichen und zentralen Teile des Landes erhalten den überwiegenden Teil ihres Jahresniederschlags während der südhemisphärischen Sommermonate (Oktober bis März) und werden daher als Sommerniederschlagszone (SRZ) bezeichnet. Diese Niederschläge werden meist durch die tropischen Ostwinde beigetragen. Die Quelle dieser Niederschläge ist der Indische Ozean, was zur Folge hat, dass Sommerniederschläge isotopisch positiv sind. In einem schmalen Streifen entlang der Westküste Südafrikas fällt der Großteil des Jahresniederschlags im südhemisphärischen Winter (April bis September), weshalb dieser Bereich als Winterniederschlagszone bezeichnet wird (WRZ). Westwinde bringen Feuchtigkeit aus dem Atlantischen Ozean in diesen Bereich Südafrikas, was zur Folge hat, dass Winterniederschläge isotopisch negativ sind. Zwischen SRZ und WRZ befindet sich ein Bereich, der sowohl von den Westwinden als auch den Ostwinden Niederschläge erhält, die somit ganzjährig und mit geringer Saisonalität auftreten. Die Isotopie der Niederschläge in diesem als Ganzjahresniederschlagszone (YRZ) bezeichneten Bereich weist jedoch deutliche Unterschiede im Jahresverlauf auf. Dies liegt an der zuvor beschriebenen Quelle der Feuchtigkeit, die in den Sommermonaten zu isotopisch

## Zusammenfassung

positiven Niederschlägen aus dem Indischen Ozean und in den Wintermonaten zu isotopisch negativen Niederschlägen aus dem Atlantischen Ozean führt.

In der Vergangenheit verfolgten zahlreiche Studien das Ziel die räumliche Verschiebung dieser drei Hauptniederschlagszonen zu rekonstruieren. Hierfür wurden beispielsweise Stalagmiten, akkumulierte Ausscheidungen von Klippschliefern (*Procavia capensis*) sowie marine und terrestrische Sedimente als Geoarchive verwendet. In Südafrika ist das Vorkommen natürlicher terrestrischer Archive jedoch sehr stark limitiert, was vor allem in der känozoischen Erosionsgeschichte des Landes begründet liegt, welche die Ausbildung von Hohlformen begrenzt, in denen terrestrische Sedimente akkumulieren können. Die meisten existierenden Paläoumweltstudien in Südafrika sind diskontinuierlich, begrenzt auf bestimmte Zeiträume, weisen eine unzureichende chronologische Kontrolle auf oder sind in nur sehr grober zeitlicher Auflösung untersucht. Darüber hinaus resultieren bisher meist nur indirekte hydrologische Proxys aus Disziplinen wie Pollenanalytik, Paläontologie sowie organischer, anorganischer und stabiler Isotopen Geochemie, was eine robuste Rekonstruktion paläoklimatischer und paläohydrologischer Dynamiken in Südafrika weiter erschwert. All das führt dazu, dass bisher kein kohärentes Bild der spätquartären Klimageschichte Südafrikas existiert. Um diese Situation zu verbessern, ist es im ersten Schritt von großer Bedeutung, geeignete Geoarchive ausfindig zu machen, für welche anschließend robuste Alters-Tiefen-Modelle erstellt werden müssen. Die Entwicklung von direkten hydrologischen Proxys und deren Untersuchung in hoher zeitlicher Auflösung sind weitere grundlegende Voraussetzungen. Werden diese Faktoren berücksichtigt, können neue Studien zu einem verbesserten Verständnis der Paläoumwelt- und Paläoklimageschichte in Südafrika beitragen.

Pflanzenbürtige Biomarker und deren isotopische Signatur haben in der Vergangenheit großes Potenzial gezeigt, um zu einem verbesserten Verständnis von paläoklimatischen und paläohydrologischen Änderungen beizutragen. Insbesondere Blattwaxse (*n*-Alkane) und Hemicellulose Zucker zeigten enormes Potenzial für paläohydrologische Studien. Dies liegt unter anderem daran, dass sie in Böden und Sedimenten sehr gut erhaltene Biomarker sind. Die komponentenspezifische Wasserstoffisotopensignatur von *n*-Alkanen ( $\delta^2\text{H}_{n\text{-alkane}}$ ) und die komponentenspezifische Sauerstoffisotopensignatur von Hemicellulose Zuckern ( $\delta^{18}\text{O}_{\text{sugar}}$ ) sind jeweils von der isotopischen Zusammensetzung des Niederschlags ( $\delta^2\text{H}_p$ ,  $\delta^{18}\text{O}_p$ ) abhängig, was beide zu einem direkten hydrologischen Proxy macht. Jedoch überprägen Umweltfaktoren wie beispielsweise die evapotranspirative Anreicherung das isotopische Signal von  $\delta^2\text{H}_{n\text{-alkane}}$  und  $\delta^{18}\text{O}_{\text{sugar}}$ . Dadurch wird die Interpretation beider Isotope erschwert, wenn diese jeweils unabhängig voneinander betrachtet werden. Zur Bewältigung dieser Limitierung können beide Isotope in einem  $\delta^2\text{H}_{n\text{-alkane}}-\delta^{18}\text{O}_{\text{sugar}}$  Ansatz (Paläohygrometer) gekoppelt werden, wodurch es möglich ist, die Isotopie des Niederschlags und relative Luftfeuchtigkeit quantitativ zu rekonstruieren. Diese beiden Proxys können ein Schlüssel für das bessere



Verständnis vergangener sowie der Modellierung zukünftiger Klimaszenarien sein und zeigen das große Potenzial von pflanzenbürtigen Biomarkern für die spätquartäre Klimaforschung in Südafrika.

Diese Arbeit hat zum Ziel, Änderungen der Paläoumwelt, des Paläoklimas und im Speziellen der Paläohydrologie während des Spätquartärs entlang der südlichen Kap Küste Südafrikas, die rezent in der YRZ liegt, zu rekonstruieren. Durch ihre Eigenschaft als direkte hydrologische Proxys sind  $\delta^2\text{H}_{n\text{-alkane}}$ ,  $\delta^{18}\text{O}_{\text{sugar}}$  und die Kopplung beider Isotope der methodische Fokus dieser Arbeit. In einem ersten Schritt wurden diese Proxys an rezentem Referenzmaterial regional kalibriert, um sie möglichst robust interpretieren und potenzielle Umwelteinflüsse bewerten zu können. Die Ergebnisse der Kalibrierungsstudie zeigen eine signifikante Korrelation von  $\delta^2\text{H}_{n\text{-alkane}}$  mit  $\delta^2\text{H}_p$ , während  $\delta^{18}\text{O}_{\text{sugar}}$  nicht mit  $\delta^{18}\text{O}_p$  korreliert. Um Umwelteinflüsse auf die Isotopensignaturen der beiden Biomarker zu evaluieren, wurde die Nettoisotopenfraktionierung berechnet, welche die Differenz zwischen Isotopie der Biomarker ( $\delta^2\text{H}_{n\text{-alkane}}$ ,  $\delta^{18}\text{O}_{\text{sugar}}$ ) und der isotopischen Zusammensetzung des Niederschlags ( $\delta^2\text{H}_p$ ,  $\delta^{18}\text{O}_p$ ) ist und als  $\epsilon_{\text{app } 2\text{H}}$  und  $\epsilon_{\text{app } 18\text{O}}$  angegeben wird. Entlang der südlichen Kap Küste zeigt  $\epsilon_{\text{app } 2\text{H}}$  keine Beeinflussung durch Umweltparameter, wohingegen der Grad der Aridität und die potentielle Evapotranspiration das Isotopensignal in den ariden Regionen Südafrikas signifikant beeinflussen. Im Gegensatz dazu zeigt  $\epsilon_{\text{app } 18\text{O}}$  eine signifikante Beeinflussung durch den Grad der Aridität und potentielle Evapotranspiration entlang der südlichen Kap Küste. Für die übrigen Teile Südafrikas können keine Aussagen getroffen werden, da diese bisher nicht untersucht wurden. Auch die Wachstumsformen der Pflanzen und deren Photosynthesemodi könnten die Isotopensignale beider Biomarker beeinflussen. Die Ergebnisse des gekoppelten  $\delta^2\text{H}_{n\text{-alkane}}-\delta^{18}\text{O}_{\text{sugar}}$  Ansatzes zeigen das große Potenzial zur robusten Rekonstruktion der isotopischen Zusammensetzung des pflanzenverfügbaren Niederschlagswassers und der relativen Luftfeuchtigkeit in Südafrika. Durch die saisonal stark unterschiedliche isotopische Zusammensetzung des Niederschlagswasser kann diese genutzt werden, um die relativen Niederschlagsbeiträge der beiden atmosphärischen Hauptzirkulationssysteme zu unterscheiden und zu rekonstruieren. Darüber hinaus reflektiert die rekonstruierte relative Luftfeuchtigkeit die lokale Feuchtigkeitsverfügbarkeit. All das zeigt den großen Mehrwert komponentenspezifischer Isotopenanalysen an pflanzenbürtigen Biomarkern und die Anwendung des gekoppelten  $\delta^2\text{H}_{n\text{-alkane}}-\delta^{18}\text{O}_{\text{sugar}}$  Ansatzes für die Paläoklimarekonstruktion, wenn diese in Sedimenten analysiert werden. Für die korrekte Interpretation der Ergebnisse sollten jedoch Vegetationsänderungen berücksichtigt werden.

Im Rahmen dieser Arbeit wurden der See Voëlvlei und das Moor Vankervelsvlei als geeignete Sedimentarchive für die Paläoumwelt- und Paläoklimarekonstruktion an der südlichen Kap Küste Südafrikas identifiziert. Basierend auf mehreren Datierungsverfahren an verschiedenen Sedimentkomponenten wurden für beide Archive sehr robuste Alters-Tiefen-Modell erstellt.

## Zusammenfassung

Während die Sedimente aus dem Voëlvlei holozänen Alters sind, weist Vankervelsvlei Sedimente holozänen und darüber hinaus auch spätquartären Alters auf. Durch die Lage beider Archive in der YRZ ist es möglich, Variationen der zwei atmosphärischen Hauptzirkulationssysteme an der südlichen Kap Küste Südafrikas zu rekonstruieren. Hierfür wurden in beiden Archiven pflanzenbürtige Biomarker Isotope und am Vankervelsvlei zudem der gekoppelte  $\delta^2\text{H}_{n\text{-alkane}}-\delta^{18}\text{O}_{\text{sugar}}$  Ansatz gemeinsam mit etablierten sedimentologischen und geochemischen Proxys in einem Multi-Proxy-Ansatz in hoher zeitlicher Auflösung untersucht. Diese Kombination von Proxys ermöglicht es erstmals einen Zusammenhang lokaler Feuchtigkeitsverfügbarkeit mit den atmosphärischen Niederschlagsquellen entlang der südlichen Kap Küste Südafrikas aufzuzeigen. Während des Holozäns bestimmen Niederschläge aus tropischen und lokalen Quellen die Feuchtigkeitsverfügbarkeit und Niederschlagssaisonalität im Untersuchungsgebiet. Das Zusammenspiel von Niederschlägen aus tropischen (Indischer Ozean), gemäßigten (Atlantischer Ozean) und lokalen Quellen führt entlang der südlichen Kap Küste zu feuchten Bedingungen und einem Ganzjahresniederschlagsregime zwischen  $\sim 7,5$  und  $\sim 5,0$  ka cal BP sowie seit  $\sim 3,0$  ka cal BP. Trockenere Bedingungen und ein Wechsel zu einem Winterniederschlagsregime mit dominanter gemäßigter Niederschlagsquelle (Atlantischer Ozean) existierte zwischen  $\sim 5,0$  und  $\sim 3,0$  ka cal BP. Der Vergleich mit weiteren Archiven in der Region unterstützt diese Ergebnisse, jedoch sind die Mechanismen dieser Klimaentwicklung weiterhin nur unzureichend geklärt. Die Erforschung der Einflüsse von Meeresoberflächentemperaturen im Südlichen Ozean, welche wahrscheinlich die Ausdehnung des antarktischen Meereises sowie der Lage der Westwindzone und damit auch der Antarktischen Oszillation (Southern Annular Mode) steuern oder die Frequenz von ENSO (El Niño-Southern Oscillation) auf das Klima entlang der südlichen Kap Küste Südafrikas bleiben Forschungsgegenstand zukünftiger Arbeiten.

An den spätquartären Sedimenten des Vankervelsvleis wurde der identische Multi-Proxy-Ansatz angewandt. Während Glazialer Phasen herrschten trockene Bedingungen im Untersuchungsgebiet. Diese stehen mit einer Absenkung des Meeresspiegels in Zusammenhang, welche wiederum zu einer Südwärts-Verschiebung der Küstenlinie um  $\sim 100$  km und somit zu erhöhter Kontinentalität führten. Während Interglazialer Phasen war das Klima am Vankervelsvlei deutlich feuchter, was in einem Meeresspiegel und einer Position der Küstenlinie vergleichbar mit ihrer rezenten Höhe und Position begründet liegt. Dieser Zusammenhang identifiziert die Höhe des Meeresspiegels auf orbitalen Zeitskalen als einen wichtigen Mechanismus für die Klimavariabilität im Untersuchungsgebiet. Die Ergebnisse dieser Arbeit werden darüber hinaus durch frühere Studien am Vankervelsvlei sowie nahegelegener Stalagmiten gestützt, die gemeinsam ein kohärentes regionales klimatisches Muster entlang der südlichen Kap Küste Südafrikas zeigen.

In dieser Arbeit konnte erstmals ein Zusammenhang der atmosphärischen Niederschlagsquellen und lokaler Feuchtigkeitsverfügbarkeit entlang der südlichen Kap Küste Südafrikas rekonstruiert werden. Dies war möglich, da komponentenspezifische stabile Wasserstoff- und Sauerstoffisotope von pflanzenbürtigen Biomarkern als direkte hydrologische Proxys genutzt wurden. Beide Isotope wurden zuerst regional kalibriert und in einem  $\delta^2\text{H}_{n\text{-alkane}}-\delta^{18}\text{O}_{\text{sugar}}$  Ansatz gekoppelt, welcher großes Potential für die Rekonstruktion der atmosphärischen Niederschlagsquelle und lokaler Feuchtigkeitsverfügbarkeit entlang der südlichen Kap Küste Südafrikas aufzeigte. Für die robuste Rekonstruktion von Änderungen der Paläoumwelt und des Paläoklimas anhand von Sedimenten waren die Erstellung eines robusten Alters-Tiefen-Modells und die Anwendung eines Multi-Proxy-Ansatzes in hoher zeitlicher Auflösung in jedem Archiv von essenzieller Bedeutung. Um die Anwendung komponentenspezifischer stabiler Isotope von pflanzenbürtigen Biomarkern in weiteren Arbeiten noch robuster zu machen, könnte die Untersuchung weiteres modernen Referenzmaterials aus der SRZ und WRZ zukünftig fokussiert werden. Für die robuste Rekonstruktion des südafrikanischen Paläoklimas könnten weitere Sedimentarchive in der SRZ und WRZ mittels komponentenspezifischer stabiler Isotopenanalysen und dem gekoppelten  $\delta^2\text{H}_{n\text{-alkane}}-\delta^{18}\text{O}_{\text{sugar}}$  Ansatz untersucht werden. Diese Archive könnten zudem der Evaluierung der räumlichen Ausdehnung des rekonstruierten paläoklimatischen Musters entlang der südlichen Kap Küste Südafrikas dienen.

# Chapter 1

---

## Introduction

---

Author: Paul Strobel

# 1 Introduction

---

## 1.1 Motivation

One of the fundamental resources for life on earth is water in sufficient quantities. It controls natural ecology and biodiversity as well as people's socio-economic activities, e.g., water supply and irrigation in agriculture. In many semi-arid and arid regions of the world, such as southern Africa, this water availability is a key aspect for future development and the current climate change has massive implications for all levels of biophysical and socio-economic processes (IPCC, 2021). Future scenarios predict rising temperatures and decreasing precipitation for southern Africa, leading to increasing aridity. Additionally, a growing number of hazardous events such as heats, droughts and fire weather will affect a wide range of socio-economic sectors, e.g., agriculture, forestry, health and ecosystems (Douville et al., 2021; Engelbrecht and Monteiro, 2021; Lee et al., 2021; Seneviratne et al., 2021). Today, South Africa is located at the intersection of two major atmospheric circulation systems, i.e., the temperate Westerlies and the monsoon-driven Easterlies. These cause the presence of distinct precipitation seasons across the country. The predicted changes in amount and seasonality of precipitation (shorter rainfall seasons, higher frequency of extreme rainfall events, associated floods) will further increase droughts, especially in the semi-arid regions in the northwestern parts of South Africa. For the more humid areas of the country, weather will be much more unpredictable (Douville et al., 2021; Engelbrecht and Monteiro, 2021; Ranasinghe et al., 2021). While monsoonal precipitation will likely increase in some parts of South Africa, a contemporary poleward shift of the temperate Westerlies and an increase in ENSO (El Niño-Southern Oscillation) frequency will lead to reduced precipitation in large areas of the country (Perren et al., 2020; Pomposi et al., 2018; Russell et al., 2006). In order to improve the prediction of future climate change in the region, the investigation of past shifts of the atmospheric circulation systems providing precipitation to South Africa, i.e., the temperate Westerlies and the monsoon-driven Easterlies, their long-term driving forces and their spatio-temporal variations is essential for the assessment of the current hydrological situation as well as for the forecast of probable variations within the regional water budget.

Sediment archives have shown the potential to enable the reconstruction of past environmental and climatic changes in high temporal resolution. However, there is a general paucity of terrestrial paleoenvironmental records of Late Quaternary age in South Africa, largely due to the region's essentially erosive Cenozoic landscape history, which has limited the potential for the accumulation of terrestrial sedimentary deposits (Haberzettl et al., 2014; Quick et al., 2015; van Zinderen Bakker, 1976; Wündsche et al., 2018). Despite this overall scarcity of terrestrial archives in South Africa, most of the few existing paleoenvironmental studies are rather

## Chapter 1

discontinuous, relate to specific periods, lack a precise chronological control or provide only coarse temporal resolution. Additionally, the use of various rather indirect paleohydrological proxies derived from methods such as palynology, paleontology as well as organic, inorganic and stable isotope geochemistry in most paleohydrological studies further complicates this situation. This leads to an incoherent picture of the evolution of moisture in South Africa during the Late Quaternary (e.g., Chase and Meadows, 2007; Chase and Quick, 2018; Haberzettl et al., 2019; Quick et al., 2016; Reinwarth et al., 2013; Wündsche et al., 2016a; Zhao et al., 2016). To overcome this situation, it is necessary to identify suitable sediment archives. Moreover, it is crucial to establish reliable chronologies and analyze direct hydrological proxies to contribute to an increased understanding of past environmental and climatic dynamics in South Africa.

During the past decades, biomarkers have evolved as valuable proxies in paleoenvironmental research and can contribute to our understanding of past hydrological variations. For example, leaf wax-derived *n*-alkanes and hemicellulose-derived sugars show great potential for paleohydrological studies as they preserve well in soils and sediments (Eglinton and Hamilton, 1967; Eglinton and Eglinton, 2008; Zech et al., 2012). The compound-specific hydrogen isotopic composition of *n*-alkanes ( $\delta^2\text{H}_{n\text{-alkane}}$ ) and the compound-specific oxygen isotopic composition of hemicellulose-derived sugars ( $\delta^{18}\text{O}_{\text{sugar}}$ ) are mostly driven by the isotopic composition of precipitation, making both a direct hydrological proxy (e.g., Herrmann et al., 2017; Sachse et al., 2012; Struck et al., 2020a). However, various environmental factors can bias the isotopic signal of  $\delta^2\text{H}_{n\text{-alkane}}$  and  $\delta^{18}\text{O}_{\text{sugar}}$ , with evapotranspirative enrichment being a very prominent factor (e.g., Sessions, 2016; Struck et al., 2020a; Tuthorn et al., 2014; Zech et al., 2015). Therefore, the potential to use both proxies for paleohydrological reconstruction has to be evaluated site-specifically. Additionally, coupling of  $\delta^2\text{H}_{n\text{-alkane}}$  and  $\delta^{18}\text{O}_{\text{sugar}}$  into a so-called “paleohygrometer” (e.g., Hepp et al., 2021; Hepp et al., 2019; Lemma et al., 2021; Tuthorn et al., 2015) has been shown to enable quantitative reconstruction of paleohydrological data, which are of great interest for modelling past and future climate scenarios. Therefore, biomarker analyzes have great potential to strongly enhance our knowledge of Late Quaternary paleoenvironmental conditions in South Africa. However, they need to be calibrated first. In combination with well-established analyzes, they can then be applied to sediment archives from South Africa in a multi-proxy approach in order to shed light on the country’s paleoenvironmental and paleoclimatic evolution during the Late Quaternary.

## 1.2 Regional setting and study area

### 1.2.1 Major circulation systems and related climate

The South African climate is driven by interactions of atmospheric and oceanic circulation systems (Tyson and Preston-Whyte, 2000; Fig 1.1). The seasonality and amount of precipitation across South Africa is related to the country’s topography. The Cape Fold Mountains surround an elevated inland plateau along the west and south coast while the

eastern escarpment runs along the east coast. These mountains and escarpments are physical barriers affecting moisture distribution across South Africa. During winter, large amounts of moisture are available due to orographic precipitation in the latitudinally trending Cape Fold Mountains in the west, whereas subsidence occurs in the interior and eastern parts (Figs. 1.1, 1.2, 1.3). Conversely, during summer, high moisture is available in the east and interior associated with orographic precipitation at the latitudinally trending eastern escarpment and convective precipitation in the interior of South Africa, while subsidence occurs in the west of South Africa (Figs. 1.1, 1.2, 1.3). Based on the spatial pattern of precipitation in South Africa throughout the year, three major rainfall zones can be classified. A narrow belt along the west coast is affected by the temperate Westerlies migrating northwards during austral winter (April to September) and bringing the majority (>66%) of the annual precipitation to the area. This area is referred to as the winter rainfall zone (WRZ) (Figs. 1.1, 1.2, 1.3A). This Westerly-derived precipitation originates from the Atlantic Ocean and is isotopically  $^2\text{H}$ - and  $^{18}\text{O}$ -depleted. The eastern and central parts of the country receive the majority (>66%) of their annual precipitation from the tropical Easterlies during austral summer (October to March). This area is designated as the summer rainfall zone (SRZ). Easterly-derived precipitation mainly originates from the Indian Ocean and is isotopically  $^2\text{H}$ - and  $^{18}\text{O}$ -enriched (Figs. 1.1, 1.2, 1.3D, E). The intermediate area between WRZ and SRZ is called the year-round rainfall zone (YRZ) because it receives precipitation from both atmospheric circulation systems throughout the year accompanied by distinct changes of the precipitation's isotopic compositions (Bowen, 2020; Bowen et al., 2005; Braun et al., 2017; Engelbrecht et al., 2015; Harris et al., 2010; Scott and Lee-Thorp, 2004; Figs. 1.1, 1.3B, C). The regional climate conditions of the YRZ, especially along the southern Cape coast, will be discussed more detailed in the following section.

Two major ocean currents exist along South Africa's coast. The Benguela Current, which flows northwards along the west coast, represents an important upwelling system of ascending nutrient-rich and cold Antarctic waters. It significantly contributes to the semi-arid conditions in the northwestern part of the country (Jury et al., 1990; Lutjeharms et al., 2001; Fig 1.1). Along the east and south coast, the Agulhas Current transports warm water masses southwestwards following the continental shelf. During summer, moisture and energy from the current are transported into the interior of the country by onshore airflow over the escarpments (Jury et al., 1993; Lutjeharms et al., 2001).

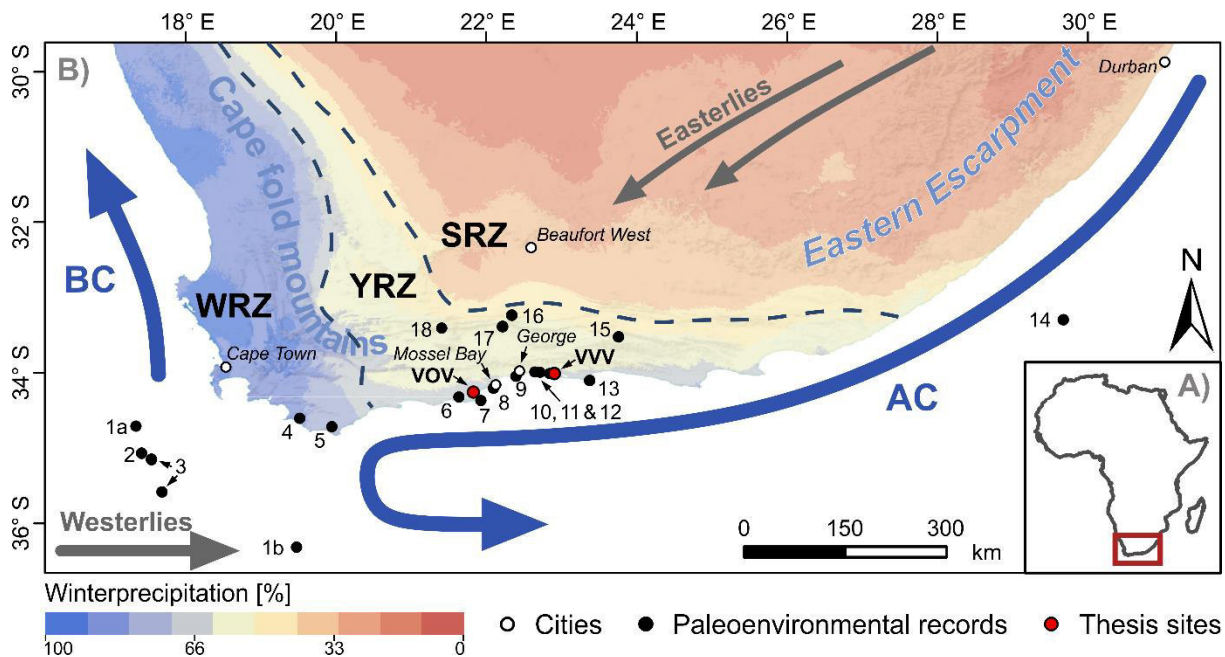


Figure 1.1: A) Simplified map of Africa. Red box highlights the area shown in B. B) The three major rainfall zones of southern Africa based on rainfall seasonality (according to Chase and Meadows, 2007) as well as atmospheric (circumpolar westerlies, the tropical easterlies) and oceanic circulation systems (Agulhas Current (AC) and the Benguela Current (BC)). The location of the Cape fold mountains and parts of the eastern escarpment are also depicted. White and black dots indicate the location of cities and studies mentioned in the text, respectively: 1a & 1b, MD02-2594 & MD96-2080 (Martínez-Méndez et al., 2010); 2, IODP U1479 (Dupont et al., 2021); 3, Cape Basin Record (Peeters et al., 2004); 4, Pearly Beach (Quick et al., 2021); 5, Agulhas Plain vleis and lunettes (Soetendalsvlei, Voëlvlei, Renosterkop, and Soutpan) (Carr et al., 2006a, 2006b); 6, Rietvlei-Still Bay (Quick et al., 2015); 7, GeoB18308-1 (Hahn et al., 2017); 8, Pinnacle Point (Bar-Matthews et al., 2010; Braun et al. 19); 9, Herolds Bay Cave (Braun et al. 2020); 10, Eilandvlei (e.g., Kirsten et al., 2018; Quick et al., 2018; Wündsche et al., 2016a, 2018); 11, Swartvlei (Birch et al., 1978; Haberzettl et al., 2019); 12, Groenvlei (e.g., Martin, 1956; Wündsche et al., 2016b); 13, Nelson Bay Cave (Cohen and Tyson, 1995); 14, CD15417-17K (Simon et al., 2013); 15, Bavianskloof (Chase et al., 2020); 16, Efflux Cave (Braun et al. 2020); 17, Cango Cave (Talma and Vogel, 1992); 18, Seweweekspoort (e.g., Chase et al., 2017). Red dots highlight the specific sites presented in this thesis, i.e., Voëlvlei (VOV) and Vankervelsvlei (VVV). Data sources – DEM: SRTM 1 arcsec; ~30 m (Jarvis et al. 2008).

Related to amount and seasonality of precipitation, distinct environmental conditions are present in South Africa. Mean annual temperatures are higher in the country's interior and at the coastal areas compared to the escarpments (Trabucco and Zomer, 2019; Figs. 1.2, 1.3). Mean annual precipitation is highest along the east and southern coast and decreases progressively towards the interior and northwestern coast (Trabucco and Zomer, 2019). Potential evapotranspiration is higher in the interior and lower along the coastal areas (Fick and Hijmans, 2017). As a result of mean annual precipitation, mean annual temperatures and potential evapotranspiration, an aridity index shows high aridity (lower values) in the interior and lower aridity (higher values) along the eastern and southern coasts (Fick and Hijmans, 2017; Fig. 1.2).



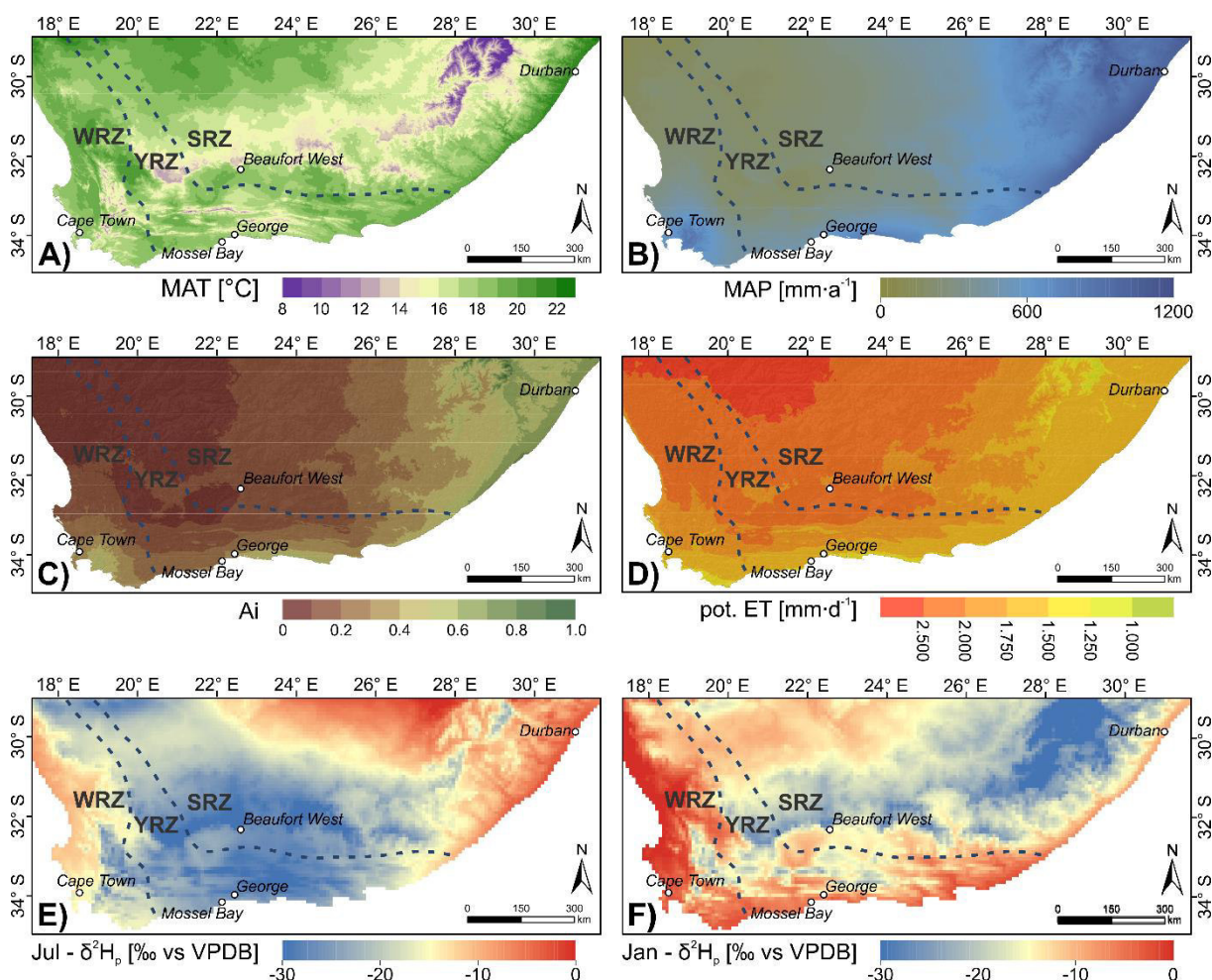


Figure 1.2: Selected environmental parameters in southern Africa: A) Mean Annual Temperature (MAT), B) Mean Annual Precipitation (MAP), C) Aridity Index (Ai), D) Potential Evapotranspiration (pot. ET) as well as the isotopic composition of precipitation ( $\delta^2\text{H}_p$ ) in July (winter) and January (summer). The three major rainfall zones (winter rainfall zone, WRZ; year-round rainfall zone, YRZ; summer rainfall zone, SRZ) and selected cities are also depicted. Data sources – MAT and MAP (Fick and Hijmans, 2017); Ai and pot. ET (Trabucco and Zomer, 2019);  $\delta^2\text{H}_p$  (Bowen and Revenaugh, 2003; Bowen et al., 2005).

### 1.2.2 Regional setting at the central southern Cape coast and the study sites

South Africa's central southern Cape coast is part of the YRZ and characterized by an almost uniform annual rainfall distribution. At the climate stations Mossel Bay and George (Fig. 1.3), average monthly precipitation contribution is  $\geq 6\%$  of the annual rainfall total (reference periods: 1988 to 1999 and 1989 to 2020, respectively) (DWD, 2021; Engelbrecht et al., 2015 SAWS, 2018). Mean annual precipitation sum is distinctly lower at Mossel Bay ( $345 \pm 61 \text{ mm} \cdot \text{a}^{-1}$ ) compared to George ( $684 \pm 162 \text{ mm} \cdot \text{a}^{-1}$ ), but rainfall patterns and isotopic composition of monthly precipitation are quite similar (Bowen, 2020; DWD, 2021; SAWS, 2018; Bowen et al., 2005; Fig. 1.3B, C). The characteristic precipitation distribution is the result of complex interactions of tropical moisture-bearing systems and the mid-latitude (temperate) Westerlies creating different weather systems along the central southern Cape coast (Engelbrecht et al., 2015; Tyson, 1986; Tyson and Preston-Whyte, 2000). Precipitation derived from temperate

## Chapter 1

Westerlies is mainly associated with contributions from ridging anticyclones and cut-off lows. These weather systems contribute 46% and 16% of the mean annual precipitation at the central southern Cape coast, respectively, and can cause extreme precipitation events on regional scale including the potential for destructive floods (Engelbrecht et al., 2015; Favre et al., 2013; Lennard, 2019; Ndarana et al., 2021; Rouault et al., 2002; Singleton and Reason, 2006; Weldon and Reason, 2014). Precipitation of tropical origin is mainly related to tropical-temperate trough cloud bands, which contribute 28% of the mean annual precipitation at the southern Cape coast (Engelbrecht et al., 2015; Hart et al., 2013; Lennard, 2019; Macron et al., 2014).

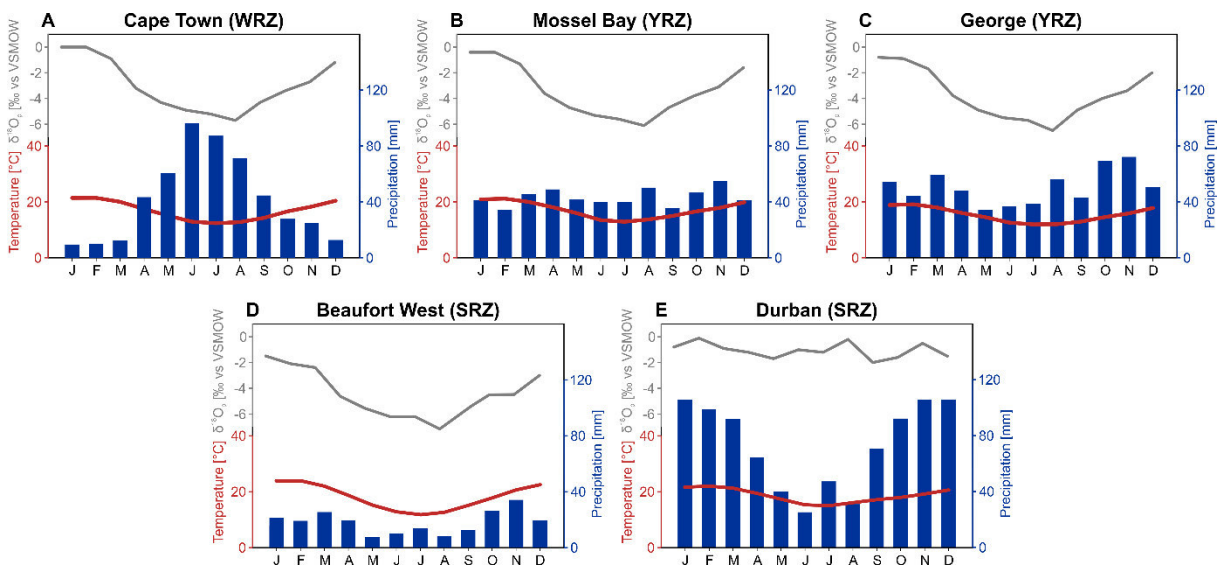


Figure 1.3: Climate diagrams for the cities of A) Cape Town, B) Mossel Bay, C) George, D) Beaufort West and E) Durban showing monthly mean precipitation and temperatures (1989-2020, except for C: 1986-2017 and D: 1979-1997) and modelled oxygen isotopic composition of monthly precipitation ( $\delta^{18}O_p$ ). See figure 1.1 and 1.2 for locations of the climate stations in South Africa. Data sources: Precipitation and temperature (DWD, 2021; SAWS, 2018);  $\delta^{18}O_p$  (Bowen et al. 2005; Bowen, 2020).

Recently, inter-annual precipitation variability was found to be linked to El Niño-Southern Oscillation (ENSO) (Engelbrecht and Landman, 2016; Favre et al., 2013; Ibebuchu, 2021b; Weldon and Reason, 2014). While precipitation contribution from tropical-temperate troughs and cut-off lows was found to be dominant, the frequency of the latter is significantly lower during ENSO compared to La Niña events. This leads to an overall decline in annual precipitation and dry conditions along South Africa's southern Cape coast during ENSO compared to La Niña events (Engelbrecht and Landman, 2016; Favre et al., 2013; Weldon and Reason, 2014).

Additionally, the atmospheric zonal mean pressure gradient between the mid-latitudes ( $\sim 40^{\circ}S$ ) and Antarctica ( $\sim 65^{\circ}S$ ), the Southern Annular Mode (SAM), was found to be a driver for modern rainfall variability in South Africa (Engelbrecht and Landman, 2016; Gillett et al., 2006;

Ilebuchi, 2021a; Marshall, 2003; Thompson and Wallace, 2000). During periods in which this pressure gradient is high, i.e., the positive state of the SAM, more precipitation occurs along South Africa's southern Cape coast (Gillett et al., 2006; Reason and Rouault, 2005). Conversely, during periods of decreased pressure gradient, i.e., the negative state of the SAM, lower precipitation occurs along the southern Cape coast (Engelbrecht and Landman, 2016; Reason and Rouault, 2005).

An additional driver of precipitation from local sources at the southern Cape coast is the Agulhas Current (Fig. 1.1), which brings moisture and energy along the coast. High sea surface temperatures provide the potential for increased precipitation from local sources due to orographic precipitation at the local topography, i.e., the Cape Fold Mountains in the adjacent interior (Chase and Quick, 2018; Engelbrecht and Landman, 2016; Engelbrecht et al., 2015; Rouault et al., 2002; Singleton and Reason, 2006).

The geology of the southern Cape coast is mainly characterized by Paleozoic quartzites of the Table Mountain Group (Cape Supergroup), siliciclastic rocks of the Bokkeveld Group (Cape Supergroup) as well as carbonate rocks of the Bredasdorp Group (Johnson et al., 2006). Soils are mostly Cambisols, Luvisols and Leptosols (Fey, 2010; Zech et al., 2014c). The potential natural vegetation of the western and southern Cape coast would mainly consist of Fynbos and only small areas would be covered by Albany Thicket (Mucina and Rutherford, 2006). Additionally, small patches of forest would cover especially the central southern Cape coast, while the adjacent hinterland would be covered by Succulent Karoo (Mucina and Rutherford, 2006). Today, large areas along the southern Cape coast are used for agriculture. The exception are several national parks and areas not usable for agriculture, such as steep slopes or too shallow soils that are still covered by natural vegetation.

Along South Africa's southern Cape coast, winter precipitation contribution increases from west to east coast while summer precipitation contribution increases from east to west (Section 1.2.1; Fig. 1.1). This leads to a distinct precipitation seasonality accompanied by variations in the isotopic composition of precipitation, which is isotopically more negative during winter compared to the more positive summer precipitation (Bowen and Revenaugh, 2003; Bowen et al., 2005; Figs. 1.2, 1.3B, C).

The first specific study area of this thesis is Lake Voëlvlei, which is located in the western parts of the YRZ (34.013° S; 22.904° E), 30 km west of Mossel Bay and ~10 km inland of the Indian Ocean coast (Fig. 1.4). Today, Voëlvlei is located at 5 m above present sea level and can be described as intermittent lake, meaning it is temporarily desiccated. The Buffels River is its major source of water and drains most parts of the lake's catchment. The catchment area stretches across 165 km<sup>2</sup> and covers altitudes between 5 and 333 m above present sea level. Voëlvlei has one outflow into the Gouritz River (Fig. 1.5). The closest located climate station (Mossel Bay) shows a mean annual precipitation sum of 350 mm·a<sup>-1</sup> (SAWS, 2018), while

## Chapter 1

modeled precipitation at Voëlvlei is  $450 \text{ mm}\cdot\text{a}^{-1}$  (Fick and Hijmans, 2017; Fig. 1.3B). Both observed and modelled precipitation is almost equally distributed over the year with each month contributing  $\geq 6\%$  to the annual precipitation sum (Fick and Hijmans, 2017; SAWS, 2018). Modelled  $\delta^2\text{H}_p$  and  $\delta^{18}\text{O}_p$  show a distinct seasonality where summer precipitation is isotopically positive but isotopically negative during winter periods (Fig. 1.3B). Seasonal variations in modeled  $\delta^2\text{H}_p$  and  $\delta^{18}\text{O}_p$  are in good agreement with observed  $\delta^2\text{H}_p$  and  $\delta^{18}\text{O}_p$  data (Bowen, 2020; Bowen et al., 2005; Braun et al., 2017). Temperatures during the summer period are higher ( $22.0 \text{ }^\circ\text{C}$ ) compared those in winters ( $12.8 \text{ }^\circ\text{C}$ ), with an annual mean of  $17.6 \text{ }^\circ\text{C}$  (SAWS, 2018; Fig. 1.3B).

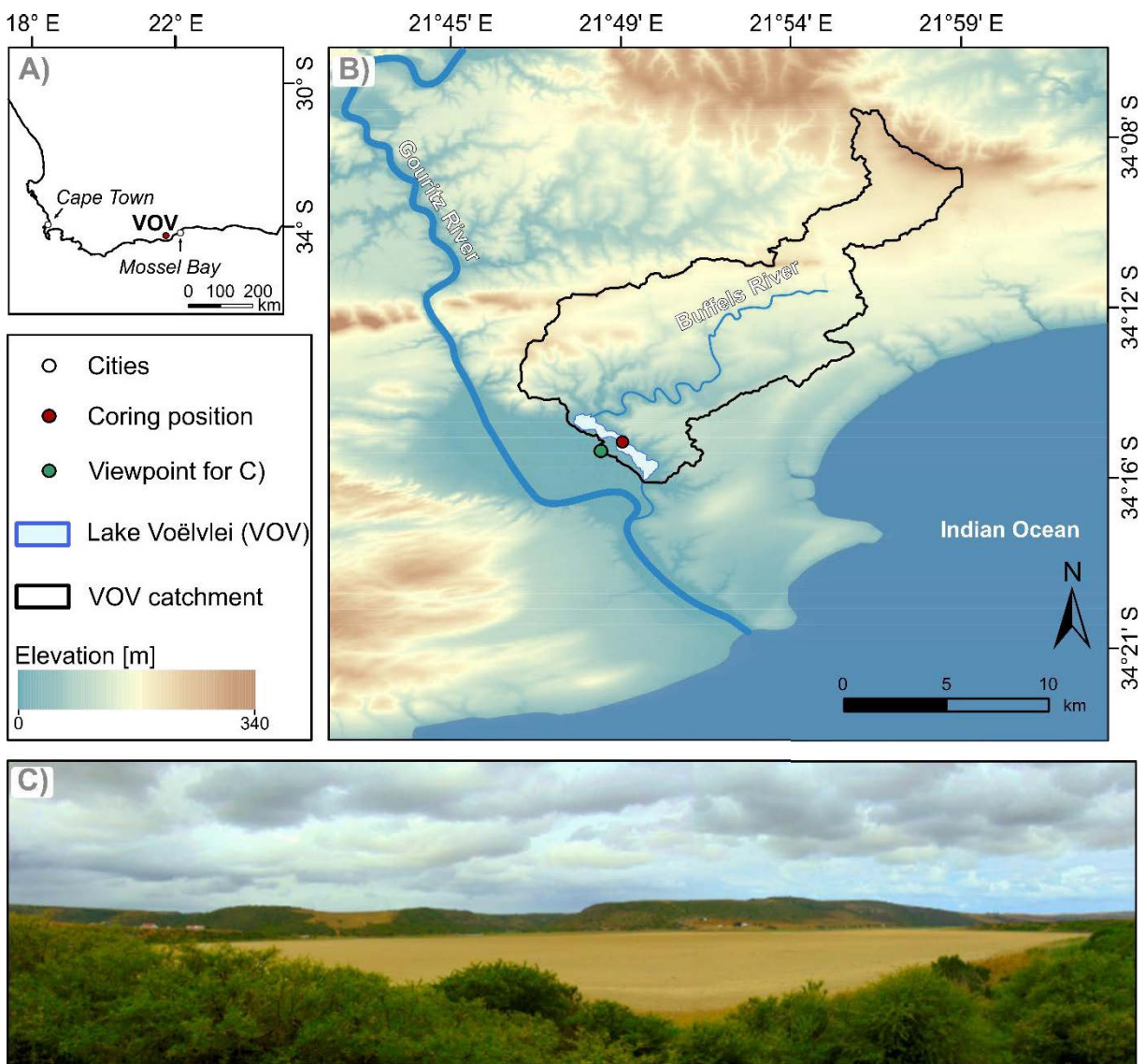


Figure 1.4: A) Location of Lake Voëlvlei (VOV) at South Africa's central southern Cape coast, B) Lake Voëlvlei (VOV), its catchment and the coring position as well as C) Image of Lake Voëlvlei, which was temporarily desiccated in November 2016 (see A for the location of the viewpoint). Data sources – DEM: SRTM 1 arcsec;  $\sim 30 \text{ m}$  (Jarvis et al. 2008).

The second specific study area is Vankervelsvlei, which is a fen located in the eastern parts of the YRZ ( $34.013^{\circ}$  S;  $22.904^{\circ}$  E), 30 km east of George and 5 km inland of the Indian Ocean coast (Fig. 1.5). Today, Vankervelsvlei is located at 152 m above present sea level and is enclosed by stabilized and cemented aeolian sand dunes of Quaternary age (205-250 ka; Bateman et al., 2011). The catchment comprises an area of  $4.1 \text{ km}^2$  and covers altitudes from 152 to 330 m above present sea level (Fig. 1.5). A closely located climate station (George Airport) shows a mean annual precipitation sum of  $690 \text{ mm}\cdot\text{a}^{-1}$  (DWD, 2021; Fig. 1.3), which is in good agreement with modeled precipitation at Vankervelsvlei ( $660 \text{ mm}\cdot\text{a}^{-1}$ ; Fick and Hijmans, 2017; Fig. 1.3 C). Typical for the YRZ, precipitation is almost equally distributed with each month contributing  $\geq 6\%$  to the annual precipitation sum (DWD, 2021). Comparable to Voëlvlei and climate data from Mossel Bay,  $\delta^2\text{H}_p$  and  $\delta^{18}\text{O}_p$  show a distinct seasonality with isotopically more positive precipitation during summer compared to more negative precipitation during winter periods (Fig. 1.3C). Temperatures during the summer period are higher ( $20.3^{\circ}\text{C}$ ) compared to those in winters ( $12.1^{\circ}\text{C}$ ), with an annual mean of  $16.4^{\circ}\text{C}$  (DWD, 2018; Fig. 1.3C).

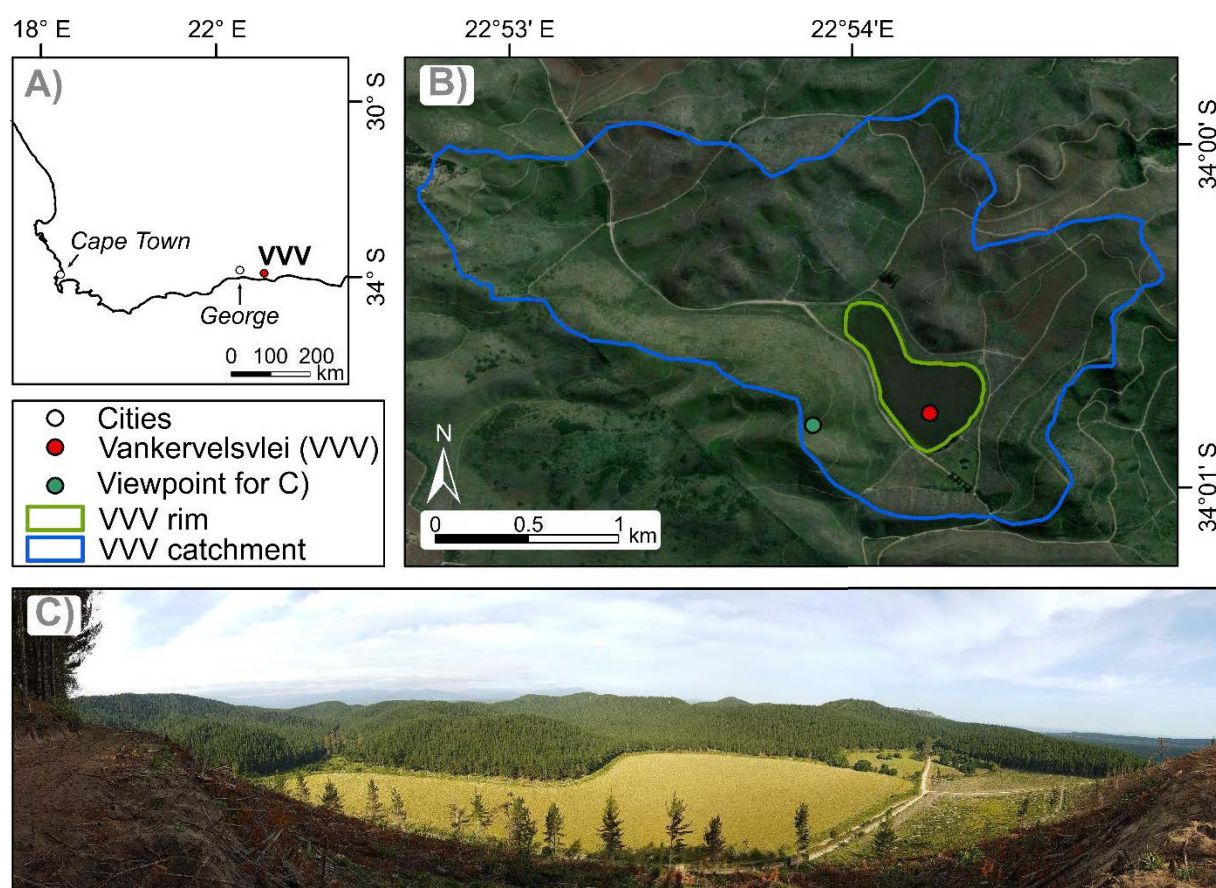


Figure 1.5: A) Location of Vankervelsvlei (VVV) at South Africa's central southern Cape coast, B) Vankervelsvlei, its catchment and the coring position as well as C) Image of Vankervelsvlei (November 2016) and parts of the catchment (see A for the location of the viewpoint). Data sources – Topographic map (ESRI Inc., 2020).

### **1.3 State of research**

This section provides an overview about the current state of research of studies with regard to paleoenvironmental and paleoclimatic reconstruction in a first subsection. Results are presented with focus on investigations located in the coastal areas of the recent YRZ. Despite that, selected studies from the adjacent interior and Southern Ocean are introduced. The second subsection, introduces compound-specific stable hydrogen and oxygen isotope analyzes of plant-derived biomarkers. Additionally, coupling both isotopes and their advantages for paleohydrological research is presented.

#### **1.3.1 Paleoclimatic background**

On South Africa's southern Cape coast, Late Quaternary paleoenvironmental and paleoclimatic research has a long history starting in the 1950s. So far, several marine deposits, rock hyrax midden, stalagmites and terrestrial sediment archives have been investigated. These studies are based on a wide variety of methods such as sedimentology, palynology, paleontology as well as organic, inorganic and stable isotope geochemistry leading to an ongoing development of suitable proxies for an understanding of past environmental changes. This section has not the aim to provide a holistic overview of existing studies but show some records of substantial impact to paleoenvironmental and paleoclimatic research in South Africa during the past decades.

Many marine deposits have been recovered off South Africa's shore providing valuable paleoenvironmental information of Late Quaternary age (Cawthra et al., 2021). For example, changes of the terrestrial vegetation composition during the past 300 ka were derived from a marine sediment record recovered off the coast of South Africa using palynological methods (Dupont et al., 2021; Figs. 1.1, 1.6). The results indicate that past sea level changes and orbital precession are the main drivers for variations in the vegetation composition of South Africa's southwestern coastal region (Dupont et al., 2021). Additional sediment cores recovered off South Africa's southern Cape coast provide information about the sea surface temperature and salinity as well as the intensity of the Agulhas current during major parts of the Late Quaternary (e.g., Bard and Rickaby, 2009; Caley et al., 2018; Caley et al., 2011; Martínez-Méndez et al., 2010; Peeters et al., 2004; Simon et al., 2013; Simon et al., 2020; Fig. 1.1). Unfortunately, most records lack temporal resolution for the Holocene.

Marine deposits that cover parts of the Holocene in higher temporal resolution were analyzed for example by Hahn et al. (2017) (Figs. 1.1, 1.7). This record spans the past ~4.1 ka and was recovered off the mouth of the Gouritz River. Their multi-proxy approach is interpreted to indicate mostly dry conditions from 4,090 to 950 cal BP and from 650 cal BP (Little Ice Age) until present day. Humid conditions are associated with the Medieval Climate Anomaly (950-650 cal BP) (Hahn et al., 2017). Additionally, sea surface temperatures were estimated based

on analyzes of molecular biomarkers (glycerol dialkyl glycerol tetraethers; GDGTs), but the temporal resolution and covered period still limit the significance of this record.

Holocene sea surface temperatures were also reconstructed based on  $\delta^{18}\text{O}$  signatures obtained from marine mollusk shells deposited at Nelson Bay Cave (Cohen, 1993; Cohen and Tyson, 1995; Fig. 1.1). However, the significance of this record is limited as the reconstructed data contain high analytical and dating uncertainties. They are also very fragmentary especially for the late Holocene. Nevertheless, the data were calibrated in the study by Kirsten et al. (2018) and likely indicate higher sea surface temperatures at the Agulhas bank around 6,600 cal BP compared to present day (Cohen and Tyson, 1995).

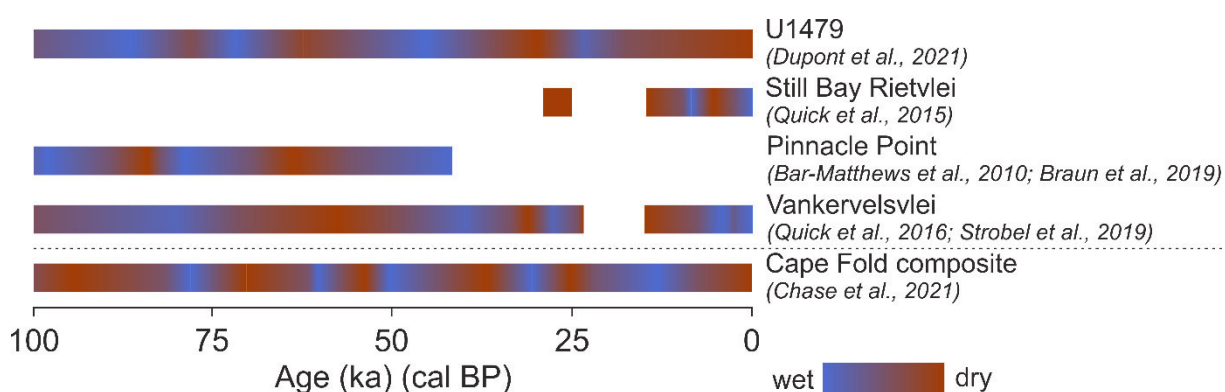


Figure 1.6: Comparison of generalized Late Quaternary palaeoclimate trends inferred from selected marine and terrestrial records from South Africa. The record below the dashed line summarizes studies located in the adjacent interior of the YRZ.

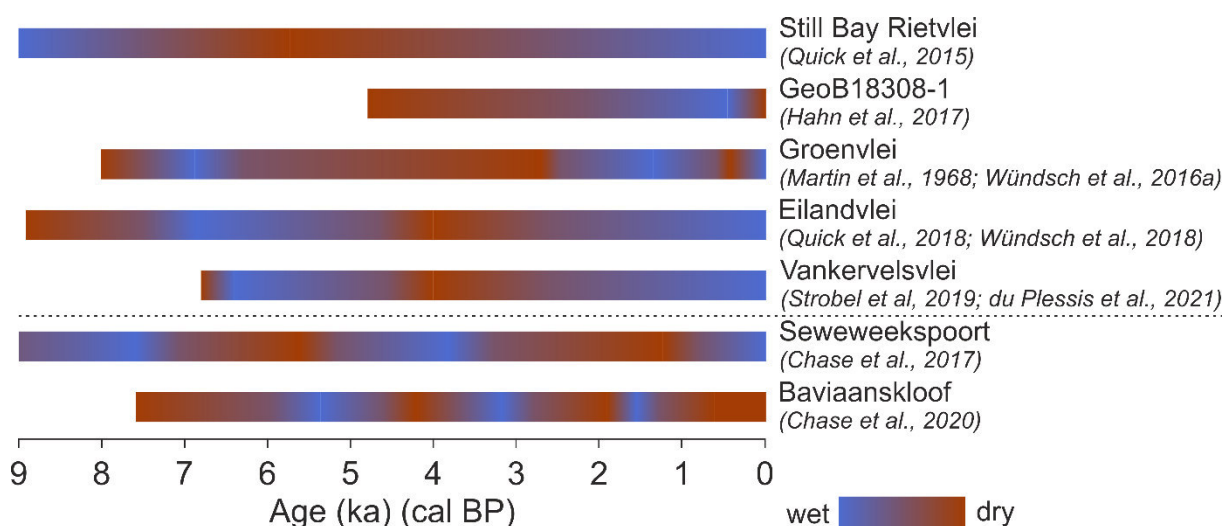


Figure 1.7: Comparison of generalized Holocene palaeoclimate trends inferred from selected terrestrial records the YRZ. Studies below the dashed line are located in the adjacent interior of South Africa's southern Cape coast.

As mentioned above, the presence of terrestrial archives for paleoenvironmental and paleoclimatic reconstruction is limited in southern Africa, which is especially true for the semi-arid and arid regions. There, the exploration of urinary and faecal accumulations of rock hyraxes (*Procavia capensis*), forming stratified middens, has been intensively carried out

## Chapter 1

during the past decades. Stable carbon ( $\delta^{13}\text{C}$ ) and nitrogen ( $\delta^{15}\text{N}$ ) isotopes in those records are thought to allow conclusions about feeding habits and moisture availability (Carr et al., 2016). A variety of hyrax midden records was established in the WRZ (Chase et al., 2019 and references therein) and recently at two sites in the YRZ. These sites are Seweweekspoort and Baviaanskloof, which are located ~235 km apart in a mountain range in the adjacent interior of the central southern Cape coast (Swartberge mountains; Fig. 1.1). The respective records cover the past ~22.3 ka and ~7.2 ka (Chase et al., 2020; Chase et al., 2017; Fig. 1.7).  $\delta^{15}\text{N}$  data are thought to indicate highest moisture availability at Seweweekspoort from 15.4 to 14.2 ka cal BP and from 11.8 to 10.7 ka cal BP, but also show distinct climatic variations during the Holocene (Fig. 1.7). Although there is a proposed correlation on multi-millennial scale of the records from Seweweekspoort and Baviaanskloof (Chase et al., 2020), it is hard to identify a coherent trend of both during the past ~7.2 ka cal BP (Fig. 1.7). Noticeable is that these midden records provide paleoenvironmental data in very high temporal resolution. However, challenges in the proxy-interpretation and the application of indirect hydrological proxies ( $\delta^{13}\text{C}$  and  $\delta^{15}\text{N}$ ) limit the significance of these records for paleoclimate and, in particular, paleohydrological reconstruction.

There is a number of stalagmites, which were analyzed for their stable carbon and oxygen isotopic composition so far. First records were established by Talma and Vogel (1992) at Cango Cave (Fig. 1.1), which is located in the Swartberge mountains, spanning the periods from ~44.4 to ~16.7 ka and from ~6.1 to present day and a depositional hiatus in between (16.7 to 6.1 ka).  $\delta^{18}\text{O}$  at Cango Cave was interpreted to indicated changes in temperature, showing generally lower temperatures from 44.4 to 16.7 ka compared to the Holocene part of the record. From ~6.1 to 2.5 ka, temperatures were general ~1-2 °C cooler than at present day including two minima at ~5 and ~3 ka. During this period, a winter rainfall regime is hypothesized to have occurred at the site (Talma and Vogel, 1992). A pronounced temperature increase is present at ~2.5 ka lasting until present likely indicating a shift to the year-round precipitation regime (Scott et al., 2003), which is today still present at Cango Cave. Close to Cango Cave, Braun et al. (2020) established  $\delta^{18}\text{O}$  and  $\delta^{13}\text{C}$ -records based on speleothems from Efflux Cave (113 to 19 ka; Fig. 1.1). Recently,  $\delta^{18}\text{O}$  and  $\delta^{13}\text{C}$  composite records were compiled based on both studies from Cango Cave and Efflux Cave, while additionally  $\delta^{13}\text{C}$ -data from Seweweekspoort were considered (Chase et al., 2021; Fig. 1.6). Variations in  $\delta^{13}\text{C}$  at the sites are linked to changes in local vegetation cover and  $\delta^{18}\text{O}$  is interpreted to infer past changes in the precipitation source (Braun et al., 2020; Chase et al., 2021). Chase et al. (2021) interpret higher  $\delta^{18}\text{O}$  values accompanied by higher  $\delta^{13}\text{C}$  values to indicate high contributions of summer rainfall and the presence of plants using the C4-photosynthetic pathway, which likely occurred for example from 113 to 80 ka. In contrast, from 25 to 17 ka lower  $\delta^{18}\text{O}$  and  $\delta^{13}\text{C}$  indicate high contribution of winter precipitation and plants using the C3 photosynthetic pathway (Chase et al., 2021). Further speleothem  $\delta^{13}\text{C}$  and  $\delta^{18}\text{O}$ -records were established at



the coastal sites Pinnacle Point spanning the periods from 90 to 52 ka and from 330 to 43 ka, and Herold Bay Cave (93 to 62 ka) (Bar-Matthews et al., 2010; Braun et al., 2019; Braun et al., 2020; Fig. 1.1, 1.6). There,  $\delta^{13}\text{C}$  and  $\delta^{18}\text{O}$ -records are also interpreted to infer past changes in vegetation and precipitation but show a partly different pattern compared to the aforementioned sites located in the Swartberge mountains (Cango Cave, Efflux Cave). Although these speleothem records provide results in high temporal resolution and chronological control, the analyzes of only one water isotope ( $\delta^{18}\text{O}$ ) make it challenging to disentangle the effects of temperature as well as precipitation source and amount.

During the past decades, the number of paleoenvironmental and paleoclimatic investigations based on terrestrial sediments at South Africa's central southern Cape coast and adjacent interior has been enormously increased. The geomorphic development of the central southern Cape coast has been analyzed by several studies providing evidence for high geomorphic activity and dune development during the Late Quaternary, e.g. from 241 to 221 ka, 159 to 143 ka, 130 to 120 ka, 92 to 87 ka and post 6 ka, which are likely associated to phases of high sea levels comparable to present day or even higher (e.g., Bateman et al., 2011; Bateman et al., 2004; Carr et al., 2007; Carr et al., 2010a; Carr et al., 2010b; Carr et al., 2006a; Illenberger, 1996). Lakes and estuaries formed between or around these aeolian deposits have been identified as excellent archives to reconstruct past environmental and climatic changes (Haberzettl et al., 2014) and the investigation of these archives already started in the 1950s. First studies by Martin (1956, 1959, 1960a, b, 1962, 1968) provide insights into Holocene paleoecological and paleohydrological changes at South Africa's central southern Cape coast mainly using palynological methods. Wetlands on the Agulhas Plain were analyzed using methods such as sedimentology, palynology and organic and inorganic geochemistry (Fig. 1.1). The results show moist conditions during MIS 3 followed by dry conditions including a potential sedimentary hiatus during MIS 2 and returned moist conditions during the Holocene (Carr et al., 2006b; Quick et al., 2015; Figs. 1.1, 1.6, 1.7). In contrast, other studies found evidence for temporary moist conditions in this area during MIS 2 (Quick et al., 2021). The number of sediment records from the Wilderness area has also been extensively increased during the past decade. There, numerous coastal lakes, rivers and estuaries have been investigated with regard to paleoenvironmental reconstruction within a comprehensive research project entitled *Regional Archives for Integrated Investigations* (RAiN) (Haberzettl et al., 2014). Investigations from Bo Langvlei (du Plessis et al., 2021b), Groenvlei (Martin, 1956, 1959, 1960a, b, 1968; Wündsche et al., 2016a; Fig. 1.7) and Swartvlei (Birch et al., 1978; Haberzettl et al., 2019) have revealed multiple paleoenvironmental records (Fig. 1.1). These coastal lakes have formed between large coastal dune cordons that lie parallel to the coast. Two outstanding sediment archives from this area are Eilandvlei and Vankervelsvlei (Fig. 1.1). Eilandvlei was analyzed in numerous studies combining a variety of methods such as sedimentology, palynology, paleontology, organic and inorganic geochemistry in high temporal

## Chapter 1

resolution and good chronological control. For example, percentages of Afrotemperate forest pollen and elemental iron in the sediments are interpreted to indicate moisture availability and runoff in the lake's catchment. Inferred from both proxies dry condition occurred from 8.9 to 7.9 ka cal BP and from 5.0 to 3.0 ka cal BP while moist conditions were present from 8.0 to 5.0 cal BP and from 3.0 cal BP until present day (du Plessis et al., 2021a; Kirsten et al., 2018; Quick et al., 2018; Reinwarth et al., 2013; Wündsche et al., 2018; Wündsche et al., 2016b; Fig. 1.7). The second archive, Vankervelsvlei, is a coastal peatland which provides sediments of Late Quaternary age (Quick et al., 2016; Strobel et al., 2019; Figs. 1.6; 1.7). Several sediment cores have been recovered from different locations at Vankervelsvlei during the past decades and first studies at the site used sedimentological, palynological as well as organic and inorganic geochemical analyses to investigate past paleoenvironmental changes (Irving, 1998; Irving and Meadows, 1997; Quick et al., 2016). The authors interpret pollen assemblages to infer past changes of winter and summer precipitation as well as temperature and evapotranspiration (Quick et al., 2016). During glacial periods, precipitation seasonality was increased due to a shift to a winter-rainfall regime, but due to lower temperatures evapotranspiration was reduced. Conversely, during interglacial periods, precipitation occurred throughout the year and higher temperatures were accompanied by higher evapotranspiration (Quick et al., 2016). Recently, du Plessis et al. (2021b) investigated a new record covering the period from 650 cal BP until present day also using palynological methods. In this study, a peak in moisture was identified at ~460 cal BP accompanied by declined temperatures during the Little Ice Age (~650-300 cal BP). From 250 cal BP until present day, anthropogenic influence overprints the local pollen spectra (du Plessis et al., 2021b). Although these early records show the potential of sediments from Vankervelsvlei for paleoenvironmental reconstruction they lack of samples and chronological control especially for major parts of the Holocene. Therefore, a newly retrieved sediment record from the site was investigated by Strobel et al. (2019) using a combination of methods such as organic and inorganic geochemistry, paleoecology and for the first time in terrestrial sediments on the central southern Cape coast leaf wax-derived *n*-alkanes and their compound-specific stable carbon and hydrogen isotope composition. Derived from elemental contents as well as  $\delta^{13}\text{C}_{n\text{-alkane}}$  and  $\delta^2\text{H}_{n\text{-alkane}}$  values, dry conditions and low wind-driven evapotranspiration likely occurred from 37 to 28 ka followed by very dry conditions leading to desiccation of the previously accumulated peat from 28 to 8.4 ka (Fig. 1.6). After the deposition of reworked soil from 8.4 to 7.2 ka, continuous peat accumulation until present day indicates wetter conditions compare to the previous sections and provides the possibility for paleoenvironmental and paleoclimatic reconstruction in high temporal resolution. During the Holocene, elemental contents and  $\delta^2\text{H}_{n\text{-alkane}}$  values are interpreted to indicate moist conditions, due to contribution of both summer and winter precipitation, but also high wind-driven evapotranspiration from 6.8 to 4.7 ka, and from 3.0 ka to 1.1 ka, which was the top of the record (Strobel et al., 2019;

Fig. 1.7). Drier condition, limited summer precipitation contribution and low wind-driven evapotranspiration occurred from 4.7 to 3.0 ka (Strobel et al., 2019). Although this study demonstrates the enormous potential of leaf waxes and their stable isotopes to infer past hydrological changes at South Africa's central southern Cape coast, it also shows the limitations of using only one water isotope, i.e., disentangling past changes in source and amount of precipitation as well as evapotranspirative enrichment.

Summarizing, the analyzes and combination of proxies as well as increasing temporal resolution and chronological control all contributed to a better understanding of paleoenvironmental conditions at South Africa's central southern Cape coast. However, the terrestrial climate signals in most records are often overprinted by marine water intrusions induced by relative sea level change during the Holocene (Martin, 1959, 1968; Wündsche et al., 2018; Wündsche et al., 2016a) or anthropogenic impacts, e.g., farming, water abstraction and dredging operations (Haberzettl et al., 2019). The applied methodological approaches in most of the studies only provide rather indirect hydrological proxies to infer past hydrological changes and comparison of the studies is limited due differences in proxies and their interpretation.

Some integrative works for example Chase and Meadows (2007), Chase et al. (2013), Chase et al. (2017), Chase et al. (2019), Miller et al. (2019), Chase et al. (2021) as well as Chase and Quick (2018) have aimed to summarize the Quaternary variability in both ocean and atmospheric circulation systems and their impact on southern African climate. These studies propose long-term macro-scale climatic influences and include a variety of forcing mechanisms such as orbital precession or the extent of the Atlantic sea ice (Berger and Loutre, 1991; Fischer et al., 2007; Nielsen et al., 2004). However, potential environmental feedbacks to past changes in the atmospheric circulation pattern are mostly derived from rather indirect hydrological proxies and thus accompanied by the uncertainties discussed in this section. Therefore, there is a need for studies analyzing archives that are suited for paleohydrological reconstruction in South Africa. Additionally, the significance of future records for paleohydrological reconstruction depends on the chronological control and the application of direct hydrological proxies.

### **1.3.2 Molecular biomarkers and their potential for paleoenvironmental reconstructions**

Molecular fossils of various living organisms can be referred to as molecular biomarkers (Eglinton and Eglinton, 2008; Peters et al., 2005). Due to their molecular structure, which consists of covalent-bounded carbon and hydrogen atoms and in some cases additional carboxyl (-COOH), carbonyl (-CO), and/or hydroxyl functional groups (-OH), molecular biomarkers are protected against degradation and preserve well in soils and sediments on

geological timescales. Some molecular biomarkers are source-specific and can refer to the environmental conditions under which they were synthesized (e.g., Castañeda and Schouten, 2011; Eglinton and Hamilton, 1967; Eglinton and Eglinton, 2008; Peters et al., 2005; Sachse et al., 2012). All this likely contributed to the increasing number of investigations using molecular biomarkers during the past decades (e.g., Bliedtner et al., 2021; Schefuß et al., 2005; Tierney et al., 2008).

### 1.3.2.1 *n*-Alkanes and their compound-specific hydrogen isotope composition

Widely analyzed molecular biomarkers are leaf wax-derived *n*-alkanes, which are synthesized by the polyketide pathway in the plant's cuticle as a protection layer against environmental stress. *n*-Alkanes are straight-chained hydrocarbons without functional groups and are formed by decarboxylation of even carbon-numbered *n*-alkanoic acids resulting in a distinct odd-over-even predominance (e.g., Eglinton and Hamilton, 1967; Eglinton and Eglinton, 2008; Sachse et al., 2012). Typically, leaf wax *n*-alkanes have carbon chains from 25 ( $nC_{25}$ ) to 35 ( $nC_{35}$ ) (e.g., Castañeda and Schouten, 2011; Eglinton and Eglinton, 2008; Struck et al., 2020b). They are chemical inert, water insoluble and relatively resistant against biochemical degradation and can therefore serve as valuable proxies to infer (past) environmental and climatic conditions (Eglinton and Hamilton, 1967; Eglinton and Eglinton, 2008; Sachse et al., 2012; Sessions, 2016). While the *n*-alkane homolog pattern likely refer to the preservation status, the power to differentiate terrestrial vegetation forms (bushes/trees vs. grasses/herbs) might be limited to certain areas (Bliedtner et al., 2018; Schäfer et al., 2016; Struck et al., 2020b).

Leaf wax-derived *n*-alkanes provide the great opportunity to analyze single compounds for their stable hydrogen isotope composition  $\delta^2H_{n\text{-alkane}}$ , which likely refers to (past) hydrological conditions (e.g., Sachse et al., 2012; Sessions, 2016). This is because  $\delta^2H_{n\text{-alkane}}$  reflects the isotopic composition of precipitation ( $\delta^2H_p$ ) modulated by various fractionation processes (Fig. 1.8). Evaporation can lead to an isotopically enrichment of soil water prior to the uptake and transport by the plants through their roots (Feakins and Sessions, 2010; Sachse et al., 2012). Neither for the uptake nor the transport via the roots isotopic fractionation has been observed as the isotopic signature of xylem water is suggested to equal soil water (Feakins and Sessions, 2010; Sachse et al., 2012). Transpiration can result in isotopic enrichment of leaf water compared to xylem water (Cernusak et al., 2016; Fig. 1.8). This leaf water is then the dominant source used for the biosynthesis of leaf wax-derived lipids, i.e., *n*-alkanes. *n*-Alkanes are usually distinctly strongly  $^2H$ -depleted compared to leaf water due to strong isotopic fractionation during biosynthesis, which is suggested to have a mean value of  $-160\text{‰}$  (e.g., Sachse et al., 2012; Sessions et al., 1999; Fig. 1.8). However, due to differences in metabolic pathways, hydrogen transfer reactions and extrinsic environmental factors biosynthetic fractionation ( $\epsilon_{\text{bio}}$ ) can largely differ (Cormier et al., 2018; Eley et al., 2014;

Griepentrog et al., 2019; Liu and An, 2019; Liu et al., 2016; Newberry et al., 2015; Sessions et al., 1999).

The apparent hydrogen isotope fractionation ( $\epsilon_{\text{app } 2\text{H}}$ ) describes the difference between  $\delta^2\text{H}_p$  and  $\delta^2\text{H}_{n\text{-alkane}}$  and integrates the three processes of isotopic fractionation mentioned above, i.e., soil water  $^2\text{H}$  enrichment, leaf-water transpiration and biosynthetic fractionation (Fig. 1.8). Thus,  $\epsilon_{\text{app } 2\text{H}}$  is a valuable proxy to analyze  $n$ -alkanes and their compound specific isotopic signatures for their environmental controls. In this context, several studies used modern reference material (i.e., topsoil and/or lake surface sediments) to investigate the correlation of  $\delta^2\text{H}_{n\text{-alkane}}$  and (growing season)  $\delta^2\text{H}_p$  around the globe with varying degree of success. For example, studies by Struck et al. (2020a) and Strobel et al. (2021b) demonstrate that  $\delta^2\text{H}_{n\text{-alkane}}$  correlates to (growing season)  $\delta^2\text{H}_p$  but show different  $\epsilon_{\text{app } 2\text{H}}$  values for the  $n$ -alkanes  $\text{C}_{29}$  ( $-126 \pm 16\text{‰}$ ) and  $\text{C}_{31}$  ( $-142 \pm 16\text{‰}$ ) in Mongolia. Overall, Struck (2022) suggests apparent fractionation to have a mean value of  $-132 \pm 15\text{‰}$  in a global compilation, but also noted a substantially larger scatter in humid than in arid climates. In contrast, several previous studies suggest that the apparent fractionation unlikely is constant on a regional scale (Aichner et al., 2010; Berke et al., 2015; Douglas et al., 2012; Hou et al., 2008; Hou et al., 2018; Li et al., 2019; Sachse et al., 2012) and show distinct dependencies, for example, on aridity (Li et al., 2019), precipitation (Aichner et al., 2010; Hou et al., 2018) and relative humidity (Hou et al., 2008; Hou et al., 2018) and also reported a wide range in  $\epsilon_{\text{app } 2\text{H}}$  with substantially smaller values for arid than humid climates (Feakins and Sessions, 2010; Li et al., 2019; Polissar and Freeman, 2010; Smith and Freeman, 2006). Recently, it was found that the plants growth form (i.e., monocot vs dicot) can have an influence on the degree of transpirative leaf water  $^2\text{H}$  enrichment. The growth zone of monocotyledon plants (grasses) is at the intercalary meristem where leaf water is not as  $^2\text{H}$ -enriched as on the more exposed parts. Therefore,  $n$ -alkanes originating from monocotyledon plants (grasses) show more negative values for  $\delta^2\text{H}_{n\text{-alkane}}$  and  $\epsilon_{\text{app } 2\text{H}}$  compared to dicotyledonous plants due to the so-called “signal-dampening” (e.g., Hepp et al., 2020; Lemma et al., 2021; Struck et al., 2020a).

While few paleoclimate studies investigated  $\delta^2\text{H}_{n\text{-alkane}}$  in sediments from South Africa (Section 1.3), only Herrmann et al. (2017) present a first study investigating  $\delta^2\text{H}_{n\text{-alkane}}$  in topsoils for their environmental control along a transect including samples from the northern parts of the SRZ, WRZ and YRZ. The results show that  $\delta^2\text{H}_{n\text{-alkane}}$  in the SRZ significantly correlates with mean annual  $\delta^2\text{H}_p$  while no correlation exists in the WRZ and YRZ.  $\epsilon_{\text{app } 2\text{H}}$  shows no significant correlation to the present vegetation, but distinctly differs between the rainfall zones (SRZ:  $-105 \pm 12\text{‰}$ , WRZ:  $-123 \pm 12\text{‰}$ , and YRZ:  $-97 \pm 11\text{‰}$ ) (Herrmann et al., 2017). Additionally, Hahn et al. (2018) investigated  $\delta^2\text{H}_{n\text{-alkane}}$  in topsoils in the SRZ, but did not aim to investigate an environmental control on the components. Although the WRZ and YRZ are of great interest

for paleohydrological studies, the environmental factors controlling  $\delta^2\text{H}_{n\text{-alkane}}$  and  $\epsilon_{\text{app } 2\text{H}}$  are not well-understood so far, which justifies the need for regional calibration studies in these regions.

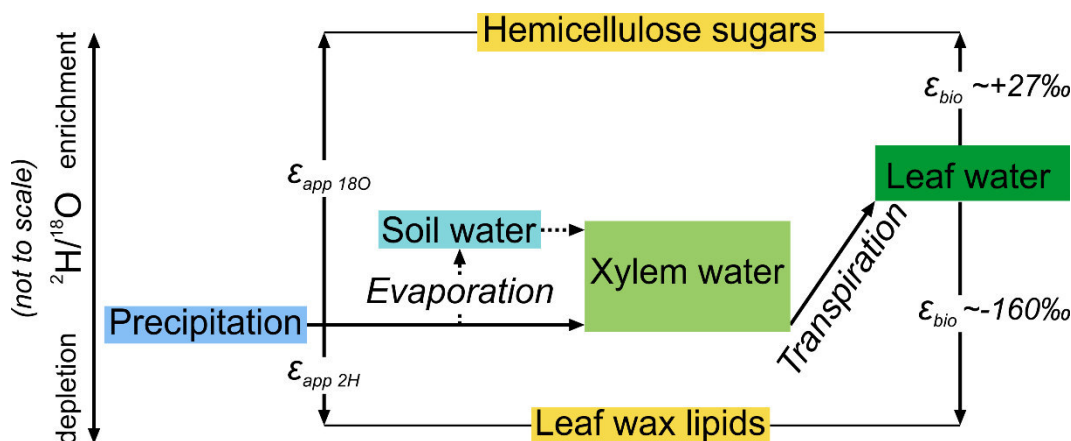


Figure 1.8: Conceptual framework designed by Strobel et al. (2020; Chapter 2) showing isotope fractionation processes between the isotopic signature of precipitation (source water) and the compound-specific hydrogen and oxygen signature of leaf wax-derived  $n$ -alkanes and hemicellulose-derived sugars, respectively. For  $\delta^2\text{H}_{n\text{-alkane}}$  the concept is based on Sachse et al. (2012) and was extended for the  $\delta^{18}\text{O}$  pathway according to Zech et al. (2014a). For  $\delta^2\text{H}$  and  $\delta^{18}\text{O}$  of monocotyledon plants (grasses) the model would have to be modified to take into account the signal dampening (e.g., Hepp et al., 2020; Lemma et al., 2021; Struck et al., 2020a; Zech et al., 2014a). Abbreviations:  $\epsilon_{\text{app}}$  – apparent fractionation of hydrogen isotopes ( $\epsilon_{\text{app } 2\text{H}}$ ) and oxygen isotopes ( $\epsilon_{\text{app } 18\text{O}}$ );  $\epsilon_{\text{bio}}$  – biosynthetic fractionation.

### 1.3.2.2 Hemicellulose-derived sugars and their compound-specific oxygen isotope composition

Another molecular biomarker that has increasingly been studied during the past years are hemicellulose-derived sugars (monosaccharides). They are part of the plants cell structure and consist of non-cyclic or cyclic hydrocarbon chains with one carbonyl group and several hydroxyl groups (Tuthorn et al., 2014). Hemicellulose-derived sugars are relatively resistant against degradation, capture source specific environmental information and provide the potential to be analyzed for their component-specific oxygen isotope ( $\delta^{18}\text{O}_{\text{sugar}}$ ) composition (Hepp et al., 2016; Mekonnen et al., 2019; Zech and Glaser, 2009; Zech et al., 2014a; Zech et al., 2012). Similar to  $\delta^2\text{H}_{n\text{-alkane}}$ , the source of  $\delta^{18}\text{O}_{\text{sugar}}$  is the isotopic composition of (growing season) precipitation ( $\delta^{18}\text{O}_{\text{p}}$ ) modulated by soil and leaf water evapotranspirative  $^{18}\text{O}$  enrichment (e.g., Tuthorn et al., 2014; Zech et al., 2014a; Fig. 1.8). Biosynthetic fractionation ( $\epsilon_{\text{bio } 18\text{O}}$ ), which has been suggested to be  $+27\text{‰}$  (Cernusak et al., 2003; Gessler et al., 2009; Hepp et al., 2021; Schmidt et al., 2001; Sternberg, 1989), leads to additional positive  $\delta^{18}\text{O}_{\text{sugar}}$  values compared to leaf water (Fig. 1.8). Significant correlation between  $\delta^{18}\text{O}_{\text{sugar}}$  and the isotopic composition of leaf water, which was recently found in a climate chamber experiment (Hepp et al., 2021), underlines that  $\epsilon_{\text{bio } 18\text{O}}$  is relatively constant over distinct environmental gradients. However, significant correlation between  $\delta^{18}\text{O}_{\text{sugar}}$  and aridity as well as anti-correlation between  $\delta^{18}\text{O}_{\text{sugar}}$  and relative humidity showing more positive  $\delta^{18}\text{O}_{\text{sugar}}$  values in

arid and less positive  $\delta^{18}\text{O}_{\text{sugar}}$  values in humid areas, demonstrate the important influence of evapotranspirative  $^{18}\text{O}$  enrichment on  $\delta^{18}\text{O}_{\text{sugar}}$  (Hepp et al., 2021; Tuthorn et al., 2014; Zech et al., 2014a). Therefore, it is not unexpected that no correlation between  $\delta^{18}\text{O}_{\text{sugar}}$  and  $\delta^{18}\text{O}_p$  could be found in several studies, indicating that  $\delta^{18}\text{O}_{\text{sugar}}$  is a valuable proxy for evapotranspirative leaf water enrichment (e.g., Hepp et al., 2021; Lemma et al., 2021; Tuthorn et al., 2014). However, similar to *n*-alkanes, it was recently found that the plants growth form (i.e., monocot vs dicot) can have an influence on the degree of transpirative leaf water  $^{18}\text{O}$  enrichment due to the growth zone of monocotyledon plants (grasses) at the intercalary meristem where leaf water is not as  $^{18}\text{O}$ -enriched as on the more exposed parts (e.g., Hepp et al., 2021; Hepp et al., 2020; Lemma et al., 2021; Struck et al., 2020a). Consequently, hemicellulose originating from monocotyledon plants show not as positive  $\delta^{18}\text{O}_{\text{sugar}}$  values compared to dicotyledonous plants due to the so-called “signal-dampening” (Hepp et al., 2020; Lemma et al., 2021; Struck et al., 2020a). Therefore, (past) changes in the vegetation composition have to be considered during the interpretation of  $\delta^{18}\text{O}_{\text{sugar}}$ . In paleoenvironmental research,  $\delta^{18}\text{O}_{\text{sugar}}$  has been successfully applied to several sediment archives, e.g. loess–paleosol sequences (Hepp et al., 2017; Zech et al., 2013) and lacustrine sediments (Bittner et al., 2021; Hepp et al., 2015; Hepp et al., 2019; Zech et al., 2014b).

### 1.3.2.3 Coupled $\delta^2\text{H}_{n\text{-alkane}}\text{--}\delta^{18}\text{O}_{\text{sugar}}$ approach

The two previous subsections demonstrate the challenges of reconstructing changes in  $\delta^2\text{H}_p$  and  $\delta^{18}\text{O}_p$  using  $\delta^2\text{H}_{n\text{-alkane}}$  and  $\delta^{18}\text{O}_{\text{sugar}}$  as single water isotopes. This is because it is challenging to disentangle (past) changes in precipitation and all other factors modulating both biomarker signals (e.g., Sessions, 2016; Tuthorn et al., 2014). To overcome these limitations it has been suggested that coupling of  $\delta^2\text{H}_{n\text{-alkane}}$  and  $\delta^{18}\text{O}_{\text{sugar}}$  in a so-called “paleohygrometer” is a powerful tool (e.g., Zech et al., 2013). The fundamental assumption of the coupled  $\delta^2\text{H}_{n\text{-alkane}}\text{--}\delta^{18}\text{O}_{\text{sugar}}$  approach (paleohygrometer) is that the isotopic composition of leaf water ( $\delta^2\text{H}_{\text{leaf water}}$  and  $\delta^{18}\text{O}_{\text{leaf water}}$ ) can be reconstructed by applying biosynthetic fractionation factors ( $\epsilon_{\text{bio}}$ ) on the measured  $\delta^2\text{H}_{n\text{-alkane}}$  and  $\delta^{18}\text{O}_{\text{sugar}}$  values. For  $\delta^2\text{H}_{n\text{-alkane}}$  a constant  $\epsilon_{\text{bio}}$  value of about  $-160\text{‰}$  (Sachse et al., 2012; Sessions et al., 1999) is applied and for  $\delta^{18}\text{O}_{\text{sugar}}$  the  $\epsilon_{\text{bio}}$  value is assumed to be  $+27\text{‰}$  (Cernusak et al., 2003; Gessler et al., 2009; Hepp et al., 2021; Schmidt et al., 2001; Sternberg et al., 1986; Yakir and DeNiro, 1990). This can be illustrated in a  $\delta^2\text{H}\text{--}\delta^{18}\text{O}$  diagram (Fig. 1.9) where the distance of the reconstructed leaf water to the global meteoric water line (GMWL) is defined as deuterium-excess (Dansgaard, 1964). Due to transpiration via the plants stomata following a local evaporation line (LEL) leaf water ( $\delta^2\text{H}_{\text{leaf water}}$  and  $\delta^{18}\text{O}_{\text{leaf water}}$ ) becomes  $^2\text{H}$ - and  $^{18}\text{O}$ -enriched and will reach isotope steady-state under constant environmental conditions (Farquhar et al., 2007; Feakins and Sessions, 2010; Fig. 1.9).

## Chapter 1

The concept is furthermore based on the fact that the isotopic composition of precipitation plots typically close to the GMWL ( $\delta^2\text{H}_p=8\cdot^{18}\text{O}_p+10$ ; Dansgaard, 1964). However, the isotope values of local precipitation plot along the local meteoric water line (LMWL), which has a slightly different slope as the GMWL, leading to lower slopes in arid continental regions compared to humid coastal sites (Craig, 1961; Dansgaard, 1964; Kendall and Coplen, 2001; Putman et al., 2019). This process is accompanied by equilibrium and kinetic isotope fractionation processes (Horita and Wesolowski, 1994; Merlivat, 1978). The isotopic composition of the plant-source water ( $\delta^2\text{H}_{\text{source water}}$  and  $\delta^{18}\text{O}_{\text{source water}}$ ) is the intercept of the LEL and the LMWL (Fig. 1.9). The difference between deuterium-excess of leaf water and reconstructed plant-source water serves as a proxy for relative humidity (RH) (e.g., Lemma et al., 2021; Tuthorn et al., 2015; Zech et al., 2013; Fig. 1.9). Further details and the mathematical background of this approach is given in Lemma et al. (2021), Hepp et al. (2021), Hepp et al. (2020), Hepp et al. (2015), Hepp et al. (2019), Hepp et al. (2017), Tuthorn et al. (2015) and Zech et al. (2013).

The proxies derived from the coupled  $\delta^2\text{H}_{n\text{-alkane}}-\delta^{18}\text{O}_{\text{sugar}}$  approach, i.e., leaf water ( $\delta^2\text{H}_{\text{leaf water}}$  and  $\delta^{18}\text{O}_{\text{leaf water}}$ ), plant-source water ( $\delta^2\text{H}_{\text{source water}}$  and  $\delta^{18}\text{O}_{\text{source water}}$ ), deuterium-excess and RH have recently been validated for example in a climate chamber experiment (Hepp et al., 2021) as well as on topsoils from Europe (Hepp et al., 2020), South America (Tuthorn et al., 2015) and Ethiopia (Lemma et al., 2021). Additionally, the approach has already been applied successfully for example to loess–paleosol sequences (Hepp et al., 2017; Zech et al., 2013) and lacustrine sediments (Hepp et al., 2015; Hepp et al., 2019; Hepp et al., 2017) demonstrating the great potential of analyzing and coupling  $\delta^2\text{H}_{n\text{-alkane}}$  and  $\delta^{18}\text{O}_{\text{sugar}}$  in paleoclimate studies.



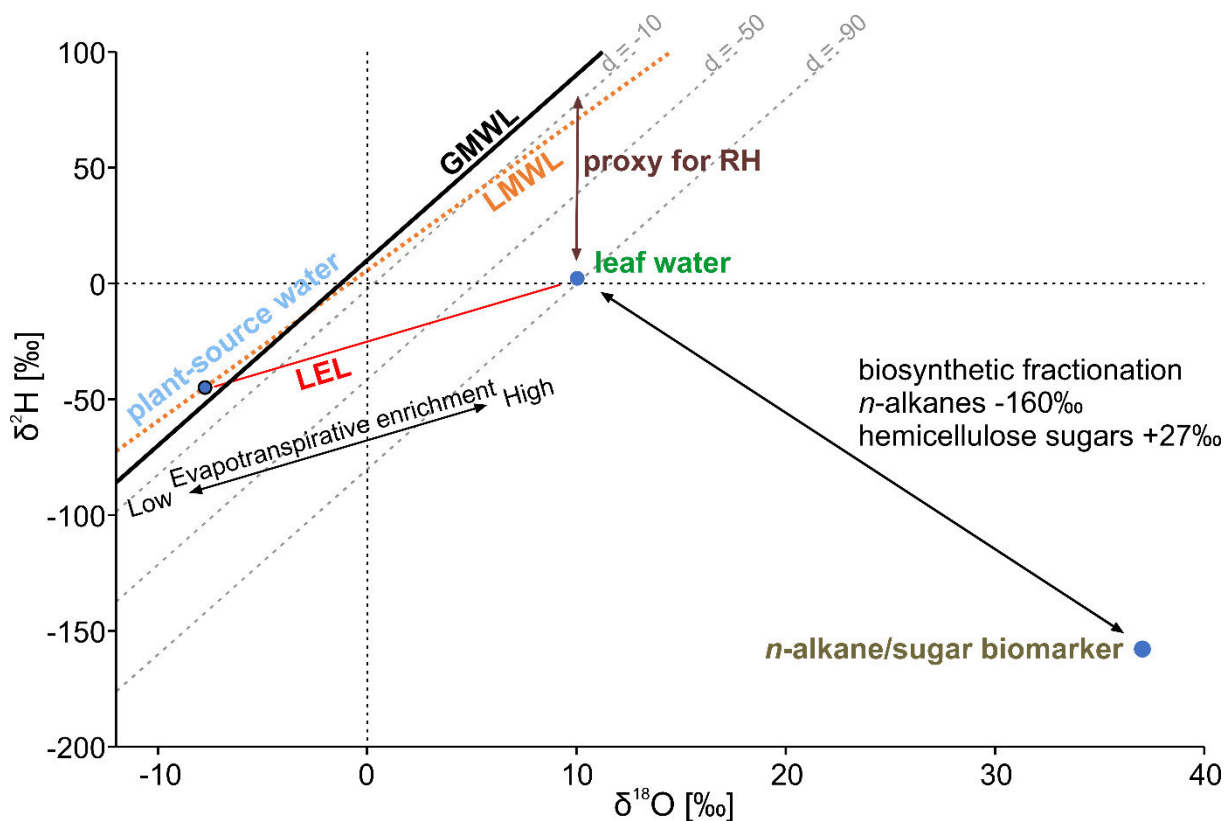


Figure 1.9: Conceptual framework of the coupled  $\delta^2\text{H}_{n\text{-alkane}}-\delta^{18}\text{O}_{\text{sugar}}$  approach (paleohygrometer) displayed as  $\delta^2\text{H}-\delta^{18}\text{O}$  diagram after Zech et al. (2013). The black double arrow indicates natural processes of evapotranspirative enrichment of leaf water along local evaporation lines (red line) and biosynthetic fractionation during biomarker synthesis. Grey dashed lines indicate the deuterium-excess, which can be used as proxy for relative humidity (brown double arrow). Abbreviations: GMWL – Global Meteoric Water Line; LMWL – Local Meteoric Water Line; LEL – Local Evaporation Line; d – deuterium-excess. Note that the model would have to be adapted for samples in which  $\delta^2\text{H}_{n\text{-alkane}}$  and  $\delta^{18}\text{O}_{\text{sugar}}$  originate from grasses due to signal dampening, but this is not part of this thesis.

#### 1.4 Thesis outline and objectives

Future scenarios predict changes in the amount and seasonality of precipitation as well as moisture availability for large parts of South Africa, which has enormous implications for all levels of biophysical and socio-economic processes. However, these predictions are based on past environmental and climatic dynamics, which are subject to considerable debate in South Africa so far (Section 1.3.1). Scarcity of suitable sediment archives for paleoenvironmental and paleoclimatic studies in South Africa may be a major factor but the ambiguous nature of existing studies may also play a role.

This PhD thesis aims to generate and interpret new proxy data to improve the understanding of Late Quaternary climate change and its drivers at South Africa's central southern Cape coast. For that purpose, the regional potential of  $\delta^2\text{H}_{n\text{-alkane}}$  and  $\delta^{18}\text{O}_{\text{sugar}}$  and their coupling for paleoenvironmental and paleoclimatic reconstruction are evaluated for the southern Cape coast of South Africa. Sediment cores from Lake Voëlvlei and the peatland Vankervelsvlei are studied through a multi-proxy approach, including the regionally calibrated biomarkers as well as assays of well-established methods such as organic and inorganic geochemistry and paleoecology, to contribute to an understanding of the lacustrine and peat systems and to gain the best possible chronological control in both sedimentary archives. New and well-established proxy data are discussed together to infer past environmental and climatic changes, their regional heterogeneity and potential drivers along South Africa's central southern Cape coast. To that end, the following objectives are addressed:

**1) Evaluation of  $\delta^2\text{H}_{n\text{-alkane}}$  and  $\delta^{18}\text{O}_{\text{sugar}}$  on modern reference material, and coupling both isotopes in the “paleohygrometer” approach for their potential to reconstruct climate in South Africa**

Do  $\delta^2\text{H}_{n\text{-alkane}}$  and  $\delta^{18}\text{O}_{\text{sugar}}$  reflect the isotopic composition of precipitation and to which degree are they affected by environmental conditions? Does coupling of  $\delta^2\text{H}_{n\text{-alkane}}$  and  $\delta^{18}\text{O}_{\text{sugar}}$  enable a more robust reconstruction of the isotopic composition of precipitation and additional relative humidity?

**2) Holocene environmental and climatic dynamics along the central southern Cape coast of South Africa**

Which trends in contributions of different precipitation sources and ecosystem moisture availability can be reconstructed? Do the results from Voëlvlei, Vankervelsvlei and other regional records provide a coherent signal for precipitation source and moisture availability along South Africa's central southern Cape coast during the Holocene?

### 3) Late Quaternary environmental and climatic dynamics on South Africa's central southern Cape coast

Do relationships between precipitation source and ecosystem moisture availability still exist during the Late Quaternary? Which drivers of paleoenvironmental changes can be derived for paleoenvironmental and paleoclimatic variations during the Late Quaternary?

**Chapter 2** is a study published in *Science of the Total Environment* entitled “*The potential of  $\delta^2\text{H}_{n\text{-alkanes}}$  and  $\delta^{18}\text{O}_{\text{sugar}}$  for paleoclimate reconstruction – A regional calibration study for South Africa*” (Strobel et al., 2020). This study investigates compound-specific  $\delta^2\text{H}_{n\text{-alkane}}$  and  $\delta^{18}\text{O}_{\text{sugar}}$  signatures in topsoils along a South African transect.  $\delta^2\text{H}_{n\text{-alkane}}$  and  $\delta^{18}\text{O}_{\text{sugar}}$  signatures and reconstructed plant-source water are all correlated with the modelled isotopic composition of precipitation in order to evaluate their potential for paleo-climate reconstruction. Correlation of the apparent fractionation of both water isotopes ( $\epsilon_{\text{app } 2\text{H}}$  and  $\epsilon_{\text{app } 18\text{O}}$ ) with climate parameters provide a test for their environmental control, i.e., the degree of evapotranspirative  $^2\text{H}$  and  $^{18}\text{O}$  enrichment. Additionally, precision and accuracy of reconstructed relative humidity derived from the coupled  $\delta^2\text{H}_{n\text{-alkane}}-\delta^{18}\text{O}_{\text{sugar}}$  approach are tested through their correlation with modelled relative humidity. The study provides a foundation for the application of compound-specific  $\delta^2\text{H}_{n\text{-alkane}}$  and  $\delta^{18}\text{O}_{\text{sugar}}$  and results of the coupled  $\delta^2\text{H}_{n\text{-alkane}}-\delta^{18}\text{O}_{\text{sugar}}$  approach in the following paleoenvironmental and paleoclimatic studies.

**Chapter 3** is a study published in *Climate of the Past* entitled “*Holocene sea level and environmental change at the southern Cape - an 8.5 kyr multi-proxy paleoclimate record from lake Voëlvlei, South Africa*” (Strobel et al., 2021a). It investigates the paleoenvironmental and paleoclimatic evolution in the western parts of South Africa's central southern Cape coast. Extensive dating was undertaken, enabling the establishment of a reliable chronology with a basal age of ~8.5 ka. Assays of organic and inorganic geochemical and paleoecological methods as well as  $\delta^2\text{H}_{n\text{-alkane}}$  are analyzed in high temporal resolution. Past sea level and environmental variations are investigated.  $\delta^2\text{H}_{n\text{-alkane}}$  is discussed in context of past changes of precipitation sources, which are likely referring to strengthened/weakened contributions of the major atmospheric circulation systems at the site. The results are further discussed in comparison to (supra-)regional paleoenvironmental records.

**Chapter 4** is a manuscript submitted to *Quaternary Science Reviews* entitled “*Reconstructing Late Quaternary precipitation and its source on the southern Cape coast of South Africa: A multi-proxy paleoenvironmental record from Vankervelsvlei*” (Strobel et al., submitted). This study refines and expands a previous published study by Strobel et al. (2019) and investigates the paleoenvironmental and paleoclimatic evolution in the eastern parts of South Africa's central southern Cape coast. The sediments have been well-dated through extensive OSL and radiocarbon dating, resulting in a basal age of ~250 ka. In an extensive multi-proxy approach,

## Chapter 1

the coupled  $\delta^2\text{H}_{n\text{-alkane}}-\delta^{18}\text{O}_{\text{sugar}}$  approach was applied to the sediments, gaining new knowledge about past environmental and climatic changes at the site. This includes the isotopic composition of precipitation (refers to contributions of precipitation from the major atmospheric circulation systems) and relative humidity (refers to local moisture availability). Results are discussed in the context of previous studies at the site. Additionally, the spatial variability of precipitation and ecosystem moisture along South Africa's central southern Cape coast is discussed in comparison to further regional records, inter alia the results discussed in **Chapter 3**.

**Chapter 5** provides a synthesis of the obtained results from **Chapters 2 to 4** and discusses potential driving forces of environmental and climatic variations at South Africa's central southern Cape coast during the Holocene and the Late Quaternary. The outcomes are further discussed in comparison to supra-regional records referring to past changes in southern hemispheric circulation pattern. **Chapter 6** concludes this thesis and provides an outlook including unresolved questions, which may represent opportunities for future research.

## References

- Aichner, B., Herzs Schuh, U., Wilkes, H., Vieth, A., Böhner, J., 2010.  $\delta D$  values of *n*-alkanes in Tibetan lake sediments and aquatic macrophytes – A surface sediment study and application to a 16ka record from Lake Koucha. *Organic Geochemistry* 41, 779-790.
- Bar-Matthews, M., Marean, C.W., Jacobs, Z., Karkanas, P., Fisher, E.C., Herries, A.I.R., Brown, K., Williams, H.M., Bernatchez, J., Ayalon, A., Nilssen, P.J., 2010. A high resolution and continuous isotopic speleothem record of paleoclimate and paleoenvironment from 90 to 53 ka from Pinnacle Point on the south coast of South Africa. *Quaternary Science Reviews* 29, 2131-2145.
- Bard, E., Rickaby, R.E.M., 2009. Migration of the subtropical front as a modulator of glacial climate. *Nature* 460, 380-383.
- Bateman, M.D., Carr, A.S., Dunajko, A.C., Holmes, P.J., Roberts, D.L., McLaren, S.J., Bryant, R.G., Marker, M.E., Murray-Wallace, C.V., 2011. The evolution of coastal barrier systems: a case study of the Middle-Late Pleistocene Wilderness barriers, South Africa. *Quaternary Science Reviews* 30, 63-81.
- Bateman, M.D., Holmes, P.J., Carr, A.S., Horton, B.P., Jaiswal, M.K., 2004. Aeolianite and barrier dune construction spanning the last two glacial–interglacial cycles from the southern Cape coast, South Africa. *Quaternary Science Reviews* 23, 1681-1698.
- Berger, A., Loutre, M.F., 1991. Insolation values for the climate of the last 10 million years. *Quaternary Science Reviews* 10, 297-317.
- Berke, M.A., Tipple, B.J., Hambach, B., Ehleringer, J.R., 2015. Life form-specific gradients in compound-specific hydrogen isotope ratios of modern leaf waxes along a North American Monsoonal transect. *Oecologia* 179, 981-997.
- Birch, G.F., du Plessis, A., Willis, J.P., 1978. Offshore and onland geological and geophysical investigation in the Wilderness Lakes Region. *Transactions of the Geological Society of South Africa* 81, 339-352.
- Bittner, L., Gil-Romera, G., Grady, D., Lamb, H.F., Lorenz, E., Weiner, M., Meyer, H., Bromm, T., Glaser, B., Zech, M., 2021. The Holocene lake-evaporation history of the afro-alpine Lake Garba Guracha in the Bale Mountains, Ethiopia, based on  $\delta^{18}O$  records of sugar biomarker and diatoms. *Quaternary Research*, 1-14.
- Bliedtner, M., Schäfer, I.K., Zech, R., von Suchodoletz, H., 2018. Leaf wax *n*-alkanes in modern plants and topsoils from eastern Georgia (Caucasus) – implications for reconstructing regional paleovegetation. *Biogeosciences* 15, 3927-3936.
- Bliedtner, M., Struck, J., Strobel, P., Salazar, G., Szidat, S., Bazarradnaa, E., Lloren, R., Dubois, N., Zech, R., 2021. Late Holocene climate changes in the Altai Region based on a first high-resolution biomarker isotope record from Lake Khar Nuur. *Geophysical Research Letters* 48, e2021GL094299.
- Bowen, G.J., 2020. The Online Isotopes in Precipitation Calculator, version 3.1. URL: <http://www.waterisotopes.org>.
- Bowen, G.J., Revenaugh, J., 2003. Interpolating the isotopic composition of modern meteoric precipitation. *Water Resources Research* 39, 1-10.
- Bowen, G.J., Wassenaar, L.I., Hobson, K.A., 2005. Global application of stable hydrogen and oxygen isotopes to wildlife forensics. *Oecologia* 143, 337-348.
- Braun, K., Bar-Matthews, M., Ayalon, A., Zilberman, T., Matthews, A., 2017. Rainfall isotopic variability at the intersection between winter and summer rainfall regimes in coastal South Africa (Mossel Bay, Western Cape Province). *South African Journal of Geology* 120, 323-340.
- Braun, K., Bar-Matthews, M., Matthews, A., Ayalon, A., Cowling, R.M., Karkanas, P., Fisher, E.C., Dyez, K., Zilberman, T., Marean, C.W., 2019. Late Pleistocene records of speleothem stable isotopic compositions from Pinnacle Point on the South African south coast. *Quaternary Research* 91, 265-288.
- Braun, K., Bar-Matthews, M., Matthews, A., Ayalon, A., Zilberman, T., Cowling, R.M., Fisher, E.C., Herries, A.I.R., Brink, J.S., Marean, C.W., 2020. Comparison of climate and environment on the

## Chapter 1

- edge of the Palaeo-Agulhas Plain to the Little Karoo (South Africa) in Marine Isotope Stages 5–3 as indicated by speleothems. *Quaternary Science Reviews* 235, 105803.
- Caley, T., Extier, T., Collins, J.A., Schefuß, E., Dupont, L., Malaizé, B., Rossignol, L., Souron, A., McClymont, E.L., Jimenez-Espejo, F.J., García-Comas, C., Eynaud, F., Martinez, P., Roche, D.M., Jorry, S.J., Charlier, K., Wary, M., Gourves, P.-Y., Billy, I., Giraudeau, J., 2018. A two-million-year-long hydroclimatic context for hominin evolution in southeastern Africa. *Nature* 560, 76-79.
- Caley, T., Kim, J.H., Malaizé, B., Giraudeau, J., Laepple, T., Caillon, N., Charlier, K., Rebaubier, H., Rossignol, L., Castañeda, I.S., Schouten, S., Sinninghe Damsté, J.S., 2011. High-latitude obliquity as a dominant forcing in the Agulhas current system. *Climate of the Past* 7, 1285-1296.
- Carr, A.S., Bateman, M.D., Holmes, P.J., 2007. Developing a 150ka luminescence chronology for the barrier dunes of the southern Cape, South Africa. *Quaternary Geochronology* 2, 110-116.
- Carr, A.S., Bateman, M.D., Roberts, D.L., Murray-Wallace, C.V., Jacobs, Z., Holmes, P.J., 2010a. The last interglacial sea-level high stand on the southern Cape coastline of South Africa. *Quaternary Research* 73, 351-363.
- Carr, A.S., Boom, A., Dunajko, A., Bateman, M.D., Holmes, P.J., Berrio, J.-C., 2010b. New evidence for the age and palaeoecology of the Knysna Formation, South Africa. *South African Journal of Geology* 113, 241-256.
- Carr, A.S., Chase, B.M., Boom, A., Medina-Sanchez, J., 2016. Stable isotope analyses of rock hyrax faecal pellets, hyraceum and associated vegetation in southern Africa: Implications for dietary ecology and palaeoenvironmental reconstructions. *Journal of Arid Environments* 134, 33-48.
- Carr, A.S., Thomas, D.S.G., Bateman, M.D., 2006a. Climatic and sea level controls on Late Quaternary eolian activity on the Agulhas Plain, South Africa. *Quaternary Research* 65, 252-263.
- Carr, A.S., Thomas, D.S.G., Bateman, M.D., Meadows, M.E., Chase, B., 2006b. Late Quaternary palaeoenvironments of the winter-rainfall zone of southern Africa: Palynological and sedimentological evidence from the Agulhas Plain. *Palaeogeography, Palaeoclimatology, Palaeoecology* 239, 147-165.
- Castañeda, I.S., Schouten, S., 2011. A review of molecular organic proxies for examining modern and ancient lacustrine environments. *Quaternary Science Reviews* 30, 2851-2891.
- Cawthra, H.C., Bergh, E.W., Wiles, E.A., Compton, J.S., 2021. Late Quaternary deep marine sediment records off southern Africa. *South African Journal of Geology* 124, 1007-1032.
- Cernusak, L.A., Barbour, M.M., Arndt, S.K., Cheesman, A.W., English, N.B., Feild, T.S., Helliker, B.R., Holloway-Phillips, M.M., Holtum, J.A.M., Kahmen, A., McInerney, F.A., Munksgaard, N.C., Simonin, K.A., Song, X., Stuart-Williams, H., West, J.B., Farquhar, G.D., 2016. Stable isotopes in leaf water of terrestrial plants. *Plant, Cell & Environment* 39, 1087-1102.
- Cernusak, L.A., Wong, S.C., Farquhar, G.D., 2003. Oxygen isotope composition of phloem sap in relation to leaf water in *Ricinus communis*. *Functional Plant Biology* 30, 1059-1070.
- Chase, B., Harris, C., de Wit, M.J., Kramers, J., Doel, S., Stankiewicz, J., 2021. South African speleothems reveal influence of high- and lowlatitude forcing over the past 113.5 k.y. *Geology*.
- Chase, B.M., Boom, A., Carr, A.S., Chevalier, M., Quick, L.J., Verboom, G.A., Reimer, P.J., 2019. Extreme hydroclimate response gradients within the western Cape Floristic region of South Africa since the Last Glacial Maximum. *Quaternary Science Reviews* 219, 297-307.
- Chase, B.M., Boom, A., Carr, A.S., Meadows, M.E., Reimer, P.J., 2013. Holocene climate change in southernmost South Africa: rock hyrax middens record shifts in the southern westerlies. *Quaternary Science Reviews* 82, 199-205.
- Chase, B.M., Boom, A., Carr, A.S., Quick, L.J., Reimer, P.J., 2020. High-resolution record of Holocene climate change dynamics from southern Africa's temperate-tropical boundary, Baviaanskloof, South Africa. *Palaeogeography, Palaeoclimatology, Palaeoecology* 539, 109518.
- Chase, B.M., Chevalier, M., Boom, A., Carr, A.S., 2017. The dynamic relationship between temperate and tropical circulation systems across South Africa since the last glacial maximum. *Quaternary Science Reviews* 174, 54-62.
- Chase, B.M., Meadows, M.E., 2007. Late Quaternary dynamics of southern Africa's winter rainfall zone. *Earth-Science Reviews* 84, 103-138.

- Chase, B.M., Quick, L.J., 2018. Influence of Agulhas forcing of Holocene climate change in South Africa's southern Cape. *Quaternary Research* 90, 303-309.
- Cohen, A.L., 1993. A holocene sea surface temperature record in mollusc shells from the South African coast, PhD thesis. University of Cape Town, Cape Town.
- Cohen, A.L., Tyson, P.D., 1995. Sea-surface temperature fluctuations during the Holocene off the south coast of Africa: implications for terrestrial climate and rainfall. *The Holocene* 5, 304-312.
- Cormier, M.-A., Werner, R.A., Sauer, P.E., Gröcke, D.R., Leuenberger, M.C., Wieloch, T., Schleucher, J., Kahmen, A., 2018.  $^2\text{H}$ -fractionations during the biosynthesis of carbohydrates and lipids imprint a metabolic signal on the  $\delta^2\text{H}$  values of plant organic compounds. *New Phytologist* 218, 479-491.
- Craig, H., 1961. Isotopic Variations in Meteoric Waters. *Science* 133, 1702-1703.
- Dansgaard, W., 1964. Stable isotopes in precipitation. *Tellus* 16, 436-468.
- Douglas, P.M.J., Pagani, M., Brenner, M., Hodell, D.A., Curtis, J.H., 2012. Aridity and vegetation composition are important determinants of leaf-wax  $\delta\text{D}$  values in southeastern Mexico and Central America. *Geochimica et Cosmochimica Acta* 97, 24-45.
- Douville, H., Raghavan, K., Renwick, J., Allan, R.P., Arias, P.A., Barlow, M., Cerezo-Mota, R., Cherchi, A., Gan, T.Y., Gergis, J., Jiang, D., Khan, A., Pokam Mba, W., Rosenfeld, D., Tierney, J., Zolina, O., 2021. Water Cycle Changes, in: Masson-Delmotte, V., Zhai, P., Pirani, A., Connors, S. L., Péan, C., Berger, S., Caud, N., Chen, Y., Goldfarb, L., Gomis, M. I., Huang, M., Leitzell, K., Lonnoy, E., Matthews, J. B. R., Maycock, T. K., Waterfield, T., Yelekçi, O., Yu, R., B. Zhou (Ed.), *Climate Change 2021: The Physical Science Basis. Contribution of Working Group I to the Sixth Assessment Report of the Intergovernmental Panel on Climate Change*. Cambridge University Press, Cambridge, In Press.
- du Plessis, N., Chase, B.M., Quick, L.J., Meadows, M.E., 2021a. A Late Holocene pollen and microcharcoal record from Eilandvlei, southern Cape coast, South Africa, in: Runge, J., Gosling, W.D., Lézine, A.-M., Scott, L. (Eds.), *Quaternary Vegetation Dynamics – The African Pollen Database*. CRC Press, London, pp. 293-300.
- du Plessis, N., Chase, B.M., Quick, L.J., Strobel, P., Haberzettl, T., Meadows, M.E., 2021b. A c. 650 year pollen and microcharcoal record from Vankervelsvlei, South Africa, in: Runge, J., Gosling, W.D., Lézine, A.-M., Scott, L. (Eds.), *Quaternary Vegetation Dynamics – The African Pollen Database*. CRC Press, London, pp. 301-308.
- Dupont, L.M., Zhao, X., Charles, C., Faith, J.T., Braun, D., 2021. Continuous vegetation record of the Greater Cape Floristic Region (South Africa) covering the past 300 thousand years (IODP U1479). *Clim. Past Discuss.* 2021, 1-32.
- DWD (Deutscher Wetterdienst) - Climate Data Center, 2021. Recent and historical dataset: Monthly mean precipitation and mean air temperature for stations Cape Town, George Airport and Durban, worldwide, version recent, last accessed: 2021-09-02. [https://opendata.dwd.de/climate\\_environment/CDC/observations\\_global/CLIMAT/](https://opendata.dwd.de/climate_environment/CDC/observations_global/CLIMAT/).
- Eglinton, G., Hamilton, R.J., 1967. Leaf Epicuticular Waxes. *Science* 156, 1322-1335.
- Eglinton, T.I., Eglinton, G., 2008. Molecular proxies for paleoclimatology. *Earth and Planetary Science Letters* 275, 1-16.
- Eley, Y., Dawson, L., Black, S., Andrews, J., Pedentchouk, N., 2014. Understanding  $^2\text{H}/^1\text{H}$  systematics of leaf wax *n*-alkanes in coastal plants at Stiffkey saltmarsh, Norfolk, UK. *Geochimica et Cosmochimica Acta* 128, 13-28.
- Engelbrecht, C.J., Landman, W.A., 2016. Interannual variability of seasonal rainfall over the Cape south coast of South Africa and synoptic type association. *Climate Dynamics* 47, 295-313.
- Engelbrecht, C.J., Landman, W.A., Engelbrecht, F.A., Malherbe, J., 2015. A synoptic decomposition of rainfall over the Cape south coast of South Africa. *Climate Dynamics* 44, 2589-2607.
- Engelbrecht, F.A., Monteiro, P.M.S., 2021. The IPCC Assessment Report Six Working Group 1 report and southern Africa: Reasons to take action. *South African Journal of Science* 117.
- ESRI Inc., 2020. World Imagery Online Basemap. Esri, DigitalGlobe, GeoEye, Earthstar Geographics, CNES/Airbus DS, USDA, USGS, Aerogrid, IGN, and the GIS User Community.

## Chapter 1

- Farquhar, G.D., Cernusak, L.A., Barnes, B., 2007. Heavy Water Fractionation during Transpiration. *Plant Physiology* 143, 11-18.
- Favre, A., Hewitson, B., Lennard, C., Cerezo-Mota, R., Tadross, M., 2013. Cut-off Lows in the South Africa region and their contribution to precipitation. *Climate Dynamics* 41, 2331-2351.
- Feakins, S.J., Sessions, A.L., 2010. Controls on the D/H ratios of plant leaf waxes in an arid ecosystem. *Geochimica et Cosmochimica Acta* 74, 2128-2141.
- Fey, M., 2010. *Soils of South Africa*. Cambridge University Press, Cambridge.
- Fick, S.E., Hijmans, R.J., 2017. WorldClim 2: new 1-km spatial resolution climate surfaces for global land areas. *International Journal of Climatology* 37, 4302-4315.
- Fischer, H., Fundel, F., Ruth, U., Twarloh, B., Wegner, A., Udisti, R., Becagli, S., Castellano, E., Morganti, A., Severi, M., Wolff, E., Littot, G., Röthlisberger, R., Mulvaney, R., Hutterli, M.A., Kaufmann, P., Federer, U., Lambert, F., Bigler, M., Hansson, M., Jonsell, U., de Angelis, M., Boutron, C., Siggaard-Andersen, M.-L., Steffensen, J.P., Barbante, C., Gaspari, V., Gabrielli, P., Wagenbach, D., 2007. Reconstruction of millennial changes in dust emission, transport and regional sea ice coverage using the deep EPICA ice cores from the Atlantic and Indian Ocean sector of Antarctica. *Earth and Planetary Science Letters* 260, 340-354.
- Gessler, A., Brandes, E., Buchmann, N., Helle, G., Rennenberg, H., Barnard, R.L., 2009. Tracing carbon and oxygen isotope signals from newly assimilated sugars in the leaves to the tree-ring archive. *Plant, Cell & Environment* 32, 780-795.
- Gillett, N.P., Kell, T.D., Jones, P.D., 2006. Regional climate impacts of the Southern Annular Mode. *Geophysical Research Letters* 33, L23704.
- Griepentrog, M., De Wispelaere, L., Bauters, M., Bodé, S., Hemp, A., Verschuren, D., Boeckx, P., 2019. Influence of plant growth form, habitat and season on leaf-wax *n*-alkane hydrogen-isotopic signatures in equatorial East Africa. *Geochimica et Cosmochimica Acta* 263, 122-139.
- Haberzettl, T., Baade, J., Compton, J., Daut, G., Dupont, L., Finch, J., Frenzel, P., Green, A., Hahn, A., Hebbeln, D., Helmschrot, J., Humphries, M., Kasper, T., Kirsten, K., Mäusbacher, R., Meadows, M., Meschner, S., Quick, L., Schefuß, E., Wündsche, M., Zabel, M., 2014. Paleoenvironmental investigations using a combination of terrestrial and marine sediments from South Africa - The RAIN (Regional Archives for Integrated iNvestigations) approach. *Zentralblatt für Geologie und Paläontologie, Teil I* 2014, 55-73.
- Haberzettl, T., Kirsten, K.L., Kasper, T., Franz, S., Reinwarth, B., Baade, J., Daut, G., Meadows, M.E., Su, Y., Mäusbacher, R., 2019. Using <sup>210</sup>Pb-data and paleomagnetic secular variations to date anthropogenic impact on a lake system in the Western Cape, South Africa. *Quaternary Geochronology* 51, 53-63.
- Hahn, A., Miller, C., Andó, S., Bouimetarhan, I., Cawthra, H.C., Garzanti, E., Green, A.N., Radeff, G., Schefuß, E., Zabel, M., 2018. The provenance of terrigenous components in marine sediments along the east coast of southern Africa. *Geochemistry, Geophysics, Geosystems* 19, 1946-1962.
- Hahn, A., Schefuß, E., Andò, S., Cawthra, H.C., Frenzel, P., Kugel, M., Meschner, S., Mollenhauer, G., Zabel, M., 2017. Southern Hemisphere anticyclonic circulation drives oceanic and climatic conditions in late Holocene southernmost Africa. *Climate of the Past* 13, 649-665.
- Harris, C., Burgers, C., Miller, J., Rawoot, F., 2010. O- and H-isotope record of Cape Town rainfall from 1996 to 2008, and its application to recharge studies of Table Mountain groundwater, South Africa. *South African Journal of Geology* 113, 33-56.
- Hart, N.C.G., Reason, C.J.C., Fauchereau, N., 2013. Cloud bands over southern Africa: seasonality, contribution to rainfall variability and modulation by the MJO. *Climate Dynamics* 41, 1199-1212.
- Hepp, J., Mayr, C., Rozanski, K., Schäfer, I.K., Tuthorn, M., Glaser, B., Juchelka, D., Stichler, W., Zech, R., Zech, M., 2021. Validation of a coupled  $\delta^2\text{H}_{n\text{-alkane}}-\delta^{18}\text{O}_{\text{sugar}}$  paleohygrometer approach based on a climate chamber experiment. *Biogeosciences* 18, 5363-5380.
- Hepp, J., Rabus, M., Anhäuser, T., Bromm, T., Laforsch, C., Sirocko, F., Glaser, B., Zech, M., 2016. A sugar biomarker proxy for assessing terrestrial versus aquatic sedimentary input. *Organic Geochemistry* 98, 98-104.



- Hepp, J., Schäfer, I.K., Lanny, V., Franke, J., Bliedtner, M., Rozanski, K., Glaser, B., Zech, M., Eglinton, T.I., Zech, R., 2020. Evaluation of bacterial glycerol dialkyl glycerol tetraether and  $2\text{H}-18\text{O}$  biomarker proxies along a central European topsoil transect. *Biogeosciences* 17, 741-756.
- Hepp, J., Tuthorn, M., Zech, R., Mügler, I., Schlütz, F., Zech, W., Zech, M., 2015. Reconstructing lake evaporation history and the isotopic composition of precipitation by a coupled  $\delta^{18}\text{O}-\delta^2\text{H}$  biomarker approach. *Journal of Hydrology* 529, 622-631.
- Hepp, J., Wüthrich, L., Bromm, T., Bliedtner, M., Schäfer, I.K., Glaser, B., Rozanski, K., Sirocko, F., Zech, R., Zech, M., 2019. How dry was the Younger Dryas? Evidence from a coupled  $\delta^2\text{H}-\delta^{18}\text{O}$  biomarker paleohygrometer applied to the Gemündener Maar sediments, Western Eifel, Germany. *Climate of the Past* 15, 713-733.
- Hepp, J., Zech, R., Rozanski, K., Tuthorn, M., Glaser, B., Greule, M., Keppler, F., Huang, Y., Zech, W., Zech, M., 2017. Late Quaternary relative humidity changes from Mt. Kilimanjaro, based on a coupled  $^2\text{H}-^{18}\text{O}$  biomarker paleohygrometer approach. *Quaternary International* 438, Part B, 116-130.
- Herrmann, N., Boom, A., Carr, A.S., Chase, B.M., West, A.G., Zabel, M., Schefuß, E., 2017. Hydrogen isotope fractionation of leaf wax *n*-alkanes in southern African soils. *Organic Geochemistry* 109, 1-13.
- Horita, J., Wesolowski, D.J., 1994. Liquid-vapor fractionation of oxygen and hydrogen isotopes of water from the freezing to the critical temperature. *Geochimica et Cosmochimica Acta* 58, 3425-3437.
- Hou, J., D'Andrea, W.J., Huang, Y., 2008. Can sedimentary leaf waxes record D/H ratios of continental precipitation? Field, model, and experimental assessments. *Geochimica et Cosmochimica Acta* 72, 3503-3517.
- Hou, J., Tian, Q., Wang, M., 2018. Variable apparent hydrogen isotopic fractionation between sedimentary *n*-alkanes and precipitation on the Tibetan Plateau. *Organic Geochemistry* 122, 78-86.
- Ibebuchi, C.C., 2021a. On the Relationship between Circulation Patterns, the Southern Annular Mode, and Rainfall Variability in Western Cape. *Atmosphere* 12, 753.
- Ibebuchi, C.C., 2021b. Revisiting the 1992 severe drought episode in South Africa: the role of El Niño in the anomalies of atmospheric circulation types in Africa south of the equator. *Theoretical and Applied Climatology* 146, 723-740.
- Illenberger, W.K., 1996. The geomorphologic evolution of the Wilderness dune cordons, South Africa. *Quaternary International* 33, 11-20.
- IPCC, 2021. *Climate Change 2021: The Physical Science Basis. Contribution of Working Group I to the Sixth Assessment Report of the Intergovernmental Panel on Climate Change*. Cambridge University Press, Cambridge.
- Irving, S.J.E., 1998. Late quaternary palaeoenvironments at Vankervelsvlei, near Knysna, South Africa, Master thesis. University of Cape Town, Rondebosch.
- Irving, S.J.E., Meadows, M.E., 1997. Radiocarbon chronology and organic matter accumulation at Vankervelsvlei, near Knysna, South Africa. *South African Geographical Journal* 79, 101-105.
- Jarvis, A., Reuter, H.I., Nelson, A., Guevara, E., 2008. Hole-filled SRTM for the globe Version 4, available from the CGIARCSI SRTM 30m Database. Available online at: <http://srtm.csi.cgiar.org>.
- Johnson, M.R., Anhausser, C.R., Thomas, R.J., 2006. *The geology of South Africa*. Geological Society of South Africa, Johannesburg/Council for Geoscience, Pretoria.
- Jury, M.R., MacArthur, C.I., Brundrit, G.B., 1990. Pulsing of the Benguela upwelling region: large-scale atmospheric controls. *South African Journal of Marine Science* 9, 27-41.
- Jury, M.R., Valentine, H.R., Lutjeharms, J.R.E., 1993. Influence of the Agulhas Current on Summer Rainfall along the Southeast Coast of South Africa. *Journal of Applied Meteorology and Climatology* 32, 1282-1287.
- Kendall, C., Coplen, T.B., 2001. Distribution of oxygen-18 and deuterium in river waters across the United States. *Hydrological Processes* 15, 1363-1393.
- Kirsten, K.L., Habertzettl, T., Wündsche, M., Frenzel, P., Meschner, S., Smit, A.J., Quick, L.J., Mäusbacher, R., Meadows, M.E., 2018. A multiproxy study of the ocean-atmospheric forcing

## Chapter 1

and the impact of sea-level changes on the southern Cape coast, South Africa during the Holocene. *Palaeogeography, Palaeoclimatology, Palaeoecology* 496, 282-291.

- Lee, J.Y., Marotzke, J., Bala, G., Cao, L., Corti, S., Dunne, J.P., Engelbrecht, F., Fischer, E., Fyfe, J.C., Jones, C., Maycock, A., Mutemi, J., Ndiaye, O., Panickal, S., Zhou, T., 2021. Future Global Climate: Scenario-Based Projections and Near-Term Information. , in: Masson-Delmotte, V., Zhai, P., Pirani, A., Connors, S.L., Péan, C., Berger, S., Caud, N., Chen, Y., Goldfarb, L., Gomis, M.I., Huang, M., Leitzell, K., Lonnoy, E., Matthews, J.B.R., Maycock, T.K., Waterfield, T., Yelekçi, O., Yu, R., Zhou, B. (Eds.), *Climate Change 2021: The Physical Science Basis. Contribution of Working Group I to the Sixth Assessment Report of the Intergovernmental Panel on Climate Change*. Cambridge University Press, Cambridge, In Press.
- Lemma, B., Bittner, L., Glaser, B., Kebede, S., Nemomissa, S., Zech, W., Zech, M., 2021.  $\delta^2\text{H}_{n\text{-alkane}}$  and  $\delta^{18}\text{O}_{\text{sugar}}$  biomarker proxies from leaves and topsoils of the Bale Mountains, Ethiopia, and implications for paleoclimate reconstructions. *Biogeochemistry* 153, 135-153.
- Lennard, C., 2019. Multi-Scale Drivers of the South African Weather and Climate, in: Knight, J., Rogerson, C.M. (Eds.), *The Geography of South Africa: Contemporary Changes and New Directions*. Springer, Cham, Switzerland, pp. 81-90.
- Li, Y., Yang, S., Luo, P., Xiong, S., 2019. Aridity-controlled hydrogen isotope fractionation between soil n-alkanes and precipitation in China. *Organic Geochemistry* 133, 53-64.
- Liu, J., An, Z., 2019. Variations in hydrogen isotopic fractionation in higher plants and sediments across different latitudes: Implications for paleohydrological reconstruction. *Science of The Total Environment* 650, 470-478.
- Liu, J., Liu, W., An, Z., Yang, H., 2016. Different hydrogen isotope fractionations during lipid formation in higher plants: Implications for paleohydrology reconstruction at a global scale. *Scientific Reports* 6, 19711.
- Lutjeharms, J.R.E., Monteiro, P.M.S., Tyson, P.D., Obura, D., 2001. The oceans around southern Africa and regional effects of global change: START Regional Syntheses. *South African Journal of Science* 97, 119-130.
- Macron, C., Pohl, B., Richard, Y., Bessafi, M., 2014. How do Tropical Temperate Troughs Form and Develop over Southern Africa? *Journal of Climate* 27, 1633-1647.
- Marshall, G.J., 2003. Trends in the Southern Annular Mode from Observations and Reanalyses. *Journal of Climate* 16, 4134-4143.
- Martin, A.R.H., 1956. The ecology and history of Groenvlei. *South African Journal of Science* 52, 187–192.
- Martin, A.R.H., 1959. The stratigraphy and history of Groenvlei, a South African coastal fen. *Australian Journal of Botany* 7, 142-167.
- Martin, A.R.H., 1960a. The Ecology of Groenvlei, a South African Fen: Part I. The Primary Communities. *Journal of Ecology* 48, 55-71.
- Martin, A.R.H., 1960b. The Ecology of Groenvlei, a South African Fen: Part II. The Secondary Communities. *Journal of Ecology* 48, 307-329.
- Martin, A.R.H., 1962. Evidence relating to the Quaternary History of the Wilderness lakes. *Transactions of the Geological Society of South Africa* 65, 19–42.
- Martin, A.R.H., 1968. Pollen Analysis of Groenvlei Lake Sediments Knysna (South Africa). *Review of Palaeobotany and Palynology* 7, 107-144.
- Martínez-Méndez, G., Zahn, R., Hall, I.R., Peeters, F.J.C., Pena, L.D., Cacho, I., Negre, C., 2010. Contrasting multiproxy reconstructions of surface ocean hydrography in the Agulhas Corridor and implications for the Agulhas Leakage during the last 345,000 years. *Paleoceanography* 25, PA4227.
- Mekonnen, B., Zech, W., Glaser, B., Lemma, B., Bromm, T., Nemomissa, S., Bekele, T., Zech, M., 2019. Chemotaxonomic patterns of vegetation and soils along altitudinal transects of the Bale Mountains, Ethiopia, and implications for paleovegetation reconstructions – Part 1: stable isotopes and sugar biomarkers. *E&G Quaternary Science Journal* 68, 177-188.
- Merlivat, L., 1978. Molecular diffusivities of  $\text{H}_2^{16}\text{O}$ ,  $\text{HD}^{16}\text{O}$ , and  $\text{H}_2^{18}\text{O}$  in gases. *The Journal of Chemical Physics* 69, 2864-2871.

- Miller, C., Finch, J., Hill, T., Peterse, F., Humphries, M., Zabel, M., Schefuß, E., 2019. Late Quaternary climate variability at Mfabeni peatland, eastern South Africa. *Climate of the Past* 15, 1153-1170.
- Mucina, L., Rutherford, M.C., 2006. The vegetation of South Africa, Lesotho and Swaziland. SANBI, Pretoria.
- Ndarana, T., Rammopo, T.S., Reason, C.J.C., Bopape, M.-J., Engelbrecht, F., Chikoore, H., 2021. Two types of ridging South Atlantic Ocean anticyclones over South Africa and the associated dynamical processes. *Atmospheric Research*, 105897.
- Newberry, S.L., Kahmen, A., Dennis, P., Grant, A., 2015. n-Alkane biosynthetic hydrogen isotope fractionation is not constant throughout the growing season in the riparian tree *Salix viminalis*. *Geochimica et Cosmochimica Acta* 165, 75-85.
- Nielsen, S.H.H., Koç, N., Crosta, X., 2004. Holocene climate in the Atlantic sector of the Southern Ocean: Controlled by insolation or oceanic circulation? *Geology* 32, 317-320.
- Peeters, F.J.C., Acheson, R., Brummer, G.-J.A., de Ruijter, W.P.M., Schneider, R.R., Ganssen, G.M., Ufkes, E., Kroon, D., 2004. Vigorous exchange between the Indian and Atlantic oceans at the end of the past five glacial periods. *Nature* 430, 661-665.
- Perren, B.B., Hodgson, D.A., Roberts, S.J., Sime, L., Van Nieuwenhuyze, W., Verleyen, E., Vyverman, W., 2020. Southward migration of the Southern Hemisphere westerly winds corresponds with warming climate over centennial timescales. *Communications Earth & Environment* 1, 58.
- Peters, K.E., Walters, C.C., Moldowan, J.M., 2005. *The Biomarker Guide: Biomarkers and Isotopes in Petroleum Exploration and Earth History*. Cambridge University Press, New York.
- Polissar, P.J., Freeman, K.H., 2010. Effects of aridity and vegetation on plant-wax  $\delta D$  in modern lake sediments. *Geochimica et Cosmochimica Acta* 74, 5785-5797.
- Pomposi, C., Funk, C., Shukla, S., Harrison, L., Magadzire, T., 2018. Distinguishing southern Africa precipitation response by strength of El Niño events and implications for decision-making. *Environmental Research Letters* 13, 074015.
- Putman, A.L., Fiorella, R.P., Bowen, G.J., Cai, Z., 2019. A Global Perspective on Local Meteoric Water Lines: Meta-analytic Insight Into Fundamental Controls and Practical Constraints. *Water Resources Research* 55, 6896-6910.
- Quick, L.J., Carr, A.S., Meadows, M.E., Boom, A., Bateman, M.D., Roberts, D.L., Reimer, P.J., Chase, B.M., 2015. A late Pleistocene–Holocene multi-proxy record of palaeoenvironmental change from Still Bay, southern Cape Coast, South Africa. *Journal of Quaternary Science* 30, 870-885.
- Quick, L.J., Chase, B.M., Carr, A.S., Chevalier, M., Grobler, B.A., Meadows, M.E., 2021. A 25,000 year record of climate and vegetation change from the southwestern Cape coast, South Africa. *Quaternary Research*, 1-18.
- Quick, L.J., Chase, B.M., Wündsche, M., Kirsten, K., Chevalier, M., Mäusbacher, R., Meadows, M., Haberzettl, T., 2018. A high-resolution record of Holocene climate and vegetation dynamics from the southern Cape coast of South Africa: pollen and microcharcoal evidence from Eilandvlei. *Journal of Quaternary Science*, 1-14.
- Quick, L.J., Meadows, M.E., Bateman, M.D., Kirsten, K.L., Mäusbacher, R., Haberzettl, T., Chase, B.M., 2016. Vegetation and climate dynamics during the last glacial period in the fynbos-afrotemperate forest ecotone, southern Cape, South Africa. *Quaternary International* 404, Part B, 136-149.
- Ranasinghe, R., Ruane, A.C., Vautard, R., Arnell, N., Coppola, E., Cruz, F.A., Dessai, S., Islam, A.S., Rahimi, M., Ruiz Carrascal, D., Sillmann, J., Sylla, M.B., Tebaldi, C., Wang, W., Zaaboul, R., 2021. Climate Change Information for Regional Impact and for Risk Assessment., in: Masson-Delmotte, V., Zhai, P., Pirani, A., Connors, S.L., Péan, C., Berger, S., Caud, N., Chen, Y., Goldfarb, L., Gomis, M.I., Huang, M., Leitzell, K., Lonnoy, E., Matthews, J.B.R., Maycock, T.K., Waterfield, T., Yelekçi, O., Yu, R., Zhou, B. (Eds.), *Climate Change 2021: The Physical Science Basis. Contribution of Working Group I to the Sixth Assessment Report of the Intergovernmental Panel on Climate Change*. Cambridge University Press, Cambridge, In Press.
- Reason, C.J.C., Rouault, M., 2005. Links between the Antarctic Oscillation and winter rainfall over western South Africa. *Geophysical Research Letters* 32, L07705.
- Reinwarth, B., Franz, S., Baade, J., Haberzettl, T., Kasper, T., Daut, G., Helmschrot, J., Kirsten, K.L., Quick, L.J., Meadows, M.E., Mäusbacher, R., 2013. A 700-Year Record on the Effects of

## Chapter 1

- Climate and Human Impact on the Southern Cape Coast Inferred from Lake Sediments of Eilandvlei, Wilderness Embayment, South Africa. *Geografiska Annaler Series A - Physical Geography* 95, 345-360.
- Rouault, M., White, S.A., Reason, C.J.C., Lutjeharms, J.R.E., Jobard, I., 2002. Ocean–Atmosphere Interaction in the Agulhas Current Region and a South African Extreme Weather Event. *Weather and Forecasting* 17, 655-669.
- Russell, J.L., Dixon, K.W., Gnanadesikan, A., Stouffer, R.J., Toggweiler, J.R., 2006. The Southern Hemisphere Westerlies in a Warming World: Propping Open the Door to the Deep Ocean. *Journal of Climate* 19, 6382-6390.
- Sachse, D., Billault, I., Bowen, G.J., Chikaraishi, Y., Dawson, T.E., Feakins, S.J., Freeman, K.H., Magill, C.R., McInerney, F.A., van der Meer, M.T.J., Polissar, P., Robins, R.J., Sachs, J.P., Schmidt, H.L., Sessions, A.L., White, J.W.C., West, J.B., Kahmen, A., 2012. Molecular Paleohydrology: Interpreting the Hydrogen- Isotopic Composition of Lipid Biomarkers from Photosynthesizing Organisms. *Annual Review of Earth and Planetary Sciences* 40, 221-249.
- SAWS (South African Weather Service), 2018. Rainfall data from the weather stations Mossel Bay and Beaufort West, Pretoria.
- Schäfer, I.K., Lanny, V., Franke, J., Eglinton, T.I., Zech, M., Vysloužilová, B., Zech, R., 2016. Leaf waxes in litter and topsoils along a European transect. *Soil* 2, 551-564.
- Schefuß, E., Schouten, S., Schneider, R.R., 2005. Climatic controls on central African hydrology during the past 20,000 years. *Nature* 437, 1003-1006.
- Schmidt, H.-L., Werner, R.A., Roßmann, A., 2001. <sup>18</sup>O Pattern and biosynthesis of natural plant products. *Phytochemistry* 58, 9-32.
- Scott, L., Holmgren, K., Talma, A.S., Woodborne, S., Vogel, J.C., 2003. Age interpretation of the Wonderkrater spring sediments and vegetation change in the Savanna Biome, Limpopo province, South Africa : research letter. *South African Journal of Science* 99, 484-488.
- Scott, L., Lee-Thorp, J.A., 2004. Holocene climatic trends and rhythms in southern Africa, in: Battarbee, R.W., Gasse, F., Stickley, C.E. (Eds.), *Past Climate Variability through Europe and Africa*. Springer, Dordrecht, pp. 69-91.
- Seneviratne, S.I., Zhang, X., Adnan, M., Badi, W., Dereczynski, C., Di Luca, A., Ghosh, S., Iskandar, I., Kossin, J., Lewis, S., Otto, F., Pinto, I., Satoh, M., Vicente-Serrano, S.M., Wehner, M., Zhou, B., 2021. Weather and Climate Extreme Events in a Changing Climate, in: Masson-Delmotte, V., Zhai, P., Pirani, A., Connors, S.L., Péan, C., Berger, S., Caud, N., Chen, Y., Goldfarb, L., Gomis, M.I., Huang, M., Leitzell, K., Lonnoy, E., Matthews, J.B.R., Maycock, T.K., Waterfield, T., Yelekçi, O., Yu, R., Zhou, B. (Eds.), *Climate Change 2021: The Physical Science Basis. Contribution of Working Group I to the Sixth Assessment Report of the Intergovernmental Panel on Climate Change*. Cambridge University Press, Cambridge, In Press.
- Sessions, A.L., 2016. Factors controlling the deuterium contents of sedimentary hydrocarbons. *Organic Geochemistry* 96, 43-64.
- Sessions, A.L., Burgoyne, T.W., Schimmelmann, A., Hayes, J.M., 1999. Fractionation of hydrogen isotopes in lipid biosynthesis. *Organic Geochemistry* 30, 1193-1200.
- Simon, M.H., Arthur, K.L., Hall, I.R., Peeters, F.J.C., Loveday, B.R., Barker, S., Ziegler, M., Zahn, R., 2013. Millennial-scale Agulhas Current variability and its implications for salt-leakage through the Indian–Atlantic Ocean Gateway. *Earth and Planetary Science Letters* 383, 101-112.
- Simon, M.H., Ziegler, M., Barker, S., van der Meer, M.T.J., Schouten, S., Hall, I.R., 2020. A late Pleistocene dataset of Agulhas Current variability. *Scientific Data* 7, 385.
- Singleton, A.T., Reason, C.J.C., 2006. Numerical simulations of a severe rainfall event over the Eastern Cape coast of South Africa: sensitivity to sea surface temperature and topography. *Tellus A: Dynamic Meteorology and Oceanography* 58, 335-367.
- Smith, F.A., Freeman, K.H., 2006. Influence of physiology and climate on  $\delta D$  of leaf wax *n*-alkanes from C3 and C4 grasses. *Geochimica et Cosmochimica Acta* 70, 1172-1187.
- Sternberg, d.L., 1989. Oxygen and Hydrogen Isotope Ratios in Plant Cellulose: Mechanisms and Applications, in: Rundel, P.W., Ehleringer, J.R., Nagy, K.A. (Eds.), *Stable Isotopes in Ecological Research*. Springer New York, New York, NY, pp. 124-141.

- Sternberg, L., Deniro, M.J., Savidge, R.A., 1986. Oxygen Isotope Exchange between Metabolites and Water during Biochemical Reactions Leading to Cellulose Synthesis. *Plant Physiology* 82, 423-427.
- Strobel, P., Bliedtner, M., Carr, A.S., Frenzel, P., Klaes, B., Salazar, G., Struck, J., Szidat, S., Zech, R., Haberzettl, T., 2021a. Holocene sea level and environmental change at the southern Cape - an 8.5 kyr multi-proxy paleoclimate record from lake Voëlvlei, South Africa. *Climate of the Past* 17, 1567-1586.
- Strobel, P., Bliedtner, M., Carr, A.S., Struck, J., du Plessis, N., Glaser, B., meadows, M.E., Quick, L.J., Zech, M., Zech, R., Haberzettl, T., submitted. Reconstructing Late Quaternary precipitation and its source on the southern Cape coast of South Africa: A multi-proxy paleoenvironmental record from Vankervelsvlei.
- Strobel, P., Haberzettl, T., Bliedtner, M., Struck, J., Glaser, B., Zech, M., Zech, R., 2020. The potential of  $\delta^2\text{H}_{n\text{-alkanes}}$  and  $\delta^{18}\text{O}_{\text{sugar}}$  for paleoclimate reconstruction – A regional calibration study for South Africa. *Science of The Total Environment* 716, 137045.
- Strobel, P., Kasper, T., Frenzel, P., Schitteck, K., Quick, L.J., Meadows, M.E., Mäusbacher, R., Haberzettl, T., 2019. Late Quaternary palaeoenvironmental change in the year-round rainfall zone of South Africa derived from peat sediments from Vankervelsvlei. *Quaternary Science Reviews* 218, 200-214.
- Strobel, P., Zech, R., Struck, J., Bazarradnaa, E., Zech, M., Bliedtner, M., 2021b. Precipitation and lake water evaporation recorded by terrestrial and aquatic *n*-alkane  $\delta^2\text{H}$  isotopes in Lake Khar Nuur, Mongolia. Preprint in revision (Earth and Space Science Open Archive).
- Struck, J., 2022. Calibration and First Application of Biomarker and Compound-Specific Isotope Analyses in Mongolia, Physical Geography, Institute of Geography. Friedrich Schiller University Jena, Jena.
- Struck, J., Bliedtner, M., Strobel, P., Bittner, L., Bazarradnaa, E., Andreeva, D., Zech, W., Glaser, B., Zech, M., Zech, R., 2020a. Leaf Waxes and Hemicelluloses in Topsoils Reflect the  $\delta^2\text{H}$  and  $\delta^{18}\text{O}$  Isotopic Composition of Precipitation in Mongolia. *Frontiers in Earth Science* 8.
- Struck, J., Bliedtner, M., Strobel, P., Schumacher, J., Bazarradnaa, E., Zech, R., 2020b. Leaf wax *n*-alkane patterns and compound-specific  $\delta^{13}\text{C}$  of plants and topsoils from semi-arid and arid Mongolia. *Biogeosciences* 17, 567-580.
- Talma, A.S., Vogel, J.C., 1992. Late Quaternary paleotemperatures derived from a speleothem from Cango Caves, Cape Province, South Africa. *Quaternary Research* 37, 203-213.
- Thompson, D.W.J., Wallace, J.M., 2000. Annular Modes in the Extratropical Circulation. Part I: Month-to-Month Variability. *Journal of Climate* 13, 1000-1016.
- Tierney, J.E., Russell, J.M., Huang, Y., Damsté, J.S.S., Hopmans, E.C., Cohen, A.S., 2008. Northern Hemisphere Controls on Tropical Southeast African Climate During the Past 60,000 Years. *Science* 322, 252-255.
- Trabucco, A., Zomer, R., 2019. Global Aridity Index and Potential Evapotranspiration (ET<sub>0</sub>) Climate Database v2. figshare. Fileset.
- Tuthorn, M., Zech, M., Ruppenthal, M., Oelmann, Y., Kahmen, A., Valle, H.F.d., Wilcke, W., Glaser, B., 2014. Oxygen isotope ratios ( $^{18}\text{O}/^{16}\text{O}$ ) of hemicellulose-derived sugar biomarkers in plants, soils and sediments as paleoclimate proxy II: Insight from a climate transect study. *Geochimica et Cosmochimica Acta* 126, 624-634.
- Tuthorn, M., Zech, R., Ruppenthal, M., Oelmann, Y., Kahmen, A., del Valle, H.F., Eglinton, T., Rozanski, K., Zech, M., 2015. Coupling  $\delta^2\text{H}$  and  $\delta^{18}\text{O}$  biomarker results yields information on relative humidity and isotopic composition of precipitation - a climate transect validation study. *Biogeosciences* 12, 3913-3924.
- Tyson, P.D., 1986. Climatic change and variability in southern Africa. Oxford University Press, Cape Town.
- Tyson, P.D., Preston-Whyte, R.A., 2000. The Weather and Climate of Southern Africa. Oxford University Press, Cape Town.
- van Zinderen Bakker, E.M., 1976. The evolution of late Quaternary paleoclimates of Southern Africa. *Palaeoecology Africa* 9, 160-202.

## Chapter 1

- Weldon, D., Reason, C.J.C., 2014. Variability of rainfall characteristics over the South Coast region of South Africa. *Theoretical and Applied Climatology* 115, 177-185.
- Wündsch, M., Haberzettl, T., Cawthra, H.C., Kirsten, K.L., Quick, L.J., Zabel, M., Frenzel, P., Hahn, A., Baade, J., Daut, G., Kasper, T., Meadows, M.E., Mäusbacher, R., 2018. Holocene environmental change along the southern Cape coast of South Africa – Insights from the Eilandvlei sediment record spanning the last 8.9 kyr. *Global and Planetary Change* 163, 51-66.
- Wündsch, M., Haberzettl, T., Kirsten, K.L., Kasper, T., Zabel, M., Dietze, E., Baade, J., Daut, G., Meschner, S., Meadows, M.E., Mäusbacher, R., 2016a. Sea level and climate change at the southern Cape coast, South Africa, during the past 4.2 kyr. *Palaeogeography Palaeoclimatology Palaeoecology* 446, 295-307.
- Wündsch, M., Haberzettl, T., Meadows, M.E., Kirsten, K.L., Kasper, T., Baade, J., Daut, G., Stoner, J.S., Mäusbacher, R., 2016b. The impact of changing reservoir effects on the C-14 chronology of a Holocene sediment record from South Africa. *Quaternary Geochronology* 36, 148-160.
- Yakir, D., DeNiro, M.J., 1990. Oxygen and Hydrogen Isotope Fractionation during Cellulose Metabolism in *Lemna gibba* L. *Plant Physiology* 93, 325-332.
- Zech, M., Glaser, B., 2009. Compound-specific  $\delta^{18}\text{O}$  analyses of neutral sugars in soils using gas chromatography–pyrolysis–isotope ratio mass spectrometry: problems, possible solutions and a first application. *Rapid Communications in Mass Spectrometry* 23, 3522-3532.
- Zech, M., Mayr, C., Tuthorn, M., Leiber-Sauheitl, K., Glaser, B., 2014a. Oxygen isotope ratios ( $^{18}\text{O}/^{16}\text{O}$ ) of hemicellulose-derived sugar biomarkers in plants, soils and sediments as paleoclimate proxy I: Insight from a climate chamber experiment. *Geochimica et Cosmochimica Acta* 126, 614-623.
- Zech, M., Tuthorn, M., Detsch, F., Rozanski, K., Zech, R., Zöller, L., Zech, W., Glaser, B., 2013. A 220ka terrestrial  $\delta^{18}\text{O}$  and deuterium excess biomarker record from an eolian permafrost paleosol sequence, NE-Siberia. *Chemical Geology* 360-361, 220-230.
- Zech, M., Tuthorn, M., Zech, R., Schlütz, F., Zech, W., Glaser, B., 2014b. A 16-ka  $\delta^{18}\text{O}$  record of lacustrine sugar biomarkers from the High Himalaya reflects Indian Summer Monsoon variability. *Journal of Paleolimnology* 51, 241-251.
- Zech, M., Werner, R.A., Juchelka, D., Kalbitz, K., Buggle, B., Glaser, B., 2012. Absence of oxygen isotope fractionation/exchange of (hemi-) cellulose derived sugars during litter decomposition. *Organic Geochemistry* 42, 1470-1475.
- Zech, M., Zech, R., Rozanski, K., Gleixner, G., Zech, W., 2015. Do *n*-alkane biomarkers in soils/sediments reflect the  $\delta^2\text{H}$  isotopic composition of precipitation? A case study from Mt. Kilimanjaro and implications for paleoaltimetry and paleoclimate research. *Isotopes in Environmental and Health Studies* 51, 508-524.
- Zech, W., Schad, P., Hintermaier-Erhard, G., 2014c. *Böden der Welt: Ein Bildatlas*, EBL-Schweitzer, Berlin, Heidelberg.
- Zhao, X., Dupont, L., Schefuß, E., Meadows, M.E., Hahn, A., Wefer, G., 2016. Holocene vegetation and climate variability in the winter and summer rainfall zones of South Africa. *The Holocene* 26, 843-857.

## Chapter 2

---

### **The potential of $\delta^2\text{H}_{n\text{-alkanes}}$ and $\delta^{18}\text{O}_{\text{sugar}}$ for paleoclimate reconstruction – A regional calibration study for South Africa**

---

Authors: Paul Strobel, Torsten Haberzettl, Marcel Bliedtner, Julian Struck, Bruno Glaser, Michael Zech, Roland Zech

Published in:  
Science of The Total Environment 716 (2020), 137045  
<https://doi.org/10.1016/j.scitotenv.2020.137045>



ELSEVIER

Contents lists available at ScienceDirect

Science of the Total Environment

journal homepage: [www.elsevier.com/locate/scitotenv](http://www.elsevier.com/locate/scitotenv)

## The potential of $\delta^2\text{H}_{n\text{-alkanes}}$ and $\delta^{18}\text{O}_{\text{sugar}}$ for paleoclimate reconstruction – A regional calibration study for South Africa

P. Strobel <sup>a,\*</sup>, T. Haberzettl <sup>b</sup>, M. Bliedtner <sup>a</sup>, J. Struck <sup>a</sup>, B. Glaser <sup>c</sup>, M. Zech <sup>d</sup>, R. Zech <sup>a</sup>

<sup>a</sup> Physical Geography, Institute of Geography, Friedrich Schiller University Jena, Jena, Germany

<sup>b</sup> Physical Geography, Institute of Geography and Geology, University of Greifswald, Germany

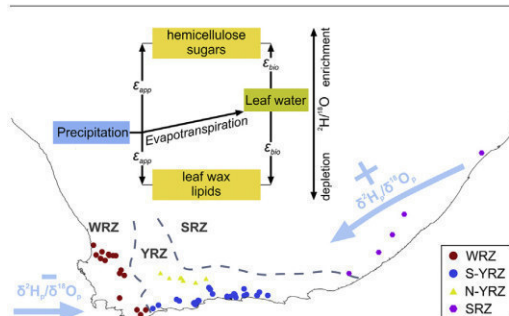
<sup>c</sup> Institute of Agronomy and Nutritional Sciences, Soil Biogeochemistry, Martin-Luther University Halle-Wittenberg, Halle (Saale), Germany

<sup>d</sup> Physical Geography with focus on Paleoenvironmental Research, Institute of Geography, Dresden University of Technology, Dresden, Germany

### HIGHLIGHTS

- $\delta^2\text{H}_{n\text{-alkanes}}$  and  $\delta^{18}\text{O}_{\text{sugar}}$  were investigated in South African topsoils.
- $\delta^2\text{H}_{n\text{-alkanes}}$  correlates with  $\delta^2\text{H}_p$ , whereas  $\delta^{18}\text{O}_{\text{sugar}}$  does not correlate with  $\delta^{18}\text{O}_p$ .
- Hydrogen apparent fractionation is not climate-dependent.
- Oxygen apparent fractionation is strongly influenced by evapotranspiration.
- Coupling  $\delta^2\text{H}_{n\text{-alkanes}}$  and  $\delta^{18}\text{O}_{\text{sugar}}$  enables to reconstruct  $\delta^2\text{H}_p$ ,  $\delta^{18}\text{O}_p$  and RH.

### GRAPHICAL ABSTRACT



### ARTICLE INFO

#### Article history:

Received 8 November 2019

Received in revised form 28 January 2020

Accepted 30 January 2020

Available online 31 January 2020

Editor: Filip M.G. Tack

#### Keywords:

Biomarkers

Leaf waxes

Hemicellulose sugars

Compound-specific hydrogen isotopes

Compound-specific oxygen isotopes

Apparent fractionation

### ABSTRACT

The hydrogen isotopic composition of leaf wax-derived  $n$ -alkanes ( $\delta^2\text{H}_{n\text{-alkanes}}$ ) is a widely applied proxy for (paleo)climatic changes. It has been suggested that the coupling with the oxygen isotopic composition of hemicellulose-derived sugars ( $\delta^{18}\text{O}_{\text{sugar}}$ ) – an approach dubbed ‘paleohygrometer’ – might allow more robust and quantitative (paleo)hydrological reconstructions. However, the paleohygrometer remains to be evaluated and tested regionally. In this study, topsoil samples from South Africa, covering extensive environmental gradients, are analysed.  $\delta^2\text{H}_{n\text{-alkanes}}$  correlates significantly with the isotopic composition of precipitation ( $\delta^2\text{H}_p$ ), whereas no significant correlation exists between  $\delta^{18}\text{O}_{\text{sugar}}$  and  $\delta^{18}\text{O}_p$ . The apparent fractionation ( $\epsilon_{\text{app}}$ ) is the difference between  $\delta^2\text{H}_{n\text{-alkanes}}$  and  $\delta^2\text{H}_p$  ( $\epsilon_{\text{app } 2\text{H}}$ ) and  $\delta^{18}\text{O}_{\text{sugar}}$  and  $\delta^{18}\text{O}_p$  ( $\epsilon_{\text{app } 18\text{O}}$ ), respectively, and integrates i) isotopic enrichment due to soil water evaporation, ii) leaf (and xylem) water transpiration and iii) biosynthetic fractionation. We find no correlation of  $\epsilon_{\text{app } 18\text{O}}$  nor for  $\epsilon_{\text{app } 2\text{H}}$  with temperature, and no correlation of  $\epsilon_{\text{app } 2\text{H}}$  with potential evapotranspiration and an aridity index. By contrast,  $\epsilon_{\text{app } 18\text{O}}$  correlates significantly with both potential evapotranspiration and the aridity index. This highlights the strong effect of evapotranspirative enrichment on  $\delta^{18}\text{O}_{\text{sugar}}$ . In study areas without plant predominance using Crassulacean Acid Metabolism (CAM), coupling  $\delta^{18}\text{O}_{\text{sugar}}$  and  $\delta^2\text{H}_{n\text{-alkanes}}$  enables to reconstruct  $\delta^2\text{H}_p$  and  $\delta^{18}\text{O}_p$  with an offset of  $\Delta\delta^2\text{H} = 6 \pm 27\%$  and  $\Delta\delta^{18}\text{O} = 0.8 \pm 3.7\%$ , respectively, as well as relative humidity (RH) with an offset of  $\Delta\text{RH} = 6 \pm 17\%$ . The paleohygrometer does, however, not work well for our study areas where CAM plants prevail (reconstructed  $\delta^{18}\text{O}_p$ ,  $\delta^2\text{H}_p$  and RH are off by 3.1%, 27.2% and 31.7%). This probably reflects plant-specific (phenological)

\* Corresponding author at: Physical Geography, Institute of Geography, Friedrich Schiller University Jena, Löbdergraben 32, 07743 Jena, Germany.  
E-mail address: paul.strobel@uni-jena.de (P. Strobel).

<https://doi.org/10.1016/j.scitotenv.2020.137045>

0048-9697/© 2020 Elsevier B.V. All rights reserved.



adaptations and/or post-photosynthetic exchange reactions related to CAM metabolism. Overall, our findings corroborate that  $\delta^2\text{H}_{n\text{-alkanes}}$  and  $\delta^{18}\text{O}_{\text{sugar}}$  are valuable proxies, and the paleohygrometer is a promising approach for paleoclimate reconstructions in southern Africa.

© 2020 Elsevier B.V. All rights reserved.

## 1. Introduction

Our understanding how past and recent climate has evolved is a necessary precondition to predict future climate changes. The temporal and spatial dynamics of atmospheric circulation patterns are particularly crucial. Various proxies have been used to reconstruct (paleo-) hydrological conditions (Quick et al., 2018; Wündsche et al., 2018; Wündsche et al., 2016). Stable hydrogen isotopes in leaf wax-derived  $n$ -alkanes ( $\delta^2\text{H}_{n\text{-alkanes}}$ ), for example, have become a widely applied hydrological proxy in paleoenvironmental research, because  $\delta^2\text{H}_{n\text{-alkanes}}$  primarily reflects the isotopic composition of precipitation ( $\delta^2\text{H}_p$ ) (e.g., Schäfer et al., 2018; Schefuß et al., 2005). However, due to evaporation, soil water used by the plants can be isotopically enriched (Flanagan and Ehleringer, 1991; Gat, 1996; Strobel et al., 2019) (Fig. 1). The isotopic signature of xylem water is considered equal to that of the used soil water, as most commonly no isotopic fractionation has been observed during water uptake and transport through the roots (Feakins and Sessions, 2010a). Transpiration then results in further isotopic enrichment of leaf water compared to xylem water (Cernusak et al., 2016) (Fig. 1). Finally, leaf water (or in the case of grasses, a mixture of xylem and leaf water) is the ultimate source used for the biosynthesis of leaf wax-derived  $n$ -alkanes (Fig. 1).  $n$ -Alkanes are usually strongly isotopically-depleted in hydrogen compared to leaf water, due to a strong hydrogen-isotopic fractionation during biosynthesis (e.g., Sachse et al., 2012; Sessions et al., 1999) (Fig. 1). Biosynthetic fractionation ( $\epsilon_{\text{bio}}$ ) can largely differ due to differences in metabolic pathways, hydrogen transfer reactions and extrinsic environmental factors (Cormier et al., 2018; Eley et al., 2014; Griepentrog et al., 2019; Liu and An, 2019; Newberry et al., 2015; Sessions et al., 1999).

The apparent hydrogen isotope fractionation ( $\epsilon_{\text{app } 2\text{H}}$ ) is defined as the difference between  $\delta^2\text{H}_p$  and  $\delta^2\text{H}_{n\text{-alkanes}}$  and integrates the three above-mentioned processes of isotopic fractionation: i) soil water enrichment (Fig. 1). Several studies have reported a wide range in  $\epsilon_{\text{app } 2\text{H}}$  with substantially smaller values for arid than in humid climates (e.g., Feakins and Sessions, 2010a; Li et al., 2019; Polissar and Freeman, 2010; Smith and Freeman, 2006). This can potentially complicate paleoclimate reconstructions, because one would need to disentangle past changes in  $\delta^2\text{H}_p$  and all other factors modulating  $\delta^2\text{H}_{n\text{-alkanes}}$ .

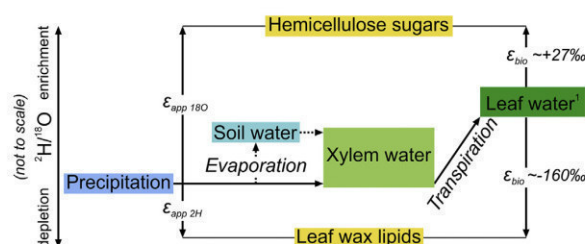


**Fig. 1.** Conceptual framework describing the hydrogen-isotope relationship between precipitation and leaf wax-derived  $n$ -alkanes as well as oxygen-isotope and hemicellulose-derived sugars, respectively. The concept is based on Sachse et al. (2012) and extended by the  $^{18}\text{O}$  pathway after Zech et al. (2014). <sup>1</sup> For  $\delta^{18}\text{O}$  of monocotyledon plants/grasses with intercalary meristems the model would have to be modified (see Zech et al., 2014). For more detailed process-related information see Sachse et al. (2012) and Zech et al. (2014). Abbreviations:  $\epsilon_{\text{bio}}$ , biosynthetic hydrogen- and oxygen-isotope fractionation;  $\epsilon_{\text{app } 2\text{H}}$ , apparent hydrogen-isotope fractionation;  $\epsilon_{\text{app } 18\text{O}}$ , oxygen-isotope fractionation.

$\delta^{18}\text{O}_{\text{cellulose}}$  (Heyng et al., 2014; Shi et al., 2019a; Shi et al., 2019b; Sternberg and DeNiro, 1983; Wissel et al., 2008), and  $\delta^{18}\text{O}$  of hemicellulose-derived sugar biomarkers (referred to as  $\delta^{18}\text{O}_{\text{sugar}}$  from now on) (Tuthorn et al., 2014; Zech and Glaser, 2009; Zech et al., 2014; Zech et al., 2012) are also used for paleoclimate and -hydrological research. Similar to leaf waxes, hemicellulose-derived sugars record the isotopic composition of precipitation modulated by evaporative enrichment of soil water, transpirative enrichment of leaf water, and biosynthetic fractionation (Fig. 1).

It has been suggested that coupling of  $\delta^2\text{H}_{n\text{-alkanes}}$  and  $\delta^{18}\text{O}_{\text{sugar}}$  can be used to disentangle changes in  $\delta^2\text{H}_p$  and  $\delta^{18}\text{O}_p$  and changes in evapo(transpi)rative leaf and lake water enrichment. For instance, Voelker et al. (2014) used  $\delta^2\text{H}$  and  $\delta^{18}\text{O}$  of tree-ring cellulose to reconstruct relative air humidity. Another approach to reconstruct air humidity is based on coupling  $\delta^2\text{H}_{n\text{-alkanes}}$  and  $\delta^{18}\text{O}_{\text{sugar}}$  results ('paleohygrometer') and was validated by Tuthorn et al. (2015) on topsoils from South America and recently by Hepp et al. (2019a) in a climate chamber experiment. Both approaches have already been applied successfully for paleoclimate reconstructions, for example in loess-paleosol sequences (Hepp et al., 2017; Zech et al., 2013), on subfossil wood (Voelker et al., 2015) and in lacustrine sediments (Hepp et al., 2015, 2019b).

South Africa has been proposed to be a key region for paleoenvironmental reconstruction, because suitable archives there should have recorded the interplay between the temperate and tropical atmospheric circulation system, i.e. the Westerlies and the monsoon driven Easterlies (Haberzettl et al., 2014). So far, several studies have analysed the hydrogen isotopic composition of leaf waxes in sedimentary archives, e.g., lake, marine and peat sediments in this area (e.g., Hahn et al., 2016, 2017; Miller et al., 2019; Strobel et al., 2019). Moreover, regional calibration studies for  $\delta^2\text{H}_{n\text{-alkanes}}$  exist (Hahn et al., 2018, 2017; Herrmann et al., 2017). However, as outlined above, the interpretation of  $\delta^2\text{H}$  alone is challenging, because it is difficult to disentangle the various influencing factors. The potential of coupling  $\delta^2\text{H}_{n\text{-alkanes}}$  and  $\delta^{18}\text{O}_{\text{sugar}}$  results remains to be evaluated.

The aim of this study is to investigate the influence of different environmental parameters on the isotopic  $\delta^2\text{H}_{n\text{-alkanes}}$  and  $\delta^{18}\text{O}_{\text{sugar}}$  composition of topsoils from South Africa and to test the potential of the paleohygrometer approach for paleoclimate reconstruction. We address the following specific questions:

- I. Do  $\delta^2\text{H}_{n\text{-alkanes}}$  and  $\delta^{18}\text{O}_{\text{sugar}}$  in South African topsoils reflect  $\delta^2\text{H}_p$  and  $\delta^{18}\text{O}_p$ ?
- II. Are  $\epsilon_{\text{app } 2\text{H}}$  and  $\epsilon_{\text{app } 18\text{O}}$  affected by environmental conditions?
- III. Does the coupling of  $\delta^2\text{H}_{n\text{-alkanes}}$  and  $\delta^{18}\text{O}_{\text{sugar}}$  enable robust reconstruction of the isotopic composition of the precipitation?
- IV. Does coupling  $\delta^2\text{H}_{n\text{-alkanes}}$  and  $\delta^{18}\text{O}_{\text{sugar}}$  enable to reconstruct relative humidity?

## 2. Material and methods

### 2.1. Geographical setting

#### 2.1.1. Climate

Three major rainfall zones currently occur in South Africa (Fig. 2). The Summer Rainfall Zone (SRZ) is located in the eastern and central parts of the country. More than 66% of rainfall occurs during austral

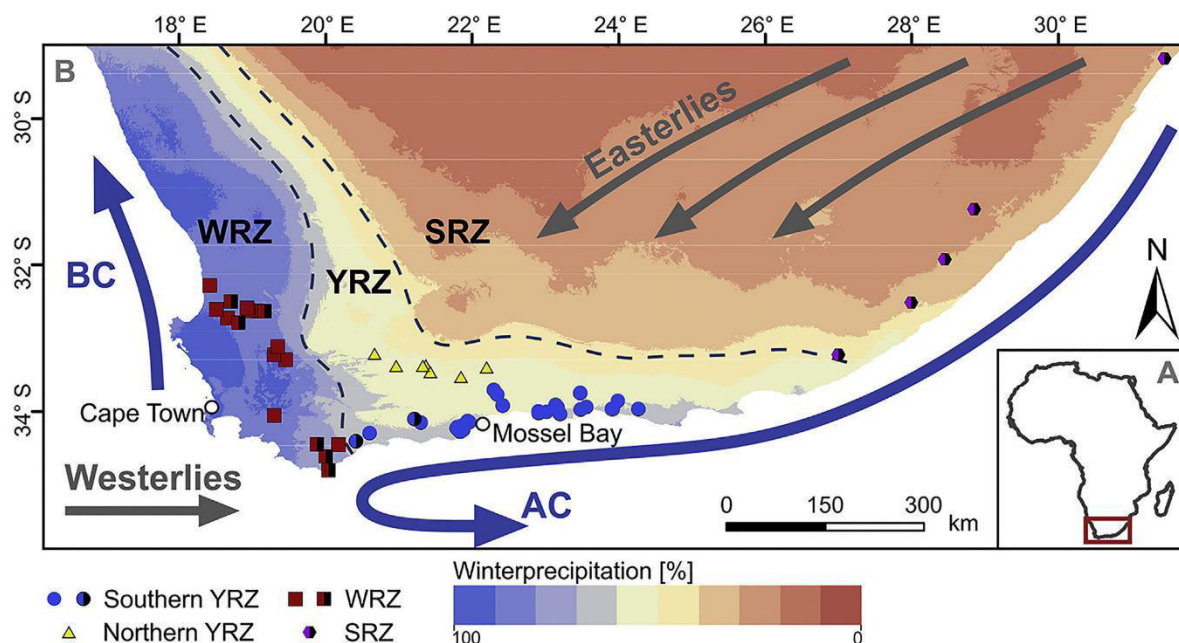


**Fig. 2.** A) Simplified map of Africa and the red box highlights the studied area. B) Location of the topsoil sampling sites. Red squares: samples from the Winter Rainfall Zone (WRZ); blue circles from the southern Year-round Rainfall Zone (YRZ), yellow triangles from the northern YRZ, and pink hexagons from the Summer Rainfall Zone (SRZ; investigated by Hahn et al., 2018). Single colour icons indicate where both  $\delta^2\text{H}_{\text{n-alkanes}}$  and  $\delta^{18}\text{O}_{\text{sugar}}$  results are available; half-black icons indicate that only  $\delta^2\text{H}_{\text{n-alkanes}}$  results are available. Additionally, the circumpolar Westerlies, the tropical Easterlies, the Agulhas Current (AC) and the Benguela Current (BC) are depicted. (Data source: Rainfall seasonality: Worldclim 2 dataset (Fick and Hijmans, 2017); Circulation systems after Chase and Meadows (2007)). (For interpretation of the references to colour in this figure legend, the reader is referred to the web version of this article.)

summer and is related to easterly winds (Easterlies), i.e. the tropical monsoonal system, which is isotopically enriched in  $^2\text{H}$  and  $^{18}\text{O}$  (Bowen and Revenaugh, 2003) (Fig. 2). Mean annual temperature (MAT) ranges from  $\sim 18$  to  $21$   $^{\circ}\text{C}$  and mean annual precipitation (MAP) from  $\sim 600$  to  $>1000$   $\text{mm}\cdot\text{a}^{-1}$  (Fick and Hijmans, 2017).

The Winter Rainfall Zone (WRZ) is a narrow belt along the west coast today, where  $>66\%$  of rainfall occurs during austral winter and is supplied by the temperate Westerlies, which are isotopically depleted in  $^2\text{H}$  and  $^{18}\text{O}$  (Bowen and Revenaugh, 2003; Harris et al., 2010) (Fig. 2). There is a distinct climate gradient from cooler, more humid conditions (MAT  $\sim 10$ – $18$   $^{\circ}\text{C}$ , MAP  $\sim 400$ – $880$   $\text{mm}\cdot\text{a}^{-1}$ ) in the south to warmer, (semi-)arid conditions (MAT  $\sim 20$ – $25$   $^{\circ}\text{C}$ , MAP  $\sim 250$   $\text{mm}\cdot\text{a}^{-1}$ ) in the north of the WRZ (Fick and Hijmans, 2017).

The intermediate area between the SRZ and WRZ is the Year-round Rainfall Zone (YRZ), which receives rainfall from both systems throughout the year (Fig. 2) (Engelbrecht et al., 2015; Scott and Lee-Thorp, 2004). As a result, the isotopic composition in the YRZ is highly variable throughout the year (Braun et al., 2017). Furthermore, a large climatic gradient exists between the inland and the coastal areas (MAT  $\sim 10$ – $20$   $^{\circ}\text{C}$ , MAP  $\sim 200$ – $850$   $\text{mm}\cdot\text{a}^{-1}$ ) (Fick and Hijmans, 2017) with more humid conditions prevailing in the latter areas. Moreover, climate conditions are modified by the regional topography, e.g. the Cape Fold Mountains in the WRZ, Outeniqua Mountains and Swartberge in the YRZ, and the Great Escarpment and the Drakensberg Mountains in the SRZ, because altitude controls temperatures and orographic effects drive local precipitation (Tyson and Preston-Whyte, 2000).

### 2.1.2. Vegetation

The biomes in the study area are Fynbos and Succulent Karoo in the west, Fynbos, Albany Thicket, Afromontane Forest and Coastal Forests (Southern and Indian Ocean Coastal Belt) along the south coast, and the interior is characterised by Nama Karoo. The modern vegetation biomes in South Africa follow the described climate gradients (Knight and

Rogerson, 2019; Mucina and Rutherford, 2006). A very detailed description of phytogeographic regions is provided by Mucina and Rutherford (2006) and Knight and Rogerson (2019). Woody C3 plants and C3 grasses dominate the Fynbos Biome, while plants using Crassulacean Acid Metabolism (CAM), including many succulents, are dominant in the (semi-)arid regions with high rainfall seasonality, such as in the Succulent Karoo and western Nama Karoo (Knight and Rogerson, 2019; Mucina and Rutherford, 2006; Vogel et al., 1978).

### 2.2. Sampling

For this study, we sampled topsoil (0–5 cm) at 59 sites (Fig. 2). Each sample consists of three subsamples that were collected within a distance of a few meters and then mixed. Our samples come from three zones: i) the southern and central part of the WRZ (MAT  $12.9$ – $18.6$   $^{\circ}\text{C}$ , MAP  $260$ – $765$   $\text{mm}\cdot\text{a}^{-1}$ , potential evapotranspiration (pot. ET)  $1375$ – $2060$   $\text{mm}\cdot\text{d}^{-1}$ , Aridity index (Ai)  $0.13$ – $0.47$ ,  $\text{RH}_{\text{RA}}$   $46$ – $75\%$ ; Fig. 3), ii) the southern humid part of the YRZ (MAT  $14.7$ – $18.2$   $^{\circ}\text{C}$ , MAP  $375$ – $810$   $\text{mm}\cdot\text{a}^{-1}$ , pot. ET  $1435$ – $1855$   $\text{mm}\cdot\text{d}^{-1}$ , Ai  $0.20$ – $0.55$ ,  $\text{RH}_{\text{RA}}$   $61$ – $71\%$ ; Fig. 3), and iii) the central (semi-)arid part of the YRZ (MAT  $13.8$ – $18.2$   $^{\circ}\text{C}$ , MAP  $200$ – $210$   $\text{mm}\cdot\text{a}^{-1}$ , pot. ET  $1760$ – $2135$   $\text{mm}\cdot\text{d}^{-1}$ , Ai  $0.10$ – $0.18$ ,  $\text{RH}_{\text{RA}}$   $50$ – $58\%$ ; Fig. 3). We have not collected samples from the SRZ, can include  $\delta^2\text{H}_{\text{n-alkanes}}$  data published by Hahn et al. (2018) from the SRZ in our dataset (MAT  $17.5$ – $21.1$   $^{\circ}\text{C}$ , MAP  $610$ – $1035$   $\text{mm}\cdot\text{a}^{-1}$ , pot. ET  $1555$ – $1700$   $\text{mm}\cdot\text{d}^{-1}$ , Ai  $0.36$ – $0.67$ ,  $\text{RH}_{\text{RA}}$   $72$ – $80\%$ ; Fig. 3).

### 2.3. Leaf wax analyses

Total lipids were extracted from the dried samples (6.2–31.1 g, depending on bulk density and TOC content) with 40 ml dichloromethane (DCM) and methanol (MeOH) (9/1, v/v) at the Institute of Geography, Friedrich Schiller University Jena. According to Bliedner et al. (2018),

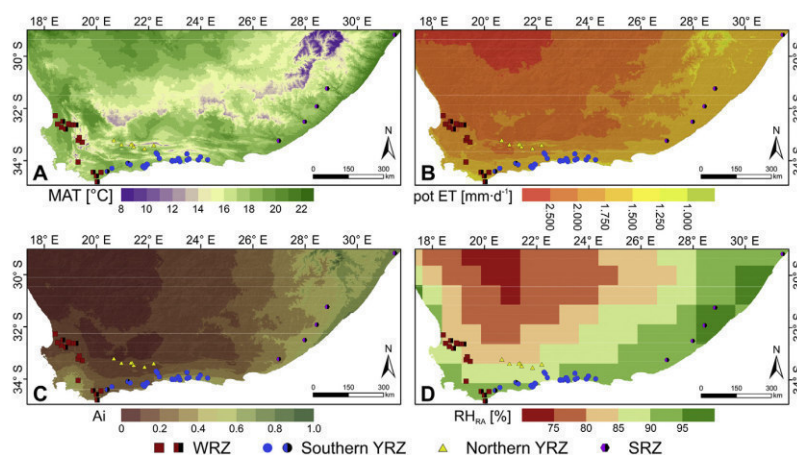


**Fig. 3.** Location of the topsoil samples compared to selected environmental parameters in southern Africa. A) Mean annual precipitation (Fick and Hijmans, 2017); B) potential evapotranspiration (pot. ET) (Trabucco and Zomer, 2019); C) aridity index (Ai: <0.03 hyper arid; 0.03–0.2 arid; 0.2–0.5 semi-arid; 0.5–0.65 dry sub-humid; >0.65 humid) (Trabucco and Zomer, 2019) and relative humidity based on ERA Interim reanalyses data (for calculation see Eq. (3);  $RH_{RA}$ ) (Dee et al., 2011).

each sample was extracted over 3 cycles using an ultrasonic bath for 15 min. The total lipid extract was separated into: i) the apolar fraction including the *n*-alkanes, ii) the polar fraction and iii) the acid fraction by solid phase extraction using aminopropyl silica gel (Supelco, 45  $\mu$ m) as stationary phase. The *n*-alkanes were eluted with 4 ml hexane and further purified over coupled silvernitate ( $AgNO_3$ ) – zeolite (Geokleen) pipette columns. The *n*-alkanes trapped in the zeolite were subsequently dissolved in hydrofluoric acid and recovered by liquid-liquid extraction using *n*-hexane.

Compound-specific stable hydrogen isotope analyses of the most abundant *n*-alkanes  $C_{31}$  and  $C_{33}$  were carried out on an IsoPrime Vision isotope ratio mass spectrometer (IRMS) (Elementar, Langensfeld, Germany), coupled to an Agilent 7890A GC (Agilent, Santa Clara, United States) via a GC5 pyrolysis or combustion interface (Elementar, Langensfeld, Germany) operating in pyrolysis mode with a Cr (ChromeHD) reactor at 1050 °C. The GC was equipped with a 30 m fused silica column (HP5-MS, 30 m, 320  $\mu$ m, 0.25  $\mu$ m). Samples were injected with a split-splitless injector in splitless mode and each sample was analysed in triplicate.  $\delta^2H$  was measured against calibrated  $H_2$  reference gas and all values are reported in permille (‰) against the Vienna Standard Mean Ocean Water (VSMOW). The precision was checked by co-analysing a standard alkane mixture (*n*- $C_{27}$ , *n*- $C_{29}$ , *n*- $C_{33}$ ) with known isotope composition (Arndt Schimmelmann, University of Indiana), injected in duplicate every nine runs. All measurements were corrected for drift, relative to the standard values in each sequence. Triplicates for the *n*- $C_{31}$  and *n*- $C_{33}$  alkanes had a standard deviation of <3.0‰, the analytical error for the standards was <1.6‰ ( $n = 50$ ). The  $H_3^+$  factor was checked every two days and stayed stable at  $4.00 \pm 0.07$  ( $n = 5$ ) during the measurements.

The weighted mean of the most abundant *n*-alkanes ( $C_{31}$  and  $C_{33}$ ) was calculated based on the relative *n*-alkane abundance in the samples and the  $\delta^2H$  isotopic composition. The weighted mean is reported as  $\delta^2H_{n\text{-alkanes}}$  in ‰ versus VSMOW.

#### 2.4. Sugar biomarker analyses

Hemicellulose-derived sugars were hydrolytically extracted from 54 dried samples (0.1–1.9 g, depending on TOC content) at the Institute of Agronomy and Nutritional Sciences, Soil Biogeochemistry, Martin Luther University Halle-Wittenberg. As a solvent, 10 ml of 4 M trifluoroacetic acid were used at 105 °C for 4 h, as described in Amelung et al. (1996). Thereafter, samples were vacuum-filtered over glass fibre filters and the extracted sugars were cleaned according to

Zech and Glaser (2009) using XAD-7 and Dowex 50WX8 columns to remove humic-like substances and cations. The purified sugar samples were rotary evaporated and derivatised with methylboronic acid (4 mg in 400  $\mu$ l pyridine) at 60 °C for 1 h. 5 $\alpha$ -Androstane and 3-O-Methyl-Glucose were used as internal standards.

The compound-specific oxygen isotope measurements were performed on a Trace GC 2000 coupled to a Delta V Advantage IRMS using an  $^{18}O$ -pyrolysis reactor (GC IsoLink) and a ConFlo IV interface (all devices from Thermo Fisher Scientific, Bremen, Germany). Samples were injected in splitless mode and measured in triplicates. For measurement precision standard blocks of derivatised sugars (arabinose, fucose, xylose) at various concentrations and known  $\delta^{18}O$  values were measured. All measurements were corrected for drift and amount dependency, as well as for hydrolytically introduced oxygen atoms which form carbonyl groups within the sugar molecules (Zech and Glaser, 2009). The standard deviation of the arabinose sample triplicate and standard duplicate measurements were 2.2‰ and <1.9‰ ( $n = 35$ ), respectively. The oxygen isotopic composition is given in the delta notation ( $\delta^{18}O$ ) in ‰ versus VSMOW.

#### 2.5. Coupling compound-specific leaf wax $\delta^2H$ and sugar $\delta^{18}O$

The coupled  $\delta^2H_{n\text{-alkanes}}-\delta^{18}O_{\text{sugar}}$  paleohygrometer approach was described in detail previously by Hepp et al. (2019b and references therein). The most fundamental assumption of the approach is that the isotopic composition of leaf water can be reconstructed by applying biosynthetic fractionation factors ( $\epsilon_{\text{bio}}$ ) on the measured  $\delta^2H_{n\text{-alkanes}}$  and  $\delta^{18}O_{\text{sugar}}$  values. For  $\delta^2H_{n\text{-alkanes}}$  a constant  $\epsilon_{\text{bio}}$  value of about  $-160\text{‰}$  (Sachse et al., 2012; Sessions et al., 1999) is applied; for  $\delta^{18}O_{\text{sugar}}$  the  $\epsilon_{\text{bio}}$  value is assumed to be  $+27\text{‰}$  (Cernusak et al., 2003; Gessler et al., 2009; Hepp et al., 2019a; Schmidt et al., 2001; Sternberg et al., 1986; Yakir and DeNiro, 1990) (Fig. 1). This can be illustrated in a  $\delta^2H-\delta^{18}O$  diagram where the distance of the reconstructed leaf water to the global meteoric water line (GMWL) is defined as deuterium-excess (Dansgaard, 1964) (Fig. 4).

The concept is furthermore based on the fact that the isotopic composition of precipitation plots typically close to the GMWL ( $\delta^2H_p = 8 \cdot \delta^{18}O_p + 10$ ; Dansgaard, 1964). However, in South Africa, two local meteoric water lines slightly deviating from GMWL were described by i) Harris et al. (2010) ( $\delta^2H = 6.51 \cdot \delta^{18}O + 8.89$ ) for Cape Town (WRZ), and ii) Braun et al. (2017) ( $\delta^2H = 7.70 \cdot \delta^{18}O + 12.10$ ) for Mossel Bay (YRZ) (Fig. 4). Depending on whether our sample location

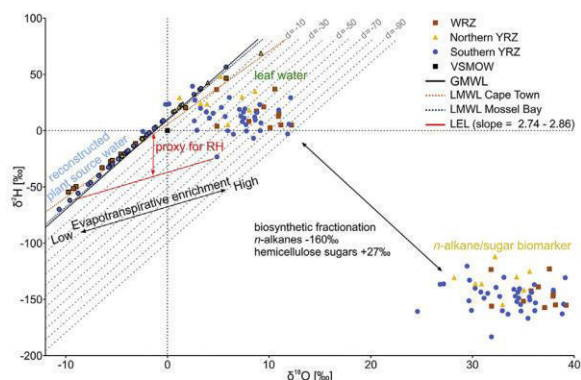


**Fig. 4.** Conceptual framework of the coupled  $\delta^2\text{H}_{n\text{-alkanes}}-\delta^{18}\text{O}_{\text{sugar}}$  paleohygrometer approach displayed as  $\delta^2\text{H}-\delta^{18}\text{O}$  diagram showing the measured  $n$ -alkanes (weighted mean of  $\text{C}_{31}$  and  $\text{C}_{33}$ ) and sugar (arabinose) biomarkers, the reconstructed leaf and plant source water, the global meteoric water line (GMWL, black line), and the local meteoric water lines (LMWL) of Cape Town (orange dashed line) and Mossel Bay (blue dashed line). The black double arrow indicates natural processes of evapotranspirative enrichment of leaf water along local evaporation lines (red line) and biosynthetic fractionation during biomarker synthesis. Grey dashed lines indicate the deuterium-excess, which can be used as proxy for relative humidity (red double arrow). (For interpretation of the references to colour in this figure legend, the reader is referred to the web version of this article.)

is in the WRZ or the YRZ, we therefore use the respective LMWL for our calculations.

We calculated equilibrium fractionation factors according to Horita and Wesolowski (1994) for each sample location based on the specific MAT. They range from 79.8 to 85.8‰ for  $^2\text{H}$  and 9.82 to 10.32‰ for  $^{18}\text{O}$ . The kinetic fractionation parameters for  $^2\text{H}$  and  $^{18}\text{O}$  are set to 25.1‰ and 28.5‰, respectively (Merlivat, 1978). This yields a specific slope for a local evaporation line (LEL) for each data point (ranging from 2.74 to 2.86). The intercept of the LEL and the LMWL (from WRZ or YRZ) is the isotopic composition of ‘reconstructed plant source water’ ( $\delta^2\text{H}_{\text{source water}}$  and  $\delta^{18}\text{O}_{\text{source water}}$ ) (Fig. 4). Moreover, the difference between deuterium-excess of the reconstructed leaf water and reconstructed plant source water can be used to estimate relative humidity ( $\text{RH}_{\text{rec}}$ ) for each sample (Fig. 4). We are aware that in grasses signal dampening has to be considered due to intercalary meristem (cf. Hepp et al., 2019b), but in our study grasses were not dominant at any sample location.

## 2.6. Data analyses

The apparent fractionation of both hydrogen- and oxygen isotopes ( $\epsilon_{\text{app } 2\text{H}}$ ,  $\epsilon_{\text{app } 18\text{O}}$ ) was calculated after Sauer et al. (2001) to test for climate/environmental control on  $\delta^2\text{H}_{n\text{-alkanes}}$  and  $\delta^{18}\text{O}_{\text{sugar}}$  (Eqs. (1) and (2)).

$$\epsilon_{\text{app } 2\text{H}} = \left( \frac{\delta^2\text{H}_{n\text{-alkanes}} + 1000}{\delta^2\text{H}_p + 1000} - 1 \right) \times 1000 [\text{‰}] \quad (1)$$

$$\epsilon_{\text{app } 18\text{O}} = \left( \frac{\delta^{18}\text{O}_{\text{sugar}} + 1000}{\delta^{18}\text{O}_p + 1000} - 1 \right) \times 1000 [\text{‰}] \quad (2)$$

$\delta^2\text{H}_p$  and  $\delta^{18}\text{O}_p$  are the isotopic signatures of precipitation, extracted from *The Online Isotopes in Precipitation Calculator* (OIPC; Version 3.1; <http://www.waterisotopes.org>) (Bowen and Revenaugh, 2003; Bowen et al., 2005; Bowen and Wilkinson, 2002), and weighted by precipitation amount of the respective precipitation zone. Accordingly, different months were used for these calculations: June, July and August (JJA) for the WRZ; annual weighted mean for the southern YRZ; and December,

January and February (DJF) for the SRZ and northern YRZ. We have to note that Herrmann et al. (2017) described the northern YRZ to be dominated by the isotopic signature of the summer months, which explains our comparison with the respective precipitation (DJF).

Sample point-specific relative humidity was calculated after Alduchov and Eskridge (1996) (Eq. (3)). For each sample point 2 m temperature ( $T$ ) and 2 m dew-point temperature ( $TD$ ) were extracted from the ERA Interim reanalyses dataset ( $\text{RH}_{\text{RA}}$ ; reference time: 1989–2018; spatial resolution:  $\sim 80$  km; Dee et al., 2011) using ‘B-spline’ interpolation tool in SAGA GIS.

$$\text{RH}_{\text{RA}} = 100 \cdot \frac{\left[ \text{EXP} \left( \frac{17.625 \cdot TD}{243.04 \cdot TD} \right) \right]}{\left[ \text{EXP} \left( \frac{17.625 \cdot T}{243.04 \cdot T} \right) \right]} [\%] \quad (3)$$

Correlations of  $\delta^2\text{H}_{n\text{-alkanes}}$ ,  $\delta^{18}\text{O}_{\text{sugar}}$ ,  $\epsilon_{\text{app}}$ ,  $\text{RH}_{\text{rec}}$  with environmental parameters were tested using weighted linear regressions. The MAT was derived from the WorldClim 2.0 dataset (1970–2000; 30s resolution; <http://worldclim.org/version2>; Fick and Hijmans, 2017), and the Aridity index (AI) and potential evapotranspiration (pot. ET) were derived from the Global Aridity Index and Potential Evapotranspiration Climate Database v2 (1970–2000; 30s resolution; Trabucco and Zomer, 2019), respectively. Regressions were calculated under consideration of the 95% confidence bands and significance of regressions was tested using analysis of variance (ANOVA) and F ratios. Goodness of fit was assumed using corrected  $R^2$  values and a student's  $t$ -test was performed to determine significant differences ( $\alpha = 0.05$ ). All statistical analyses were performed using the statistical software OriginPro 2017.

## 3. Results and discussion

### 3.1. $\delta^2\text{H}_{n\text{-alkanes}}$ and $\delta^{18}\text{O}_{\text{sugar}}$ vs. precipitation

Along the investigated South African transect, there is a significant correlation of  $\delta^2\text{H}_{n\text{-alkanes}}$  and  $\delta^2\text{H}_p$  (own samples  $n = 59$ , and additionally eight samples from five locations in the SRZ from Hahn et al. (2018), Fig. 5). Significant differences are calculated for samples from the S-YRZ compared to N-YRZ and SRZ (Fig. 5). Samples from the WRZ, N-YRZ and SRZ do not differ significantly (Fig. 5). The correlation of  $\delta^{18}\text{O}_{\text{sugar}}$  ( $n = 54$ ) with  $\delta^{18}\text{O}_p$  is not significant, however, the isotopic  $\delta^{18}\text{O}_{\text{sugar}}$  composition of the samples from the WRZ differs significantly from those of the S-YRZ and N-YRZ (Fig. 5).

South Africa is characterised by large differences in  $\delta^2\text{H}_p$  and  $\delta^{18}\text{O}_p$ , with precipitation brought by the Westerlies (WRZ) being depleted in  $^2\text{H}$  and  $^{18}\text{O}$  and brought by the Easterlies (SRZ) being enriched in  $^2\text{H}$  and  $^{18}\text{O}$  (Figs. 2, 5) (Braun et al., 2017; Harris et al., 2010). The significant overall trend in our data follows the isotopic composition of precipitation and shows more negative  $\delta^2\text{H}_{n\text{-alkanes}}$  values for the Westerly-dominated WRZ and the more positive  $\delta^2\text{H}_{n\text{-alkanes}}$  values for the Easterly-dominated SRZ (Fig. 5). Although only partly significant, the differences in the median  $\delta^2\text{H}_{n\text{-alkanes}}$  values of the WRZ and S-YRZ are distinctly more negative than in the N-YRZ and SRZ, which points out that  $\delta^2\text{H}_{n\text{-alkanes}}$  follows the  $\delta^2\text{H}_p$  signature (Fig. 5). It has to be noted that the range of the intra-zonal  $\delta^2\text{H}_{n\text{-alkanes}}$  data is substantially wider than the range of  $\delta^2\text{H}_p$  (Fig. 5). Overall, the positive correlation between  $\delta^2\text{H}_{n\text{-alkanes}}$  and  $\delta^2\text{H}_p$  of the vegetation period was also found in several studies in different ecosystems (Herrmann et al., 2017; Li et al., 2019). However, due to phenological adaptations, the definition of the vegetation period for each ecoregion in South Africa is not trivial, but is generally considered to be related to the main precipitation seasonality (Matimati et al., 2013; Wessels et al., 2011).

The significant difference in  $\delta^2\text{H}_{n\text{-alkanes}}$  of the humid S-YRZ compared to the (semi-)arid N-YRZ (Fig. 5) highlights that other biases possibly influence the  $\delta^2\text{H}_{n\text{-alkanes}}$  signal, because both regions are located in the YRZ and precipitation is thought to be contributed by both the

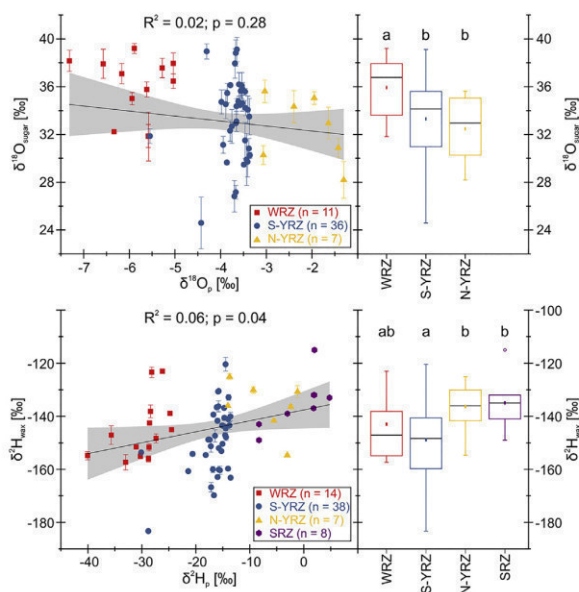


**Fig. 5.** Correlation of  $\delta^{18}\text{O}_{\text{sugar}}$  with  $\delta^{18}\text{O}_p$  and  $\delta^2\text{H}_{n\text{-alkanes}}$  with  $\delta^2\text{H}_p$  related to the seasonal precipitation of the sampling sites (WRZ: JJA; S-YRZ: mean annual; N-YRZ and SRZ: DJF; for sample classification see Boxplot labels and Fig. 2) derived from OIPC data (Bowen and Revenaugh, 2003; Bowen et al., 2005; Bowen and Wilkinson, 2002) and weighted by monthly precipitation data by Fick and Hijmans (2017). The overall linear fit (black line) including  $R^2$ , 95% confidence interval (grey area) and  $p$ -value were calculated. The boxplots indicate median values (black lines), mean values (squares), interquartile ranges with lower (25%) and upper (75%) quartiles (box), 1.5 interquartile range (whiskers) and outliers (circles). Letters indicate significant differences ( $\alpha = 0.05$ ;  $p < 0.05$ ).

Westerlies and the Easterlies. However, Herrmann et al. (2017) described the isotopic signature of the N-YRZ to be more influenced by Easterly-related summer rainfall contribution, which underlines our results since the N-YRZ data are within the range of the SRZ (Fig. 5). However, due to largely different environmental conditions in the S-YRZ and N-YRZ (Fig. 3), soil water enrichment and leaf water transpiration may differ for both transects. In the drier regions of South Africa soil water is possibly more affected by evaporation, leading to a  $^2\text{H}$  enrichment of soil water used by the plants (Herrmann et al., 2017). However, in this study, soil water enrichment cannot be excluded, but is considered to be negligible, since most plants use deeper water sources not affected by soil water enrichment (e.g., Feakins and Sessions, 2010a; Kahmen et al., 2013b). Additionally, earlier studies found  $^2\text{H}$ -enriched leaf water due to leaf transpiration in drier regions (Griepentrog et al., 2019; Kahmen et al., 2013a; Kahmen et al., 2013b; Sachse et al., 2012). As a consequence, evapo(transpi)ration possibly leads to higher  $\delta^2\text{H}_{n\text{-alkanes}}$  composition in drier areas like the N-YRZ (Feakins and Sessions, 2010a; Kahmen et al., 2013a; Smith and Freeman, 2006), and will be addressed more in detail in the next section.

The S-YRZ, however, is not only affected by rain bearing systems from the large atmospheric circulation systems but also by moisture-derived from local sources (Engelbrecht and Landman, 2016; Engelbrecht et al., 2015; Tyson and Preston-Whyte, 2000). This overlap can complicate the assignment of moisture sources (Braun et al., 2017; Harris et al., 2010). The topography of the YRZ further complicates such relationships because the Outeniqua Mountains and Swartberge serve as a source of much greater topographic/microclimatic variability than in the interior. The resulting orographic effects possibly lead to specific microclimates in mountainous areas of the YRZ, including higher precipitation rates on the windward sides of slopes and lower rates on the leeward sides (Houze, 2012), as well as small scale differences in  $\delta^2\text{H}_p$  composition due to local convection and rainout (Harris et al.,

2010), as described for other mountain areas (Araguás-Araguás et al., 2000; Bowen and Revenaugh, 2003; Holdsworth et al., 1991; Siegenthaler and Oeschger, 1980; Zongxing et al., 2016). Such small-scale variations are not reflected in  $\delta^2\text{H}_p$ . These complex and small-scale processes likely explain the large intra-zonal range of the  $\delta^2\text{H}_{n\text{-alkanes}}$  data for the S-YRZ, but also for the WRZ, where the Cape Fold Mountains are an orographic barrier (Herrmann et al., 2017). Moreover, the used OIPC data include only two time series datasets from Cape Town and Mossel Bay for the study area resulting in a spatial resolution of 5 arc sec ( $\sim 10$  km) (Bowen and Revenaugh, 2003; Bowen et al., 2005; Bowen and Wilkinson, 2002). The spatial resolution and the limited availability of measured data possibly lead to uncertainties concerning the isotopic composition of  $\delta^2\text{H}_p$  and  $\delta^{18}\text{O}_p$ .

Also for  $\delta^{18}\text{O}_{\text{sugar}}$ , the intra-zonal  $\delta^{18}\text{O}_{\text{sugar}}$  variability is larger than the one of  $\delta^{18}\text{O}_p$  (Fig. 5) and accompanied by the above mentioned uncertainties regarding  $\delta^{18}\text{O}_p$ . Still, there is a significant difference between WRZ compared to S-YRZ and N-YRZ with the WRZ data being more enriched in  $^{18}\text{O}$  compared to both datasets from the YRZ (Fig. 5). Since Westerly-derived precipitation is depleted in  $^{18}\text{O}$ , this result is against expectation at first glance. However, Tuthorn et al. (2014) did not observe a correlation between  $\delta^{18}\text{O}_{\text{sugar}}$  and  $\delta^{18}\text{O}_p$  for a South American transect, either. They argued that soil water evaporation, leaf water transpiration and seasonality effects are dominant drivers biasing the  $\delta^{18}\text{O}_{\text{sugar}}$  signal. The present study confirms this assumption for the comparison of the  $\delta^{18}\text{O}_{\text{sugar}}$  and the  $\delta^{18}\text{O}_p$  signal. It can be concluded, that plant-related and/or environmental factors strongly bias the  $\delta^{18}\text{O}_{\text{sugar}}$  signal compared to  $\delta^{18}\text{O}_p$ , which might also be true but in lesser extent for the relation of  $\delta^2\text{H}_{n\text{-alkanes}}$  and  $\delta^2\text{H}_p$ .

### 3.2. Apparent fractionation vs. climate

To account for potential evapo(transpi)ration on the biomarker isotopes, the apparent fractionation ( $\epsilon_{\text{app}}$ ) was calculated for oxygen and hydrogen isotopes along the transect and correlated with climate parameters (Eqs. (1) and (2); Fig. 6). Since CAM plants are dominant in the N-YRZ and their isotopic signals rather reflect plant-related (phenological) adaptations than climatic influences, those samples were excluded from the following climate correlations and the calculation of the overall trend. However, the CAM-influenced  $\epsilon_{\text{app}}$  values from the N-YRZ will be discussed later.

Along the transect, oxygen  $\epsilon_{\text{app}}$  ( $\epsilon_{\text{app } 18\text{O}}$ ) values from the WRZ ( $40.4 \pm 3.0\text{‰}$ ) are significantly higher compared to  $\epsilon_{\text{app } 18\text{O}}$  from the S-YRZ ( $37.1 \pm 3.5\text{‰}$ ), and significant correlations exist between  $\epsilon_{\text{app } 18\text{O}}$  and the potential evapotranspiration and the Aridity index (Fig. 6). In contrast, hydrogen  $\epsilon_{\text{app}}$  ( $\epsilon_{\text{app } 2\text{H}}$ ) did not differ significantly between WRZ ( $-130 \pm 10\text{‰}$ ) and S-YRZ ( $-136 \pm 12\text{‰}$ ) as well as WRZ and SRZ ( $-126.7 \pm 8.6\text{‰}$ ) but differs significantly between S-YRZ and SRZ (Fig. 6). However, no significant correlations exist between  $\epsilon_{\text{app } 2\text{H}}$  of the overall dataset and potential evapotranspiration and the Aridity index (Fig. 6).

Neither for  $\epsilon_{\text{app } 2\text{H}}$  nor for  $\epsilon_{\text{app } 18\text{O}}$  there is a significant correlation with MAT or with growing season temperature in this study (Fig. 6), although previous studies described an effect of temperature on  $\epsilon_{\text{app}}$  (Feakins and Sessions, 2010a; Li et al., 2019; Sachse et al., 2012). The significant correlations of  $\epsilon_{\text{app } 18\text{O}}$  compared to potential evapotranspiration and Aridity index shows that there is a major influence of evapo(transpi)ration on the biomarker signal (Fig. 6). This becomes especially obvious in the WRZ, where  $\epsilon_{\text{app } 18\text{O}}$  is significantly higher compared to the S-YRZ and confirms the assumption by Tuthorn et al. (2014), who described  $\delta^{18}\text{O}_{\text{sugar}}$  to be very sensitive for evapo(transpi)ration on the biomarker signal. There is no significant overall trend of  $\epsilon_{\text{app } 2\text{H}}$  against the climate parameters, and thus  $\epsilon_{\text{app } 2\text{H}}$  is obviously not affected by climate-related evapo(transpi)ration enrichment (Fig. 6). Other studies described that  $\epsilon_{\text{app } 2\text{H}}$  can vary between vegetation types (e.g. grasses, shrubs; Kahmen et al., 2013b), photosynthetic pathway (Feakins and Sessions, 2010b; Gamarra et al., 2016; Liu and

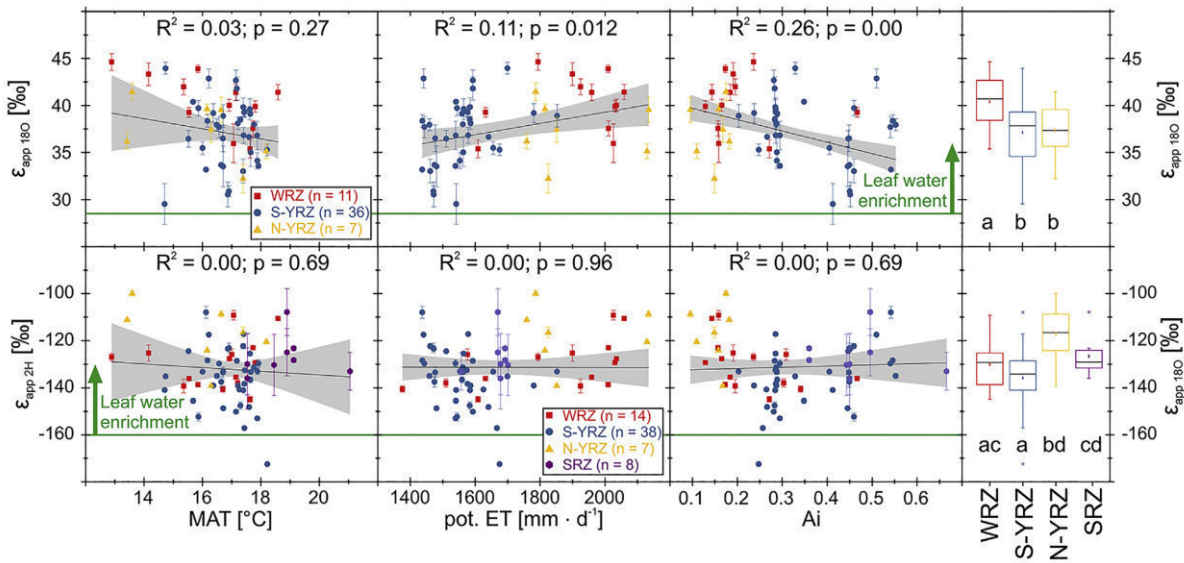


**Fig. 6.** Correlation of  $\epsilon_{app\ 18O}$  and  $\epsilon_{app\ 2H}$  (see Eqs. (1) and (2) for calculation) with mean annual temperature (MAT), potential evapotranspiration (pot. ET) and Aridity index (Ai). The overall linear fit (black line) including  $R^2$ , 95% confidence interval (grey area) and  $p$ -values were calculated. Please note that N-YRZ data points reflecting prevailing CAM plants were not included in the trendline calculations (see main text). The vertical distance between the green line and the sample points indicates leaf water enrichment. The boxplots indicate median values (black lines), mean values (squares), interquartile ranges with lower (25%) and upper (75%) quartiles (box), 1.5 interquartile range (whiskers) and outliers (circles). Letters indicate significant differences ( $\alpha = 0.05$ ;  $p < 0.05$ ). (For interpretation of the references to colour in this figure legend, the reader is referred to the web version of this article.)

Yang, 2008), leaf shape (Gao et al., 2015) and water use efficiency (Hou et al., 2007; Liu and Yang, 2008). Moreover, large differences in  $\epsilon_{app\ 2H}$  were reported for arid vs. humid climates with substantially more negative values for the latter (e.g., Feakins and Sessions, 2010a; Li et al., 2019; Polissar and Freeman, 2010; Smith and Freeman, 2006). Our study shows no systematic climate-driven  $\epsilon_{app\ 2H}$  pattern and reveals to be relatively constant.

Basically, the apparent fractionation integrates three processes: i) soil water enrichment, ii) leaf-water transpiration, and iii) biosynthetic fractionation (Fig. 1). In detail, soil water enrichment (i) and leaf and xylem water transpiration (ii) are described to be most sensitive to relative humidity, with greater  $^2H$  enrichment in arid than in humid climates (Hou et al., 2018; Kahmen et al., 2013a, 2013b; Li et al., 2019; Polissar and Freeman, 2010; Smith and Freeman, 2006). Biosynthetic fractionation (iii) is mostly considered to be stable but may change under drier conditions leading to less negative  $\epsilon_{app\ 2H}$  values (Gamarrá et al., 2016; Li et al., 2019 and references therein). As mentioned before, soil water enrichment cannot be excluded in this study, but is considered to be negligible, since most plants use deeper water sources not affected by soil water enrichment (e.g., Feakins and Sessions, 2010a; Kahmen et al., 2013b). As a consequence, the distance between the  $\epsilon_{app}$  values and the biosynthetic fractionation factor ( $\delta^{18}O = +27\%$ ;  $\delta^{2H} = -160\%$ ) is suggested to reflect leaf water enrichment due to evapotranspiration (Fig. 6). For the WRZ and S-YRZ, changes in  $\epsilon_{app}$  due to plant-specific (phenological) adaptations cannot be excluded, but the correlation of  $\epsilon_{app\ 18O}$  with potential evapotranspiration and the Aridity index make  $^{18}O$  leaf water enrichment driven by evapotranspiration very likely, whereas  $^2H$  leaf water enrichment seems to be relatively constant (Fig. 6). A limiting factor for the calculation of  $\epsilon_{app}$  is the possible insufficient spatial resolution of  $\delta^{2H}_p$  and  $\delta^{18}O_p$  (Bowen and Revenaugh, 2003; Bowen et al., 2005; Bowen and Wilkinson, 2002), which may not consider small scale variability (cf. Section 3.1).

The N-YRZ shows a different picture due to the presence of many plants using the CAM metabolism with (some unusual) drought adaptations as previously described by Carr et al. (2014 and references therein). In the (semi-)arid N-YRZ, where potential evapotranspiration and Aridity index are in the range of the WRZ (Fig. 3),  $\epsilon_{app\ 18O}$  values are

surprisingly low and differences compared to the more humid S-YRZ reveal no significance (Fig. 6). Thus, the high evaporative environmental conditions in the N-YRZ are not reflected by  $\epsilon_{app\ 18O}$ . In contrast, evapotranspiration-related processes seem to have a major influence on  $\epsilon_{app\ 2H}$  in the N-YRZ, showing significantly highest values (Fig. 6). The contrary results of  $\epsilon_{app\ 18O}$  and  $\epsilon_{app\ 2H}$  are partly surprising as Sternberg and DeNiro (1983) described  $\delta^{18}O$  in cellulose to be not dependent on the photosynthetic pathway (C3, C4, CAM), however, our results show more negative  $\epsilon_{app\ 18O}$  values in the CAM-dominated N-YRZ. Moreover, Feakins and Sessions (2010b) suggest that low  $\epsilon_{app\ 2H}$  values are common as a result of increasing usage of CAM metabolism. In contrast,  $\epsilon_{app\ 2H}$  is least negative in the N-YRZ, which is thus against the expectation in this area, but already discussed by Herrmann et al. (2017). In (semi-)arid environments plants also use water vapour, cloud moisture and fog as additional moisture sources (Helliker and Griffiths, 2007; Schulze, 1997). The moisture supply from water vapour and fog can considerably exceed the amount of precipitation in (semi-)arid environments (Matimati et al., 2013; Schulze, 1997), which is possibly imprinted in the biomarkers' isotope signal (Helliker and Griffiths, 2007). Moreover, Feakins and Sessions (2010b) highlight, that exchange reactions related to CAM metabolism occur during night-time, when relative humidity is very high. All these issues considerably complicate the interpretation of our N-YRZ dataset. Concerning  $\epsilon_{app\ 18O}$ , the following three processes lead to higher  $\epsilon_{app\ 18O}$  values (Fig. 2). Since soil water enrichment (i) is considered to be negligible, we hypothesise that plant-specific (phenological) adaptations might reduce leaf water transpiration (ii), and/or variations in biosynthetic fractionation (iii) likely contribute to the unexpected low  $\epsilon_{app\ 18O}$  values in the N-YRZ. In addition, several studies indicate post-photosynthetic exchange reactions effecting  $\delta^{18}O$  in plants, which might lead to low  $\epsilon_{app\ 18O}$  values in the N-YRZ (Barbour, 2007; Sternberg, 2009; Sternberg et al., 2006), but possibly do not bias  $\epsilon_{app\ 2H}$ .

### 3.3. Reconstructed plant source water vs. precipitation

The isotopic composition of reconstructed plant source water ranges between  $-10.7$  to  $9.2\%$  and  $-70$  to  $69\%$  for  $\delta^{18}O_{source\ water}$  and

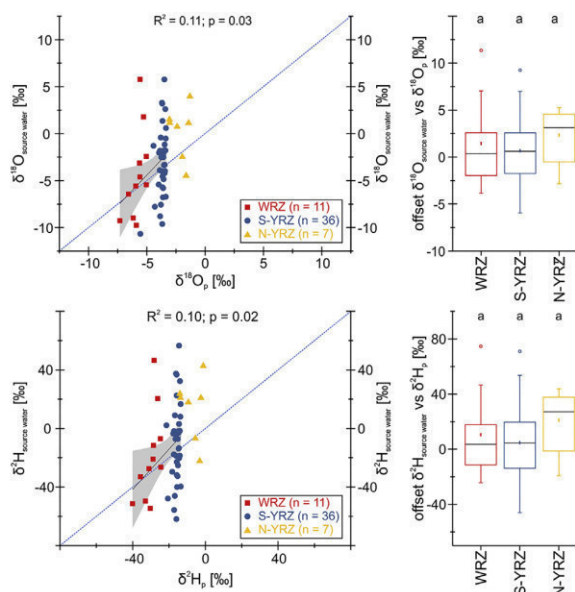


**Fig. 7.** Correlation between  $\delta^{18}\text{O}_{\text{source water}}$  and  $\delta^{18}\text{O}_p$ , as well as  $\delta^2\text{H}_{\text{source water}}$  and  $\delta^2\text{H}_p$ , related to the seasonal precipitation of the samples (WRZ: JJA; S-YRZ: mean annual; N-YRZ and SRZ: DJF; for sample classification see Fig. 2) derived from OIPC data (Bowen and Revenaugh, 2003; Bowen et al., 2005; Bowen and Wilkinson, 2002) and weighted by monthly precipitation data by Fick and Hijmans (2017). The overall linear fit excluding the N-YRZ data (black line),  $R^2$ , 95% confidence interval (grey area) and p-values were calculated and a 1:1 relationship was integrated in each diagram (light blue dashed line). The offset of  $\delta^{18}\text{O}_{\text{source water}}$  to  $\delta^{18}\text{O}_p$  and  $\delta^2\text{H}_{\text{source water}}$  to  $\delta^2\text{H}_p$  is shown in the boxplots, which indicate median values (black lines), mean values (squares), interquartile ranges with lower (25%) and upper (75%) quartiles (box), 1.5 interquartile range (whiskers) and outliers (circles). Letters indicate a significant difference ( $\alpha = 0.05$ ;  $p < 0.05$ ). (For interpretation of the references to colour in this figure legend, the reader is referred to the web version of this article.)

$\delta^2\text{H}_{\text{source water}}$ , respectively (Fig. 7). Based on the OIPC data, this study has a precipitation signal ranging between  $\sim -5.8$  to  $\sim -3.2\text{‰}$  and  $\sim -10$  to  $\sim -30\text{‰}$  for  $\delta^{18}\text{O}$  and  $\delta^2\text{H}$ , respectively (Fig. 7). Again, N-YRZ sample were excluded for the calculation of the overall trend. Significant correlations exist between both the reconstructed  $\delta^{18}\text{O}_{\text{source water}}$  and  $\delta^{18}\text{O}_p$  as well as  $\delta^2\text{H}_{\text{source water}}$  and  $\delta^2\text{H}_p$  (Fig. 7). This demonstrates that reconstructed plant source water reflects precipitation. For each sample the offset between reconstructed source water and the respective  $\delta^{18}\text{O}_p$  and  $\delta^2\text{H}_p$  was calculated (Fig. 7). Although not significant, the median offset of the samples from the N-YRZ ( $\delta^{18}\text{O} = 3.1\text{‰}$ ;  $\delta^2\text{H} = 27.2\text{‰}$ ) is distinctly larger compared to the WRZ ( $\delta^{18}\text{O} = 0.4\text{‰}$ ;  $\delta^2\text{H} = 3.6\text{‰}$ ) and the S-YRZ ( $\delta^{18}\text{O} = 0.6\text{‰}$ ;  $\delta^2\text{H} = 4.5\text{‰}$ ) (Fig. 7).

Reconstructed plant source water shows a considerably larger range ( $\delta^{18}\text{O} = \sim -19.9\text{‰}$ ;  $\delta^2\text{H} = \sim -139\text{‰}$ ) compared to the range of the OIPC data ( $\delta^{18}\text{O} = \sim -6\text{‰}$ ;  $\delta^2\text{H} = \sim -20\text{‰}$ ) (Bowen and Revenaugh, 2003; Bowen et al., 2005; Bowen and Wilkinson, 2002) (Fig. 7). Moreover, reconstructed source water shows a large intra-zonal scattering including potential small-scale variations of source water, which is less pronounced in the OIPC data (Fig. 7). As described before, the spatial resolution of the OIPC data is possibly insufficient to reliably show the isotopic composition of the source water (cf. Section 3.1). The significant overall trend of reconstructed source water of both  $\delta^{18}\text{O}_{\text{source water}}$  and  $\delta^2\text{H}_{\text{source water}}$  reflects the  $\delta^{18}\text{O}_p$  and  $\delta^2\text{H}_p$  better than the relation of  $\delta^{18}\text{O}_{\text{sugar}}$  and  $\delta^2\text{H}_{n\text{-alkanes}}$  compared to  $\delta^{18}\text{O}_p$  and  $\delta^2\text{H}_p$  (cf. Section 3.1), which is due to consideration of the site-specific evapo(transpi)rative enrichment in the paleohygrometer approach. This is especially true for  $\delta^{18}\text{O}$  and also observed by Tuthorn et al. (2015). This highlights the added value of coupling both  $\delta^{18}\text{O}_{\text{sugar}}$  and  $\delta^2\text{H}_{n\text{-alkanes}}$ . Overall, plant source water can be reconstructed for study areas where CAM plants do not prevail with an

offset of  $\Delta\delta^{18}\text{O} = 0.8 \pm 3.7\text{‰}$  for  $\delta^{18}\text{O}_{\text{source water}}$  ( $1\sigma$ ) and  $\Delta\delta^2\text{H} = 6 \pm 27\text{‰}$  for  $\delta^2\text{H}_{\text{source water}}$  ( $1\sigma$ ), respectively (Fig. 7).

Due to CAM metabolism,  $\delta^{18}\text{O}_{\text{sugar}}$  values in the N-YRZ seem to be affected by post-photosynthetic exchange reactions (cf. Section 3.2) resulting in too low values. In contrast,  $\delta^2\text{H}_{n\text{-alkanes}}$  shows a large evapotranspirative enrichment. This explains why source water is reconstructed too enriched for both  $\delta^{18}\text{O}$  and  $\delta^2\text{H}$  (Figs. 4; 7). The understanding of the variability related to the source water (e.g., water vapour, fog, precipitation) and its isotopic composition as well as post-photosynthetic exchange reactions related to CAM metabolism seem to be not adequate to reliably reconstruct source water in the N-YRZ.

#### 3.4. Reconstructed vs. modelled relative humidity

The reconstructed relative humidity ( $\text{RH}_{\text{rec}}$ ) of the overall dataset ranges between  $\sim 32$  and  $\sim 109\%$  (Fig. 8). Calculated relative humidity based on ERA Interim reanalyses data ( $\text{RH}_{\text{RA}}$ ) spans a range of 46 to 74% (Fig. 8). Excluding again the samples from the N-YRZ, there is a significant overall correlation between for  $\text{RH}_{\text{rec}}$  and  $\text{RH}_{\text{RA}}$  (Fig. 8). Based on this study, RH can be reconstructed with an offset of about  $\Delta\text{RH} = 6 \pm 17\%$  excluding study areas with CAM plant predominance. There is a significant larger median offset between  $\text{RH}_{\text{rec}}$  and  $\text{RH}_{\text{RA}}$  in the CAM-dominated N-YRZ ( $\Delta\text{RH} = 31.7\%$ ) compared to WRZ ( $\Delta\text{RH} = -5.1\%$ ) and S-YRZ ( $\Delta\text{RH} = 3.9\%$ ) (Fig. 8). Thus, especially the N-YRZ highlights the influence of plant-specific adaptations concerning oxygen and hydrogen fractionation in (semi-)arid environments. Distinct hampered  $\epsilon_{\text{app } 180}$  enrichment leads to an overestimation of  $\text{RH}_{\text{rec}}$  and represents a limitation of the paleohygrometer approach. Feakins and Sessions (2010b) highlighted, that exchange reactions related to the CAM metabolism occur during night-time, when relative humidity is very high. Therefore,  $\text{RH}_{\text{rec}}$  potentially reflects night-time RH in the N-YRZ, whereas WRZ and S-YRZ RH mainly reflects day-time RH due to C3 metabolism. However, due to least negative  $\epsilon_{\text{app } 2\text{H}}$  values this seems to be unlikely. Rather, the biased  $\epsilon_{\text{app } 180}$  values lead to overestimated  $\text{RH}_{\text{rec}}$  values due to plant-specific (phenological) adaptations and/or post-photosynthetic exchange reactions in the N-YRZ.

To further validate the  $\text{RH}_{\text{rec}}$  data, either observed/measured and/or modelled (reanalyses) data would be necessary. However, long-term observations are very scarce for the studied area and reanalyses data including relative humidity are limited as well. Moreover, their spatial resolution is often insufficient (spatial resolution between e.g.,  $-0.7^\circ$ – $2.5^\circ$  ( $\sim 80$ – $\sim 220$  km; e.g., Dee et al., 2011; Kalnay et al., 1996) to validate

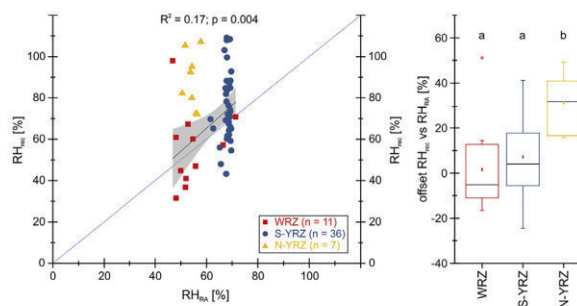


**Fig. 8.** Correlation between reconstructed relative humidity ( $\text{RH}_{\text{rec}}$ ) and sample-specific calculated relative humidity based on ERA Interim reanalyses data ( $\text{RH}_{\text{RA}}$ , see Eq. (3) for calculation; Dee et al., 2011). The overall linear fit excluding the N-YRZ data (black line),  $R^2$ , 95% confidence interval (grey area) and p-values were calculated as well as a 1:1 relationship was integrated in each diagram (light blue dashed line). The boxplots indicate median values (black lines), mean values (squares), interquartile ranges with lower (25%) and upper (75%) quartiles (box), 1.5 interquartile range (whiskers) and outliers (circles). Letters indicate significant differences ( $\alpha = 0.05$ ;  $p < 0.05$ ). (For interpretation of the references to colour in this figure legend, the reader is referred to the web version of this article.)

a proxy which is very sensitive on small scale changes. Therefore, it is expected that  $RH_{RA}$  underestimate the range and variability of RH.

#### 4. Conclusions

- In South Africa,  $\delta^2H_{n\text{-alkanes}}$  correlates significantly with the isotopic composition of precipitation ( $\delta^2H_p$ ). By contrast, there is no significant correlation between  $\delta^{18}O_{\text{sugar}}$  and  $\delta^{18}O_p$ . The spatial resolution of the comparative data is possibly insufficient to detect small-scale variations in  $\delta^2H_p$  and  $\delta^{18}O_p$ .
- Potential evapotranspiration and Aridity index have a significant influence on  $\epsilon_{\text{app } 18O}$  whereas  $\epsilon_{\text{app } 2H}$  shows no significant correlations. Neither for  $\epsilon_{\text{app } 18O}$  nor for  $\epsilon_{\text{app } 2H}$ , there was found a correlation with temperature. These findings highlight the effect of evapotranspirative enrichment on  $\delta^{18}O_{\text{sugar}}$ .
- Coupling  $\delta^{18}O_{\text{sugar}}$  and  $\delta^2H_{n\text{-alkanes}}$  enables to reconstruct plant source water with an offset of  $\Delta\delta^{18}O = 0.8 \pm 3.7\%$  and  $\Delta\delta^2H = 6 \pm 27\%$ , respectively, which significantly correlates with  $\delta^{18}O_p$  and  $\delta^2H_p$ .  $RH_{\text{rec}}$  shows a significant correlation with  $RH_{RA}$ , and enables to reconstruct RH with an offset of  $\Delta RH = 6 \pm 17\%$  excluding study areas with CAM plant predominance. However, there are distinct uncertainties regarding possible insufficient spatial resolution of the comparative data ( $RH_{RA}$ ).
- Due to the predominance of plants using CAM metabolism in the N-YRZ, reconstructed source water and  $RH_{\text{rec}}$  show a distinct offset ( $\Delta\delta^{18}O = 3.1\%$ ;  $\Delta\delta^2H = 27.2\%$ ;  $\Delta RH = 31.7\%$ ) compared to  $\delta^{18}O_p$ ,  $\delta^2H_p$  and  $RH_{RA}$ . This highlights that compared to  $\delta^2H_{n\text{-alkanes}}$  plant-specific (phenological) adaptations and/or post-photosynthetic exchange reactions related to reduced  $\delta^{18}O_{\text{sugar}}$  enrichment lead to an overestimation of reconstructed source water and  $RH_{\text{rec}}$  in CAM-dominated (semi-)arid region of South Africa.
- Future work focussing on disentangling the three processes i) soil water evaporation, ii) leaf and xylem water transpiration and iii)  $\epsilon_{\text{bio}}$  under both (semi-)arid and humid conditions as well as metabolism-related post-photosynthetic exchange reactions is needed to reduce the uncertainties of the applied approach.
- Although uncertainties exist, the present study corroborates that  $\delta^{18}O_{\text{sugar}}$ ,  $\delta^2H_{n\text{-alkanes}}$ , reconstructed source water and  $RH_{\text{rec}}$  are valuable proxies to better understand past and recent spatiotemporal variation in precipitation and relative humidity in South Africa.

#### Declaration of competing interest

PS, TH, MB, JS, BG, MZ and RZ declare that they have no conflict of interest.

#### Acknowledgements

This study was funded by the German Research Foundation (DFG) (grant no.: HA 5089/11-1; ZE 860/6-1) and the German Federal Ministry of Education and Research (BMBF) (grant no.: 03G0862B; 03F0798C). The investigations were conducted within the collaborative project "Regional Archives for Integrated Investigations" (RAiN), which is embedded in the international research programme SPACES (Science Partnership for the Assessment of Complex Earth System Processes). We further want to acknowledge the BMBF project TRACES (Tracing Human and Climate impacts in South Africa). PS gratefully acknowledges the support by a fellowship from the state of Thuringia (Landesgraduiertenstipendium). Particularly acknowledged are M. Wagner and P. Rauh for supporting sample preparation. Special thanks go to M. Benesch, L. Bittner, N. Blaibach, T. Bromm, C. Heinrich, M. Lerch, H. Maennicke, I. Pätz, N. Ueberschaar and J. Wintel for assistance in the lab. We also want to thank K.L. Delaney, L.J. Quick and M.E. Meadows for their useful information and supporting the planning of the field trip.

#### References

- Alduchov, O.A., Eskridge, R.E., 1996. Improved magnus form approximation of saturation vapor pressure. *J. Appl. Meteorol.* 35, 601–609.
- Ameling, W., Cheshire, M.V., Guggenberger, G., 1996. Determination of neutral and acidic sugars in soil by capillary gas-liquid chromatography after trifluoroacetic acid hydrolysis. *Soil Biol. Biochem.* 28, 1631–1639.
- Araguás-Araguás, L., Froehlich, K., Rozanski, K., 2000. Deuterium and oxygen-18 isotope composition of precipitation and atmospheric moisture. *Hydrol. Process.* 14, 1341–1355.
- Barbour, M.M., 2007. Stable oxygen isotope composition of plant tissue: a review. *Funct. Plant Biol.* 34, 83–94.
- Bliedtner, M., Schäfer, I.K., Zech, R., von Suchodoletz, H., 2018. Leaf wax n-alkanes in modern plants and topsoils from eastern Georgia (Caucasus) – implications for reconstructing regional paleovegetation. *Biogeosciences* 15, 3927–3936.
- Bowen, G.J., Revenaugh, J., 2003. Interpolating the isotopic composition of modern meteoric precipitation. *Water Resour. Res.* 39, 1–10.
- Bowen, G.J., Wilkinson, B., 2002. Spatial distribution of  $\delta^{18}O$  in meteoric precipitation. *Geology* 30, 315–318.
- Bowen, G.J., Wassenaar, L.L., Hobson, K.A., 2005. Global application of stable hydrogen and oxygen isotopes to wildlife forensics. *Oecologia* 143, 337–348.
- Braun, K., Bar-Matthews, M., Ayalon, A., Zilberman, T., Matthews, A., 2017. Rainfall isotopic variability at the intersection between winter and summer rainfall regimes in coastal South Africa (Mossel Bay, Western Cape Province). *S. Afr. J. Geol.* 120, 323–340.
- Carr, A.S., Boom, A., Grimes, H.L., Chase, B.M., Meadows, M.E., Harris, A., 2014. Leaf wax n-alkane distributions in arid zone South African flora: environmental controls, chemotaxonomy and palaeoecological implications. *Org. Geochem.* 67, 72–84.
- Cernusak, L.A., Wong, S.C., Farquhar, G.D., 2003. Oxygen isotope composition of phloem sap in relation to leaf water in *Ricinus communis*. *Funct. Plant Biol.* 30, 1059–1070.
- Cernusak, L.A., Barbour, M.M., Arndt, S.K., Cheesman, A.W., English, N.B., Feild, T.S., Helliker, B.R., Holloway-Phillips, M.M., Holtum, J.A.M., Kahmen, A., Mcnerney, F.A., Munksgaard, N.C., Simonin, K.A., Song, X., Stuart-Williams, H., West, J.B., Farquhar, G.D., 2016. Stable isotopes in leaf water of terrestrial plants. *Plant Cell Environ.* 39, 1087–1102.
- Chase, B.M., Meadows, M.E., 2007. Late Quaternary dynamics of southern Africa's winter rainfall zone. *Earth Sci. Rev.* 84, 103–138.
- Cormier, M.-A., Werner, R.A., Sauer, P.E., Grücke, D.R., Leuenberger, M.C., Wieloch, T., Schleucher, J., Kahmen, A., 2018. 2H-fractionations during the biosynthesis of carbohydrates and lipids imprint a metabolic signal on the  $\delta^2H$  values of plant organic compounds. *New Phytol.* 218, 479–491.
- Dansgaard, W., 1964. Stable isotopes in precipitation. *Tellus* 16, 436–468.
- Dee, D.P., Uppala, S.M., Simmons, A.J., Berrisford, P., Poli, P., Kobayashi, S., Andrae, U., Balmasda, M.A., Balsamo, G., Bauer, P., Bechtold, P., Beljaars, A.C.M., van de Berg, L., Bidlot, J., Bormann, N., Delsol, C., Dragani, R., Fuentes, M., Geer, A.J., Haimberger, L., Healy, S.B., Hersbach, H., Hölm, E.V., Isaksen, I., Källberg, P., Köhler, M., Matricardi, M., McNally, A.P., Monge-Sanz, B.M., Morcrette, J.-J., Park, B.-K., Peubey, C., de Rosnay, P., Tavolato, C., Thépaut, J.-N., Vitart, F., 2011. The ERA-interim reanalysis: configuration and performance of the data assimilation system. *Q. J. Meteorol. Soc.* 137, 553–597.
- Eley, Y., Dawson, L., Black, S., Andrews, J., Pedentchouk, N., 2014. Understanding 2H/1H systematics of leaf wax n-alkanes in coastal plants at Stiffkey saltmarsh, Norfolk, UK. *Geochim. Cosmochim. Acta* 128, 13–28.
- Engelbrecht, C.J., Landman, W.A., 2016. Interannual variability of seasonal rainfall over the Cape south coast of South Africa and synoptic type association. *Clim. Dyn.* 47, 295–313.
- Engelbrecht, C.J., Landman, W.A., Engelbrecht, F.A., Malherbe, J., 2015. A synoptic decomposition of rainfall over the Cape south coast of South Africa. *Clim. Dyn.* 44, 2589–2607.
- Feakins, S.J., Sessions, A.L., 2010a. Controls on the D/H ratios of plant leaf waxes in an arid ecosystem. *Geochim. Cosmochim. Acta* 74, 2128–2141.
- Feakins, S.J., Sessions, A.L., 2010b. Crassulacean acid metabolism influences D/H ratio of leaf wax in succulent plants. *Org. Geochem.* 41, 1269–1276.
- Fick, S.E., Hijmans, R.J., 2017. WorldClim 2: new 1-km spatial resolution climate surfaces for global land areas. *Int. J. Climatol.* 37, 4302–4315.
- Flanagan, L.B., Ehleringer, J.R., 1991. Stable isotope composition of stem and leaf water: applications to the study of plant water use. *Funct. Ecol.* 5, 270–277.
- Gamarra, B., Sachse, D., Kahmen, A., 2016. Effects of leaf water evaporative 2H-enrichment and biosynthetic fractionation on leaf wax n-alkane  $\delta^2H$  values in C3 and C4 grasses. *Plant Cell Environ.* 39, 2390–2403.
- Gao, L., Guimond, J., Thomas, E., Huang, Y., 2015. Major trends in leaf wax abundance,  $\delta^2H$  and  $\delta^{13}C$  values along leaf venation in five species of C3 plants: physiological and geochemical implications. *Org. Geochem.* 78, 144–152.
- Gat, J.R., 1996. Oxygen and hydrogen isotopes in the hydrologic cycle. *Annu. Rev. Earth Planet. Sci.* 24, 225–262.
- Gessler, A., Brandes, E., Buchmann, N., Helle, G., Rennenberg, H., Barnard, R.L., 2009. Tracing carbon and oxygen isotope signals from newly assimilated sugars in the leaves to the tree-ring archive. *Plant Cell Environ.* 32, 780–795.
- Griepentrog, M., De Wispelaere, L., Bauters, M., Bodé, S., Hemp, A., Verschuren, D., Boeckx, P., 2019. Influence of plant growth form, habitat and season on leaf-wax n-alkane hydrogen-isotopic signatures in equatorial East Africa. *Geochim. Cosmochim. Acta* 263, 122–139.
- Haberzettl, T., Baade, J., Compton, J., Daut, G., Dupont, L., Finch, J., Frenzel, P., Green, A., Hahn, A., Hebbeln, D., Helmschrot, J., Humphries, M., Kasper, T., Kirsten, K., Mäusbacher, R., Meadows, M., Meschner, S., Quick, L., Schefuß, E., Wüdsch, M., Zabel, M., 2014. Paleoenvironmental investigations using a combination of terrestrial and marine



- sediments from South Africa - the RAIN (Regional Archives for Integrated Investigations) approach. *Zentralblatt für Geologie und Paläontologie, Teil I* 2014, 55–73.
- Hahn, A., Compton, J.S., Meyer-Jacob, C., Kirsten, K.L., Lucassens, F., Pérez Mayo, M., Schefuß, E., Zabel, M., 2016. Holocene paleo-climatic record from the South African Namaqualand mudbelt: a source to sink approach. *Quat. Int.* 404 (Part B), 121–135.
- Hahn, A., Schefuß, E., Andò, S., Cawthra, H.C., Frenzel, P., Kugel, M., Meschner, S., Mollenhauer, G., Zabel, M., 2017. Southern Hemisphere anticyclonic circulation drives oceanic and climatic conditions in late Holocene southernmost Africa. *Clim. Past* 13, 649–665.
- Hahn, A., Miller, C., Andò, S., Bouimetarhan, I., Cawthra, H.C., Garzanti, E., Green, A.N., Radeff, G., Schefuß, E., Zabel, M., 2018. The provenance of terrigenous components in marine sediments along the east coast of southern Africa. *Geochem. Geophys. Geosyst.* 9, 1946–1962.
- Harris, C., Burgers, C., Miller, J., Rawoot, F., 2010. O- and H-isotope record of Cape Town rainfall from 1996 to 2008, and its application to recharge studies of Table Mountain groundwater. *South Africa. S. Afr. J. Geol.* 113, 33–56.
- Helliker, B.R., Griffiths, H., 2007. Toward a plant-based proxy for the isotope ratio of atmospheric water vapor. *Glob. Chang. Biol.* 13, 723–733.
- Hepp, J., Tuthorn, M., Zech, R., Mügler, I., Schlütz, F., Zech, W., Zech, M., 2015. Reconstructing lake evaporation history and the isotopic composition of precipitation by a coupled  $\delta^{18}\text{O}$ - $\delta^2\text{H}$  biomarker approach. *J. Hydrol.* 529, 622–631.
- Hepp, J., Zech, R., Rozanski, K., Tuthorn, M., Glaser, B., Greule, M., Keppler, F., Huang, Y., Zech, W., Zech, M., 2017. Late Quaternary relative humidity changes from Mt. Kilimanjaro, based on a coupled 2H-18O biomarker paleohygrometer approach. *Quat. Int.* 438 (Part B), 116–130.
- Hepp, J., Glaser, B., Juchelka, D., Mayr, C., Rozanski, K., Schäfer, I.K., Stiehler, W., Tuthorn, M., Zech, R., Zech, M., 2019a. Validation of a coupled  $\delta^2\text{H}$ -alkane- $\delta^{18}\text{O}$  sugar paleohygrometer approach based on a climate chamber experiment. *Biogeosci. Discuss.* 2019, 1–30.
- Hepp, J., Wüthrich, L., Bromm, T., Bliedtner, M., Schäfer, I.K., Glaser, B., Rozanski, K., Sirocco, F., Zech, R., Zech, M., 2019b. How dry was the younger dryas? Evidence from a coupled  $\delta^2\text{H}$ - $\delta^{18}\text{O}$  biomarker paleohygrometer applied to the Gemündener Maar sediments, Western Eifel, Germany. *Clim. Past* 15, 713–733.
- Herrmann, N., Boom, A., Carr, A.S., Chase, B.M., West, A.G., Zabel, M., Schefuß, E., 2017. Hydrogen isotope fractionation of leaf wax n-alkanes in southern African soils. *Org. Geochem.* 109, 1–13.
- Heyng, A.M., Mayr, C., Lücke, A., Wissel, H., Striewski, B., 2014. Late Holocene hydrologic changes in northern New Zealand inferred from stable isotope values of aquatic cellulose in sediments from Lake Pupuke. *J. Paleolimnol.* 51, 485–497.
- Holdsworth, G., Fogarasi, S., Krouse, H.R., 1991. Variation of the stable isotopes of water with altitude in the Saint Elias mountains of Canada. *J. Geophys. Res.-Atmos.* 96, 7483–7494.
- Horita, J., Wesolowski, D.J., 1994. Liquid-vapor fractionation of oxygen and hydrogen isotopes of water from the freezing to the critical temperature. *Geochim. Cosmochim. Acta* 58, 3425–3437.
- Hou, J., D'Andrea, W.J., MacDonald, D., Huang, Y., 2007. Evidence for water use efficiency as an important factor in determining the  $\delta\text{D}$  values of tree leaf waxes. *Org. Geochem.* 38, 1251–1255.
- Hou, J., Tian, Q., Wang, M., 2018. Variable apparent hydrogen isotopic fractionation between sedimentary n-alkanes and precipitation on the Tibetan Plateau. *Org. Geochem.* 122, 78–86.
- Houze, R.A.J., 2012. Orographic effects on precipitating clouds. *Rev. Geophys.* 50.
- Kahmen, A., Hoffmann, B., Schefuß, E., Arndt, S.K., Cernusak, L.A., West, J.B., Sachse, D., 2013a. Leaf water deuterium enrichment shapes leaf wax n-alkane  $\delta\text{D}$  values of angiosperm plants II: observational evidence and global implications. *Geochim. Cosmochim. Acta* 111, 50–63.
- Kahmen, A., Schefuß, E., Sachse, D., 2013b. Leaf water deuterium enrichment shapes leaf wax n-alkane  $\delta\text{D}$  values of angiosperm plants I: experimental evidence and mechanistic insights. *Geochim. Cosmochim. Acta* 111, 39–49.
- Kalnay, E., Kanamitsu, M., Kistler, R., Collins, W., Deaven, D., Gandin, L., Iredell, M., Saha, S., White, G., Woollen, J., Zhu, Y., Chelliah, M., Ebisuzaki, W., Higgins, W., Janowiak, J., Mo, K.C., Ropelewski, C., Wang, J., Leetmaa, A., Reynolds, R., Jenne, R., Joseph, D., 1996. The NCEP/NCAR 40-year reanalysis project. *Bull. Am. Meteorol. Soc.* 77, 437–472.
- Knight, J., Rogerson, C.M., 2019. *The Geography of South Africa*, World Regional Geography Book Series, p. 326.
- Li, Y., Yang, S., Luo, P., Xiong, S., 2019. Aridity-controlled hydrogen isotope fractionation between soil n-alkanes and precipitation in China. *Org. Geochem.* 133, 53–64.
- Liu, J., An, Z., 2019. Variations in hydrogen isotopic fractionation in higher plants and sediments across different latitudes: implications for paleohydrological reconstruction. *Sci. Total Environ.* 650, 470–478.
- Liu, W., Yang, H., 2008. Multiple controls for the variability of hydrogen isotopic compositions in higher plant n-alkanes from modern ecosystems. *Glob. Chang. Biol.* 14, 2166–2177.
- Matimati, I., Musil, C.F., Raitt, L., February, E., 2013. Non rainfall moisture interception by dwarf succulents and their relative abundance in an inland arid South African ecosystem. *Ecology* 6, 818–825.
- Merlivat, L., 1978. Molecular diffusivities of H<sub>2</sub>16O, HD16O, and H<sub>2</sub> 18O in gases. *J. Chem. Phys.* 69, 2864–2871.
- Miller, C., Finch, J., Hill, T., Peterse, F., Humphries, M., Zabel, M., Schefuß, E., 2019. Late Quaternary climate variability at Mfabeni peatland, eastern South Africa. *Clim. Past* 15, 1153–1170.
- Mucina, L., Rutherford, M.C., 2006. *The Vegetation of South Africa, Lesotho and Swaziland*. SANBI, Pretoria.
- Newberry, S.L., Kahmen, A., Dennis, P., Grant, A., 2015. n-Alkane biosynthetic hydrogen isotope fractionation is not constant throughout the growing season in the riparian tree *Salix viminalis*. *Geochim. Cosmochim. Acta* 165, 75–85.
- Polissar, P.J., Freeman, K.H., 2010. Effects of aridity and vegetation on plant-wax  $\delta\text{D}$  in modern lake sediments. *Geochim. Cosmochim. Acta* 74, 5785–5797.
- Quick, L.J., Chase, B.M., Wüdsch, M., Kirsten, K., Chevalier, M., Mäusbacher, R., Meadows, M., Haberzettl, T., 2018. A high-resolution record of Holocene climate and vegetation dynamics from the southern Cape coast of South Africa: pollen and microcharcoal evidence from Eilandvlei. *J. Quat. Sci.* 1–14.
- Sachse, D., Billault, I., Bowen, G.J., Chikaraishi, Y., Dawson, T.E., Feakins, S.J., Freeman, K.H., Magill, C.R., McInerney, F.A., van der Meer, M.T.J., Polissar, P., Robins, R.J., Sachs, J.P., Schmidt, H.L., Sessions, A.L., White, J.W.C., West, J.B., Kahmen, A., 2012. Molecular paleohydrology: interpreting the hydrogen-isotopic composition of lipid biomarkers from photosynthesizing organisms. *Annu. Rev. Earth Planet. Sci.* 40, 221–249.
- Sauer, P.E., Eglinton, T.L., Hayes, J.M., Schimmelmann, A., Sessions, A.L., 2001. Compound-specific D/H ratios of lipid biomarkers from sediments as a proxy for environmental and climatic conditions. *Geochim. Cosmochim. Acta* 65, 213–222.
- Schäfer, I.K., Bliedtner, M., Wolf, D., Kolb, T., Zech, J., Faust, D., Zech, R., 2018. A  $\delta^{13}\text{C}$  and  $\delta^2\text{H}$  leaf wax record from the Late Quaternary loess-paleosol sequence El Paraíso, Central Spain. *Palaeogeogr. Palaeoclimatol. Palaeoecol.* 507, 52–59.
- Schefuß, E., Schouten, S., Schneider, R.R., 2005. Climatic controls on central African hydrology during the past 20,000 years. *Nature* 437, 1003–1006.
- Schmidt, H.-L., Werner, R.A., Rofmann, A., 2001. 18O pattern and biosynthesis of natural plant products. *Phytochemistry* 58, 9–32.
- Schulze, R.E., 1997. *Climate*. In: Cowling, R.M., Richardson, D.M., Pierce, S.M. (Eds.), *Vegetation of Southern Africa*. Cambridge University Press, pp. 21–41.
- Scott, L., Lee-Thorp, J.A., 2004. Holocene climatic trends and rhythms in southern Africa. In: Battarbee, R.W., Gasse, F., Stickley, C.E. (Eds.), *Past Climate Variability Through Europe and Africa*. Springer, Dordrecht, pp. 69–91.
- Sessions, A.L., Burgoyne, T.W., Schimmelmann, A., Hayes, J.M., 1999. Fractionation of hydrogen isotopes in lipid biosynthesis. *Org. Geochem.* 30, 1193–1200.
- Shi, F., Rao, Z., Cao, J., Huang, C., Wu, D., Yang, W., Sun, W., 2019a. Meltwater is the dominant water source controlling  $\alpha$ -cellulose  $\delta^{18}\text{O}$  in a vascular-plant-dominated alpine peatland in the Altai Mountains, Central Asia. *J. Hydrol.* 572, 192–205.
- Shi, F., Rao, Z., Li, Y., Cao, J., Shi, X., Li, C., Sun, W., 2019b. Precipitation  $\delta^{18}\text{O}$  recorded by the  $\alpha$ -cellulose  $\delta^{18}\text{O}$  of plant residues in surface soils: evidence from a broad environmental gradient in inland China. *Glob. Biogeochem. Cycles* 33, 1440–1468.
- Siegenthaler, U., Oeschger, H., 1980. Correlation of 18O in precipitation with temperature and altitude. *Nature* 285, 314–317.
- Smith, F.A., Freeman, K.H., 2006. Influence of physiology and climate on  $\delta\text{D}$  of leaf wax n-alkanes from C3 and C4 grasses. *Geochim. Cosmochim. Acta* 70, 1172–1187.
- Sternberg, L., 2009. Oxygen stable isotope ratios of tree-ring cellulose: the next phase of understanding. *New Phytol.* 181, 553–562.
- Sternberg, L., DeNiro, M.J., 1983. Isotopic composition of cellulose from C3, C4 and CAM plants growing near one another. *Science* 220, 947–949.
- Sternberg, L., Deniro, M.J., Savidge, R.A., 1986. Oxygen isotope exchange between metabolites and water during biochemical reactions leading to cellulose synthesis. *Plant Physiol.* 82, 423–427.
- Sternberg, L., Pinzon, M.C., Anderson, W.T., Jahren, A.H., 2006. Variation in oxygen isotope fractionation during cellulose synthesis: intramolecular and biosynthetic effects. *Plant Cell Environ.* 29, 1881–1889.
- Strobel, P., Kasper, T., Frenzel, P., Schittek, K., Quick, L.J., Meadows, M.E., Mäusbacher, R., Haberzettl, T., 2019. Late Quaternary palaeoenvironmental change in the year-round rainfall zone of South Africa derived from peat sediments from Vankersveldvlei. *Quat. Sci. Res.* 218, 200–214.
- Trabucco, A., Zomer, R., 2019. Global Aridity Index and Potential Evapotranspiration (ETO) Climate Database v2. Figshare. Fileset.
- Tuthorn, M., Zech, M., Ruppenthal, M., Oelmann, Y., Kahmen, A., Valle, H.F., Wilcke, W., Glaser, B., 2014. Oxygen isotope ratios (18O/16O) of hemicellulose-derived sugar biomarkers in plants, soils and sediments as paleoclimate proxy II: insight from a climate transect study. *Geochim. Cosmochim. Acta* 126, 624–634.
- Tuthorn, M., Zech, R., Ruppenthal, M., Oelmann, Y., Kahmen, A., del Valle, H.F., Eglinton, T., Rozanski, K., Zech, M., 2015. Coupling delta H-2 and delta O-18 biomarker results yields information on relative humidity and isotopic composition of precipitation - a climate transect validation study. *Biogeosciences* 12, 3913–3924.
- Tyson, P.D., Preston-Whyte, R.A., 2000. *The Weather and Climate of Southern Africa*. Oxford University Press, Cape Town.
- Voelker, S.L., Brooks, J.R., Meinzer, F.C., Roden, J., Pazdur, A., Pawelczyk, S., Hartsough, P., Snyder, K., Plavcová, L., Šantrůček, J., 2014. Reconstructing relative humidity from plant  $\delta^{18}\text{O}$  and  $\delta\text{D}$  as deuterium deviations from the global meteoric water line. *Ecol. Appl.* 24, 960–975.
- Voelker, S.L., Stambaugh, M.C., Guyette, R.P., Feng, X., Grimm, D.A., Leavitt, S.W., Panyushkina, I., Grimm, E.C., Marsicek, J.P., Shuman, B., Brandon Curry, B., 2015. Deglacial hydroclimate of midcontinental North America. *Quat. Res.* 83, 336–344.
- Vogel, J.C., Fuls, A., Ellis, R.P., 1978. The geographical distribution of kranz grasses in South Africa. *S. Afr. J. Sci.* 74, 209–215.
- Wessels, K., Steenkamp, K., von Maltitz, G., Archibald, S., 2011. Remotely sensed vegetation phenology for describing and predicting the biomes of South Africa. *Appl. Veg. Sci.* 14, 49–66.
- Wissel, H., Mayr, C., Lücke, A., 2008. A new approach for the isolation of cellulose from aquatic plant tissue and freshwater sediments for stable isotope analysis. *Org. Geochem.* 39, 1545–1561.
- Wüdsch, M., Haberzettl, T., Kirsten, K.L., Kasper, T., Zabel, M., Dietze, E., Baade, J., Daut, G., Meschner, S., Meadows, M.E., Mäusbacher, R., 2016. Sea level and climate change at the southern Cape coast, South Africa, during the past 4.2 kyr. *Palaeogeogr. Palaeoclimatol. Palaeoecol.* 446, 295–307.
- Wüdsch, M., Haberzettl, T., Cawthra, H.C., Kirsten, K.L., Quick, L.J., Zabel, M., Frenzel, P., Hahn, A., Baade, J., Daut, G., Kasper, T., Meadows, M.E., Mäusbacher, R., 2018. Holocene environmental change along the southern Cape coast of South Africa - insights

- from the Eilandvlei sediment record spanning the last 8.9 kyr. *Glob. Planet. Chang.* 163, 51–66.
- Yakir, D., DeNiro, M.J., 1990. Oxygen and hydrogen isotope fractionation during cellulose metabolism in *Lemna gibba* L. *Plant Physiol.* 93, 325–332.
- Zech, M., Glaser, B., 2009. Compound-specific  $\delta^{18}\text{O}$  analyses of neutral sugars in soils using gas chromatography–pyrolysis–isotope ratio mass spectrometry: problems, possible solutions and a first application. *Rapid Commun. Mass Spectrom.* 23, 3522–3532.
- Zech, M., Werner, R.A., Juchelka, D., Kalbitz, K., Buggle, B., Glaser, B., 2012. Absence of oxygen isotope fractionation/exchange of (hemi-) cellulose derived sugars during litter decomposition. *Org. Geochem.* 42, 1470–1475.
- Zech, M., Tuthorn, M., Detsch, F., Rozanski, K., Zech, R., Zöller, L., Zech, W., Glaser, B., 2013. A 220ka terrestrial  $\delta^{18}\text{O}$  and deuterium excess biomarker record from an eolian permafrost paleosol sequence, NE-Siberia. *Chem. Geol.* 360–361, 220–230.
- Zech, M., Mayr, C., Tuthorn, M., Leiber-Sauheitl, K., Glaser, B., 2014. Oxygen isotope ratios ( $^{18}\text{O}/^{16}\text{O}$ ) of hemicellulose-derived sugar biomarkers in plants, soils and sediments as paleoclimate proxy I: insight from a climate chamber experiment. *Geochim. Cosmochim. Acta* 126, 614–623.
- Zongxing, L., Qi, F., Song, Y., Wang, Q.J., Yang, J., Yongge, L., Jianguo, L., Xiaoyan, G., 2016. Stable isotope composition of precipitation in the south and north slopes of Wushaoling Mountain, northwestern China. *Atmos. Res.* 182, 87–101.

## Chapter 3

---

### **Holocene sea level and environmental change at the southern Cape – an 8.5 kyr multi-proxy paleoclimate record from lake Voëlvlei, South Africa.**

---

Authors: Paul Strobel, Marcel Bliedtner, Andrew S. Carr,  
Peter Frenzel, Björn Klaes, Gary Salazar, Julian Struck,  
Sönke Szidat, Roland Zech, Torsten Haberzettl

Published in:  
Climate of the Past 17 (2021), 1567-1586  
<https://doi.org/10.5194/cp-17-1567-2021>

Clim. Past, 17, 1567–1586, 2021  
<https://doi.org/10.5194/cp-17-1567-2021>  
 © Author(s) 2021. This work is distributed under  
 the Creative Commons Attribution 4.0 License.



Climate  
of the Past

Open Access

## Holocene sea level and environmental change at the southern Cape – an 8.5 kyr multi-proxy paleoclimate record from Lake Voëlvlei, South Africa

Paul Strobel<sup>1</sup>, Marcel Bliedtner<sup>1</sup>, Andrew S. Carr<sup>2</sup>, Peter Frenzel<sup>3</sup>, Björn Klaes<sup>4</sup>, Gary Salazar<sup>5</sup>, Julian Struck<sup>1</sup>, Sönke Szidat<sup>5</sup>, Roland Zech<sup>1</sup>, and Torsten Haberzettl<sup>6</sup>

<sup>1</sup>Physical Geography, Institute of Geography, Friedrich Schiller University Jena, Jena, Germany

<sup>2</sup>School of Geography, Geology and the Environment, University of Leicester, Leicester, UK

<sup>3</sup>Institute of Geosciences, Friedrich Schiller University Jena, Jena, Germany

<sup>4</sup>Department of Geology, Trier University, Trier, Germany

<sup>5</sup>Department of Chemistry, Biochemistry and Pharmaceutical Sciences and Oeschger Centre for Climate Change Research, University of Bern, Bern, Switzerland

<sup>6</sup>Physical Geography, Institute for Geography and Geology, University of Greifswald, Greifswald, Germany

**Correspondence:** Paul Strobel ([paul.strobel@uni-jena.de](mailto:paul.strobel@uni-jena.de))

Received: 28 September 2020 – Discussion started: 26 October 2020

Revised: 26 May 2021 – Accepted: 13 June 2021 – Published: 28 July 2021

**Abstract.** South Africa is a key region to reconstruct and understand past changes in atmospheric circulation, i.e. temperate westerlies and tropical easterlies. However, due to the scarcity of natural archives, South Africa’s environmental evolution during the late Quaternary remains highly debated. Many available sediment archives are peri-coastal lakes and wetlands; however, the paleoenvironmental signals in these archives are often overprinted by sea-level changes during the Holocene. This study presents a new record from the coastal wetland Voëlvlei, which is situated in the year-round rainfall zone of South Africa on the southern Cape coast. It presents an ideal sedimentary archive to investigate both sea level and environmental changes. A 13 m long sediment core was retrieved and analysed using a multi-proxy approach. The chronology reveals a basal age of 8440<sup>+200</sup>/<sub>–250</sub> cal BP. Paleoecological and elemental analyses indicate marine incursions from ca. 8440 to ca. 7000 cal BP with a salinity optimum occurring at 7090<sup>+170</sup>/<sub>–200</sub> cal BP. At ca. 6000 cal BP, the basin of Voëlvlei was in-filled with sediment resulting in an intermittent (sporadically desiccated) freshwater lake similar to present.

In contrast to previous investigations which used indirect proxies for hydrological reconstructions, here we apply a combined biomarker–sedimentological approach that allows the potential identification of precipitation sources, in com-

bination with relative estimates of moisture availability. Increasing moisture is observed throughout the record starting from 8440<sup>+200</sup>/<sub>–250</sub> cal BP with contributions from both westerlies and easterlies from ca. 8440 to ca. 7070 cal BP. Westerly-derived rainfall dominates from ca. 7070 to ca. 6420 cal BP followed by a distinct shift to an easterly dominance at ca. 6420 cal BP. An overall trend to westerly dominance lasting until ca. 2060 cal BP is followed by a trend towards an easterly dominance to the present, but both phases show several intense, short-term variations. These variations are also evident in other regional studies, highlighting that the source and seasonality of precipitation has varied distinctly on the southern Cape during the Holocene. Comparison of the Voëlvlei record with other regional studies suggests a coherent trend in the overall moisture evolution along the southern Cape coast during the past 8500 years.

### 1 Introduction

A record-breaking drought occurred in South Africa from 2015 to 2017, and future climate projections predict increasing drought for large parts of the country (Engelbrecht and Engelbrecht, 2016; Engelbrecht et al., 2011). To make climate models and predictions of future hydrological change

more reliable, robust paleoclimate reconstructions using direct hydrological proxies are necessary but have been rare in South Africa up to now (Haberzettl et al., 2014). Southern Africa's past and present climate has been driven by complex interactions between two major oceanic and atmospheric circulation systems, i.e. the Benguela and Agulhas currents, and the westerlies and easterlies (Tyson and Preston-Whyte, 2000) (Fig. 1a). Today, three major rainfall zones occur in South Africa. While the eastern and central parts of the country receive most rainfall (> 66%) from tropical moisture-bearing atmospheric circulation systems during austral summer (summer rainfall zone, SRZ), a narrow belt along the west coast receives most rainfall (> 66%) from temperate westerlies during the austral winter (winter rainfall zone, WRZ) (Fig. 1a). An intermediary area between the SRZ and WRZ receives rainfall from both systems throughout the year (year-round rainfall zone, YRZ) (Fig. 1a) (Engelbrecht et al., 2015; Scott and Lee-Thorp, 2004), and this includes the southern Cape coast, which is the focus area for this study.

The YRZ has been the focus of most paleoenvironmental and associated paleoclimatic research in this region. Here, the southern Cape coast, in particular the Wilderness area with its numerous coastal lakes including Bo Langvlei (du Plessis et al., 2020), Eilandvlei (Kirsten et al., 2018a, b; Quick et al., 2018; Reinwarth et al., 2013; Wündsche et al., 2018, 2016b), Groenvlei (Martin, 1959, 1968; Wündsche et al., 2016a) and Swartvlei (Birch et al., 1978; Haberzettl et al., 2019), has yielded multiple paleoenvironmental records (Fig. 1b). These coastal lakes have formed between large coastal dune cordons that lie parallel to the coast. However, the terrestrial climate signals in these coastal archives are often overprinted by marine water intrusions induced by relative sea level change during the Holocene (Martin, 1959, 1968; Reinwarth et al., 2013; Wündsche et al., 2018, 2016a) or anthropogenic impacts, e.g. farming, water abstraction and dredging operations (Haberzettl et al., 2019). Further paleoenvironmental information from this area is available from, for example, peatlands (Quick et al., 2016; Strobel et al., 2019), speleothems (Braun et al., 2018, 2020; Talma and Vogel, 1992), rock hyrax middens (Chase et al., 2019, 2020, 2017, 2018, 2015) and marine sediments (Hahn et al., 2017) (Fig. 1a). However, the climate evolution of South Africa is still debated, reflecting potential spatial variability in climate drivers at the regional scale, and the application of different methodological approaches in various studies (Chase and Quick, 2018; Strobel et al., 2019). Consequently, our understanding of environmental dynamics and changing interactions between tropical and temperate climate systems affecting the YRZ is limited.

Compound-specific stable isotope analyses of hydrogen and carbon isotopes of long-chain  $n$ -alkanes ( $\geq C_{25}$ ;  $\delta^2H_{n\text{-alkane}}$ ,  $\delta^{13}C_{n\text{-alkane}}$ ) are valuable proxies that complement established methodological approaches related to paleoenvironmental and paleohydrological changes in sediment

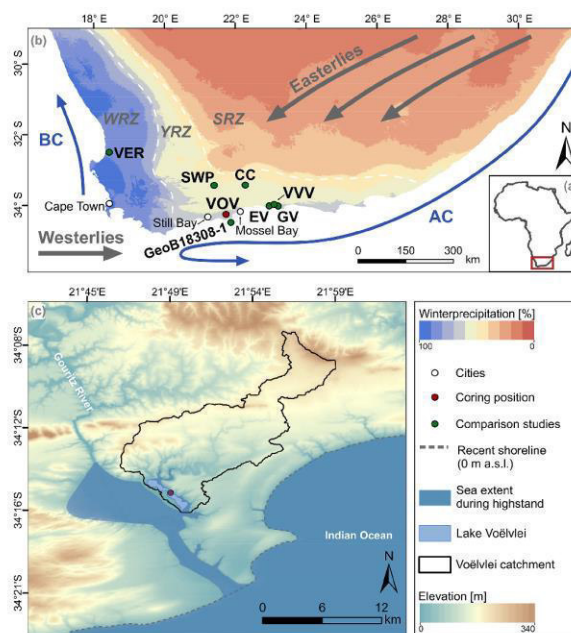


**Figure 1.** (a) Simplified map of Africa. The red box highlights the studied area. (b) Location of Lake Voëlvlei (VOV) and studies mentioned in the text (Cango Cave: CC, Talma and Vogel, 1992; Eilandvlei: EV, Quick et al., 2018; Wündsche et al., 2018; Groenvlei: GV, Wündsche et al., 2016a; Seweweekspoort: SWP, Chase et al., 2017; Verlorenvlei: VER, Kirsten et al., 2020; and Vankervelsvlei: VVV, Strobel et al., 2019). Additionally, the circumpolar westerlies, the tropical easterlies, the Agulhas Current (AC) and the Benguela Current (BC) are depicted. (c) Voëlvlei, its catchment, the coring position as well as a paleo-sea level highstand (+5 m) and the recent shoreline (data sources – rainfall seasonality: WorldClim 2 dataset, Fick and Hijmans, 2017; circulation systems after Chase and Meadows, 2007; DEM: SRTM 1 arcsec; ~ 30 m, Jarvis et al., 2008).

archives, e.g. grain size analyses, geochemistry and palynology. Long-chain  $n$ -alkanes are leaf waxes produced by higher terrestrial plants and serve as valuable biomarkers as they remain well preserved in soils and sediments over millennia because of their low water solubility and high resistance to degradation (Eglinton and Eglinton, 2008; Sachse et al., 2012; Sessions, 2016). In South Africa, the  $\delta^2H_{n\text{-alkane}}$  signal shows potential to reconstruct the isotopic signal of precipitation and thus directly refers to the precipitation source (Herrmann et al., 2017; Strobel et al., 2020). However,  $\delta^2H_{n\text{-alkane}}$  has rarely been used in terrestrial archives at the southern Cape coast (Strobel et al., 2019).

$\delta^{13}C_{n\text{-alkane}}$  is a suitable proxy to infer past changes in the vegetation composition (e.g. Diefendorf and Freimuth, 2017) as well as variations in plant water use efficiency and thus drought stress (Diefendorf and Freimuth, 2017; Struck et al., 2020). Therefore, using the climatic information from both leaf wax isotopes enables climate reconstructions based

on the isotopic signal of precipitation, which can reflect local water availability. Further, leaf wax-derived *n*-alkanes can be used as a chronological marker since they can be dated using  $^{14}\text{C}$  analyses (Bliedtner et al., 2020, 2018; Douglas et al., 2014; Gierga et al., 2016; Haas et al., 2017).

Here we present a sediment record from Voëlvlei, today an intermittent lake (sporadically desiccated), to reconstruct past sea level and environmental changes at the southern Cape coast of South Africa. A multi-proxy approach has been applied to the sediments, comprising compound-specific stable isotope analyses of leaf waxes as well as sedimentological assays of inorganic and organic elemental compositions, and paleoecological analyses on fossil remains. Specifically we aim to

- i. establish a robust chronology based on diverse dating approaches on different sediment compounds,
- ii. disentangle marine and climate influences during the development of Voëlvlei, and
- iii. infer variations in local moisture availability and the source of precipitation.

## 2 Site description

Voëlvlei is situated ca. 40 km east of Still Bay and 30 km west of Mossel Bay, at an elevation of 5 m above present sea level (a.s.l.) ca. 10 km inland of the Indian Ocean coast. Today, Voëlvlei has an area of 3.8 km<sup>2</sup> (max. length 4.2 km; max. width 0.7 km) and the catchment has an area of 165 km<sup>2</sup> (database: SRTM 1 arcsec; Jarvis et al., 2008) (Fig. 1c). The catchment altitudes vary between 5 and 333 m a.s.l. (database: SRTM 1 arcsec; Jarvis et al., 2008) and is drained by one ephemeral river (Buffels River), which enters Voëlvlei to the north. A barrier elevated up to 17 m a.s.l. (database: SRTM 1 arcsec; Jarvis et al., 2008) defines the southern border of the Voëlvlei catchment. Voëlvlei has one intermittent outflow in the south-west at 6 m a.s.l. (SRTM 1 arcsec; Jarvis et al., 2008) and drains into the Gouritz river (Fig. 1c).

The geology is characterized by Palaeozoic quartzites of the Table Mountain Group (Cape Supergroup), mudrock–sandstones of the Bokkeveld Group (Cape Supergroup), Mesozoic mudrock–sandstone conglomerates (Uitenhage Group) and Cenozoic limestone–sandstone conglomerates (Bredasdorp Group) (Johnson et al., 2006). Soils have high aluminium and iron concentrations and are mostly Cambisols and Leptosols (Fey, 2010; Zech et al., 2014).

The potential natural vegetation (i.e. that which would be expected to occur in the absence of human impact) consists of variations of fynbos, and only small areas along the main drainage system would be covered by Albany thicket (Mucina and Rutherford, 2006). Today, large areas of the catchment are used for agriculture. The steep slopes of the drainage system are mainly unmanaged and covered by plant communities of the fynbos and Albany thicket.

Mean annual precipitation at the study site is 450 mm yr<sup>-1</sup> (Fick and Hijmans, 2017), and rainfall is almost equally distributed throughout the year. Winter precipitation is linked to the temperate westerlies related to the Atlantic ocean as moisture source, and summer precipitation is associated with the tropical easterlies and the Indian Ocean as moisture source (Engelbrecht and Landman, 2016). Moreover, orographic rainfall occurs from local sources due to onshore flows related to ridging anticyclones (Weldon and Reason, 2014). The isotopic composition of precipitation ( $\delta^2\text{H}_p$ ) is  $^2\text{H}$ -depleted during winter and  $^2\text{H}$ -enriched during summer periods, with a modelled annual mean of  $-13 \pm 1\%$  (Table 1) (Bowen, 2018; Bowen et al., 2005; Braun et al., 2017; Harris et al., 2010). Mean annual temperature is 17.6 °C and slightly higher temperatures during summer (22 °C) lead to semi-arid climatic conditions at the study site today (Fick and Hijmans, 2017).

## 3 Material and methods

For this study, the 13 m long sediment core (VOV16) was retrieved from Voëlvlei (34.259° S; 21.826° E; Fig. 1c) in 2016 using a percussion hammer coring system (inner core diameter 5 cm) and transported to the Physical Geography laboratory of the Friedrich Schiller University Jena where it was stored under dark and cool (ca. 4 °C) conditions until processing. Cores were opened, cleaned and photo-documented, and their sedimentological properties and sediment colour were described in detail following the standard protocols of the Physical Geography laboratory at Friedrich Schiller University Jena.

### 3.1 Chronology

#### 3.1.1 Radiocarbon dating of macro particle, bulk TOC and *n*-alkane samples

The chronology of the sediment record is based on  $^{14}\text{C}$  ages from 1 organic plant-macro particle, 3 charcoal samples, 15 bulk organic samples and 7 *n*-alkane samples (compound-class). In total, 12 of the bulk organic samples and the organic plant-macro particle were analysed using accelerator mass spectrometry (AMS) at the Poznan Radiocarbon Laboratory, Poland. Three bulk organic, three charcoal and seven *n*-alkane samples (see Sect. 3.7 for sample extraction prior to measurement) were analysed with the Mini Carbon Dating System (MICADAS) AMS coupled to an element analyser (Ruff et al., 2010; Salazar et al., 2015; Szidat et al., 2014) at the LARA AMS Laboratory, University of Bern, Switzerland.  $^{14}\text{C}$  results from the LARA AMS were reported as  $\text{F}^{14}\text{C}$  and corrected for cross-contamination and constant contamination after Salazar et al. (2015).

**Table 1.** Modelled isotopic hydrogen composition of precipitation at Voëlvlei (latitude: 34.013° S; longitude: 22.904° E; elevation: 5 m) (Bowen, 2018; Bowen et al., 2005).

	January	February	March	April	May	June	July	August	September	October	November	December
$\delta^2\text{H}_p$ [‰ vs. V-SMOW]	6	4	3	-12	-21	-26	-29	-33	-23	-16	-12	-4

### 3.1.2 OSL dating

A split (half) section of the core was sub-sampled under red light conditions at the University of Leicester luminescence dating laboratory. The upper 5–6 mm of the sediment surface was removed, and the core section was sampled over a depth range of 70 mm. Sediment within 6–7 mm of the core tube inner surface was not sampled but was used for an estimation of sample water content. This (dry) material as well as material from the upper surface was homogenized and used for dose rate analysis. The sediment for equivalent dose analysis was soaked in sodium hexametaphosphate and then wet sieved. The core sediments yielded very limited amounts of sand-sized material, most of which was less than 100  $\mu\text{m}$ . This necessitated the use of the fine sand range 55–90  $\mu\text{m}$  for equivalent dose analysis. This material was prepared using standard methods (e.g. Aitken, 1985; Preusser et al., 2008; Wintle, 1997). This involved treatment with dilute (10 %) hydrochloric acid (to remove carbonates) and (32 %) hydrogen peroxide (to remove organics). The sample was then dried and density separated to isolate the < 2.7  $\text{g cm}^{-3}$  and > 2.58  $\text{g cm}^{-3}$  (quartz) fraction, before etching for 45 min in 48 % hydrofluoric acid, washing in dilute hydrochloric acid (HF, to remove fluorides) and dry sieving (55  $\mu\text{m}$ ). The HF etch removed any remaining K feldspars and also served to etch the ( $\alpha$ -irradiated) outer surface of the quartz grains.

Dose rates were determined using the same core material used to estimate water content via inductively coupled plasma mass spectrometry (ICP-MS) for U and Th and ICP-OES for K analyses at the University of Leicester. The concentrations of U, Th and K were converted to annual dose rates following Guérin et al. (2011) with corrections for grain size (Mejdahl, 1979), water content (Aitken, 1985) and HF etching (Bell, 1979). Cosmic dose rates were determined using the reported sample depth following Prescott and Hutton (1994) with a 5 % relative uncertainty included. Final age uncertainties incorporate 3 % relative uncertainties for the dose rate conversion factors, grain size attenuation factor, water attenuation and HF etching, propagated in quadrature. HF etching is assumed to have entirely removed the  $\alpha$ -irradiated outer portion of the quartz grains. It was assumed that the as-measured water content was appropriate with a 3 % (absolute content) uncertainty propagated to the final dose rate uncertainty. In the absence of robust direct evidence for a substantially different water content in the past, we have utilized the modern sample water content. The 3 % absolute uncertainty associated with this will account for some fluctuations through time. For reference, a 10 % (absolute) change

in water content results in an age difference of approximately 700 years.

All luminescence measurements were performed on a Risø DA20 TL/OSL reader. Stimulation (40 s at 125 °C) was provided by blue LEDs (stimulation wavelength 470 nm) with OSL signals detected with an EMI 9235QA photomultiplier tube via a U-340 detection filter. Laboratory irradiations were delivered by a  $^{90}\text{Sr}$  beta source with a dose rate (at the time of measurement) of ca. 7.58  $\text{Gy min}^{-1}$ . Sample equivalent doses ( $D_e$ ) were determined using the single-aliquot regeneration (SAR) protocol (Murray and Wintle, 2000, 2003; Wintle and Murray, 2006). All single-aliquot measurements were carried out on small (1 to 2 mm) aliquots, which given the grain size fraction analysed means there are likely > 1000 grains per aliquot (e.g. Duller, 2008).

A dose recovery preheat experiment was used to assess the suitability of the SAR protocol in general, and the most appropriate preheating conditions. The overall dose recovery ratio across all preheating temperatures (160–260 °C) was  $0.97 \pm 0.03$  ( $n = 22$ ; zero overdispersion), with a ratio of  $1.00 \pm 0.02$  ( $n = 3$ ) for the chosen preheat temperature combination of 240 °C for 10 s (natural regeneration points) and a 220 °C cut heat for the test dose measurements. All SAR analyses comprised a 7-regeneration point sequence, which included a repeated (recycling) regeneration dose point, an IR depletion regeneration dose point to check for K feldspar contamination (Duller, 2003) and a zero-dose point. The 4 (unique) point dose response curve was generated using the initial 0.64 s of stimulation, with a background signal from the last 8 s. Analyses were carried out in the “Analyst” software. Dose response curves were fitted with saturating exponential fits, with  $D_e$  uncertainties incorporating counting statistics, curve fitting uncertainties and a 1 % systematic uncertainty (Duller, 2007) (all calculated within the Risø Analyst software). The uncertainty in the final  $D_e$  estimate also incorporates an additional beta source calibration uncertainty (3 %).

### 3.1.3 Age modelling

For the final age–depth modelling, all aforementioned dates were used. Bulk organic and *n*-alkane  $^{14}\text{C}$  ages from the terrestrial part of the sediment core were calibrated with the SHcal20 data calibration curve (Hogg et al., 2020), whereas  $^{14}\text{C}$  ages from the marine part of the record were calibrated with the Marine20 calibration curve (Heaton et al., 2020) and additionally corrected for a marine reservoir effect using a  $\Delta R$  of  $134 \pm 38$   $^{14}\text{C}$  years as previously reported by Wünd-

sch et al. (2016b) (Table 1). For the compound-class *n*-alkane samples, the SHCal20 calibration curve (Hogg et al., 2020) was applied due to a predominance of terrestrial synthesized long-chain *n*-alkanes (C<sub>29</sub>, C<sub>31</sub>, C<sub>33</sub>) in the samples (see Sect. 4.3; Table 1). The terrestrial organic plant-macro particle and charcoal found in the marine part of the record were calibrated with the SHCal20 curve (Hogg et al., 2020) (Table 1). All calibrations were done with the online version of the Calib 8.2 software (Stuiver et al., 2020). The final age-depth profile was modelled with the R software package Bacon 2.4.3 (Blaauw and Christen, 2011), using the same calibration datasets. In the following, ages are reported as median ages including the upper and lower limit of the 95 % confidence interval.

### 3.2 Grain size analyses

For grain size measurement 50 mg sample aliquots were treated with H<sub>2</sub>O<sub>2</sub> (10 %) to remove organic matter, HCl (10 %) for the destruction of carbonates and Na<sub>4</sub>P<sub>2</sub>O<sub>7</sub>/Na<sub>2</sub>CO<sub>3</sub> for dispersion. The grain size distribution of each sample was determined with a Laser Particle Sizer (FRITSCH ANALYSETTE 22 Microtec, FRITSCH, Germany) and a wet dispersion unit at the Physical Geography laboratory of the University of Greifswald. Before the measurement, samples were treated with ultrasound for 60 s and subsequently measured in duplicate. The grain size distribution is calculated in 99 classes between 0.08–2000 µm. The mean and median grain size as well as fractions of clay, silt and sand of each sample were calculated.

### 3.3 Paleontological analyses

A selection of 23 sediment samples representing all lithological units and focusing on the assumed transition from an estuarine to a freshwater environment were processed and analysed micropaleontologically. About 3–7 mL of sediment from 1 cm thick sediment slices of the core was washed with tap water through stacked sieves of 63 and 200 µm mesh size. After drying the sieve residues on a heating plate at ca. 50 °C, all microfossils were picked under a low-power stereomicroscope and transferred to microfossil slides for later identification and counting. Microfossils, fragments of macrofossils and charcoal were documented semi-quantitatively as rare (1–2 specimens), common (> 2), abundant (> 10) and very abundant (> 100). Identification relies on Benson and Maddocks (1964), Martens et al. (1996), and Fürstenberg et al. (2017) for Ostracoda and on Schmitt-Sinns (2008) and Fürstenberg et al. (2017) for Foraminifera. Additional macrofossils found during the lithological description, sampling of the core and processing the microfossils were identified, counted and used for paleoecological interpretation. These were all snails with identification relying mainly on Branch et al. (2010) and the mollusc section of the World Register of Marine Species (<http://www.marinespecies.org/>, last access:

8 July 2020). Bivalves could not be identified because they occurred only as fragments. Paleoecological information was drawn from the papers listed above for identification plus Murray (2006) and Kirsten et al. (2018a). All paleontological material will be stored at the South African Museum of Natural History in Cape Town.

### 3.4 Elemental analyses

XRF data (Al, Br, Zr) were collected every 1 cm down-core using two generator settings (30 kV, 1 mA, 15 s; 15 kV, 0.2 mA, 15 s) for detection of different elemental groups with the XRF Core Scanner II (AVAATECH Serial No. 2) at MARUM at the University of Bremen. The split core surface was covered with a 4 µm thin SPEXCerti Prep Ultralene I foil to avoid contamination of the XRF measurement unit and desiccation of the sediment. The data reported here were acquired by a Canberra X-PIPS Silicon Drift Detector (SDD; Model SXD 15C-150-500) with 150 eV X-ray resolution, the Canberra Digital Spectrum Analyzer DAS 1000 and an Oxford Instruments 50 W XTF5011 X-Ray tube with rhodium (Rh) target material. Raw data spectra were processed by the analysis of X-ray spectra by iterative least square software (WIN AXIL) package from Canberra Eurisys. The data were normalized by elemental Zr counts, i.e. Al/Zr and Br/Zr, and plotted as log ratios, primarily to eliminate sediment matrix errors (water content, surface roughness and grain size variations) (Weltje and Tjallingii, 2008).

Moreover, 150 sample aliquots at 8 cm intervals were freeze dried (–53 °C, for > 48 h), ground and sieved to a size < 40 µm. Aluminium (Al), calcium (Ca) and sodium (Na) concentrations were measured with an ICP-OES 725-ES (VARIAN, USA) at the Physical Geography laboratory of the Friedrich Schiller University Jena. A total of 0.2 g of the samples was processed using a microwave-assisted modified aqua regia digestion of 2 mL HCl (32 %) and 4 mL HNO<sub>3</sub> (65 %). Error estimates were based on triple measurements of three samples (VOV\_243, VOV\_651, VOV\_1186; numbers indicate sample depth) (relative error: Al 3.7 %; Ca: 5.4 %; Na: 5.3 %). Samples of the reference material LGC6 187 (river sediment) were measured as well to calculate the relative analytical error which was 1.1 % for Al and Ca, and 10 % for Na.

Total nitrogen (TN) and total carbon (TC) were analysed with a CNS analyser (EuroVector EA 3000, HEKAtech GmbH, Germany) at the Physical Geography laboratory of the University of Greifswald. Concentrations of total organic carbon (TOC) were determined with the same device after treatment with 3 % and 20 % HCl at 80 °C to remove carbonates. Error estimates were based on triple measurements of 30 samples (mean relative error: N: 8.9 %; TOC: 2.9 %). Total inorganic carbon (TIC) was calculated as difference between TC [%] and TOC [%].



### 3.5 Biogenic silica (BiSi)

Biogenic silica (BiSi) concentrations were determined following Ohlendorf and Sturm (2008). BiSi and Al concentrations were measured using an ICP-OES 725-ES (VARIAN, USA) at the Physical Geography laboratory of the Friedrich Schiller University Jena. A correction factor of one (BiSi : Al; 1 : 1) was applied to account for dissolving aluminosilicates.

### 3.6 Powder X-ray diffraction (XRD)

The identification of the mineral composition of 50 powdered samples (e.g. Pecharsky and Zavalij, 2009) from representative core sections was carried out using an X-ray diffractometer (D8-Discover, Bruker AXS) equipped with a CuK $\alpha$  X-ray tube and a gas proportional counter (HI-STAR area detector, Bruker AXS) at Friedrich Schiller University Jena. The qualitative analyses and interpretation of the diffractograms was conducted at Trier University using Bruker DIFFRAC plus 5.0 software. The occurrence of specific mineral phases (low, medium, high) was roughly estimated based on XRD peak intensities in conjunction with the elaborated geochemistry of the investigated sediment sections. For all measurements the quartz peak at 3.342 Å was accepted as internal standard.

### 3.7 Biomarker analyses of *n*-alkane distributions and stable isotope compositions

Total lipids of the sediment samples (14.5–31.4 g) were extracted with 40 mL dichloromethane (DCM) and methanol (MeOH) (9/1, *v/v*) using an ultrasonic bath over three 15 min cycles. The total lipid extract was separated by solid phase extraction using aminopropyl silica gel (Supelco, 45  $\mu$ m) as the stationary phase. The *n*-alkanes were eluted with 4 mL hexane and further purified over coupled silvernitrate (AgNO<sub>3</sub>) – zeolite (Geokleen) pipette columns. The *n*-alkanes trapped in the zeolite were subsequently dissolved in HF and recovered by liquid–liquid extraction using *n*-hexane. An Agilent 7890 gas chromatograph equipped with an Agilent HP5MS column (30 m, 320  $\mu$ m, 0.25  $\mu$ m film thickness) and a flame ionization detector (GC-FID) was used for identification and quantification of the *n*-alkanes, relative to external *n*-alkane standards (*n*-alkane mix *n*-C<sub>21</sub>–*n*-C<sub>40</sub>, Supelco).

*n*-Alkane concentrations were calculated as the sum of C<sub>25</sub> to C<sub>35</sub> and are given in  $\mu$ g g<sup>-1</sup> dry weight. Odd-over-even predominance (OEP) values (Eq. 1) were determined following Hoefs et al. (2002). Low values (< 5) indicate an enhanced state of degradation (Bugge et al., 2010; Zech et al., 2010). The average chain length (ACL) (Eq. 2) was calculated from the odd-numbered *n*-alkanes (Poynter et

al., 1989).

$$\text{OEP} = \left( \frac{nC_{27} + nC_{29} + nC_{31} + nC_{33}}{nC_{26} + nC_{28} + nC_{30} + nC_{32}} \right) \quad (1)$$

$$\text{ACL} = \frac{27 \cdot nC_{27} + 29 \cdot nC_{29} + 31 \cdot nC_{31} + 33 \cdot nC_{33}}{nC_{27} + nC_{29} + nC_{31} + nC_{33}} \quad (2)$$

Compound-specific stable hydrogen isotope analyses of the C<sub>31</sub> and C<sub>33</sub> *n*-alkanes were carried out on an IsoPrime vision IRMS, coupled to an Agilent 7890A GC via a GC5 pyrolysis or combustion interface operating in pyrolysis modus with a MaxChrome and silver wool packed reactor at 1050 °C. Samples were injected with a split–splitless injector. The GC was equipped with 30 m fused silica column (HP5-MS, 0.32 mm, 0.25  $\mu$ m). Each sample was analysed in triplicate, except for single measurements of three samples (VOV\_915, VOV\_128, VOV\_111; numbers indicate sediment depth) due to insufficient compound abundance.  $\delta^2\text{H}_{n\text{-alkane}}$  was measured against calibrated H<sub>2</sub> reference gas and all values are reported in ‰ against VSMOW. The precision was checked by co-analysing a standard alkane mixture (*n*-C<sub>27</sub>, *n*-C<sub>29</sub>, *n*-C<sub>33</sub>) with known isotope composition (Arndt Schimmelmann, University of Indiana), injected in duplicate every nine runs. All measurements were corrected for drift and amount dependency, relative to the standard values in each sequence. Triplicates for the C<sub>31</sub> and C<sub>33</sub> alkanes had a standard deviation of < 4.0‰; the analytical error for the standards was < 1.7‰ (*n* = 68). The H<sub>3</sub><sup>+</sup> factor was checked every 2 d and stayed stable at 4.40 ± 0.03 during measurements.

Compound-specific stable carbon isotope analyses of C<sub>31</sub> and C<sub>33</sub> *n*-alkanes were carried out on an IsoPrime vision IRMS, coupled to an Agilent 7890A GC via a GC5 pyrolysis or combustion interface operating in combustion modus with a CuO and silver wool packed reactor at 850 °C. Samples were injected with a split–splitless injector. The GC was equipped with 30 m fused silica column (HP5-MS, 0.32 mm, 0.25  $\mu$ m).  $\delta^{13}\text{C}_{n\text{-alkane}}$  values were calibrated against CO<sub>2</sub> reference gas of known isotopic composition and all carbon isotope values are given in ‰ against VPDB. Triplicate injections were conducted for each sample and measurement accuracy was controlled in the same way as for the  $\delta^2\text{H}_{n\text{-alkane}}$  analyses. Triplicates for the C<sub>31</sub> and C<sub>33</sub> alkanes had a standard deviation of < 0.2‰; the analytical error for the standards was < 0.2‰ (*n* = 83).

## 4 Results

### 4.1 Lithology and chronology

The sediment sequence is 13 m long and consists of three lithological units defined by differences in sediment colour and grain size (Fig. 2). Unit A from 13 to 4.51 m depth consists of dark greyish material and is dominated by silt. Within this unit, several thin greyish clayey and yellowish sandy layers are present. Unit B from 4.51 to 0.78 m sediment

depth consists of brownish to reddish silty material. In the lower parts of Unit B thin greyish clayey layers are observed. Unit C from 0.78 m sediment depth to the top is dominated by dark brown silty material. Moreover, two layers (0.53–0.44; 0.31–0 m sediment depth) can be separated through changes in colour and granulometric structure in Unit C (Fig. 2).

The chronology reveals a basal age of  $8440^{+200}/_{-250}$  cal BP (Fig. 2, Table 2) and considering a 95 % confidence interval 76 % of the ages overlap with the age–depth model. In Unit A,  $^{14}\text{C}$  ages from the bulk samples are stratigraphically consistent, except for two samples at 11.19 and 5.66 m sediment depth, which are too young for their stratigraphic position. The  $^{14}\text{C}$  age ranges of a terrestrial organic plant-macro particle and a reservoir-corrected bulk sediment sample at 9.63 and 9.61 m overlap. At 4.57 m sediment depth, two charcoal samples and a reservoir-corrected bulk sediment sample distinctly overlap as well. Above the bulk sediment sample at 4.57 m sediment depth, four bulk sediment samples are too old for their stratigraphic position and are not in stratigraphic order (Units B and C). In contrast,  $^{14}\text{C}$  ages obtained from the *n*-alkane samples are distinctly younger and are in stratigraphic order in Units B and C (Table 2; Fig. 2).

Consistent with the good dose recovery results the OSL sample produced a bright, rapidly decaying quartz OSL signal (reduced to ca. 2 % of the initial signal within 1 s). None of the analysed aliquots exhibited recycling ratios or IR ratios beyond/below (respectively) 10 % of unity or recuperation (zero dose signal) > 1 % of the natural signal. The equivalent dose distribution however is overdispersed ( $40 \pm 5$  %; Table 3), even after removal of one very high (125 Gy) outlier, and despite the considerable signal averaging that is likely given the use of the fine sand fraction for analysis. In the context of the analysed core, its likely antiquity, and the otherwise excellent performance of the sample implied by the dose recovery experiment and internal checks within the SAR protocol, a parsimonious explanation of this broad distribution is the presence of unbleached or incompletely bleached grains. Indeed, the age obtained from the central age model equivalent dose estimate is  $10 \pm 1$  ka, which is implausible given the stratigraphic position of the sample (Fig. 2). Application of a three-component minimum age model (MAM) (Galbraith et al., 1999) administered in the R package “Luminescence” (Burrow, 2019) produces a  $D_e$  estimate of  $20.3 \pm 2.4$  Gy and an age of  $6.8 \pm 0.8$  ka (Table 3). While caution is required when applying this approach to multi-grain aliquots (especially those with considerable signal averaging as here), the minimum age estimate is much more concordant with the radiocarbon ages from this section of the core and the broader age–depth model for the whole sequence (Fig. 2). In addition, the MAM-derived OSL age is in stratigraphic order with the  $^{14}\text{C}$  ages derived from the *n*-alkane and charcoal samples (Fig. 2).

#### 4.2 Geochemical and paleontological analyses

Significant correlations (Pearson’s  $r$ ;  $\alpha < 0.05$ ) were obtained for the log-normalized XRF scanning data for Br/Zr and Al/Zr compared to the quantitative elemental contents of Na and Al, respectively ( $r$ :  $\text{Log}(\text{Br}/\text{Zr})/\text{Na} = 0.82$ ;  $r$ :  $\text{Log}(\text{Al}/\text{Zr})/\text{Al} = 0.71$ ; Fig. 3). Na concentrations range from  $2090 \pm 110$  to  $10390 \pm 550$  ppm over the sequence. Both Na contents and Br/Zr ratios show highest values in Unit A (13–4.51 m sediment depth). Several minima in the Br/Zr ratios derived from XRF-scanning data are not visible in the Na concentrations due to the higher sample resolution of the XRF data (Fig. 3). Both Na concentration and Br/Zr ratios distinctly decrease above 4.51 m sediment depth, but an increase is noticeable in Unit C (< 0.78 m sediment depth) (Fig. 3). Al concentrations range from  $39300 \pm 1500$  to  $82900 \pm 3100$  ppm, and both Al contents and Al/Zr ratios show high values over large parts of the sediment record. As mentioned previously, Al/Zr ratios show minima in Unit A, which are not visible in the Al concentrations due to the higher sample resolution of the XRF-scanning data (Fig. 3). Noticeable are distinct low concentrations of Al and Al/Zr ratios from 4.51 to 2.91 m sediment depth and at 1.82 m sediment depth, with an increasing trend to the top of the record (Fig. 3).

TOC and N range from 0.16 % to 3.94 % and 0.03 % to 0.48 % respectively; they show high values in the lower parts of the core (> 4.51 m sediment depth) and distinctly decrease above 4.51 m sediment depth and increase thereafter again (Fig. 3). The C/N molar ratio ranges between 1.9 and 13.6 over the whole sequence with high values between 5.15 and 4.27 m sediment depth (Fig. 3). TIC ranges from 0 % to 0.86 % with noticeable peaks between 6.91 and 6.51, and at 4.83, 2.59 and 1.74 m sediment depth (Fig. 3). Ca concentrations show a similar pattern to TIC and range from  $2830 \pm 150$  to  $28900 \pm 1600$  ppm (Fig. 3). BiSi concentrations range from  $0.8 \pm 0.02$  % to  $2.8 \pm 0.08$  % with low values in the lower parts of the record (> 6.99 m sediment depth), except for high values between 10.98 and 10.10 m sediment depth ( $1.6 \pm 0.05$  % to  $2.2 \pm 0.07$  %) (Fig. 3). They show high values for the upper part of the record < 6.91 m sediment depth (Fig. 3).

Apart from the selected mineral components of the XRD measurements displayed in Fig. 3, all samples have a predominance of quartz, feldspars and micas. Calcite follows the patterns of TIC and Ca and shows highest abundances between 11.46 and 10.18 as well as 3.87 and 2.19 m sediment depth (Fig. 3). The other sections have only medium to low proportions of calcite (Fig. 3). The presence of gypsum is restricted to depths between 9.62 and 9.14 m as well as 5.47 and 5.23 m (Fig. 3). However, an absence of calcite and/or gypsum at the distinct peaks of TIC and Ca (e.g. 2.59 and 1.74 m sediment depth) is likely due to the lower sample resolution of the XRD measurements compared to the elemental data (Fig. 3). High proportions of halite are present in

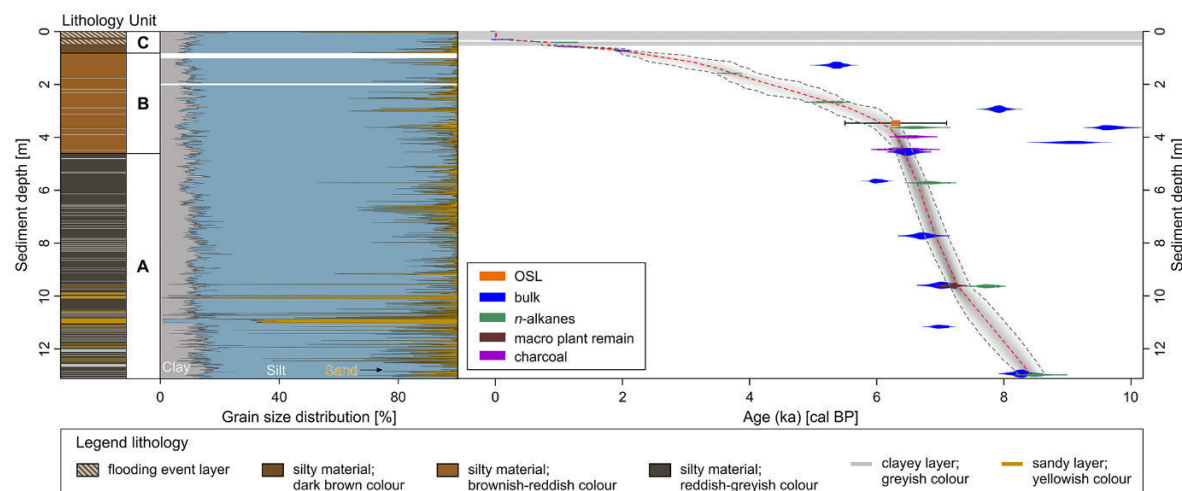


**Figure 2.** Left: lithology and grain size distribution (clay, silt, sand) of the VOV16 record from Voëlvei. Right: age–depth model of the sediment record from Voëlvei. Calibrated radiocarbon ages are displayed as probability density functions of the  $2\sigma$  distributions (blue: bulk sediment; green: compound-class *n*-alkane samples; brown: macro plant remain). Calibration and age–depth modelling was carried out using the R software package Bacon 2.4.3 (Blauuw and Christen, 2011).

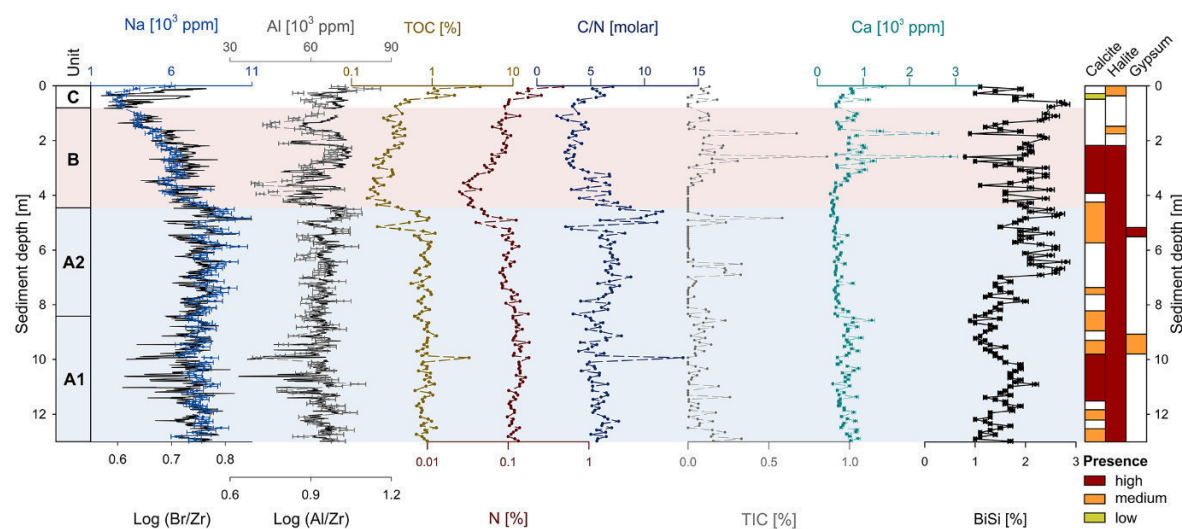


**Figure 3.** Lithological units, sodium (Na) content and  $\text{Log}_{10}$  ratio of bromine (Br) and zirconium (Zr), aluminium (Al) and  $\text{Log}_{10}$  ratio of Al and Zr, contents of total organic carbon (TOC), total nitrogen (N), molar C/N ratio, total inorganic carbon (TIC), calcium (Ca), and biogenic silica (BiSi) derived from the sediment core VOV16 from Voëlvei. The presence of selected mineral components is also depicted.

large parts of the sediment record ( $> 2.19$  m sediment depth; Fig. 3).

*n*-Alkane concentrations range from  $0.22$  to  $5.23 \mu\text{g g}^{-1}$  with high values in Unit A and distinctly lower concentrations in Unit B and C (Fig. 4). All samples show a distinct odd-over-even predominance (4.0–15.5), and the ACL ranges from 29.9 to 31.4. Consequently,  $\text{C}_{29}$ ,  $\text{C}_{31}$  and  $\text{C}_{33}$  are the predominant *n*-alkane chain-lengths in all samples

(Fig. 4).  $\delta^{13}\text{C}_{n\text{-alkane}}$  values range from  $-28.10 \pm 0.16 \text{‰}$  to  $-22.72 \pm 0.06 \text{‰}$  with more negative values at the bottom of Unit A (13.0–12.58 m composite depth), followed by less negative values (12.58–8.85 m composite depth), which show a decreasing trend upwards (Fig. 4). Notably are three higher  $\delta^{13}\text{C}_{n\text{-alkane}}$  values in the upper parts of Unit A between 6.35 and 4.51 m sediment depth (Fig. 4).  $\delta^2\text{H}_{n\text{-alkane}}$  values range from  $-154.4 \pm 1.3 \text{‰}$  to  $-129.6 \pm 1.1 \text{‰}$  with

**Table 2.** Conventional radiocarbon ages as well as  $2\sigma$  calibrated age ranges and median calibrated ages (Calib 8.2) (Stuiver et al., 2020) using the SHCal20 and Marine20 calibration curve (Heaton et al., 2020; Hogg et al., 2020) of dated bulk sediment, *n*-alkanes and organic macro particle (OMP) samples from the VOV16 record. Samples from the marine and brackish parts of the record were reservoir corrected using a  $\Delta R$  of  $134 \pm 38$   $^{14}\text{C}$  years after Wüdsch et al. (2016b). 1: SHCal20; 2: Marine20 and reservoir corrected using a  $\Delta R$  of  $134 \pm 38$   $^{14}\text{C}$  years after Wüdsch et al. (2016b).

Sediment depth depth [m]	Lab ID	$1\sigma$ conventional $^{14}\text{C}$ age [BP]	Dated material	Median cal age and $2\sigma$ error [cal BP]	Calibration
0.29	Poz-94013	$660 \pm 30$	bulk	$610^{+75}/_{-25}$	1
0.32	BE-9770.1.1	$-85 \pm 120$	bulk	$100^{+85}/_{-85}$	1
0.44	BE-12027.1.1	$1250 \pm 140$	<i>n</i> -alkanes	$1110^{+250}/_{-130}$	1
0.51	BE-9772.1.1	$1855 \pm 120$	bulk	$1740^{+270}/_{-270}$	1
0.59	BE-9772.1.1	$1360 \pm 120$	bulk	$1210^{+470}/_{-250}$	1
0.75	Poz-96323	$2080 \pm 35$	bulk	$2000^{+170}/_{-80}$	1
1.29	Poz-94014	$5330 \pm 50$	bulk	$5370^{+410}/_{-210}$	2 <sup>a</sup>
1.59	BE-12026.1.1	$3470 \pm 90$	<i>n</i> -alkanes	$3690^{+455}/_{-240}$	1
2.68	BE-12025.1.1	$4630 \pm 100$	<i>n</i> -alkanes	$5280^{+520}/_{-310}$	1
2.95	Poz-96324	$7780 \pm 50$	bulk	$7920^{+380}/_{-190}$	2 <sup>a</sup>
3.64	BE-12024.1.1	$5830 \pm 130$	<i>n</i> -alkanes	$6600^{+590}/_{-290}$	1
3.65	Poz-94016	$9250 \pm 80$	bulk	$9660^{+550}/_{-250}$	2 <sup>a</sup>
3.99	BE-13598.1.1	$5780 \pm 120$	charcoal	$6550^{+500}/_{-250}$	1
4.21	Poz-98909	$8750 \pm 170$	bulk	$9060^{+900}/_{-480}$	2 <sup>a</sup>
4.57	Poz-98910	$6380 \pm 40$	bulk	$6490^{+370}/_{-190}$	2
4.57	BE-13597.1.1	$5550 \pm 110$	charcoal	$6310^{+450}/_{-210}$	1
4.57	BE-13596.1.1	$5800 \pm 120$	charcoal	$6570^{+500}/_{-270}$	1
5.66	Poz-94017	$5740 \pm 40$	bulk	$5800^{+370}/_{-200}$	2 <sup>b</sup>
5.73	BE-12023.1.1	$6020 \pm 100$	<i>n</i> -alkanes	$6830^{+470}/_{-230}$	1
7.74	Poz-94018	$6590 \pm 50$	bulk	$6720^{+420}/_{-210}$	2
9.61	Poz-94021	$6850 \pm 50$	bulk	$7020^{+410}/_{-210}$	2
9.63	Poz-94020	$6310 \pm 50$	OMP	$7200^{+160}/_{-50}$	1
9.64	BE-12022.1.1	$6940 \pm 110$	<i>n</i> -alkanes	$7750^{+370}/_{-180}$	1
11.19	Poz-94022	$6620 \pm 50$	bulk	$6760^{+420}/_{-210}$	2 <sup>b</sup>
12.95	Poz-94023	$8110 \pm 50$	bulk	$8270^{+370}/_{-210}$	2
12.99	BE-12021.1.1	$7750 \pm 110$	<i>n</i> -alkanes	$8510^{+460}/_{-190}$	1

<sup>a</sup> and <sup>b</sup> Samples that are too old and too young, respectively.

**Table 3.** Equivalent dose measurements on sample VOV16-1. 24 aliquots were measured (\*  $n$  = number of aliquots, a 25th aliquot with a  $D_e$  of  $\sim 125$  Gy was excluded prior to analysis).

Average sediment depth [m]	Water content (%)	U (ppm)	Th (ppm)	K (%)	Dose rate (Gy ka <sup>-1</sup> )	CAM $D_e$ (Gy) (n)	CAM OD [%]	MAM $D_e$ (Gy)	CAM age (ka)	MAM age (ka)
3.50	18	2.8	12.9	2.0	$3.01 \pm 0.12$	$31.0 \pm 2.8$ (24)*	$40 \pm 6$	$20.3 \pm 2.3$	$10.3 \pm 1.0$	$6.8 \pm 0.8$

less negative values at the bottom followed by a trend to more negative values in Unit A. Unit B shows less negative  $\delta^2\text{H}_{n\text{-alkane}}$  values at the bottom followed by more negative  $\delta^2\text{H}_{n\text{-alkane}}$  values at the top and in Unit C (Fig. 4).

Paleontological analyses of the 33 macrofossil samples and 23 microfossil samples revealed 56 snail specimens representing six species. In descending order of abundance these are *Turritella capensis* (Krauss, 1848), which is clearly dom-

inant, the rare *Assiminea globulus* (Conolly, 1939), *Hydrobia* sp., *Natica tecta* (Anton, 1839), *Nassarius kraussianus* (Dunker, 1846) and a fragment of an unidentified gastropod species (Fig. 5). The microfossil associations show a higher diversity. The dominating foraminifer taxon is *Ammonia parkinsoniana* (d'Orbigny, 1839), followed by *Quinqueloculina* sp., and the rare *Trochammina inflata* (Montagu, 1808) and *Haynesina* sp. All other foraminifer taxa are

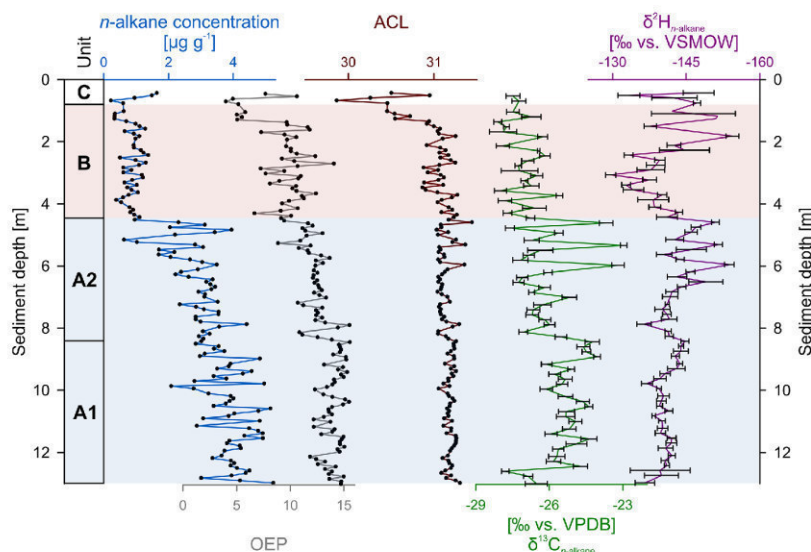


**Figure 4.** Concentration, odd-over-even predominance (OEP) and average chain length (ACL) of leaf wax  $n$ -alkanes and their stable isotopic composition for hydrogen ( $\delta^2\text{H}_{n\text{-alkane}}$ ) and carbon ( $\delta^{13}\text{C}_{n\text{-alkane}}$ ) of the Voëlvlei sediment record.

represented by only one test each (*Bolivina* sp., *Cribrorhynchium articulatum* (d'Orbigny, 1839), *Spirillina* sp. and an unidentified trochamminid). The most abundant ostracod species are *Sulcostocythere knysnaensis* (Benson and Maddocks, 1964) and juveniles of *Loxococoncha parameridionalis*? (Benson and Maddocks, 1964); rare ostracods are a myodocopid specimen and juvenile *Agelaiella* valves as well as the freshwater species *Sarscypridopsis aculeata* (Costa, 1847), *Cyprilla humilis* (Sars, 1924) and an unidentifiable fragment of a larger species. Microfossils identified on a group level only are ephippia of cladocerans, gyrogonites of charophytes, *Plumatella*-like bryozoan statoblasts, mollusc and insect fragments, fish bone remains, fruits, and seeds as well as unidentifiable plant remains. Charcoal was found in large quantities in many samples.

Unit A1 shows a high diversity and contains most of the marine-brackish snails and high numbers of foraminifera. The ostracod fauna is dominated by brackish water taxa. Shell and fish bone fragments are abundant. Unit A2 looks similar to Unit A1 but is generally more variable in abundances and diversity. Macrofossils, i.e. marine-brackish snails, become rare. Salt marsh foraminifera, fruits and seeds occur for the first time. Units B and C lack marine-brackish snails, brackish ostracods and salt marsh foraminifera, and foraminifera in general are documented with a single test at the base of the zone only. In Unit B and C, freshwater ostracods occur for the first time and freshwater taxa in general dominate. Fragments of shells, plants, insects and charcoal disappear in Unit B and C (Fig. 5).

## 5 Discussion

### 5.1 Chronostratigraphy

Micropaleontological, organic and inorganic analyses show that three different depositional settings exist for the sediment sequence from Voëlvlei (Figs. 3, 5). In the lower part of the sequence (Unit A), the high concentrations of Na, TOC and N; high Br/Zr ratios; and a marine/brackish gastropod species assemblage indicate a marine/brackish depositional setting from 13 to 4.51 m sediment depth (Figs. 2, 3, 5). Corresponding reservoir-corrected bulk sediment  $^{14}\text{C}$  ages as well as the terrestrial organic plant-macro particle and charcoal  $^{14}\text{C}$  ages are all stratigraphically consistent and range from  $8510^{+280}/_{-200}$  to  $6310^{+450}/_{-210}$  calBP suggesting that the sediments were rapidly deposited (Fig. 2). The overlap of the bulk and the plant-macro particle age and the bulk and charcoal ages confirm the suitability of the reservoir correction and application of the Marine20 calibration curve (Heaton et al., 2020) for bulk samples in Unit A. The only exception are the bulk  $^{14}\text{C}$  ages at 11.19 and 5.66 m sediment depth, which are too young for their stratigraphic position. This is probably due to an increased input of terrestrial organic carbon during this time, indicated by corresponding high inputs of sand, reduced Al contents and lower Al/Zr ratios (Figs. 2, 3). This likely added less  $^{14}\text{C}$ -depleted material, affecting the marine organic carbon stock and diluting the reservoir effect. As we cannot calculate the precise contribution of terrestrial organic carbon, these  $^{14}\text{C}$  ages were excluded from the age model in a second modelling iteration (Heaton et al., 2020; Hogg et al., 2020)

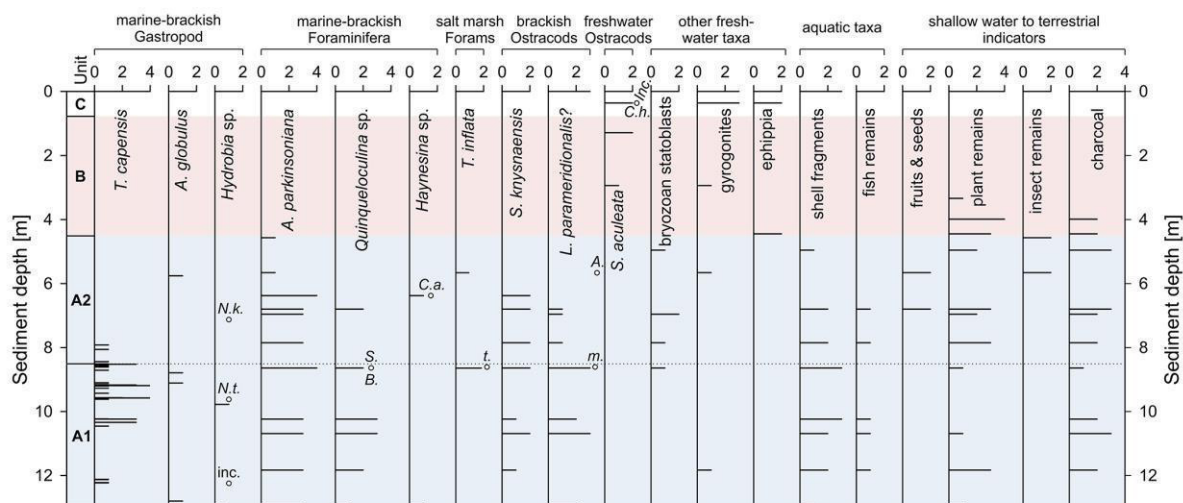


**Figure 5.** Distribution of micropaleontological taxa and charcoal in core VOV16. Units are based on distribution of micropaleontological taxa and lithological characteristics. Additional macrofossils were picked from the lowest part of the core where they are relatively abundant. All abundances are given semi-quantitatively (0 – absent, 1 – rare, 2 – common, 3 – abundant, 4 – very abundant). Single occurrences of taxa are indicated by empty circles and abbreviated name (*Nassarius kraussianus*, *Natica tecta*, *Bolivina* sp., *Spirillina* sp., *Cribrorhynchium articulatum*, *trochamminid foraminifer*, *Aglaiella*, *myodocopid ostracod*, *Cyprilla humilis*).

(Fig. 2). At Voëlvlei, *n*-alkanes show a clear dominance of the  $C_{31}$  and  $C_{33}$  homologues and thus are of terrestrial origin (Boom et al., 2014; Chambers et al., 2014; Strobel et al., 2020). We therefore calibrated them with the terrestrial SHCal20 calibration curve. We note that a minor contribution of the shorter chain lengths ( $<C_{25}$ ) to the dated compound-class *n*-alkane samples, which are potentially synthesized by aquatic plants, for example, and may show a marine reservoir effect, leading to overly old  $^{14}C$  ages when calibrated using a SHCal20 calibration curve. The aforementioned dominance of long-chain *n*-alkanes, however, makes a terrestrial origin likely and the distinct overlap with marine-calibrated and reservoir-corrected bulk  $^{14}C$  ages support the application of the SHCal20 calibration curve to the compound-class *n*-alkane samples (Fig. 2).

At 4.51 m sediment depth, a distinct shift in the depositional setting occurred with decreasing Na concentrations, Br/Zr ratios, and TOC and N concentrations, pointing towards a change from a marine/brackish environment to a fresher lacustrine environmental setting (Figs. 3, 5). At these depths bulk  $^{14}C$  ages are much older than their stratigraphic position, possibly reflecting the deposition of degraded, pre aged sediments via erosion of old organic carbon from deeper soil horizons within the catchment (Bliedtner et al., 2020; Douglas et al., 2018; Haas et al., 2020). The OSL age (3.50 m sediment depth) is stratigraphically more consistent than the bulk  $^{14}C$  ages. Since a MAM was applied it is likely that this age more closely reflects the timing of deposition, but the presence of partially or unbleached sand grains also potentially implies an input from older sediments at this

time, supporting the interpretation of the bulk  $^{14}C$  age overestimations. Compound-class *n*-alkane  $^{14}C$  ages are stratigraphically consistent in Units B and C. We therefore infer that leaf waxes are derived from topsoils in the catchment and are rapidly deposited in the sediment archive (Bliedtner et al., 2020; Haas et al., 2017). Therefore, the incorporated climate signal should be close to that of the timing of deposition, and *n*-alkane-based proxies, i.e.  $\delta^2H_{n-alkane}$  and  $\delta^{13}C_{n-alkane}$ , yield paleoenvironmental information that can also be interpreted robustly.

## 5.2 Marine influence and lake development

South Africa, especially the southern Cape coast, is known to have experienced distinct environmental changes related to relative sea level fluctuations during the Holocene (Cooper et al., 2018; Kirsten et al., 2018b; Marker and Miller, 1993; Reddering, 1988; Wüdsch et al., 2018, 2016a). Voëlvlei can contribute to our understanding of sea level changes during the Holocene due to its present location at an elevation of 5 m a.s.l. and the high temporal resolution of its Early and Middle Holocene depositional record. Inferred from lithological characteristics, paleoecological and elemental analyses, which indicate variable intrusion of marine water, the record suggests three eco-zones, of which one can be subdivided in two subzones (Units A1, A2, and B and C) (Fig. 6).

During the period between 8440  $^{+200}/_{-250}$  and 7070  $^{+160}/_{-200}$  cal BP (Unit A1), the dominant gastropod is *Turritella capensis*, which is a common species in sandy coastal lagoons in South Africa today (Branch et

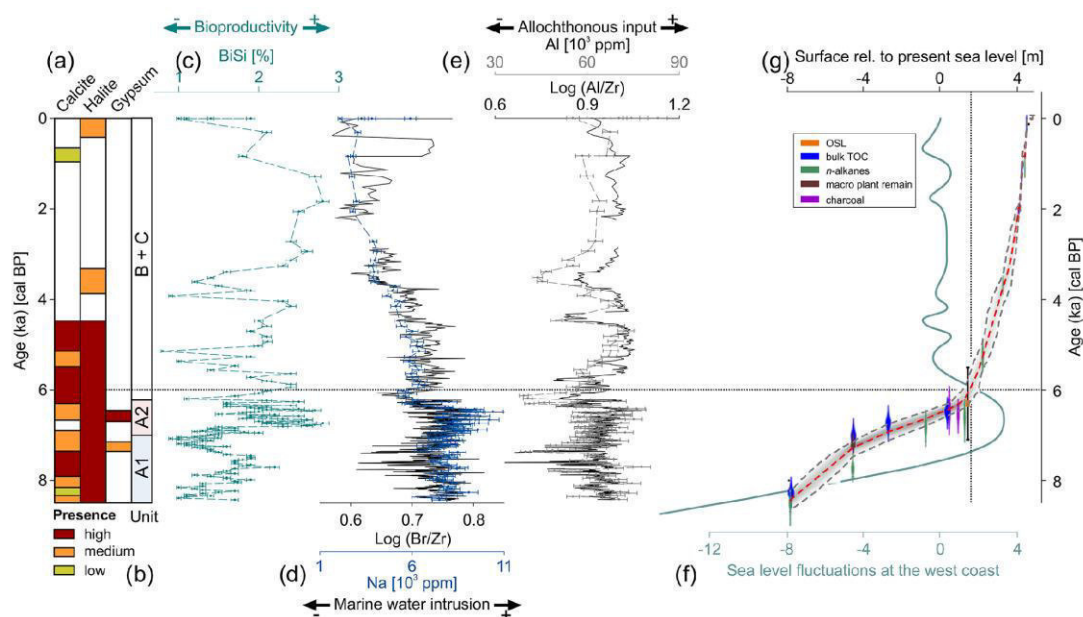


**Figure 6.** (a) Occurrence of selected mineral components in the VOV16 sediment record, (b) lithological and paleoecological units (A1 – subtidal marine-brackish, A2 – intratidal brackish, B+C freshwater to terrestrial), (c) biogenic silica (BiSi) content, (d) Na content and Log (Br/Zr) ratios, (e) Al content and Log (Al/Zr) ratios from Voëlvlei. (f) Sea level curve for the west coast of South Africa (Compton, 2006; Cooper et al., 2018) and (g) the lake floor of Voëlvlei relative to the present sea level.

al., 2010), preferring the mid-intertidal zone (Walters and Griffiths, 1987) (Figs. 5, 6). The rarer gastropod *Assimineia globulus* is known to be abundant on upper intertidal mudflats of South African estuaries (Barnes, 2018), whereas the small gastropod *Hydrobia* prefers the upper salt marshes of South Africa (Branch et al., 2010). The single occurrences of *Natica tecta* and *Nassarius kraussianus* point to estuarine mudflats (Branch et al., 2010) (Figs. 5, 6). Abundant brackish water ostracods and foraminifera indicate permanent water cover at the coring site during this period. In summary, these fauna reflect an estuarine and shallow subtidal environment close to intertidal mudflats. The abundance of plant remains and fragments of shells and fish bones point to shallow water as well. Therefore, we assume the respective core depths reflect an elevation slightly below the past sea level, which is in line with the paleo-surface of Lake Voëlvlei, i.e. 8.0 to 3.5 m below present sea level (b.s.l.) from 8440<sup>+200</sup>/<sub>-250</sub> to 7070<sup>+160</sup>/<sub>-200</sub> cal BP (Fig. 6). The low diversity of foraminifera is typical for lower salinity conditions; the dominant small and unornamented *Ammonia* species, *Quinqueloculina* and *Haynesina*, are consistent with this brackish water inference (Murray, 2006) (Figs. 5, 6). The same applies to the brackish water ostracod fauna, which are dominated by the estuarine species *Sulcostocythere knysnaensis* and *Loxoconcha parameridionalis* (Fürstenberg et al., 2017; Kirsten et al., 2018a) (Figs. 5, 6). The complete

absence of open marine microfossils, especially planktonic foraminifera and echinoderm fragments, indicates an inner estuarine position in the core locality without direct marine inflow, even under high-energy conditions. The few bryozoan statoblasts and gyrogonites of charophytes all derive from freshwater environments (Frenzel, 2019; Kirsten et al., 2018a) and point to an unconfined exchange with river water. The highest salinity for the entire core is probably reached at 7090<sup>+170</sup>/<sub>-200</sub> cal BP when the abundance and diversity of the foraminifera reach a maximum and a myodocpid ostracod was found (Figs. 5, 6). The coring position was ca. 3.65 m b.s.l. during this time (Fig. 6). Therefore, sea level was likely at the present height or slightly lower.

Between 7070<sup>+170</sup>/<sub>-200</sub> and 6420<sup>+130</sup>/<sub>-140</sub> cal BP (Unit A2), continued inner estuarine, brackish water conditions are indicated by a similar assemblage of taxa as observed in Unit A1. Intertidal gastropods typical for Unit A1, however, are now very rare, suggesting decreasing tidal influence and probably decreasing salinity (Figs. 5, 6). Salt marsh foraminifera occur only in Unit A2, albeit in low numbers (Fig. 6). This points to a very shallow water depth under marine/brackish conditions and a close shoreline (Strachan et al., 2017), which is in good agreement with the occurrence of fruits and seeds (only occurring in this unit), and the abundant plant remains. However, the high variability in the abundance of many taxa indicates unstable

conditions compared to Unit A1. Freshwater inflow is implied by floating bryozoan statoblasts and charophyte gyrogonites (Frenzel, 2019) (Figs. 5, 6). The respective paleosurface of Lake Voëlvlei was ca. 3.5 m b.s.l. to 0.5 m a.s.l. from 7070  $^{+170}_{-200}$  to 6420  $^{+130}_{-140}$  cal BP (Fig. 6), indicating a sea level higher than the present during this time.

Elemental (Br/Zr ratios, Na contents) and mineralogical data support phases of marine water intrusion at Voëlvlei. Bromide salts are common in sea water but occur in very low concentrations in freshwater systems (Song and Müller, 1993). In aqueous environments the dominant species is  $\text{Br}^-$ , which substitutes the salt constituent chloride ( $\text{Cl}^-$ ) in the sea salt lattice during crystallization (Ullman, 1995). Halite (NaCl) also originates from marine waters, and thus Br, Na and halite can be used as indicators of marine water intrusion (Babel and Schreiber, 2014; Olsen et al., 2012; Wüdsch et al., 2018). High values of the marine indicators from the elemental analysis (Na, Br/Zr ratios) and the presence of halite in the sediments are in good agreement with our micropaleontological data indicating marine water intrusions in Units A1 and A2 (8440  $^{+200}_{-250}$  to 6420  $^{+130}_{-140}$  cal BP; Fig. 6). Furthermore, the occurrence of calcite in both units as well as gypsum from 7260  $^{+110}_{-210}$  to 7180  $^{+150}_{-200}$  cal BP and 6590  $^{+150}_{-160}$  to 6550  $^{+150}_{-160}$  cal BP also points towards shallow water conditions as also indicated by the micropaleontology results (Fig. 6). Such shallow water conditions support bioproductivity (BiSi) increases in Unit A1 and A2 which reached a maximum at ca. 6740  $^{+170}_{-170}$  cal BP (Fig. 6). The elevation of the lake floor rapidly increases from ca. 8 m b.s.l. at 8440  $^{+200}_{-250}$  (base of the VOV16 record) to ca. 0.5 m a.s.l. at 6420  $^{+130}_{-140}$  cal BP (Unit A1 and A2; Fig. 6). Therefore, results imply a higher sea level compared to today until 6420  $^{+130}_{-140}$  cal BP and thus lend further support for a proposed local/regional Holocene relative sea level maximum of about +3.8 m a.s.l. (ca. 7600–5800 cal BP) (Cooper et al., 2018) on the southern Cape.

The micropaleontological associations of Units B and C (6420  $^{+130}_{-140}$  cal BP until today) are completely different from those of Unit A1 and A2 (Figs. 5, 6). Many samples are devoid of microfossils and freshwater taxa dominate other samples. One single test of the foraminifer *Ammonia* sp. found in the lowermost part of unit B is the only brackish water taxon (Murray, 2006). This was likely reworked from older sediments where this species is very abundant (Figs. 5, 6). Therefore, we assume freshwater or athalassic conditions for samples with aquatic taxa. New to Unit B and C are the freshwater ostracod species *Sarscypridopsis aculeata* and ehippia of cladocerans, which are typical of non-permanent water bodies (Frenzel, 2019; Meisch, 2000). They likely reflect the transformation of Voëlvlei to a non-permanent lake and terrestrial habitat. The lower part of Unit B contains variable amounts of plant remains and charcoal, indicating river transport. Their later disappearance points to an isolation of the basin while silting up.

Decreasing elemental marine indicators (Na, Br/Zr ratios) support reduced intrusion of marine waters from 6420  $^{+130}_{-140}$  cal BP (Fig. 6). Sedimentation rates markedly decrease while the occurrence of calcite (6290  $^{+240}_{-150}$ –4590  $^{+590}_{-550}$  cal BP) further supports shallow water conditions in Units B and C (Fig. 6). While further silting up led to the isolation of the sediment surface above the present sea level (0 m a.s.l.) from 6510  $^{+140}_{-150}$  cal BP (Fig. 6), marine water intrusion was likely absent from 4300  $^{+490}_{-570}$  cal BP when the sediment surface reached 3 m a.s.l. This is based on considering a still elevated sea level of about +1 m a.s.l. (5300–4200 cal BP) (Cooper et al., 2018) and a tidal range comparable to today (neap tide: 0.6–0.8 m, spring tide: 1.8–2 m) (Rautenbach et al., 2019).

Overall, the results only provide evidence of marine water intrusion in the Voëlvlei system rather than sea level index points and thus cannot be used to generate or corroborate an exact relative sea-level curve (e.g. Compton, 2006; Cooper et al., 2018). However, in comparison to local/regional records the results of this study are in line with the findings from Eilandvlei (Kirsten et al., 2018b; Wüdsch et al., 2018) and Groenvlei (Wüdsch et al., 2016a), which indicate a rising sea level during the Early Holocene and a high stand during the Middle Holocene. The proxies used in this study generally support the assumed sea-level evolution at the southern Cape coast of South Africa (Kirsten et al., 2018b; Marker and Miller, 1993; Reddering, 1988; Wüdsch et al., 2018, 2016a). In (supra-)regional comparison, these results are also in line with studies from the west coast of South Africa (Baxter and Meadows, 1999; Carr et al., 2015; Kirsten et al., 2020) and Namibia (Compton, 2006), as reviewed in Cooper et al. (2018), showing a rapid sea level rise to a maximum of +3.8 m a.s.l. (ca. 7600–5800 cal BP), followed by a decrease to +1 m a.s.l. (5300–4200 cal BP) and a relatively constant sea level, comparable to the present, thereafter (Fig. 6).

### 5.3 Paleoenvironmental and paleoclimate evolution

The main driver of the  $\delta^2\text{H}_{n\text{-alkane}}$  signal at Voëlvlei is the  $\delta^2\text{H}$  variability of the precipitation source (Strobel et al., 2020) although it has to be noted that variations in the vegetation composition, e.g. varying biosynthetic fractionation, evapotranspirative enrichment and water use efficiency, may all potentially alter the  $\delta^2\text{H}_{n\text{-alkane}}$  signal (Hou et al., 2007; Sachse et al., 2012). However, modern precipitation suggests that westerly-derived precipitation is  $^2\text{H}$ -depleted and easterly-derived precipitation is  $^2\text{H}$ -enriched (Bowen, 2018; Bowen et al., 2005; Braun et al., 2017; Harris et al., 2010; Table 1). This is also imprinted in modern reference material from topsoils (Hahn et al., 2018; Strobel et al., 2020) (mean  $\delta^2\text{H}_{n\text{-alkane}}$  values from topsoils from WRZ and SRZ are  $-145 \pm 10\text{‰}$  and  $-135 \pm 10\text{‰}$ , respectively), pointing to the “source effect” as the domi-



nant driver of the  $\delta^2\text{H}_{n\text{-alkane}}$  signal at Voëlvlei.  $\delta^2\text{H}_{n\text{-alkane}}$  values from Voëlvlei are moderate from 8440  $^{+200}/_{-250}$  to 7070  $^{+160}/_{-200}$  cal BP, which imply a year-round precipitation regime, i.e. contributions of both westerly- and easterly-derived precipitation (Fig. 7a).

Year-round precipitation is accompanied by less negative  $\delta^{13}\text{C}_{n\text{-alkane}}$  values between 8440  $^{+200}/_{-250}$  and 7070  $^{+160}/_{-200}$  cal BP, likely indicating overall dry conditions for this period at Voëlvlei (Fig. 7e). These dry conditions potentially led to a sparse vegetation cover and runoff (induced by occasional events), which likely carried extremely variable grain sizes and amounts of allochthonous input (Al concentration, Al/Zr ratios) (Fig. 7g). Minimum values in Al concentrations and Al/Zr ratios are assumed to be caused by layers consisting almost exclusively of sand ( $\text{SiO}_2$ ) and thus imply high allochthonous inputs (Figs. 2, 7h) at this time. Similarly at Vankervelsvlei, input of reworked soil material during this time is interpreted to be the result of low vegetation cover in the catchment (Strobel et al., 2019). This interpretation of dry conditions between 8440  $^{+200}/_{-250}$  and 7070  $^{+160}/_{-200}$  cal BP is also in line with the findings from Eilandvlei, where low Afrotropical forest (AFT) pollen percentages are interpreted as overall dry conditions between ca. 8500 and 7000 cal BP (Quick et al., 2018) (Fig. 7d), and a study at Seweweekspoort, where less positive  $\delta^{15}\text{N}$  values are also interpreted to indicate moderately dry conditions (Chase et al., 2017) (Fig. 7c) resulting in a consistent moisture signal in the YRZ during this time.

At 7020  $^{+170}/_{-200}$  cal BP, moister conditions are indicated by a distinct shift to more negative  $\delta^{13}\text{C}_{n\text{-alkane}}$  values and evidence for increased allochthonous inputs (Al content, Al/Zr ratios), which lasts until the present. However, there are decreases in allochthonous inputs from 6420  $^{+130}/_{-140}$  to 6080  $^{+320}/_{-240}$  cal BP, and at 4480  $^{+580}/_{-540}$  and 3530  $^{+500}/_{-470}$  cal BP (Fig. 7g). The latter event is accompanied by distinctly negative  $\delta^{13}\text{C}$  values (Fig. 7e) whereas the earlier one only shows slightly more negative values. This potentially indicates a denser vegetation cover and reduced runoff-induced sediment input, which are supported by the presence of freshwater taxa during this time (Fig. 5). However, drier conditions inferred from reduced allochthonous input could also be possible due to drought-induced changes of the vegetation composition indicated by a higher proportion of plants using CAM metabolism. These could possibly reduce drought stress and therefore the influence of water use efficiency to  $^{13}\text{C}$ -enrichment in the  $n$ -alkanes (Diefendorf and Freimuth, 2017). Overall it is difficult to interpret the variations in the core between 4480  $^{+580}/_{-540}$  and 3530  $^{+500}/_{-470}$  cal BP. They interrupt a trend towards moister conditions but cannot be ultimately attributed to moister or drier conditions.

Noticeable in the record are three data points at 6670  $^{+170}/_{-170}$ , 6560  $^{+150}/_{-160}$  and 6440  $^{+130}/_{-140}$  cal BP showing the least negative  $\delta^{13}\text{C}_{n\text{-alkane}}$  values, which exceed all other measurements and are accompanied by dis-

tinctly negative  $\delta^2\text{H}_{n\text{-alkane}}$  values (grey dots in Fig. 7a, d). For those three samples, the climate signal is possibly overprinted by local effects of plants that grow at shallower water depths and/or at the shoreline of the lake. While less negative  $\delta^{13}\text{C}_{n\text{-alkane}}$  values point to the presence of plants using  $\text{C}_4$  and/or CAM metabolism (Boom et al., 2014; Carr et al., 2015; Diefendorf and Freimuth, 2017), the  $\delta^2\text{H}_{n\text{-alkane}}$  signal with more negative values can be biased by the photosynthetic mode and also salinity (Aichner et al., 2017; Feakins and Sessions, 2010; Ladd and Sachs, 2012; Sachse et al., 2012). Therefore, disentangling the regional climate and local overprinting is challenging for the three aforementioned data points. However, since allochthonous input is high (Al concentration, Al/Zr ratios; Fig. 7g), we hypothesize overall moist conditions since 7020  $^{+170}/_{-200}$  cal BP.

Moister conditions are accompanied by more negative  $\delta^2\text{H}_{n\text{-alkane}}$  values from 7020  $^{+170}/_{-200}$  to 6420  $^{+130}/_{-140}$  cal BP, which are likely indicative of an increased contribution of westerly-derived precipitation (Fig. 7a). At the same time as the aforementioned reduction of the allochthonous inputs, there is also a marked shift to less negative  $\delta^2\text{H}_{n\text{-alkane}}$  values at 6420  $^{+130}/_{-140}$  implying an increased contribution of easterly-derived precipitation (Fig. 7a). Afterwards,  $\delta^2\text{H}_{n\text{-alkane}}$  values are variable but have an overall trend from less negative to more negative  $\delta^2\text{H}_{n\text{-alkane}}$  values lasting until 2060  $^{+140}/_{-200}$  cal BP, which is likely suggest a return from an easterly- to a more dominantly westerly-derived precipitation regime (Fig. 7a). However, already at the beginning, this period is interrupted by a short phase of somewhat more negative values from 5560  $^{+430}/_{-470}$  to 5150  $^{+340}/_{-330}$ , indicating more westerly-derived precipitation (Fig. 7a). From 2060  $^{+140}/_{-200}$  cal BP until the present, less negative  $\delta^2\text{H}_{n\text{-alkane}}$  values imply an increased contribution of easterly-derived precipitation (Fig. 7a), which occurs within a trend towards moister conditions ( $\delta^{13}\text{C}_{n\text{-alkane}}$ ) (Fig. 7e).

Moist conditions between ca. 7000 and ca. 4700 cal BP are in line with studies from the central southern Cape coast (Quick et al., 2018; Strobel et al., 2019; Wündsche et al., 2018). At ca. 4700 cal BP, a rapid shift in climate was also detected in numerous studies located in the YRZ. In the Wilderness area, dry conditions and low wind-driven evapotranspiration were reconstructed during this time (Quick et al., 2018; Strobel et al., 2019; Wündsche et al., 2018) (Fig. 7d). After 4700 cal BP, the overall trend in increasing moisture availability at the central southern Cape coast is again in line with our findings at Voëlvlei (du Plessis et al., 2020; Quick et al., 2018; Strobel et al., 2019; Wündsche et al., 2018).  $\delta^2\text{H}_{n\text{-alkane}}$  and  $\delta^{13}\text{C}_{n\text{-alkane}}$  from marine sediments recovered off the mouth of the Gouritz River (GeoB18308-2; Fig. 1) show a very similar pattern to Voëlvlei over the past 4000 cal BP (Hahn et al., 2017) (Fig. 7). Those findings thus support our findings from Voëlvlei and suggest a consistent regional picture for the southern Cape coast.

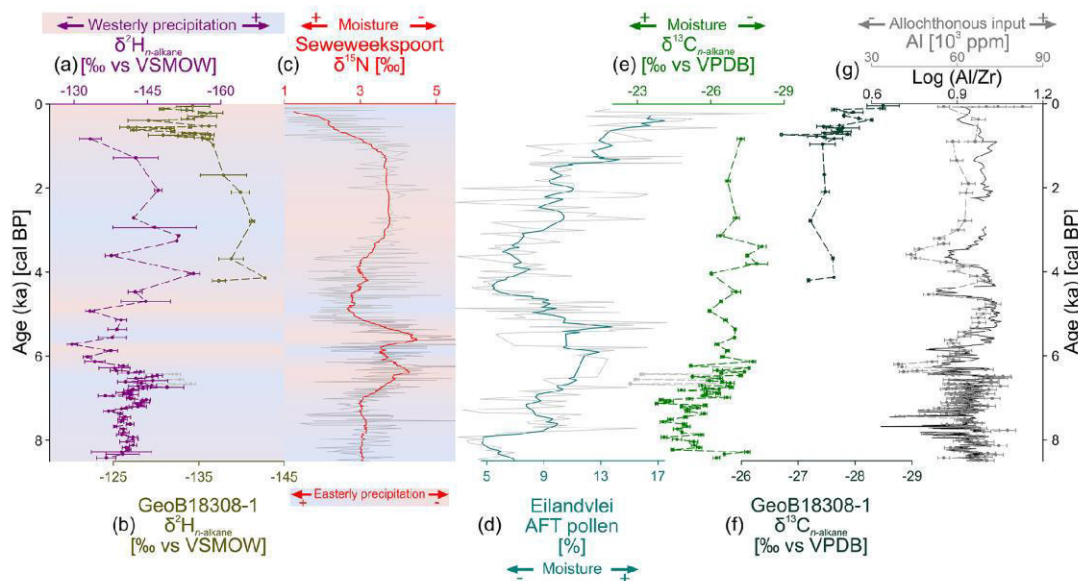


**Figure 7.** (a)  $\delta^2\text{H}_{n\text{-alkane}}$  from Voëlvlei compared to (b)  $\delta^2\text{H}_{n\text{-alkane}}$  from GeoB18308-1 (Hahn et al., 2017), (c)  $\delta^{15}\text{N}$  from Seweweekspoort (Chase et al., 2017), (d) Afrotropical forest pollen (AFT) from Eilandvlei (Quick et al., 2018), (e)  $\delta^{13}\text{C}_{n\text{-alkane}}$  from Voëlvlei, (f)  $\delta^{13}\text{C}_{n\text{-alkane}}$  from GeoB18308-1 (Hahn et al., 2017), and (g) aluminium (Al) content and Log Al/Zr ratio from Voëlvlei. The locations of the studies are depicted in Fig. 1.

At Seweweekspoort, ca. 100 km inland,  $\delta^{15}\text{N}$  values follow the pattern of  $\delta^2\text{H}_{n\text{-alkane}}$  from Voëlvlei, and climate is thought to have been dry from ca. 7000 to ca. 4700 cal BP and ca. 3000 to ca. 1000 cal BP due to reduced easterly-related precipitation (Chase et al., 2017) (Fig. 7c). Intense short-term variations to wetter conditions at Seweweekspoort contradict the aforementioned results from the Wilderness area at ca. 5700 and ca. 4900 cal BP but are well reflected by spikes in the  $\delta^2\text{H}_{n\text{-alkane}}$  record from Voëlvlei which shows shifts towards less negative  $\delta^2\text{H}_{n\text{-alkane}}$  values and increased easterly-related precipitation contributions (Fig. 7a, c).

In this context, previous studies hypothesize that the non-dominant component of the temperate (westerly)/tropical (easterly) dynamic determines hydro-climatic variability in southern Africa (e.g. Chase et al., 2017, 2015). More precisely, this means that although easterly-derived (westerly-derived) precipitation is relatively low in the western (eastern) parts of the YRZ, variability in the overall moisture signal is thought to strongly depend on moisture contribution from this minor component (e.g. Chase et al., 2017, 2015). The  $\delta^2\text{H}_{n\text{-alkane}}$  values of this study imply increased westerly-derived precipitation during drier phases at Seweweekspoort and increased easterly-derived precipitation during moister phases at Seweweekspoort (Fig. 7c), at a time generally characterized by a trend towards moister conditions at Voëlvlei (Fig. 7e). Moist conditions between 7000 and 5500 cal BP were also found in the north-south-trending Cape Fold Mountains in the Western Cape (Chase et

al., 2019, and references therein), indicating an overall moist period for south-western South Africa during this time which is perfectly in line with the increased westerly precipitation contribution at Voëlvlei.

However, an opposite pattern is proposed to exist between sites located inland of the Cape Fold mountains (e.g. Seweweekspoort, Katbakkies Pass) and coastal sites from the southern Cape coast (e.g. Eilandvlei) (Chase and Quick, 2018; Quick et al., 2018). There are still discrepancies due to the comparison of different proxies in these studies compared to those from the southern Cape coast. Comparing our  $\delta^2\text{H}_{n\text{-alkane}}$  record from Voëlvlei, which is representative of fluctuations in the major moisture sources, with the  $\delta^{15}\text{N}$  from Seweweekspoort (Chase et al., 2017), in detail many similarities are apparent, confirming the assumption that hydrological variations at Seweweekspoort are distinctly driven by variations in easterly-derived precipitation. However, on the South Coast of South Africa including Voëlvlei the overall moisture evolution is not restricted to one moisture source and thus driven by a combination of both westerly- and easterly-derived precipitation.

The topmost sediments of Voëlvlei mainly consist of two fluvial flooding events (at  $830^{+110}/_{-110}$  and  $10^{+10}/_{-10}$  cal BP) which deposited large amounts of sediment (ca. 15 and ca. 30 cm, respectively; Figs. 2, 7). Considering the chronological uncertainties (dating and modelling errors), the most recent flooding event can likely be associated with the so called “Laingsburg flood” from January 1981

(Damm and Hagedorn, 2010 and references therein). In marine sediments recovered off the mouth of the Gouritz River (GeoB18308-2; Fig. 1) major flooding events were detected between 650 and 300 cal BP and thus support our findings (Hahn et al., 2017).

## 6 Conclusions

Our multi-proxy record from Voëlvlei provides new insights into the sea level and paleoclimate history of the past 8.5 ka at the southern Cape Coast. Various dating approaches including OSL and  $^{14}\text{C}$  of bulk TOC, organic macrofossils, charcoal and *n*-alkanes were applied to establish a robust chronology. Three temporal eco-zones can be characterized for Voëlvlei. These are related to sea level variations and are in line with results of regional investigations in implying a subtidal marine-brackish followed by an intratidal brackish system from 8440  $^{+200}/_{-250}$  to 6420  $^{+130}/_{-140}$  cal BP, and a freshwater to terrestrial system due to silting up of Voëlvlei thereafter. In terms of climate, the combined biomarker-sedimentological approach allows the additional identification of changing precipitation sources, in combination with an estimation of moisture availability. Dry conditions accompanied by a year-round precipitation contribution prevail from 8440  $^{+200}/_{-250}$  to 7070  $^{+160}/_{-200}$  cal BP followed by moister conditions and more westerly-derived precipitation contributions from 7070  $^{+160}/_{-200}$  to 6420  $^{+130}/_{-140}$  cal BP. This was followed by a distinct shift to an easterly dominance at 6420 cal BP, before an overall trend to a westerly dominance, which lasted until 2060 cal BP. This is followed by a trend towards an easterly dominance, but both phases show several intense short-term variations.

These results are in good agreement with previous studies with regard to sea-level change on the western and southern coast of South Africa. The paleohydrological evolution of Voëlvlei is comparable to previous investigations from the Southern Cape coast during the past 8.5 ka, demonstrating an interplay of both westerly- and easterly-derived precipitation contribution. Hydrological variations at Seweweekspoort, located within the interior of central southern South Africa, a region hypothesized to show distinct hydroclimatic trends (relative to the coastal zones) through the Holocene, show many similarities to the Voëlvlei  $\delta^2\text{H}_{n\text{-alkane}}$  record, suggesting a need to further consider in more detail regional-scale complexities and coastal-inland contrasts in paleoclimatic trajectories. Thus, the Voëlvlei  $\delta^2\text{H}_{n\text{-alkane}}$  record provides valuable insights into the source of precipitation at the Southern Cape coast during the past 8.5 ka.

**Data availability.** All data within the paper will be available at PANGAEA.

**Supplement.** The supplement related to this article is available online at: <https://doi.org/10.5194/cp-17-1567-2021-supplement>.

**Author contributions.** PS, RZ and TH designed the study. PS, MB, ASC, PF, BK, GS, JS and SS carried out the laboratory and analytical analyses. All authors contributed to the writing of the paper and data discussion.

**Competing interests.** The authors declare that they have no conflict of interest.

**Disclaimer.** Publisher's note: Copernicus Publications remains neutral with regard to jurisdictional claims in published maps and institutional affiliations.

**Acknowledgements.** Sediment cores were recovered within the RAiN project funded by the German Federal Ministry of Education and Research (BMBF). Paul Strobel gratefully acknowledges the support by a fellowship from the state of Thuringia (Landesgraduiertenstipendium). Particularly acknowledged are Christopher Berndt, Nico Blaubach, Tobias Eggert, Christian Gregori, Patricia Rauh, Mike Steinich and Magdalena Wagner for assistance in the lab. Gerhard Daut is thanked for supporting the XRD measurements. Nadia du Plessis, Jussi Baade, Sayed Hess, Christian Gregori, Roland Mäusbacher and Michael E. Meadows are thanked for their fieldwork contributions and constructive discussions. The participants of the 2019 course on Paleoenvironmental Analysis at Friedrich Schiller University Jena supported us in micropaleontological sample preparation and picking of microfossils for an initial batch of subsamples.

**Financial support.** This study was funded by the German Research Foundation (DFG) (grant nos. HA 5089/11-1 and ZE 860/6-1).

**Review statement.** This paper was edited by Keely Mills and reviewed by Hayley Cawthra and three anonymous referees.

## References

- Aichner, B., Hilt, S., Périllon, C., Gillefalk, M., and Sachse, D.: Biosynthetic hydrogen isotopic fractionation factors during lipid synthesis in submerged aquatic macrophytes: Effect of groundwater discharge and salinity, *Org. Geochem.*, 113, 10–16, 2017.
- Aitken, M. J.: Thermoluminescence Dating, Academic Press, London, ISBN: 9780120463800, 1985.
- Babel, M. and Schreiber, B. C.: Geochemistry of Evaporites and Evolution of Seawater, in: *Treatise on Geochemistry*, 2nd edn., edited by: Holland, H. D. and Turekian, K. K., Elsevier, Oxford, 483–560, <https://doi.org/10.1016/B978-0-08-095975-7.00718-X>, 2014.

- Barnes, R. S. K.: Little-known and phylogenetically obscure South African estuarine microgastropods (Mollusca: Truncatelloidea) as living animals, *J. Nat. Hist.*, 52, 87–113, 2018.
- Baxter, A. J. and Meadows, M. E.: Evidence for Holocene sea level change at Verlorenvlei, Western Cape, South Africa, *Quatern. Int.*, 56, 65–79, 1999.
- Bell, W. T.: Thermoluminescence dating: radiation dose rate data, *Archaeometry*, 21, 243–245, 1979.
- Benson, R. H. and Maddocks, R. F.: Recent ostracodes of Knysna Estuary, Cape Province, Union of South Africa, *The University of Kansas Palaeontological Contributions*, article no. 5, 1964.
- Birch, G. F., du Plessis, A., and Willis, J. P.: Offshore and onland geological and geophysical investigation in the Wilderness Lakes Region, *Transactions of the Geological Society of South Africa*, 81, 339–352, 1978.
- Blaauw, M. and Christen, J. A.: Flexible Paleoclimate Age-Depth Models Using an Autoregressive Gamma Process, *Bayesian Anal.*, 6, 457–474, 2011.
- Bliedtner, M., von Suchodoletz, H., Schäfer, I., Welte, C., Salazar, G., Szidat, S., Haas, M., Dubois, N., and Zech, R.: Age and origin of leaf wax *n*-alkanes in fluvial sediment–paleosol sequences and implications for paleoenvironmental reconstructions, *Hydrol. Earth Syst. Sci.*, 24, 2105–2120, <https://doi.org/10.5194/hess-24-2105-2020>, 2020.
- Bliedtner, M., Zech, R., Kühn, P., Schneider, B., Zielhofer, C., and von Suchodoletz, H.: The potential of leaf wax biomarkers from fluvial soil-sediment sequences for paleovegetation reconstructions – Upper Alazani River, central southern Greater Caucasus (Georgia), *Quaternary Sci. Rev.*, 196, 62–79, 2018.
- Boom, A., Carr, A. S., Chase, B. M., Grimes, H. L., and Meadows, M. E.: Leaf wax *n*-alkanes and  $\delta^{13}\text{C}$  values of CAM plants from arid southwest Africa, *Org. Geochem.*, 67, 99–102, 2014.
- Bowen, G. J.: The Online Isotopes in Precipitation Calculator, version 3.1, available at: <http://www.waterisotopes.org>, last access: 12 February 2018.
- Bowen, G. J., Wassenaar, L. L., and Hobson, K. A.: Global application of stable hydrogen and oxygen isotopes to wildlife forensics, *Oecologia*, 143, 337–348, 2005.
- Branch, G. M., Griffiths, C. L., Branch, M. L., and Beckley, L. E.: Two oceans: A guide to the marine life of southern Africa, *Struik Nature*, Cape Town, ISBN: 9781770077720, 2010.
- Braun, K., Bar-Matthews, M., Ayalon, A., Zilberman, T., and Matthews, A.: Rainfall isotopic variability at the intersection between winter and summer rainfall regimes in coastal South Africa (Mossel Bay, Western Cape Province), *S. Afr. J. Geol.*, 120, 323–340, 2017.
- Braun, K., Bar-Matthews, M., Matthews, A., Ayalon, A., Zilberman, T., Cowling, R. M., Fisher, E. C., Herries, A. I. R., Brink, J. S., and Marean, C. W.: Comparison of climate and environment on the edge of the Palaeo-Agulhas Plain to the Little Karoo (South Africa) in Marine Isotope Stages 5–3 as indicated by speleothems, *Quaternary Sci. Rev.*, 235, 105803, <https://doi.org/10.1016/j.quascirev.2019.06.025>, 2020.
- Braun, K., Bar-Matthews, M., Matthews, A., Ayalon, A., Cowling, R. M., Karkanas, P., Fisher, E. C., Dyez, K., Zilberman, T., and Marean, C. W.: Late Pleistocene records of speleothem stable isotopic compositions from Pinnacle Point on the South African south coast, *Quaternary Res.*, 91, 265–288, 2018.
- Buggle, B., Wiesenberg, G. L. B., and Glaser, B.: Is there a possibility to correct fossil *n*-alkane data for postsedimentary alteration effects?, *Appl. Geochem.*, 25, 947–957, 2010.
- Burrow, C.: Calc\_MinDose(): Apply the (un-)logged minimum age model (MAM) after Galbraith et al. (1999) to a given De Distribution. Function version 0.4.4, in: *Luminescence: Comprehensive Luminescence Dating Data Analysis*, edited by: Kreutzer, S., Burrow, C., Dietze, M., Fuchs, M. C., Schmidt, C., Fischer, M., and Friedrich, J., R package version 0.9.3, 2019. 2019.
- Carr, A. S., Boom, A., Chase, B. M., Meadows, M. E., and Grimes, H. L.: Holocene sea level and environmental change on the west coast of South Africa: evidence from plant biomarkers, stable isotopes and pollen, *J. Paleolimnol.*, 53, 415–432, 2015.
- Chambers, F. M., Brain, S. A., Mauquoy, D., McCarroll, J., and Daley, T.: The “Little Ice Age” in the Southern Hemisphere in the context of the last 3000 years: Peat-based proxy-climate data from Tierra del Fuego, *Holocene*, 24, 1649–1656, 2014.
- Chase, B. M. and Meadows, M. E.: Late Quaternary dynamics of southern Africa’s winter rainfall zone, *Earth-Sci. Rev.*, 84, 103–138, 2007.
- Chase, B. M. and Quick, L. J.: Influence of Agulhas forcing of Holocene climate change in South Africa’s southern Cape, *Quaternary Res.*, 90, 303–309, 2018.
- Chase, B. M., Lim, S., Chevalier, M., Boom, A., Carr, A. S., Meadows, M. E., and Reimer, P. J.: Influence of tropical easterlies in southern Africa’s winter rainfall zone during the Holocene, *Quaternary Sci. Rev.*, 107, 138–148, 2015.
- Chase, B. M., Chevalier, M., Boom, A., and Carr, A. S.: The dynamic relationship between temperate and tropical circulation systems across South Africa since the last glacial maximum, *Quaternary Sci. Rev.*, 174, 54–62, 2017.
- Chase, B. M., Faith, J. T., Mackay, A., Chevalier, M., Carr, A. S., Boom, A., Lim, S., and Reimer, P. J.: Climatic controls on Later Stone Age human adaptation in Africa’s southern Cape, *J. Hum. Evol.*, 114, 35–44, 2018.
- Chase, B. M., Boom, A., Carr, A. S., Chevalier, M., Quick, L. J., Verboom, G. A., and Reimer, P. J.: Extreme hydroclimate response gradients within the western Cape Floristic region of South Africa since the Last Glacial Maximum, *Quaternary Sci. Rev.*, 219, 297–307, 2019.
- Chase, B. M., Boom, A., Carr, A. S., Quick, L. J., and Reimer, P. J.: High-resolution record of Holocene climate change dynamics from southern Africa’s temperate-tropical boundary, Baviaanskloof, South Africa, *Palaeogeogr. Palaeoclimatol.*, 539, 109518, <https://doi.org/10.1016/j.palaeo.2019.109518>, 2020.
- Compton, J. S.: The mid-Holocene sea-level highstand at Bogenfels Pan on the southwest coast of Namibia, *Quaternary Res.*, 66, 303–310, 2006.
- Cooper, J. A. G., Green, A. N., and Compton, J. S.: Sea-level change in southern Africa since the Last Glacial Maximum, *Quaternary Sci. Rev.*, 201, 303–318, 2018.
- Damm, B. and Hagedorn, J.: Holocene floodplain formation in the southern Cape region, South Africa, *Geomorphology*, 122, 213–222, 2010.
- Diefendorf, A. F. and Freimuth, E. J.: Extracting the most from terrestrial plant-derived *n*-alkyl lipids and their carbon isotopes from the sedimentary record: A review, *Org. Geochem.*, 103, 1–21, 2017.

- Douglas, P. M. J., Pagani, M., Eglinton, T. I., Brenner, M., Hodell, D. A., Curtis, J. H., Ma, K. F., and Breckenridge, A.: Pre-aged plant waxes in tropical lake sediments and their influence on the chronology of molecular paleoclimate proxy records, *Geochim. Cosmochim. Ac.*, 141, 346–364, 2014.
- Douglas, P. M. J., Pagani, M., Eglinton, T. I., Brenner, M., Curtis, J. H., Breckenridge, A., and Johnston, K.: A long-term decrease in the persistence of soil carbon caused by ancient Maya land use, *Nat. Geosci.*, 11, 645–649, 2018.
- du Plessis, N., Chase, B. M., Quick, L. J., Habertzettl, T., Kasper, T., and Meadows, M. E.: Vegetation and climate change during the Medieval Climate Anomaly and the Little Ice Age on the southern Cape coast of South Africa: Pollen evidence from Bo Langvlei, The Holocene, 30, 1716–1727, <https://doi.org/10.1177/0959683620950444>, 2020.
- Duller, G. A. T.: Distinguishing quartz and feldspar in single grain luminescence measurements, *Radiat. Meas.*, 37, 161–165, 2003.
- Duller, G. A. T.: Assessing the error on equivalent dose estimates derived from single aliquot regenerative dose measurements, *Ancient TL*, 25, 15–24, 2007.
- Duller, G. A. T.: Single-grain optical dating of Quaternary sediments: why aliquot size matters in luminescence dating, *Boreas*, 37, 589–612, 2008.
- Eglinton, T. I. and Eglinton, G.: Molecular proxies for paleoclimatology, *Earth Planet. Sc. Lett.*, 275, 1–16, 2008.
- Engelbrecht, C. J. and Engelbrecht, F. A.: Shifts in Koppen-Geiger climate zones over southern Africa in relation to key global temperature goals, *Theor. Appl. Climatol.*, 123, 247–261, 2016.
- Engelbrecht, C. J. and Landman, W. A.: Interannual variability of seasonal rainfall over the Cape south coast of South Africa and synoptic type association, *Clim. Dynam.*, 47, 295–313, 2016.
- Engelbrecht, C. J., Landman, W. A., Engelbrecht, F. A., and Malherbe, J.: A synoptic decomposition of rainfall over the Cape south coast of South Africa, *Clim. Dynam.*, 44, 2589–2607, 2015.
- Engelbrecht, F. A., Landman, W. A., Engelbrecht, C. J., Landman, S., Bopape, M. M., Roux, B., McGregor, J. L., and Thatcher, M.: Multi-scale climate modelling over Southern Africa using a variable-resolution global model, *Water Sa*, 37, 647–658, 2011.
- Feakins, S. J. and Sessions, A. L.: Crassulacean acid metabolism influences D/H ratio of leaf wax in succulent plants, *Org. Geochem.*, 41, 1269–1276, 2010.
- Fey, M.: Soils of South Africa, Cambridge University Press, Cambridge, ISBN 9781107000506, 2010.
- Fick, S. E. and Hijmans, R. J.: WorldClim 2: new 1-km spatial resolution climate surfaces for global land areas, *Int. J. Climatol.*, 37, 4302–4315, 2017.
- Frenzel, P.: Fossils of the southern Baltic Sea as palaeoenvironmental indicators in multi-proxy studies, *Quatern. Int.*, 511, 6–21, 2019.
- Fürstenberg, S., Gründler, N., Meschner, S., and Frenzel, P.: Microfossils in surface sediments of brackish waters on the west coast of South Africa and their palaeoecological implications, *Afr. J. Aquat. Sci.*, 42, 329–339, 2017.
- Galbraith, R. F., Roberts, R. G., Laslett, G. M., H., Y., and Olley, J. M.: Optical dating of single and multiple grains of quartz from Jinnium rock shelter, northern Australia: part I, Experimental design and statistical models, *Archaeometry*, 41, 339–364, 1999.
- Gierga, M., Hajdas, I., van Raden, U. J., Gilli, A., Wacker, L., Sturm, M., Bernasconi, S. M., and Smittenberg, R. H.: Long-stored soil carbon released by prehistoric land use: Evidence from compound-specific radiocarbon analysis on Soppensee lake sediments, *Quaternary Sci. Rev.*, 144, 123–131, 2016.
- Guérin, G., Mercier, N., and Adamiec, G.: Dose-rate conversion factors: update, *Ancient TL*, 29, 5–8, 2011.
- Haas, M., Bliedtner, M., Borodynkin, I., Salazar, G., Szidat, S., Eglinton, T. I., and Zech, R.: Radiocarbon Dating of Leaf Waxes in the Loess-Paleosol Sequence Kurtak, Central Siberia, *Radiocarbon*, 59, 165–176, 2017.
- Haas, M., Kaltenrieder, P., Ladd, S. N., Welte, C., Strasser, M., Eglinton, T. I., and Dubois, N.: Land-use evolution in the catchment of Lake Murten, Switzerland, *Quaternary Sci. Rev.*, 230, 106154, <https://doi.org/10.1016/j.quascirev.2019.106154>, 2020.
- Habertzettl, T., Baade, J., Compton, J., Daut, G., Dupont, L., Finch, J., Frenzel, P., Green, A., Hahn, A., Hebbeln, D., Helmschrot, J., Humphries, M., Kasper, T., Kirsten, K., Mäusbacher, R., Meadows, M., Meschner, S., Quick, L., Schefuß, E., Wüdsch, M., and Zabel, M.: Paleoenvironmental investigations using a combination of terrestrial and marine sediments from South Africa – The RAIN (Regional Archives for Integrated iNvestigations) approach, *Zbl. Geol. Pal.*, Heft 1, 55–73, 2014.
- Habertzettl, T., Kirsten, K. L., Kasper, T., Franz, S., Reinwarth, B., Baade, J., Daut, G., Meadows, M. E., Su, Y., and Mäusbacher, R.: Using <sup>210</sup>Pb-data and paleomagnetic secular variations to date anthropogenic impact on a lake system in the Western Cape, South Africa, *Quat. Geochronol.*, 51, 53–63, 2019.
- Hahn, A., Schefuß, E., Andò, S., Cawthra, H. C., Frenzel, P., Kugel, M., Meschner, S., Mollenhauer, G., and Zabel, M.: Southern Hemisphere anticyclonic circulation drives oceanic and climatic conditions in late Holocene southernmost Africa, *Clim. Past*, 13, 649–665, <https://doi.org/10.5194/cp-13-649-2017>, 2017.
- Hahn, A., Miller, C., Andò, S., Bouimetarhan, I., Cawthra, H. C., Garzanti, E., Green, A. N., Radeff, G., Schefuß, E., and Zabel, M.: The Provenance of Terrigenous Components in Marine Sediments Along the East Coast of Southern Africa, *Geochem. Geophys. Geosy.*, 19, 1946–1962, 2018.
- Harris, C., Burgers, C., Miller, J., and Rawoot, F.: O- and H-isotope record of Cape Town rainfall from 1996 to 2008, and its application to recharge studies of Table Mountain groundwater, South Africa, *S. Afr. J. Geol.*, 113, 33–56, 2010.
- Heaton, T. J., Köhler, P., Butzin, M., Bard, E., Reimer, R. W., Austin, W. E. N., Bronk Ramsey, C., Grootes, P. M., Hughen, K. A., Kromer, B., Reimer, P. J., Adkins, J., Burke, A., Cook, M. S., Olsen, J., and Skinner, L. C.: Marine20 – the marine radiocarbon age calibration curve (0–55,000 cal BP), *Radiocarbon*, 62, 779–820, <https://doi.org/10.1017/RDC.2020.68>, 2020.
- Herrmann, N., Boom, A., Carr, A. S., Chase, B. M., West, A. G., Zabel, M., and Schefuß, E.: Hydrogen isotope fractionation of leaf wax *n*-alkanes in southern African soils, *Org. Geochem.*, 109, 1–13, 2017.
- Hoefs, M. J. L., Rijpstra, W. I. C., and Sinninghe Damsté, J. S.: The influence of oxic degradation on the sedimentary biomarker record I: evidence from Madeira Abyssal Plain turbidites, *Geochim. Cosmochim. Ac.*, 66, 2719–2735, 2002.
- Hogg, A. G., Heaton, T. J., Hua, Q., Palmer, J. G., Turney, C. S. M., Southon, J., Bayliss, A., Blackwell, P. G., Boswijk, G., Bronk Ramsey, C., Pearson, C., Petchey, F., Reimer, P.,

- Reimer, R., and Wacker, L.: SHCal20 Southern Hemisphere calibration, 0–55,000 years cal BP, *Radiocarbon*, 62, 759–778, <https://doi.org/10.1017/RDC.2020.59>, 2020.
- Hou, J., D'Andrea, W. J., MacDonald, D., and Huang, Y.: Evidence for water use efficiency as an important factor in determining the  $\delta D$  values of tree leaf waxes, *Org. Geochem.*, 38, 1251–1255, 2007.
- Jarvis, A., Reuter, H. I., Nelson, A. and Guevara, E.: Hole-filled SRTM for the globe Version 4, CGIARCSI SRTM 90m Database, available at: <http://srtm.csi.cgiar.org> (last access: 8 February 2021), 2008.
- Johnson, M. R., Anhausser, C. R., and Thomas, R. J.: The geology of South Africa, Geological Society of South Africa, Johannesburg/Council for Geoscience, Pretoria, 2006.
- Kirsten, K. L., Fell, J., Frenzel, P., Meschner, S., Kasper, T., Wüdsch, M., Meadows, M., and Haberzettl, T.: The spatial heterogeneity of micro- and meio-organisms and their significance in understanding coastal system dynamics, *Estuar. Coast. Shelf S.*, 213, 98–107, 2018a.
- Kirsten, K. L., Haberzettl, T., Wüdsch, M., Frenzel, P., Meschner, S., Smit, A. J., Quick, L. J., Mäusbacher, R., and Meadows, M. E.: A multiproxy study of the ocean-atmospheric forcing and the impact of sea-level changes on the southern Cape coast, South Africa during the Holocene, *Palaeogeogr. Palaeoclimatol.*, 496, 282–291, 2018b.
- Kirsten, K. L., Kasper, T., Cawthra, H. C., Strobel, P., Quick, L. J., Meadows, M. E., and Haberzettl, T.: Holocene variability in climate and oceanic conditions in the winter rainfall zone of South Africa – inferred from a high resolution diatom record from Verlorenvlei, *J. Quaternary Sci.*, 35, 572–581, 2020.
- Ladd, S. N. and Sachs, J. P.: Inverse relationship between salinity and *n*-alkane  $\delta D$  values in the mangrove *Avicennia marina*, *Org. Geochem.*, 48, 25–36, 2012.
- Marker, M. E. and Miller, D. E.: A mid-Holocene high stand of the sea at Knysna, *S. Afr. J. Sci.*, 89, 100–102, 1993.
- Martens, K., Davies, B. R., Baxter, A. J., and Meadows, M. E.: A contribution to the taxonomy and ecology of the Ostracoda (Crustacea) from Verlorenvlei (Western Cape, South Africa), *Afr. Zool.*, 31, 22–36, 1996.
- Martin, A. R. H.: The stratigraphy and history of Groenvlei, a South African coastal fen, *Aust. J. Bot.*, 7, 142–167, 1959.
- Martin, A. R. H.: Pollen Analysis of Groenvlei Lake Sediments Knysna (South Africa), *Rev. Palaeobot. Palyno.*, 7, 107–144, 1968.
- Meisch, C.: Crustacea: Ostracoda, in: *Süßwasserfauna von Mitteleuropa*, edited by: Schwoerbel, J. and Zwick, P., Spektrum Akademischer Verlag, Heidelberg, Berlin, ISBN: 978-3827410016, 2000.
- Mejdahl, V.: Thermoluminescence dating: Beta-dose attenuation in quartz grains, *Archaeometry*, 21, 61–72, 1979.
- Mucina, L. and Rutherford, M. C.: *The vegetation of South Africa, Lesotho and Swaziland, SANBI*, Pretoria, ISBN: 9781919976211, 2006.
- Murray, A. S. and Wintle, A. G.: Luminescence dating of quartz using an improved single-aliquot regenerative-dose protocol, *Radiat. Meas.*, 32, 57–73, 2000.
- Murray, A. S. and Wintle, A. G.: The single aliquot regenerative dose protocol: potential for improvements in reliability, *Radiat. Meas.*, 37, 377–381, 2003.
- Murray, J. W.: *Ecology and applications of benthic foraminifera*, Cambridge University Press, Cambridge, ISBN: 9780511535529, 2006.
- Ohlendorf, C. and Sturm, M.: A modified method for biogenic silica determination, *J. Paleolimnol.*, 39, 137–142, 2008.
- Olsen, J., Kjær, K. H., Funder, S., Larsen, N. K., and Ludikova, A.: High-Arctic climate conditions for the last 7000 years inferred from multi-proxy analysis of the Bliss Lake record, North Greenland, *J. Quaternary Sci.*, 27, 318–327, 2012.
- Pecharsky, V. K. and Zavalij, P. Y.: *Fundamentals of Powder Diffraction and Structural Characterization of Materials*, Springer, Boston, ISBN: 9780387095783, 2009.
- Poynter, J. G., Farrimond, P., Robinson, N., and Eglinton, G.: Aeolian-Derived Higher Plant Lipids in the Marine Sedimentary Record: Links with Palaeoclimate, in: *Paleoclimatology and Paleometeorology: Modern and Past Patterns of Global Atmospheric Transport*, edited by: Leinen, M. and Sarinthein, M., Springer Netherlands, Dordrecht, 435–462, 1989.
- Preusser, F., Degering, D., Fuchs, M., Hilgers, A., Kadereit, A., Klasek, N., Krubetschek, M., Richter, D., and Spencer, J. Q. G.: Luminescence dating: basics, methods and applications, *E&G Quaternary Sci. J.*, 57, 95–149, <https://doi.org/10.3285/eg.57.1-2.5>, 2008.
- Prescott, J. R. and Hutton, J. T.: Cosmic ray contributions to dose rates for luminescence and ESR dating: Large depths and long-term time variations, *Radiat. Meas.*, 23, 497–500, 1994.
- Quick, L. J., Meadows, M. E., Bateman, M. D., Kirsten, K. L., Mäusbacher, R., Haberzettl, T., and Chase, B. M.: Vegetation and climate dynamics during the last glacial period in the fynbos-afrotropical forest ecotone, southern Cape, South Africa, *Quatern. Int.*, 404, 136–149, 2016.
- Quick, L. J., Chase, B. M., Wüdsch, M., Kirsten, K., Chevalier, M., Mäusbacher, R., Meadows, M., and Haberzettl, T.: A high-resolution record of Holocene climate and vegetation dynamics from the southern Cape coast of South Africa: pollen and microcharcoal evidence from Eilandvlei, *J. Quaternary Sci.*, 33, 487–500, 2018.
- Rautenbach, C., Barnes, M. A., and de Vos, M.: Tidal characteristics of South Africa, *Deep-Sea Res. Pt. I*, 150, 103079, <https://doi.org/10.1016/j.dsr.2019.103079>, 2019.
- Reddering, J. S. V.: Evidence for a middle Holocene transgression, Keurbooms estuary, South Africa, *Palaeoecol. Afr.*, 19, 79–86, 1988.
- Reinwarth, B., Franz, S., Baade, J., Haberzettl, T., Kasper, T., Daut, G., Helmschrot, J., Kirsten, K. L., Quick, L. J., Meadows, M. E., and Mäusbacher, R.: A 700-Year Record on the Effects of Climate and Human Impact on the Southern Cape Coast Inferred from Lake Sediments of Eilandvlei, Wilderness Embayment, South Africa, *Geogr. Ann. A*, 95, 345–360, 2013.
- Ruff, M., Fahrni, S., Gäggeler, H. W., Hajdas, I., Suter, M., Sval, H. A., Szidat, S., and Wacker, L.: On-line Radiocarbon Measurements of Small Samples Using Elemental Analyzer and MICADAS Gas Ion Source, *Radiocarbon*, 52, 1645–1656, 2010.
- Sachse, D., Billault, I., Bowen, G. J., Chikaraishi, Y., Dawson, T. E., Feakins, S. J., Freeman, K. H., Magill, C. R., McInerney, F. A., van der Meer, M. T. J., Polissar, P., Robins, R. J., Sachs, J. P., Schmidt, H. L., Sessions, A. L., White, J. W. C., West, J. B., and Kahmen, A.: Molecular Paleohydrology: Interpreting the Hydrogen-Isotopic Composition of Lipid Biomarkers from Pho-

- tosynthesizing Organisms, *Annu. Rev. Earth Pl. Sc.*, 40, 221–249, 2012.
- Salazar, G., Zhang, Y. L., Agrios, K., and Szidat, S.: Development of a method for fast and automatic radiocarbon measurement of aerosol samples by online coupling of an elemental analyzer with a MICADAS AMS, *Nucl. Instrum. Meth. B*, 361, 163–167, 2015.
- Schmitt-Sinns, J.: *Rezente benthische Foraminiferen im Bereich des Benguelastroms, Südwestafrika Verbreitungsmuster und ihre steuernden Faktoren*, PhD thesis, University of Bonn, Germany 2008.
- Scott, L. and Lee-Thorp, J. A.: Holocene climatic trends and rhythms in southern Africa, in: *Past Climate Variability through Europe and Africa*, edited by: Battarbee, R. W., Gasse, F., and Stickley, C. E., Springer, Dordrecht, ISBN: 978-90-481-6593-3, 2004.
- Sessions, A. L.: Factors controlling the deuterium contents of sedimentary hydrocarbons, *Org. Geochem.*, 96, 43–64, 2016.
- Song, Y. and Müller, G.: Freshwater sediments: Sinks and sources of bromine, *Naturwissenschaften*, 80, 558–560, 1993.
- Strachan, K. L., Hill, T. R., Finch, J. M., Barnett, R. L., and Frenzel, P.: Distribution of Salt-Marsh Foraminifera in Two South African Estuaries and the Application as Sea-Level Indicators, *J. Coastal Res.*, 33, 619–631, 2017.
- Strobel, P., Kasper, T., Frenzel, P., Schitteck, K., Quick, L. J., Meadows, M. E., Mäusbacher, R., and Haberzettl, T.: Late Quaternary palaeoenvironmental change in the year-round rainfall zone of South Africa derived from peat sediments from Vankervelsvlei, *Quaternary Sci. Rev.*, 218, 200–214, 2019.
- Strobel, P., Haberzettl, T., Bliedtner, M., Struck, J., Glaser, B., Zech, M., and Zech, R.: The potential of  $\delta^2\text{H}_{n\text{-alkanes}}$  and  $\delta^{18}\text{O}_{\text{sugar}}$  for paleoclimate reconstruction – A regional calibration study for South Africa, *Sci. Total Environ.*, 716, 137045, <https://doi.org/10.1016/j.scitotenv.2020.137045>, 2020.
- Struck, J., Bliedtner, M., Strobel, P., Schumacher, J., Bazarradnaa, E., and Zech, R.: Leaf wax *n*-alkane patterns and compound-specific  $\delta^{13}\text{C}$  of plants and topsoils from semi-arid and arid Mongolia, *Biogeosciences*, 17, 567–580, <https://doi.org/10.5194/bg-17-567-2020>, 2020.
- Stuiver, M., Reimer, P. J., and Reimer, R. W.: CALIB 8.2 [WWW program], available at: <http://calib.org/>, last access: 20 August 2020.
- Szidat, S., Salazar, G. A., Vogel, E., Battaglia, M., Wacker, L., Synal, H.-A., and Türler, A.: 14C Analysis and Sample Preparation at the New Bern Laboratory for the Analysis of Radiocarbon with AMS (LARA), *Radiocarbon*, 56, 561–566, 2014.
- Talma, A. S. and Vogel, J. C.: Late Quaternary paleotemperatures derived from a speleothem from Congo Caves, Cape Province, South Africa, *Quaternary Res.*, 37, 203–213, 1992.
- Tyson, P. D. and Preston-Whyte, R. A.: *The Weather and Climate of Southern Africa*, Oxford University Press, Cape Town, ISBN: 9780195718065, 2000.
- Ullman, W. J.: The fate and accumulation of bromide during playa salt deposition: An example from Lake Frome, South Australia, *Geochim. Cosmochim. Ac.*, 59, 2175–2186, 1995.
- Walters, W. L. and Griffiths, C. L.: Patterns of distribution, abundance and shell utilization amongst hermit crabs, *Diogenes brevis*, *S. Afr. J. Zool.*, 22, 269–277, 1987.
- Weldon, D. and Reason, C. J. C.: Variability of rainfall characteristics over the South Coast region of South Africa, *Theor. Appl. Climatol.*, 115, 177–185, 2014.
- Weltje, G. J. and Tjallingii, R.: Calibration of XRF core scanners for quantitative geochemical logging of sediment cores: Theory and application, *Earth Planet. Sc. Lett.*, 274, 423–438, 2008.
- Wintle, A. G.: Luminescence dating: laboratory procedures and protocols, *Rad. Meas.*, 27, 769–817, 1997.
- Wintle, A. G. and Murray, A. S.: A review of quartz optically stimulated luminescence characteristics and their relevance in single-aliquot regeneration dating protocols, *Rad. Meas.*, 41, 369–391, 2006.
- Wündsche, M., Haberzettl, T., Kirsten, K. L., Kasper, T., Zabel, M., Dietze, E., Baade, J., Daut, G., Meschner, S., Meadows, M. E., and Mäusbacher, R.: Sea level and climate change at the southern Cape coast, South Africa, during the past 4.2 kyr, *Palaeogeogr. Palaeoclimatol.*, 446, 295–307, 2016a.
- Wündsche, M., Haberzettl, T., Meadows, M. E., Kirsten, K. L., Kasper, T., Baade, J., Daut, G., Stoner, J. S., and Mäusbacher, R.: The impact of changing reservoir effects on the C-14 chronology of a Holocene sediment record from South Africa, *Quat. Geochronol.*, 36, 148–160, 2016b.
- Wündsche, M., Haberzettl, T., Cawthra, H. C., Kirsten, K. L., Quick, L. J., Zabel, M., Frenzel, P., Hahn, A., Baade, J., Daut, G., Kasper, T., Meadows, M. E., and Mäusbacher, R.: Holocene environmental change along the southern Cape coast of South Africa – Insights from the Eilandvlei sediment record spanning the last 8.9 kyr, *Global Planet. Change*, 163, 51–66, 2018.
- Zech, M., Bugge, B., Leiber, K., Marković, S., Glaser, B., Hambach, U., Huwe, B., Stevens, T., Sümegi, P., Wiesenberg, G., and Zöller, L.: Reconstructing Quaternary vegetation history in the Carpathian Basin, SE-Europe, using *n*-alkane biomarkers as molecular fossils: Problems and possible solutions, potential and limitations, *E&G Quaternary Sci. J.*, 58, 148–155, <https://doi.org/10.3285/eg.58.2.03>, 2010.
- Zech, W., Schad, P., and Hintermaier-Erhard, G.: *Böden der Welt: Ein Bildatlas*, EBL-Schweitzer, Berlin; Heidelberg, ISBN: 9783642365744, 2014.

## Chapter 4

---

### **Reconstructing Late Quaternary precipitation and its source on the southern Cape coast of South Africa: A multi-proxy paleoenvironmental record from Vankervelsvlei**

---

Authors: Paul Strobel, Marcel Bliedtner, Andrew S. Carr, Julian Struck, Nadia du Plessis, Bruno Glaser, Michael E. Meadows, Lynne J. Quick, Michael Zech, Roland Zech, Torsten Haberzettl

Submitted to:  
Quaternary Science Reviews



Title:

**Reconstructing Late Quaternary precipitation and its source on the southern Cape coast of South Africa: A multi-proxy paleoenvironmental record from Vankervelsvlei**

Authors:

Strobel, P.\*<sup>1</sup>, Bliedtner, M.<sup>1</sup>, Carr, A. S.<sup>2</sup>, Struck, J.<sup>1</sup>, du Plessis, N.<sup>3,4</sup>, Glaser, B.<sup>5</sup>, Meadows, M.E.<sup>3,6</sup>, Quick, L.J.<sup>4</sup>, Zech, M.<sup>7</sup>, Zech, R.<sup>1</sup>, Haberzettl, T.<sup>8</sup>

\* Corresponding author: Physical Geography, Institute of Geography, Friedrich Schiller University Jena, Loebdergraben 32, 07743 Jena, Germany, paul.strobel@uni-jena.de, +49 (0)3641 9 48807

<sup>1</sup> Physical Geography, Institute of Geography, Friedrich Schiller University Jena, Jena, Germany

<sup>2</sup> School of Geography, Geology and the Environment, University of Leicester, Leicester, UK

<sup>3</sup> Department of Environmental and Geographical Science, University of Cape Town, Rondebosch, South Africa

<sup>4</sup> African Centre for Coastal Palaeoscience, Nelson Mandela University, Port Elizabeth, South Africa

<sup>5</sup> Institute of Agricultural and Nutritional Sciences, Soil Biogeochemistry, Martin-Luther University Halle-Wittenberg, Halle (Saale), Germany

<sup>6</sup> School of Geographic Sciences, East China Normal University, Shanghai, People's Republic of China

<sup>7</sup> Heisenberg Chair of Physical Geography with Focus on Paleoenvironmental Research, Institute of Geography, Technische Universität Dresden, Dresden, Germany

<sup>8</sup> Physical Geography, Institute for Geography and Geology, University of Greifswald, Greifswald, Germany

## Abstract

The Late Quaternary climate history of South Africa and, in particular, potential changes in atmospheric circulation have been subject to considerable debate. To some extent, this is due to a scarcity of natural archives and on the other hand the available indirect hydrological proxies are not suited to distinguishing between precipitation originating from temperate Westerlies and tropical Easterlies. This study presents a paleoenvironmental record from Vankervelsvlei, a wetland located on the southern Cape coast in the year-round rainfall zone of South Africa. A 15 m long sediment record was retrieved from this site and analysed using a multi-proxy approach including, for the first time in this region, analysis of both  $\delta^2\text{H}$  and  $\delta^{18}\text{O}$  isotopes to investigate hydrological changes during the Late Quaternary. Our data suggest the driest conditions of the past ~250 ka likely occurred from MIS 6 to MIS 5e, which still caused sediment deposition at Vankervelsvlei, and MIS 2 showing the absence of sedimentation. Moist conditions occurred from MIS 5e to 5a and during parts of MIS 3 while drier conditions prevailed between MIS 5a and early MIS 3 and at the transition from MIS 3 to MIS 2. Besides changes in the amount and proportional contribution of precipitation contributions from Westerlies during glacial and Easterlies during interglacial periods, relative sea-level change has adjusted the degree of continentality at Vankervelsvlei, which had a distinct impact on the hydrological balance during the Late Quaternary. High-resolution analyses of the Middle- and Late-Holocene parts of the record show moist conditions and increased Easterly/locally-derived summer precipitation contributions from 7,230  $^{+160}_{-210}$  to 4,890  $^{+280}_{-180}$  cal BP and after 2,840  $^{+350}_{-330}$  cal BP. Dry conditions, accompanied by the reduction of Easterly/locally-derived summer rainfall and increased seasonality occurred from 4,890  $^{+280}_{-180}$  to 2,840  $^{+350}_{-330}$  cal BP. Our findings highlight that source and seasonality of precipitation play a major role in the hydrological balance of the southern Cape coastal region. By comparing the Vankervelsvlei record to other regional studies, we infer a coherent trend in the overall moisture evolution along South Africa's southern Cape coast during the Late Quaternary.

*Keywords: paleoclimate; leaf waxes, hemicellulose sugars, compound-specific oxygen, hydrogen and carbon isotopes; relative humidity; coupled  $\delta^2\text{H}_{n\text{-alkane}}-\delta^{18}\text{O}_{\text{sugar}}$  paleohygrometer*

# 1 Introduction

South Africa is a key region for paleoenvironmental reconstructions, because of its location between the temperate and the tropical atmospheric circulation systems, i.e. the temperate Westerlies and the monsoon-driven Easterlies (Chase and Meadows, 2007; Cockcroft et al., 1987; Haberzettl et al., 2014; van Zinderen Bakker, 1976). However, there is a general paucity of Late Quaternary terrestrial paleoenvironmental records, largely due to South Africa's essentially erosive Cenozoic landscape history, which has limited the potential for the accumulation of terrestrial sedimentary deposits (Haberzettl et al., 2014; Quick et al., 2015; van Zinderen Bakker, 1976; Wündsche et al., 2018). Despite this scarcity of terrestrial archives in South Africa, several proxy and model-based paleoenvironmental studies have been carried out during the past decades. Most of those studies use rather discontinuous sediment records, leading to a contrasting picture of the South African moisture evolution during the Late Quaternary, which is further complicated by the use of various rather indirect paleohydrological proxies (e.g. Chase and Meadows, 2007; Chase and Quick, 2018; Cockcroft et al., 1987; Reinwarth et al., 2013; Singarayer and Burrough, 2015; Wündsche et al., 2016; Zhao et al., 2016).

To provide clearer insights into paleohydrological changes, it has been proposed that compound-specific stable isotope analyses of leaf wax-derived long-chain *n*-alkanes ( $> C_{25}$ ) are a proxy with great potential to complement established methodological approaches in sediment archives (e.g. Hahn et al., 2017; Hahn et al., 2021; Miller et al., 2020; Strobel et al., 2021; Strobel et al., 2019). Long-chain *n*-alkanes are produced as leaf waxes in higher terrestrial plants and remain well preserved in soils and sediments over millennia due to their low water solubility and high resistance against degradation (Eglinton and Eglinton, 2008; Sachse et al., 2012; Sessions, 2016). They serve as valuable biomarkers because their hydrogen isotope composition ( $\delta^2H_{n\text{-alkane}}$ ) is driven by the isotopic composition of precipitation ( $\delta^2H_p$ ) (Herrmann et al., 2017; Strobel et al., 2020). However, various fractionation processes occur from the moisture source to its fixation in the leaf waxes, which may bias the precipitation isotope signal and complicate interpretation, with evapotranspirative enrichment being a prominent factor (Sachse et al., 2012; Sessions, 2016; Zech et al., 2015). In the mid-latitudes, the  $\delta^2H_{n\text{-alkane}}$  signal is mainly controlled by the isotopic signal of the moisture source (Schäfer et al., 2018; Strobel et al., 2020; Wirth and Sessions, 2016). However, in existing studies using  $\delta^2H_{n\text{-alkane}}$  in a single water-isotope-approach for paleohydrological reconstruction it is challenging to disentangle precipitation source and amount, and especially the influence of evapotranspirative enrichment (e.g. Hahn et al., 2017; Miller et al., 2020; Strobel et al., 2019). Similarly, single isotope studies using stable oxygen isotopes ( $\delta^{18}O$ ) from speleothems in this region, have also found it challenging to disentangle the effects of temperature and precipitation source (Bar-Matthews et al., 2010; Braun et al., 2019; Braun et al., 2020; Talma

## Chapter 4

and Vogel, 1992).  $\delta^{18}\text{O}_{\text{cellulose}}$  (Heyng et al., 2014; Shi et al., 2019a; Shi et al., 2019b; Sternberg and DeNiro, 1983; Wissel et al., 2008) and  $\delta^{18}\text{O}$  of hemicellulose-derived sugar biomarkers ( $\delta^{18}\text{O}_{\text{sugar}}$ ) (Struck et al., 2020; Tuthorn et al., 2014; Zech and Glaser, 2009; Zech et al., 2014; Zech et al., 2012) may also be used for paleoclimatic and -hydrological research. Similar to leaf waxes, hemicellulose-derived sugars record the isotopic composition of precipitation ( $\delta^{18}\text{O}_p$ ) and are prominently modulated by evaporative enrichment, highlighting the challenges of single-water isotope studies again.

For organic rich sediments there is potential to disentangle some of these effects by measuring more than one water isotope from the same sample. It has been suggested that by coupling  $\delta^2\text{H}_{n\text{-alkane}}$  and  $\delta^{18}\text{O}_{\text{sugar}}$  analyses, it is possible to disentangle changes in  $\delta^2\text{H}_p$  and  $\delta^{18}\text{O}_p$  and changes in evapotranspirative leaf and lake water enrichment. For instance, Voelker et al. (2014) used  $\delta^2\text{H}$  and  $\delta^{18}\text{O}$  of tree-ring cellulose to reconstruct relative air humidity. Another approach to reconstruct air humidity is based on coupling  $\delta^2\text{H}_{n\text{-alkane}}$  and  $\delta^{18}\text{O}_{\text{sugar}}$  results ('paleohygrometer') and was validated in a climate chamber experiment (Hepp et al., 2021) as well as on topsoils from Europe (Hepp et al., 2020), South America (Tuthorn et al., 2015), Ethiopia (Lemma et al., 2021) and South Africa (Strobel et al., 2020). Both approaches have already been applied successfully for paleoclimate reconstructions, for example in loess–paleosol sequences (Hepp et al., 2017; Zech et al., 2013), on subfossil wood (Voelker et al., 2015) and in lacustrine sediments (Hepp et al., 2015; Hepp et al., 2019).

Given the demonstrated complexities of reconstructing paleoclimate and -hydrology on the southern Cape coast, the potential advantages of this coupled isotope approach are readily apparent. Here we applied this coupled approach to a sediment record from Vankervelsvlei, a fen located at South Africa's southern Cape coast spanning large parts of the Late Quaternary (Irving, 1998; Irving and Meadows, 1997; Quick et al., 2016). In contrast to other near coastal wetlands in the Wilderness region, Vankervelsvlei has not been influenced by sea water intrusions in the past. Our study aims to support, refine and expand the previously published study by Strobel et al. (2019), which investigated parts of the here presented composite record, in higher temporal-resolution and with new proxies. Using this combined multi-isotope approach that incorporates both water isotopes, i.e. compound-specific  $\delta^2\text{H}_{n\text{-alkane}}$  and  $\delta^{18}\text{O}_{\text{sugar}}$ , as well as compound-specific  $\delta^{13}\text{C}_{n\text{-alkane}}$  together with established assemblages of inorganic and organic elemental analyses this paper aims to:

- i) infer past variations in precipitation source and moisture availability at Vankervelsvlei, and to consider the potential regional paleoclimatic scenarios that may have driven such variability and
- ii) provide a high-resolution terrestrial record for the Middle- and Late-Holocene to disentangle changes in local precipitation source, moisture availability and relative humidity by coupling of  $\delta^2\text{H}_{n\text{-alkane}}$  and  $\delta^{18}\text{O}_{\text{sugar}}$ .

## 2 Site description

Vankervelsvlei is situated at an elevation of 152 m above present sea level (a.s.l.) about 5 km inland of the Indian Ocean coast at South Africa's southern Cape (Fig. 1). Vankervelsvlei is an irregular shaped depression enclosed by stabilised and cemented dunes, which are approximately 250 to 205 ka old (Bateman et al., 2011; Illenberger, 1996), separating Vankervelsvlei from the present coast (Fig. 1D). These Middle to Late Pleistocene dune systems and landwards even older coversand deposits are unconformably underlain by Quartzites of the Table Mountain Group (Cape Supergroup) and Palaeozoic (Ordovician-Silurian) Peninsula Formation sandstones (Carr et al., 2010; Johnson et al., 2006). Shallow and nutrient-poor generally acidic and leached soils predominate the region (e.g., Alisols and Luvisols) (Geldenhuys, 1988; Irving and Meadows, 1997). The potential natural vegetation consists of variations of Fynbos and Afromontane forest (Mucina and Rutherford, 2006). Today, the steep slopes of the catchment are used as a commercial pine (*Pinus*) plantation and the vegetation growing on the fen predominantly consists of Cyperaceae with some ferns (Pteridophytes) and mosses (Bryophytes) (Quick et al., 2016). The fen itself has an area of 0.34 km<sup>2</sup> and the catchment comprises an area of 4.1 km<sup>2</sup> (Fig. 1D). The morphology of the catchment ranges from 330 to 152 m a.s.l. (Database: SRTM 1 arc-second (NASA JPL, 2013)) with no permanent surface inflow and no surface outlet (Fig. 1D).

The past and present climate of southern Africa is driven by variable interactions of oceanic (the Benguela current on the west coast and the Agulhas current along the east and south coasts) and atmospheric circulation systems (Tyson and Preston-Whyte, 2000) (Fig. 1 B). Today, three major rainfall seasonality zones occur in South Africa. In the eastern and central parts of the country, the majority of the rainfall is associated with tropical moisture-bearing atmospheric circulation systems (Easterlies) during the austral summer (summer rainfall zone, SRZ). A narrow belt along the west coast is dominated by precipitation supplied by temperate Westerlies during the austral winter (winter rainfall zone, WRZ) (Fig. 1 B). The year-round rainfall zone (YRZ) represents the intermediate area between the SRZ and WRZ and receives rainfall from both systems throughout the year (Fig. 1 B) (Engelbrecht et al., 2015; Scott and Lee-Thorp, 2004), which includes the relatively humid southern Cape coast where Vankervelsvlei is located.

Besides the Atlantic and Indian Ocean as major sources of precipitation (Westerlies (austral winter) and Easterlies (austral summer)), on the southern Cape coast, ridging anticyclones produce onshore flow that leads to orographic rainfall from local sources (Engelbrecht and Landman, 2016; Weldon and Reason, 2014). The analyses of recent precipitation data from George Airport, located ca. 50 km west of Vankervelsvlei (Fig. 1C), reveals a mean annual precipitation of 690 mm·a<sup>-1</sup> (1981-2020) (DWD Climate Data Center,

2020) for the coastal areas of the YRZ, but highly variable precipitation during recent years without significant seasonality (Fig. 1C, E).

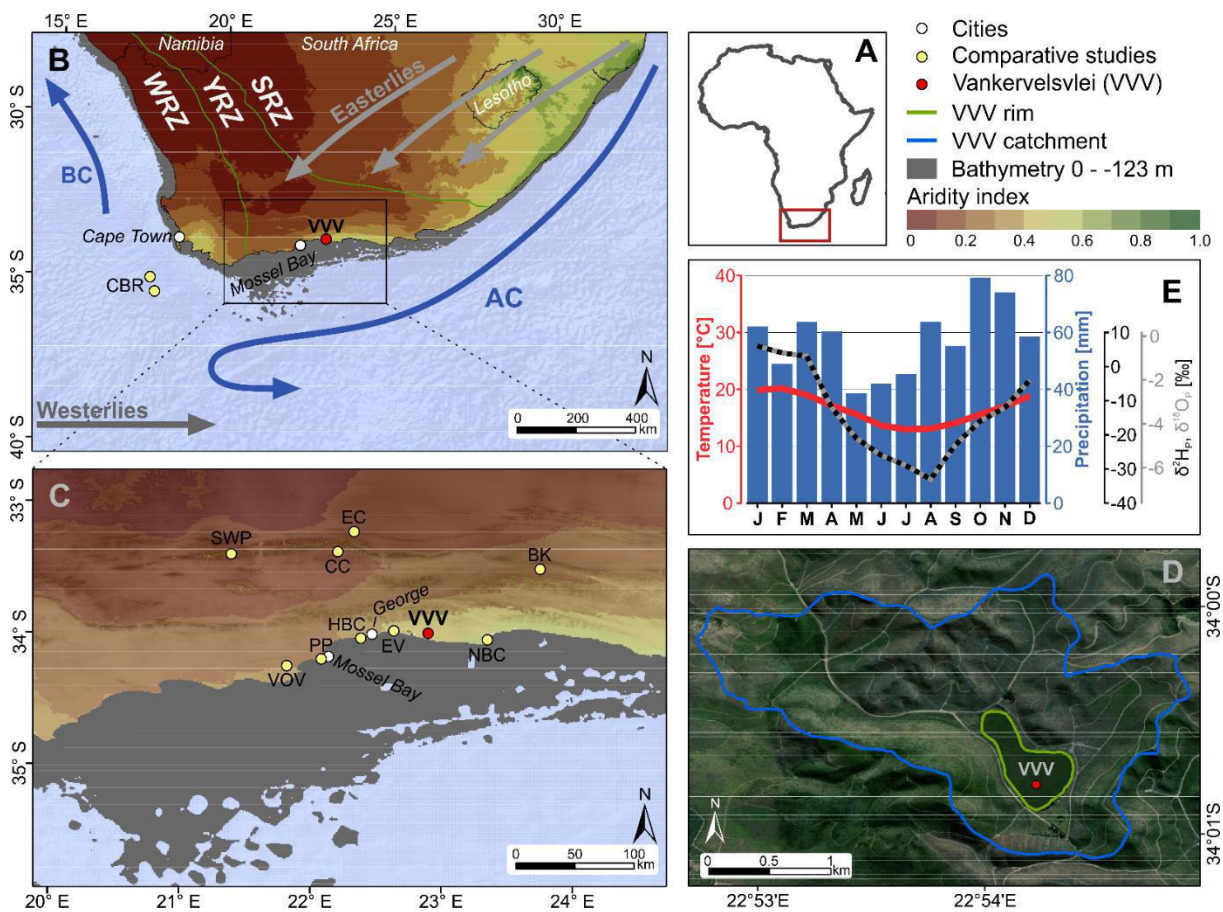


**Figure 1:** **A)** Simplified map of Africa. The red box is magnified in **B)** **B)** Location of Vankervelsvlei (red dot, labelled VVV) and the three major rainfall zones of South Africa, i.e. winter-rainfall zone (WRZ), year-round rainfall zone (YRZ) and summer rainfall zone (SRZ) after Chase and Meadows (2007) derived from Worldclim 2 dataset (Fick and Hijmans, 2017). Additionally, the circumpolar Westerlies, the tropical Easterlies, the Agulhas Current (AC), the Benguela Current (BC) and the Aridity Index (brown to green colour, Trabucco and Zomer, 2019) are depicted. The grey area shows the part of the shelf that was exposed during the sea level low stand of  $-123$  m (BODC, 2014; Waelbroeck et al., 2002). The yellow dots show the location of the Cape Basin Record (CBR; Peeters et al., 2004). **C)** Vankervelsvlei and selected studies mentioned in the text (yellow dots: Voëlvlei (VOV, Strobel et al., 2020) Pinnacle Point (PP, Bar-Matthews et al., 2010; Braun et al., 2019), Herolds Bay Cave (HBC, Braun et al., 2020), Eilandvlei (EV, Quick et al., 2018, Wündsche et al., 2018), Nelson Bay Cave (NBC, Cohen and Tyson, 1995), Baviaanskloof (BK, Chase et al., 2020), Efflux Cave (EC, Braun et al., 2020), Cango Cave (CC, Talma and Vogel, 1992), Seweweekspoort (SWP, Chase et al., 2017)). **D)** Topographic map (ESRI Inc., 2020) including catchment and rim of Vankervelsvlei as well as the coring position. **E)** Climate diagram illustrating the seasonal variability of precipitation and temperature (1981–2020; Station: George Airport (DWD Climate Data Center, 2020)) as well as the variability of  $\delta^2\text{H}_p$  and  $\delta^{18}\text{O}_p$  (Bowen, 2020; Bowen and Revenaugh, 2003) at Vankervelsvlei.

Although the annual precipitation distribution is quite uniform,  $\delta^2\text{H}_p$  and  $\delta^{18}\text{O}_p$  are highly variable throughout the year (Braun et al., 2017; Harris et al., 2010). The modelled isotopic composition of precipitation ( $\delta^2\text{H}_p$ ,  $\delta^{18}\text{O}_p$ ) is  $^2\text{H}$ - and  $^{18}\text{O}$ -depleted during winter ( $-26$  to  $-33\text{‰}$  and  $-5.5$  to  $-6.5\text{‰}$  for  $\delta^2\text{H}_p$  and  $\delta^{18}\text{O}_p$ , respectively), and  $^2\text{H}$ - and  $^{18}\text{O}$ -enriched during summer

periods ( $-4$  to  $+6\text{‰}$  and  $-2.0$  to  $-0.8$  for  $\delta^2\text{H}_p$  and  $\delta^{18}\text{O}_p$ , respectively) (Table 1) (Bowen, 2020; Bowen et al., 2005), which are in good agreement with recently observed data (Braun et al., 2017; Harris et al., 2010). Temperatures are generally uniform with an annual mean of  $16.5\text{ °C}$  (1989-2020) (DWD Climate Data Center, 2020). South-westerly winds predominate in the region and mountain wind conditions, especially in the winter months, can periodically result in anomalously high temperatures in the area (Quick et al., 2016).

*Table 1: Modelled hydrogen and oxygen isotopic composition of the contemporary precipitation at Vankervelsvlei (Lat:  $34.013^\circ\text{ S}$ ; Lon:  $22.904^\circ\text{ E}$ ; Elevation:  $152\text{ m}$ ) (Bowen, 2020; Bowen et al., 2005).*

	Jan	Feb	Mar	Apr	May	Jun	Jul	Aug	Sep	Oct	Nov	Dec
$\delta^2\text{H}_p$ [‰ vs. V-SMOW]	6	4	3	-12	-21	-26	-29	-33	-23	-16	-12	-4
$\delta^{18}\text{O}_p$ [‰ vs. V-SMOW]	-0.8	-0.8	-1.6	-3.7	-4.8	-5.5	-5.7	-6.5	-4.9	-3.9	-3.3	-2.0

### 3 Material and methods

#### 3.1 Composite sediment record compilation

For this study, four parallel piston cores (UWITEC, Mondsee, Austria) (VVV16-4, 0-0.8 m depth; VVV16-1, 0.8 to 13.0 m depth including core loss between 2 and 3.9 m depth; VVV16-2, 9.8-13.8 m depth, VVV16-6; 4 to 15.0 m depth; inner diameter 90 mm) were retrieved from Vankervelsvlei ( $34.013^\circ\text{ S}$ ;  $22.904^\circ\text{ E}$ ) (Fig. 1 C). The topmost sediments were recovered using a push core (VVV16-4; 0 to 0.8 m depth; inner diameter 90 mm). Together these four drives equated to a composite sediment core depth of 15 m with a gap from 3.9 to 2 m composite depth due to core loss (Fig. 3).

#### 3.2 Chronology

##### 3.2.1 Radiocarbon dating

$^{14}\text{C}$  ages were determined on seven organic plant-macro particles and nine bulk TOC samples at the Poznan Radiocarbon Laboratory, Poland. Besides three ages at the top of the sequence, which were recently published by du Plessis et al. (2021),  $^{14}\text{C}$  ages of organic macro particles and bulk TOC were published by Strobel et al. (2019) (see Supplementary Information; Table S1).

##### 3.2.2 Optically Stimulated Luminescence dating (OSL)

For OSL dating, short sections of core tubes ( $\sim 20\text{ cm}$ ) were opened under subdued red light at the University of Leicester. From these samples,  $\sim 5\text{ cm}$  subsamples were used for analyses

## Chapter 4

of coarse grained quartz, except for the lowermost two samples where the feldspar fraction was used for age determination (see Supplementary Information for more details on the OSL dating methods).

### 3.2.3 Age-depth modelling

For age-depth modelling in the lower part of the record (15.0 to 11.18 m composite depth) only the obtained OSL ages were used. For the upper part of the sediment sequence,  $^{14}\text{C}$  ages on organic plant-macro particles and bulk organic matter published by Strobel et al. (2019) and du Plessis et al. (2021) were recalibrated with the SHCal20 calibration curve (Hogg et al., 2020). All calibrations were done with the online version of the Calib 8.2 software (Stuiver et al., 2020). The final age-depth profile relation was modelled with the R software package Bacon 2.4.3 (Blaauw and Christen, 2011), using the same calibration data set. In the following, ages are reported as median ages including the upper and lower limit of the 95% confidence interval.

### 3.3 Physical properties and elemental analyses

Sample aliquots were freeze-dried ( $-50\text{ }^{\circ}\text{C}$ ,  $<72\text{ h}$ ), and aluminium (Al) and iron (Fe) contents were measured with an ICP-OES 725-ES (VARIAN, California, USA). 0.2 g of the samples were processed using a microwave-assisted modified aqua regia digestion of 2 ml HCl (32%) and 4 ml  $\text{HNO}_3$  (65%). Error estimates are based on triple measurements of five individual samples (relative errors: Al  $<5.6\%$ ; Fe:  $<5.1\%$ ). Samples of the reference material LGC6 187 (river sediment) were measured as well to calculate the relative analytical error which was  $<0.79\%$  and  $<0.49\%$  for Al and Fe, respectively.

X-ray fluorescence (XRF) data were obtained using an ITRAX XRF-core scanner (Croudace et al., 2006) at GEOPOLAR (University of Bremen). Scanning was done with a Mo-tube with a step size of 1 cm and a count time of 30 s per step; tube settings were kept constant for all cores using a voltage of 30 kV and a current of 30 mA. Element intensities were given as counts (cts), which were subsequently normalised by the total number of counts to minimize a bias resulting from matrix changes and tube aging.

### 3.4 Leaf wax analyses

Total lipids of the sediment samples (0.3 to 38.3 g) were extracted with 40 ml dichloromethane (DCM) and methanol (MeOH) (9/1, v/v) using an ultrasonic bath over three 15 min cycles. The total lipid extract was separated by solid phase extraction using aminopropyl silica gel (Supelco,  $45\text{ }\mu\text{m}$ ) as stationary phase. The *n*-alkanes were eluted with 4 ml hexane and further purified over coupled silvernitrate ( $\text{AgNO}_3$ -; Supelco, 60-200 mesh) - zeolite (Geokleen) pipette columns. The *n*-alkanes trapped in the zeolite were subsequently dissolved in hydrofluoric acid and recovered by liquid-liquid extraction using *n*-hexane. An Agilent 7890 gas chromatograph



equipped with an Agilent HP5MS column (30 m, 320  $\mu\text{m}$ , 0.25  $\mu\text{m}$  film thickness) and a flame ionization detector (GC-FID) was used for identification and quantification of the *n*-alkanes, relative to external *n*-alkane standards (*n*-alkane mix *n*-C<sub>21</sub> - *n*-C<sub>40</sub>, Supelco).

Compound-specific stable hydrogen isotope analyses of the C<sub>29</sub> and C<sub>31</sub> *n*-alkanes were carried out on an IsoPrime vision IRMS, coupled to an Agilent 7890A GC via a GC5 pyrolysis or combustion interface operating in pyrolysis modus with a MaxChrome and silver wool packed reactor at 1050 °C. Samples were injected splitless with a split–splitless injector. The GC was equipped with a 30 m fused silica column (HP5-MS, 0.32 mm, 0.25  $\mu\text{m}$ ). Each sample was analysed in triplicate, except 13 samples in the lower part of the sequence due to insufficient compound abundance.  $\delta^2\text{H}_{n\text{-alkane}}$  was measured against calibrated H<sub>2</sub> reference gas and all values are reported in per mille against VSMOW. The precision was checked by co-analysing a standard alkane mixture (*n*-C<sub>27</sub>, *n*-C<sub>29</sub>, *n*-C<sub>33</sub>) with known isotope composition (Arndt Schimmelmann, University of Indiana), injected in duplicate every nine runs. All measurements were corrected for drift and amount dependency, relative to the standard values in each sequence. Triplicates for the C<sub>29</sub> and C<sub>31</sub> alkanes in the upper part and lower part of the sequence had a standard deviation of <3.7‰ and <8.0‰, respectively, except for two samples in the upper part (VVV16\_618 and VVV16\_648 with 11‰ and 16‰, respectively). The analytical error for the standards was <1.5 and <3.2‰ for the upper and lower part of the sequence (*n* = 44 and 40). The H<sub>3</sub><sup>+</sup> factor was checked every two days and stayed stable at 3.9±0.1 during measurements.

Compound-specific stable carbon isotope analyses of C<sub>29</sub> and C<sub>31</sub> *n*-alkanes were carried out on an IsoPrime vision IRMS, coupled to an Agilent 7890A GC via a GC5 pyrolysis or combustion interface operating in combustion modus with a CuO packed reactor at 850 °C. Samples were injected splitless with a split–splitless injector. The GC was equipped with 30 m fused silica column (HP5-MS, 0.32 mm, 0.25  $\mu\text{m}$ ).  $\delta^{13}\text{C}$  values were calibrated against CO<sub>2</sub> reference gas of known isotopic composition and all carbon isotope values are given in per mille against VPDB. Triplicate injections were conducted for each sample and measurement accuracy was controlled in the same way as for the  $\delta^2\text{H}$  analyses. Triplicates for the C<sub>29</sub> and C<sub>31</sub> alkanes had a standard deviation of <0.3‰, the analytical error for the standards was <0.2‰ (*n* = 38).

### 3.5 Sugar biomarker analyses

Hemicellulose-derived sugars were hydrolytically extracted from 28 dried samples (0.1 to 1.9 g, depending on TOC content) at the Institute of Agricultural and Nutritional Sciences, Soil Biogeochemistry, Martin Luther University Halle-Wittenberg. Samples were extracted with 10 ml of 4 M trifluoroacetic acid at 105 °C for 4 h, as described in Amelung et al. (1996). Thereafter, samples were vacuum-filtered over glass fibre filters and the extracted sugars were

cleaned according to Zech and Glaser (2009) using XAD-7 and Dowex 50WX8 columns to remove humic-like substances and cations. The purified sugar samples were rotary evaporated and derivatised with methylboronic acid (4 mg in 400  $\mu$ l pyridine) at 60 °C for 1 h. 5 $\alpha$ -Androstane and 3-O-Methyl-Glucose were used as internal standards.

The compound-specific oxygen isotope measurements were performed on a Trace GC 2000 coupled to a Delta V Advantage IRMS using an  $^{18}\text{O}$ -pyrolysis reactor (GC IsoLink) and a ConFlo IV interface (all devices from Thermo Fisher Scientific, Bremen, Germany). Samples were injected in splitless mode and measured in triplicates. For measurement precision, standard blocks of derivatised sugars (arabinose, fucose, xylose) at various concentrations and known  $\delta^{18}\text{O}$  values were measured. Arabinose and Fucose were less abundant compared to Xylose and therefore not considered for compound-specific oxygen isotope analyses. All measurements were corrected for drift and amount dependency, as well as for hydrolytically introduced oxygen atoms which form carbonyl groups within the sugar molecules (Zech and Glaser, 2009). The standard deviation of the sugar sample triplicate measurements for the upper and lower part of the sequence were <2.0‰ and <3.1‰, respectively. Standard duplicate measurements had a standard deviation of <2.6‰ ( $n = 11$ ). The oxygen isotopic composition is given in the delta notation ( $\delta^{18}\text{O}$ ) in per mille versus VSMOW.

### 3.6 Coupling compound-specific leaf wax $\delta^2\text{H}$ and sugar $\delta^{18}\text{O}$

The coupled  $\delta^2\text{H}_{n\text{-alkane}}-\delta^{18}\text{O}_{\text{sugar}}$  approach (paleohygrometer) was previously described in detail by e.g. Hepp et al. (2015), Hepp et al. (2017), Hepp et al. (2019), Hepp et al. (2020), Hepp et al. (2021), Lemma et al. (2021) and Tuthorn et al. (2015). The fundamental assumption of the approach is that the isotopic composition of leaf water can be reconstructed by applying biosynthetic fractionation factors ( $\epsilon_{\text{bio}}$ ) on the measured  $\delta^2\text{H}_{n\text{-alkane}}$  and  $\delta^{18}\text{O}_{\text{sugar}}$  values. For  $\delta^2\text{H}_{n\text{-alkane}}$  a constant  $\epsilon_{\text{bio}}$  value of about -160‰ (Sachse et al., 2012; Sessions et al., 1999) is applied; for  $\delta^{18}\text{O}_{\text{sugar}}$  the  $\epsilon_{\text{bio}}$  value is assumed to be +27‰ (Cernusak et al., 2003; Gessler et al., 2009; Hepp et al., 2021; Schmidt et al., 2001; Sternberg et al., 1986; Yakir and DeNiro, 1990). This can be illustrated in a  $\delta^2\text{H}-\delta^{18}\text{O}$  diagram where the distance of the reconstructed leaf water to the global meteoric water line (GMWL) is defined as deuterium-excess (Dansgaard, 1964) (Fig. 2).

The concept is furthermore based on the fact that the isotopic composition of precipitation plots typically close to the GMWL ( $\delta^2\text{H}_p=8\cdot^{18}\text{O}_p+10$ ; Dansgaard, 1964). However, on the central southern Cape coast of South Africa, a local meteoric water line (LMWL) slightly deviating from the GMWL was described by Braun et al. (2017) ( $\delta^2\text{H}=7.70\cdot\delta^{18}\text{O}+12.10$ ). This LMWL was used for our calculations. We calculated equilibrium fractionation factors according to Horita and Wesolowski (1994) based on modern MAT, i.e. 16.4 °C (DWD Climate Data Center, 2020), resulting in 82.1‰ for  $^2\text{H}$  and 10.0‰ for  $^{18}\text{O}$ . The kinetic fractionation factor for

$^2\text{H}$  and  $^{18}\text{O}$  is set to 25.1‰ and 28.5‰, respectively (Merlivat, 1978). This yields a specific slope for a local evaporation line (LEL) of 2.78. The intercept of the LEL and the LMWL is the isotopic composition of reconstructed plant-source water ( $\delta^2\text{H}$  and  $\delta^{18}\text{O}$ ) (Fig. 2). The difference between deuterium-excess of the reconstructed leaf water and reconstructed plant-source water is then used to estimate the relative humidity (RH) for each sample (Fig. 2).

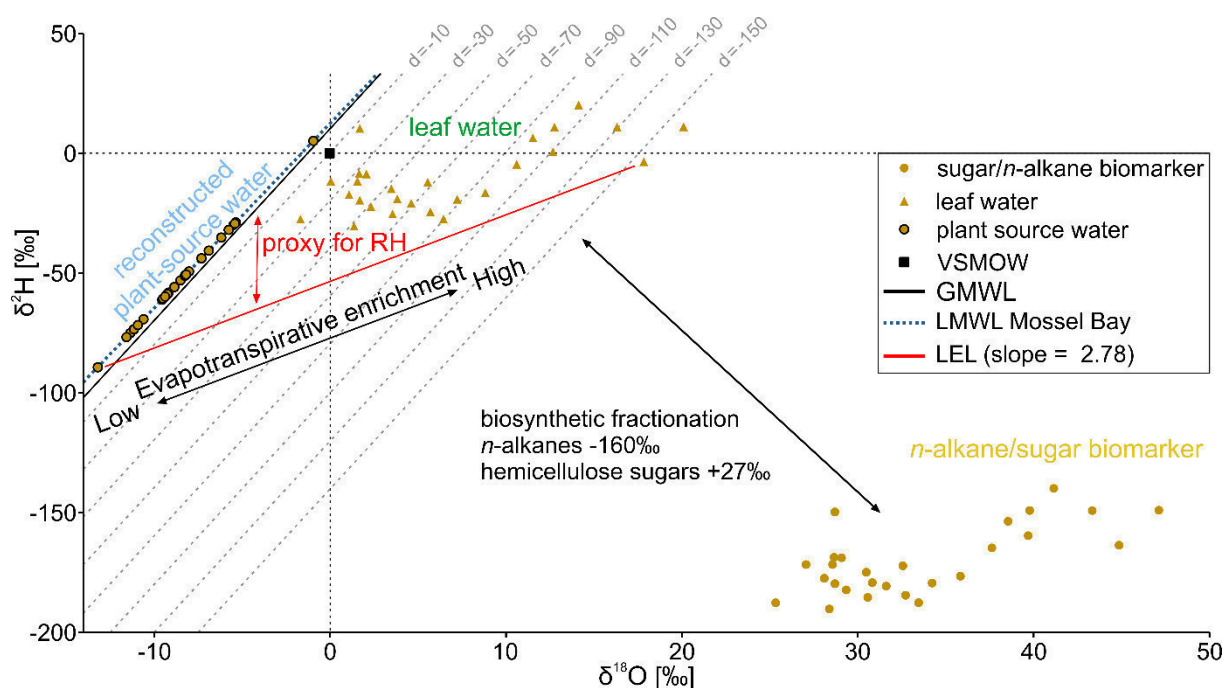


Figure 2: Coupled  $\delta^2\text{H}_{n\text{-alkane}}-\delta^{18}\text{O}_{\text{sugar}}$  approach (paleohygrometer) displayed as  $\delta^2\text{H}-\delta^{18}\text{O}$  diagram showing the  $\delta^2\text{H}$  of  $n$ -alkanes (weighted mean of  $\text{C}_{29}$  and  $\text{C}_{31}$ ) and  $\delta^{18}\text{O}$  of sugar (xylose) biomarkers, the reconstructed leaf and plant-source water, the global meteoric water line (GMWL, black line), and the local meteoric water line (LMWL) from Mossel Bay (blue dashed line; Braun et al., 2017). The black double arrows indicates natural processes of evapotranspirative enrichment of leaf water along local evaporation lines (red line) and biosynthetic fractionation during biomarker synthesis, respectively. Grey dashed lines indicate the deuterium-excess, which can be used as proxy for relative humidity (red double arrow).

## 4 Results

### 4.1 Lithology and Chronology

The composite sediment record from Vankervelsvlei, consists of five lithological units derived from distinct changes in sediment color and physical properties (Fig. 3). Unit A from 15.0 to 13.0 m composite depth consists nearly exclusively of sand (89 to 90%) and low organic content (TOC: 0.05 to 3.3%) (Supplementary Information; Figs. S2 and S3). We observed that humic-rich water penetrated into the core section from 14.8 to 14.0 m composite depth between coring drives and those sediments were therefore excluded for biogeochemical analyses. However, the bottom of Unit A (15.0-14.8 m composite depth) was considered to be suitable for optical methods, i.e. OSL dating. The remaining parts of Unit A, i.e. 15.0 to 14.8 m composite depth and 14.0 to 13.0 m composite depth, have a yellowish colour and two

## Chapter 4

brownish layers within a sandy matrix at 14.0 and 13.3 m composite depths are notable (Fig. 3). Unit B from 13.0 to 11.18 m composite depth has a dark brown, dark grey and/or blackish colour and consists of very fine material (clay: 7-21%, silt: 61 to 90%) and higher organic contents than Unit A (1.3-7.1%). A ~1 cm thick black layer marks the transition from Unit B to C at 11.18 m composite depth. This has been found in all sediment cores hitherto recovered from Vankervelsvlei, including earlier studies (e.g. Quick et al., 2016), and allows parallelisation of the sediment cores. Unit C and the transition to Unit D contains gravel-sized yellowish and reddish aggregates in a fine matrix. The transition zone to Unit D itself (10.32 to 9.68 m composite depth) is composed of dark brown, almost completely degraded, organic-rich material with some yellowish aggregates. Unit C and the transition to Unit D likely consist of reworked (soil) material (Strobel et al., 2019) and thus were both excluded from paleoenvironmental reconstruction. Unit D from 9.68 to 0.8 m composite depth consists of dark brown, reddish to black peat material (TOC: 48-54%). In the lower parts of Unit D, several reddish organic macro remains are present. Sediments are missing between 3.9 and 2.0 m depth, due to core loss during recovery. Sediments from Unit E from 0.8 to 0 m composite depth consist of well-preserved organic material (TOC: 45-46%) including roots and macro remains and are of yellowish to reddish colour (Fig. 3).

The chronology of the lower part of the sediment sequence (Units A and B; 15.0 to 11.18 m composite depth) shows stratigraphically consistent OSL ages and provides a basal age of  $256\pm 19$  ka (Fig. 3). Between Unit B and C (i.e. at 11.18 m composite depth), a sedimentary hiatus was inferred by Strobel et al. (2019), which is confirmed with the new investigations in this study (see section 5.1 for discussion). In the upper part of the sediment sequence, the uncertainties of an OSL age at the bottom of Unit D (i.e.  $8.0\pm 0.5$  ka in 10.15 to 9.95 m composite depth), which is not included in age-depth-modelling, overlaps with the  $^{14}\text{C}$ -based chronology in this part of the sediment sequence (Fig. 3).  $^{14}\text{C}$  ages of bulk TOC and organic macro particles in Units D and E are stratigraphically consistent and indicate higher sedimentation rates compared to the Units below (Fig. 3).

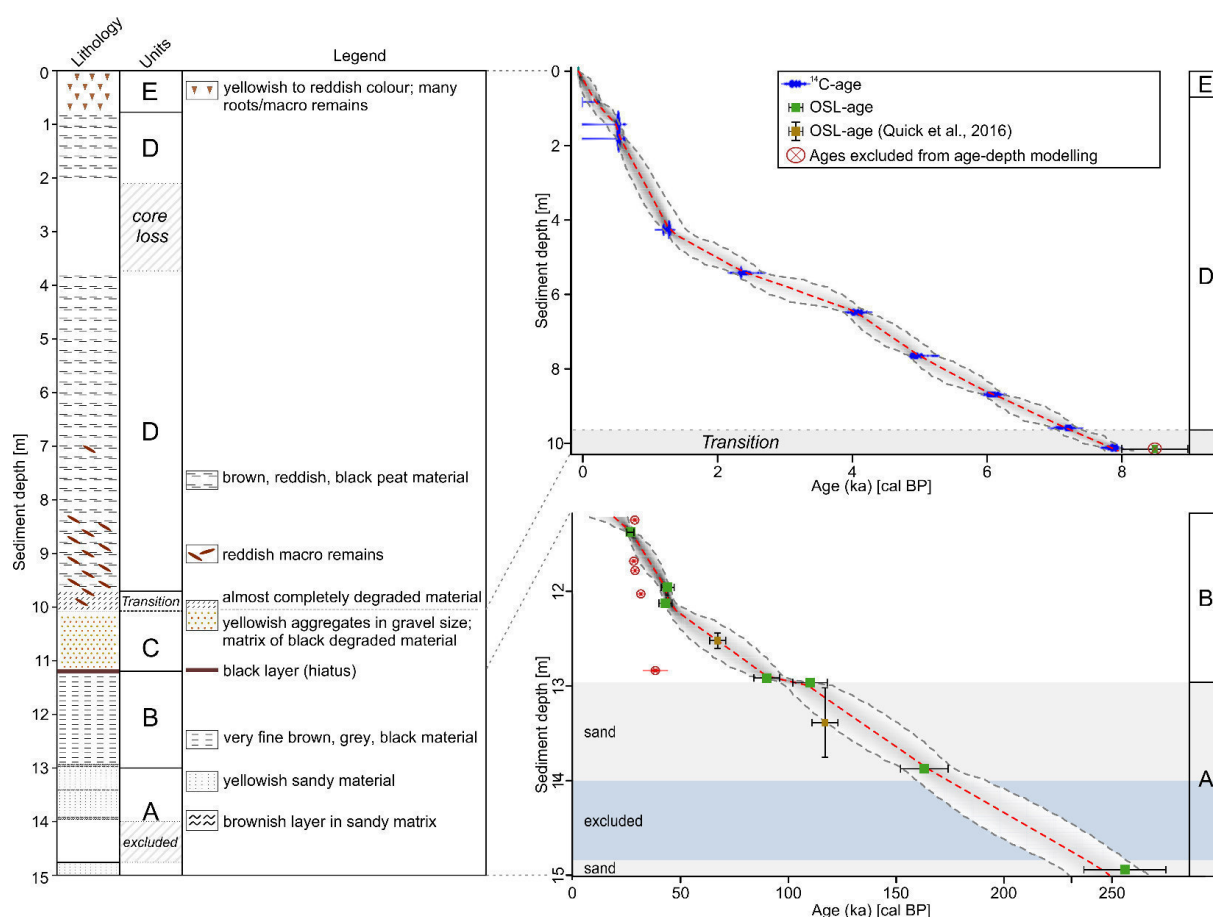


Figure 3: Left: Lithology of the VVV16 composite record from Vankervelsvlei. Right: Age-depth models of the sediment record from Vankervelsvlei. Lithological units are shown on the right. Calibrated radiocarbon ages are displayed as probability density functions of the  $2\sigma$  distributions. OSL ages are shown as boxes including  $1\sigma$  error bars. Calibration and age-depth modelling was carried out using the R software package Bacon 2.4.3 (Blaauw and Christen, 2011). For comparison and confirmation of our age-depth model two OSL ages from sediment core VVV10.1 (Quick et al., 2016) including age ( $1\sigma$  horizontal error bars) and depth uncertainty (vertical error bars) are also depicted, but were not used for age-depth modelling.

## 4.2 Element and isotope analyses as well as paleohygrometer approach

To provide the highest possible resolution, we extended the previously published data by Strobel et al. (2019), i.e. elemental (Al, Fe) contents,  $\delta^{2}\text{H}_{n\text{-alkane}}$ , and  $\delta^{13}\text{C}_{n\text{-alkane}}$  ( $n=23$ ) by new obtained data from this study ( $n=128$ ). Elemental contents of Al and Fe show low to intermediate values in Unit A ( $1,520\pm 85$  to  $13,110\pm 740$  ppm and  $1,040\pm 190$  to  $4,150\pm 770$  ppm, respectively), highest values in Unit B ( $27,500\pm 1,400$  to  $76,800\pm 3,800$  ppm and  $7,300\pm 1,400$  to  $16,400\pm 3,000$  ppm, respectively) and lowest values in Unit E ( $371\pm 21$  to  $2,720\pm 150$  ppm and  $168\pm 31$  to  $2,250\pm 420$  ppm, respectively) (Fig. 4). Normalized XRF-scanning Fe counts follow the pattern of Al and Fe contents (Fig. 4). Strobel et al. (2019) ascribed Al variations to dust input coupled to varying wind at Vankervelsvlei based on the assumption that a fluvial transport of sediments to the coring position at the centre of the peatland is very unlikely as vegetation growing on the peatland acts like a filter for aquatic particle transport. Hence we

## Chapter 4

use XRF-scanning Fe as high-resolution parameter whereas Al-counts are too low for interpretation.

$\delta^{13}\text{C}_{n\text{-alkane}}$  values have a wide range from  $-32.0\pm 0.1$  to  $-28.0\pm 0.2\text{‰}$  in Units A and B (Fig. 4). In Units D and E  $\delta^{13}\text{C}_{n\text{-alkane}}$  values are generally more negative than in Units A and B ( $-33.0\pm 0.1$  to  $-30.2\pm 0.1\text{‰}$ ).  $\delta^{13}\text{C}_{n\text{-alkane}}$  values mainly reflect past changes in the vegetation composition (C3, C4, CAM) (e.g. Diefendorf and Freimuth, 2017) and/or variations in C3 plants water use efficiency (WUE) (Farquhar et al., 1989; Hou et al., 2007).

In Units A and B,  $\delta^2\text{H}_{n\text{-alkane}}$  values vary from  $-167.3\pm 3.8$  to  $-139.9\pm 1.8\text{‰}$ . Marked shifts are present in Unit D and E ( $-190.5\pm 0.7$  to  $-149.7\pm 0.6\text{‰}$ ), which on average are associated with more negative  $\delta^2\text{H}_{n\text{-alkane}}$  values than Units A and B.  $\delta^{18}\text{O}_{\text{sugar}}$  values are more positive in Unit B ( $37.6\pm 0.6$  to  $47.1\pm 1.1\text{‰}$ ) compared to Units D and E ( $25.3\pm 2.0$  to  $47.1\pm 1.2\text{‰}$ ; Fig. 4). The results of the coupled  $\delta^2\text{H}_{n\text{-alkane}}-\delta^{18}\text{O}_{\text{sugar}}$ -approach (paleohygrometer) provide d-excess values from  $-143.4\pm 8.4$  to  $-82.3\pm 4.0\text{‰}$  in Unit B, and  $-88.6\pm 2.3$  to  $-1.1\pm 0.6\text{‰}$  in Units D and E (Fig 6). Reconstructed plant-source water ranges from  $-89.3$  to  $-29.4\text{‰}$  for  $\delta^2\text{H}$  and from  $-13.2$  to  $-5.4\text{‰}$  for  $\delta^{18}\text{O}$  in Unit B, and from  $-76.8$  to  $5.0\text{‰}$  and from  $-11.5$  to  $-0.9$  in Unit D and E, respectively. Reconstructed RH is lower in Unit B (17.8 to 50.1%) than in Units D and E (46.8 to 93%) (Fig 4). Elemental contents (Al and Fe) and  $\delta^2\text{H}_{n\text{-alkane}}$  show significant correlations ( $r = 0.78$  to  $0.80$ ;  $\alpha = 0.05$ ) and Fe also significantly correlates with reconstructed plant-source water ( $r = 0.45$ ;  $\alpha = 0.05$ , Fig. 4).

Based on modern isotopic variability in rainfall, we anticipate that changes in reconstructed plant-source water ( $\delta^{18}\text{O}$  and  $\delta^2\text{H}$ ) reflect changes in the isotopic composition of precipitation related to changes in the precipitation source, i.e. i) Westerlies (Atlantic Ocean), ii) Easterlies (Indian Ocean) and iii) local sources (Strobel et al., 2020). Reconstructed RH reflects growing season air RH (Hepp et al., 2021; Strobel et al., 2020). This leads to the assumption that RH is higher during phases of generally (year-round) and/or seasonally moist conditions, whereas during periods of low RH conditions were either generally drier and/or precipitation seasonality was increased, i.e. the reduction of either summer or winter precipitation. Similar to  $\delta^2\text{H}_{n\text{-alkane}}$ ,  $\delta^{18}\text{O}_{\text{sugar}}$  records the isotopic composition of precipitation but is prominently modulated by evapotranspirative enrichment (Strobel et al., 2020; Struck et al., 2020) and thus is a sensitive proxy for changes in the precipitation-evaporation balance at Vankervelsvlei.

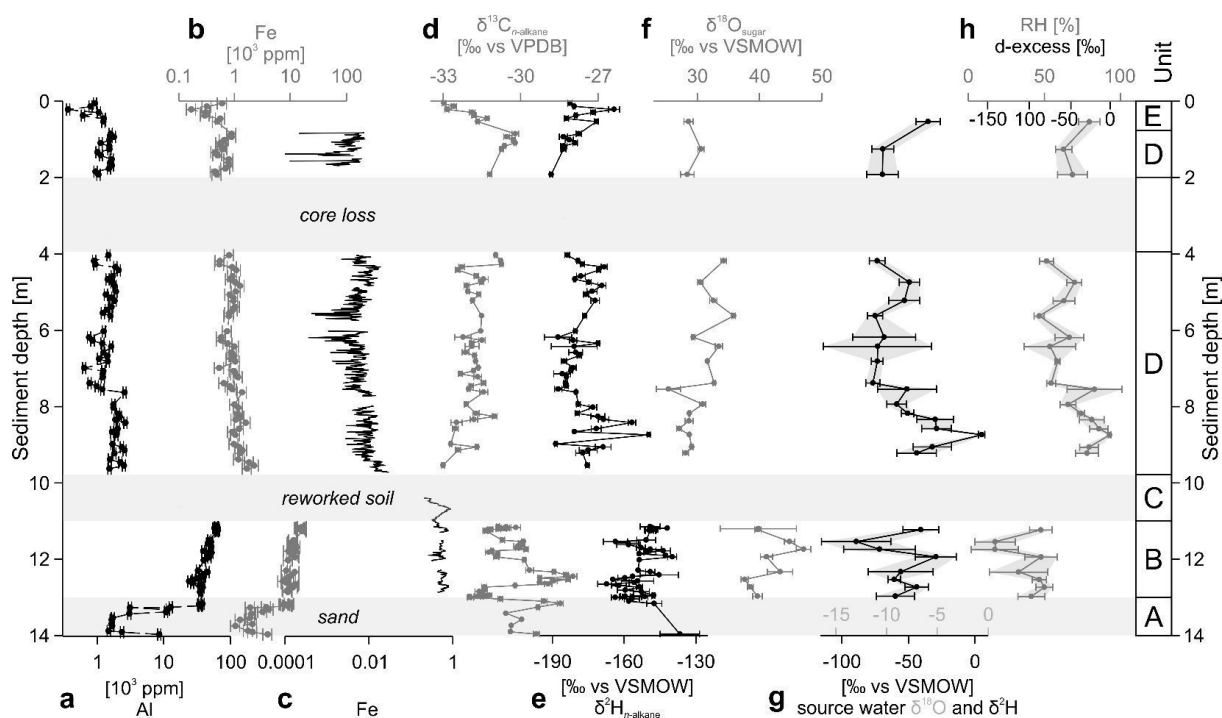


Figure 4: a) Al and b) Fe contents, c) normalised Fe, d)  $\delta^{13}\text{C}_{n\text{-alkane}}$ , e)  $\delta^2\text{H}_{n\text{-alkane}}$  and f)  $\delta^{18}\text{O}_{\text{sugar}}$  as well as g) the isotopic composition of the reconstructed source water, h) d-excess and relative humidity derived from the coupled isotope approach from the VVV16 sediment sequence. Error bars and the grey shaded area in g) and h) indicate expanded uncertainties derived from the uncertainty propagation law. Lithological units are depicted at the right. Note  $\text{Log}_{10}$  scale for a), b) and c).

## 5 Discussion

### 5.1 Chronostratigraphy

The basal age of  $256 \pm 19$  ka of the sediment sequence from Vankervelsvlei is in the range of the dunes underlying and surrounding Vankervelsvlei, i.e. 205 to 250 ka BP (Bateman et al., 2011) (Table S4) and indicates that the depression hosting Vankervelsvlei today was formed contemporaneously and that we recovered the entire sedimentary sequence yielding paleoenvironmental information. However, due to the infiltration of humic-rich water into the core section from 14.8 to 14.0 m composite depth between coring drives, those sediments had to be excluded from paleoenvironmental reconstruction. Bulk TOC  $^{14}\text{C}$  ages published in a previous investigation from Vankervelsvlei (Strobel et al., 2019) showed a distinct offset to the revised OSL-based age-depth model presented here (Fig. 3). As these  $^{14}\text{C}$  ages of bulk TOC are close to the dating limit of  $^{14}\text{C}$  only minor amounts of young carbon likely bias these dating results (e.g., Briant and Bateman, 2009). At Vankervelsvlei, we hypothesise that percolating waters containing leached organic carbon may account for the too young bulk  $^{14}\text{C}$  ages. Additionally, two brownish layers at 14.0 and 13.3 m composite depth are likely a result of this percolating water (Fig. 3). Mandiola et al. (2021) analysed the age of water in several depths within the Vankervelsvlei deposits, revealing modern  $^{14}\text{C}$  ages for water in deeper layers (~6.3 m below surface). Although dissolved organic matter was not analysed in the study by

## Chapter 4

Mandiola et al. (2021), the presence of percolating water supports our aforementioned hypothesis of alteration of bulk radiocarbon ages. Similarly,  $^{14}\text{C}$  ages in the Vankervelsvlei study by Quick et al. (2016) were also not in stratigraphic order and showed a distinct offset to OSL ages, also supporting our hypothesis. Vertical (re-)deposition of carbon in sediments leading to biased  $^{14}\text{C}$  ages was also recently observed by e.g. Briant et al. (2018), Colarossi et al. (2020) and Palstra et al. (2021), but the new stratigraphic consistent OSL data reveal robust age information for this parts of the record.

In the upper part of Unit B, the chronology implies a sedimentary hiatus at 11.18 m sediment depth. The hiatus was previously ascribed to desiccation from  $28,050^{+510}_{-600}$  to  $8,360^{+730}_{-810}$  cal BP (Strobel et al., 2019). Considering modelling and dating errors of the new OSL-based chronology, we can confirm a sedimentary hiatus during MIS 2 and the transition to MIS 1 ( $20.3^{+5.2}_{-14}$  ka to  $7,230^{+160}_{-210}$  cal BP), which well matches to reconstructed dryenvironmental conditions at further regional archives (see section 5.2.1 for detailed discussion). After the deposition of reworked soil material in Unit C and the transition to Unit D (likely in MIS 2 and/or the Early-Holocene), continuous sedimentation re-started in the Middle-Holocene, i.e.  $7,230^{+160}_{-210}$  cal BP lasting until present day (Fig. 3).

Several sediment cores have been recovered from different locations at Vankervelsvlei during the past decades (Irving and Meadows, 1997; Quick et al., 2016). However, the comparability of those cores to the composite record developed here is limited due to missing sections (especially in the youngest part), lithological inconsistencies and occasionally poor chronological control of the previous studies. Nevertheless, the sediment cores investigated by Quick et al. (2016) can roughly be parallelised to the lower part of our composite record (Units A and B). The stratigraphic location of an OSL age of  $117\pm 6$  ka in core VVV10.1 (Quick et al., 2016) between our ages of  $163\pm 11$  and  $110\pm 8.1$  ka supports our chronology (Fig. 3). Another OSL age of  $67.2\pm 3.7$  ka from core VVV10.1 (Quick et al., 2016) is also stratigraphically consistent, being located between the two new OSL ages of  $90\pm 6$  ka and  $43\pm 3$  ka in this study (Fig. 3). Unfortunately, it is not possible to better match records inhibiting a precise inclusion of all VVV10.1 ages from Quick et al. (2016).

## 5.2 Paleoenvironmental- and climate evolution

### 5.2.1 Late Quaternary

The sediments lying between the two lowermost OSL-ages, i.e.  $256^{+19}_{-19}$  and  $110^{+8}_{-8}$  ka (late MIS 8 to early MIS 7 and MIS 5e), consist almost exclusively of sand limiting paleoenvironmental inferences for this period. However, high sand contents likely indicate significant geomorphic activity at Vankervelsvlei area and within the surrounding area. This is consistent with studies of the history of dune formation within the Wilderness Embayment, with



two periods of barrier dune construction identified during MIS 6 and 5e, i.e. from 159 to 143 ka and from 130 to 120 ka, respectively (Bateman et al., 2011). Quick et al. (2016) reported that no pollen was preserved in these sandy sediments dating 140 to 115 ka at Vankervelsvlei, which is consistent with our record.

From 171  $^{+16}/_{-13}$  to 136  $^{+16}/_{-16}$  ka,  $\delta^{13}\text{C}_{n\text{-alkane}}$  values imply a contribution from vegetation using CAM and/or C4 photosynthesis, and/or decreased moisture availability (water use efficiency; WUE) at Vankervelsvlei (Fig. 5).  $n$ -Alkane amounts were too low for  $\delta^2\text{H}_{n\text{-alkane}}$  measurements to be used as an indicator of precipitation source. Similarly, elemental Fe is too low for interpretation and cannot be used for this period. From 136  $^{+16}/_{-16}$  to 112  $^{+12}/_{-11}$  ka more positive  $\delta^{13}\text{C}_{n\text{-alkane}}$  values, in comparison to the previous period, imply drier conditions and that more plants were using CAM and/or C4 photosynthetic mode. Although there are only a few samples that yield sufficient  $n$ -alkane amounts for  $\delta^2\text{H}_{n\text{-alkane}}$  measurements, negative values indicate high contribution of Westerly-derived winter precipitation at the same time. From 112  $^{+12}/_{-11}$  to 103  $^{+7}/_{-7}$  ka (MIS 5e, 5d), from 88  $^{+8}/_{-8}$  to 82  $^{+10}/_{-12}$  ka (MIS 5c, 5b) and from 42  $^{+2}/_{-2}$  to 39  $^{+4}/_{-5}$  ka (MIS 3)  $\delta^{13}\text{C}_{n\text{-alkane}}$  values clearly indicate a dominant contribution of plants using C3 photosynthetic mode. These periods are accompanied by more positive  $\delta^2\text{H}_{n\text{-alkane}}$  values indicating high contributions of both winter (Westerly-derived) and summer (Easterly-/locally-derived) precipitation and likely a year-round rainfall regime. In contrast, plants using CAM and/or C4 photosynthetic mode are present at Vankervelsvlei from 82  $^{+10}/_{-12}$  to 42  $^{+2}/_{-2}$  ka (MIS 5a to early MIS 3), from 39  $^{+4}/_{-5}$  to 20  $^{+5}/_{-12}$  ka (transition from MIS 3 to MIS 2) (Fig. 5). Contemporaneously, more negative  $\delta^2\text{H}_{n\text{-alkane}}$  values indicate high Westerly-derived winter precipitation contribution and thus a shift to a winter-rainfall regime. Unfortunately, the full suite of proxy data is not available between 103  $^{+7}/_{-7}$  and 88  $^{+8}/_{-8}$  ka due to a lack of samples.

Plant-source water ( $\delta^2\text{H}$  and  $\delta^{18}\text{O}$ ) and RH values show minor variations from MIS 5d to MIS 2 and a most prominent shift from moist to very dry conditions at the transition from MIS 3 to MIS 2 (Fig. 5). Although the temporal resolution of these proxies is limited, this study demonstrates the applicability of the coupled  $\delta^2\text{H}_{n\text{-alkane}}-\delta^{18}\text{O}_{\text{sugar}}$  approach (paleohygrometer) in sediments of Late Quaternary age. High-resolution elemental Fe cannot be interpreted prior to MIS 5c, but indicates maxima of minerogenic input at the transitions from MIS 5b to 5a, MIS 4 to MIS 3 and MIS 3 to MIS 2 suggesting increased importance of wind during these periods at Vankervelsvlei (Fig. 5). While minerogenic input is low during phases of dominant Westerly-derived winter precipitation it increases during periods of precipitation contributions from both Westerly- and Easterly-/locally-derived precipitation. This indicates a potential relation of wind-driven minerogenic and Easterly-/locally-derived precipitation (Fig. 5).

Trends in  $\delta^{13}\text{C}_{n\text{-alkane}}$  from this study correspond well with changes in the occurrence of Succulent/Drought Resistant (SDR) pollen (Fig. 5g) from sediment core VVV10.1 (Quick et al., 2016). The SDR pollen sum is dominated by *Euphorbia* and was previously interpreted to

## Chapter 4

indicate local drought at Vankervelsvlei (Quick et al., 2016). Distinctly more negative  $\delta^{13}\text{C}_{n\text{-alkane}}$  and low SDR pollen imply greater moisture availability and limited rainfall seasonality from 88  $^{+8}/_{-8}$  to 82  $^{+10}/_{-12}$  ka (MIS 5c, 5b) (year-round-rainfall regime). Accordingly, more positive  $\delta^{13}\text{C}_{n\text{-alkane}}$  values and high SDR pollen imply drier conditions and increased rainfall seasonality from 82  $^{+10}/_{-12}$  to 42  $^{+2}/_{-2}$  ka (MIS 5a to MIS 3). From 42  $^{+2}/_{-2}$  to 37  $^{+5}/_{-5}$  ka (MIS 3), more negative  $\delta^{13}\text{C}_{n\text{-alkane}}$  values and lower SDR pollen indicate a return to moist and less seasonal conditions. This is followed by a trends towards more positive  $\delta^{13}\text{C}_{n\text{-alkane}}$  and higher SDR pollen percentages indicating drier conditions from 37  $^{+5}/_{-5}$  to 20  $^{+5}/_{-12}$  ka (transition from MIS 3 to MIS 2) (Fig. 5).

Several speleothem records have been developed in the YRZ during the past decades. However, data gaps in the speleothems limit a comparability to our record from MIS 6 to MIS 5d but more positive  $\delta^{13}\text{C}$  values suggest dry conditions during early MIS 6 followed by even more positive  $\delta^{13}\text{C}$  values indicating even drier conditions in MIS 5 e at Pinnacle Point (Staircase Cave; ~80 km SW of Vankervelsvlei; Braun et al., 2019), which is in good agreement with our data. An additional record from Pinnacle Point (PP29; Braun et al., 2020) supports moist conditions from MIS 5d to MIS 5b due to negative  $\delta^{13}\text{C}$  values. Most records show initial and/or continuing speleothem growth after ~90 ka and provide climate information in high temporal resolution, e.g. at Herolds Bay Cave, Pinnacle Point (Crevice Cave, PP29) and Efflux Cave (respective locations: ~50 km SW, ~80 km SW and ~100 km NW of Vankervelsvlei) (see Fig. 1C for location) (Bar-Matthews et al., 2010; Braun et al., 2019; Braun et al., 2020). Although the temporal resolution of the Vankervelsvlei record is lower than at these sites,  $\delta^{13}\text{C}$ -records from the speleothems perfectly resemble the  $\delta^{13}\text{C}_{n\text{-alkane}}$  trends from Vankervelsvlei (Fig. 5). Therefore, all records together provide a coherent environmental picture at the southern Cape coast of more vegetation using CAM and/or C4 photosynthetic mode during MIS 4 compared to MIS 5b and MIS 3 (Fig. 5). Unfortunately, comparison of our proxies for precipitation source to  $\delta^{18}\text{O}$  from speleothem is limited because it is challenging to disentangle the effects of temperature and precipitation source in the latter (e.g. Braun et al., 2019 and discussion therein). Overall, several paleoclimate records located at or near the present day southern Cape coast show relatively coherent trends with evidence from several proxies indicating (supra-)regional driving forces leading to the observed pattern during the Late Quaternary.

The pattern of our  $\delta^2\text{H}_{n\text{-alkane}}$ -record is resembled by changes in the global mean sea level (GMSL) (Waelbroeck et al., 2002; Fig. 5) indicating changes in precipitation sources on glacial-interglacial scale. More positive  $\delta^2\text{H}_{n\text{-alkane}}$  values indicate a high contribution of Easterly- and/or locally-derived precipitation during high sea level (interglacial periods) and negative  $\delta^2\text{H}_{n\text{-alkane}}$  values occur during low sea level low (glacial periods) indicating high proportions of Westerly-derived precipitation (Waelbroeck et al., 2002; Fig. 5). However, the

ocean as a precipitation source becomes isotopically enriched during glacial periods due to the so called 'ice effect' (Dansgaard, 1964; Friedman et al., 1964), which is opposed to our observed pattern and therefore dampens the magnitude in our  $\delta^2\text{H}_{n\text{-alkane}}$ -record from Vankervelsvlei.

Additionally, during glacial periods, sea level was distinctly lower than at present, with the coastline south of its present position, increasing continentality at Vankervelsvlei (Cawthra et al., 2014; Cawthra et al., 2021; Strobel et al., 2019). This was likely most pronounced during MIS 6 and MIS 2 (~90-100 km) and to a lesser degree during MIS 4 (~20-30 km) (BODC, 2014; Cawthra et al., 2014; Lisiecki and Raymo, 2005; Waelbroeck et al., 2002). We therefore suggest that variations in the GMSL are a distinct driver of climate variability at the southern Cape coast leading to increased continentality and drier conditions during glacial compared to interglacial periods. This is consistent with the absence of peat accumulation at Vankervelsvlei during MIS 2 (discussed below).

The hiatus from  $20^{+5}/_{-12}$  ka to  $7,330^{+200}/_{-230}$  cal ka BP likely indicates drought conditions at Vankervelsvlei, leading to desiccation and degradation of the previously accumulated peat during MIS 2 (Quick et al., 2016; Strobel et al., 2019). Drier conditions during MIS 2 were also found for example at Rietvlei, located ~150 km to the west of Vankervelsvlei (Quick et al., 2015) supporting our interpretation at Vankervelsvlei. During MIS 2, sea level was lower than present, i.e. ~123 m b.s.l., which led to an exposure of the Paleo-Agulhas Plain, and thus continentality at Vankervelsvlei distinctly increased due to a migration of the coastline ~90 km to the south of its present position during this time (BODC, 2014; Cawthra et al., 2014; Cawthra et al., 2021; Waelbroeck et al., 2002). Modelled temperatures and precipitation (seasonality) imply lower mean annual temperatures (i.e. 2 to 4°C), and reduced precipitation, due to increased continentality of this area, resulting in overall dry conditions during MIS 2 (Engelbrecht et al., 2019). There is one speleothem record from Cango Cave for the southern Cape coast covering the LGM, which also shows a distinct hiatus during parts of MIS 2 (i.e. from 16,660 to 6,110 cal BP) (Talma and Vogel, 1992) contemporaneous with the dry conditions inferred from the hiatus. Hence, conditions during MIS 2 at the southern Cape were likely distinctly drier than during the past  $\sim 110^{+13}/_{-11}$  ka when peat accumulation likely started at Vankervelsvlei. Conversely, both proxy (e.g. Chase et al., 2017; Chase and Meadows, 2007) and modelled data (e.g. Cockcroft et al., 1987; Engelbrecht et al., 2019) indicate moister conditions in the interior and at the south-north aligned Cape Fold Mountains and the western escarpment of South Africa inter alia due to reduced temperatures leading to an increased effective ecosystem moisture availability.

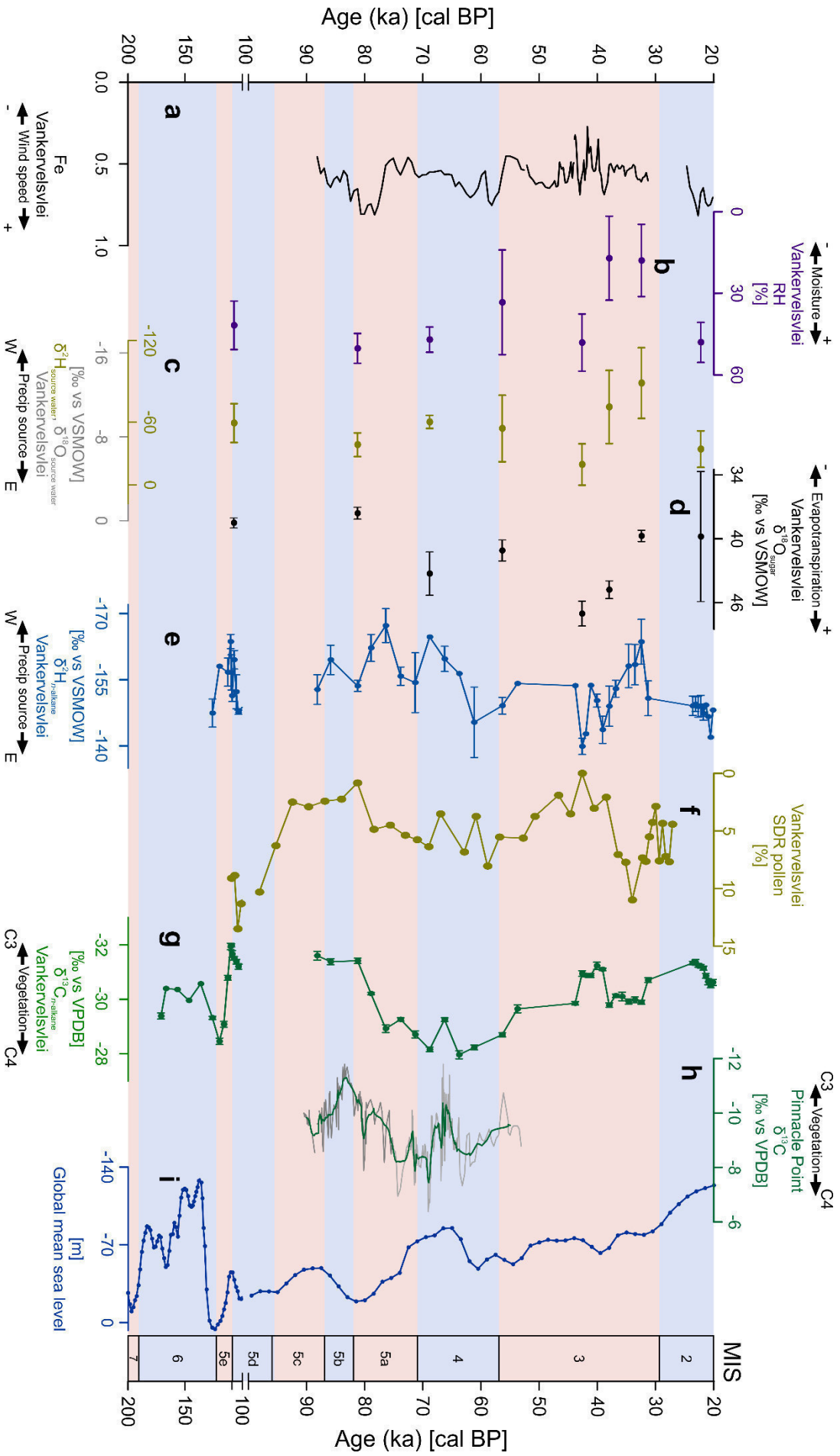


*Figure 5: Late Quaternary inorganic and organic down-core geochemistry of the VVV16 sediment record as indicators a) for wind (Fe), b) relative humidity (RH; moisture), c), e) precipitation source (W = Westerlies, E = Easterlies and/or local sources), d) evapotranspiration and g) vegetation composition and/or C3 plants water use efficiency. For comparative purposes f) percentages of succulent/drought resistant (SDR) pollen from Vankervelsvlei are shown (Quick et al., 2016). Note that these pollen results are from an earlier study on VVV and are plotted on their original independent age scale. Additionally, (supra-)regional paleoenvironmental records are plotted: h)  $\delta^{13}\text{C}$  from Pinnacle point (grey line original data; coloured line running mean of eleven data points) (Bar-Matthews et al., 2010) and i) Global mean sea level (Waelbroeck et al., 2002). Marine Isotope Stages (MIS, (Lisiecki and Raymo, 2005)) are shown on the right. See Fig. 1 for location of the studies. Note axis break at 100 ka.*

## 5.2.2 Holocene

### **Middle- and Late-Holocene**

According to the slightly positive  $\delta^{18}\text{O}_{\text{sugar}}$  values evapotranspiration is low from 7,230  $^{+160}/_{-210}$  to 4,890  $^{+280}/_{-180}$  cal BP (Fig. 6). More positive values of  $\delta^2\text{H}_{n\text{-alkane}}$  and plant-source water as well as high RH values indicate distinct precipitation contributions from tropical Easterlies and/or local sources and moist conditions year-round. Contemporaneously, high Fe values likely indicate wind induced minerogenic input at Vankervelsvlei. We therefore suggest that wind induced minerogenic input increases when precipitation contribution from Easterlies and local sources is high.

From 4,890  $^{+280}/_{-180}$  to 2,710  $^{+590}/_{-310}$  cal BP, increased Westerly-derived precipitation is indicated by distinctly negative values of  $\delta^2\text{H}_{n\text{-alkane}}$  and reconstructed plant-source water. During this period, RH is low and distinct positive  $\delta^{18}\text{O}_{\text{sugar}}$  values indicate high evapotranspirative enrichment, which likely implies dry summer conditions, and a reduced or absent precipitation contribution from the Easterlies and/or local sources. Low elemental Fe values point to less wind induced minerogenic input, which again seems to be coupled with low precipitation contribution from Easterlies and/or local sources (Fig. 6).

From 2,710  $^{+590}/_{-310}$  cal BP until present day variable, but overall more positive values of reconstructed plant-source water and increased RH likely imply an increased precipitation contribution from Easterlies and/or local sources and overall moist conditions, comparable to present day. This is underlined by a trend to less positive  $\delta^{18}\text{O}_{\text{sugar}}$  values indicating low evapotranspirative enrichment (Fig. 6). High-resolution  $\delta^2\text{H}_{n\text{-alkane}}$  and Fe values follow the aforementioned trend, but show a further short period of distinctly increased Easterly-derived summer precipitation contribution accompanied by increased wind induced minerogenic input from 2,350  $^{+290}/_{-190}$  to 1,210  $^{+240}/_{-140}$  cal BP. In the uppermost parts of the record, highly variable conditions are derived from distinct changes in  $\delta^2\text{H}_{n\text{-alkane}}$  and Fe values (Fig. 6).

## Chapter 4

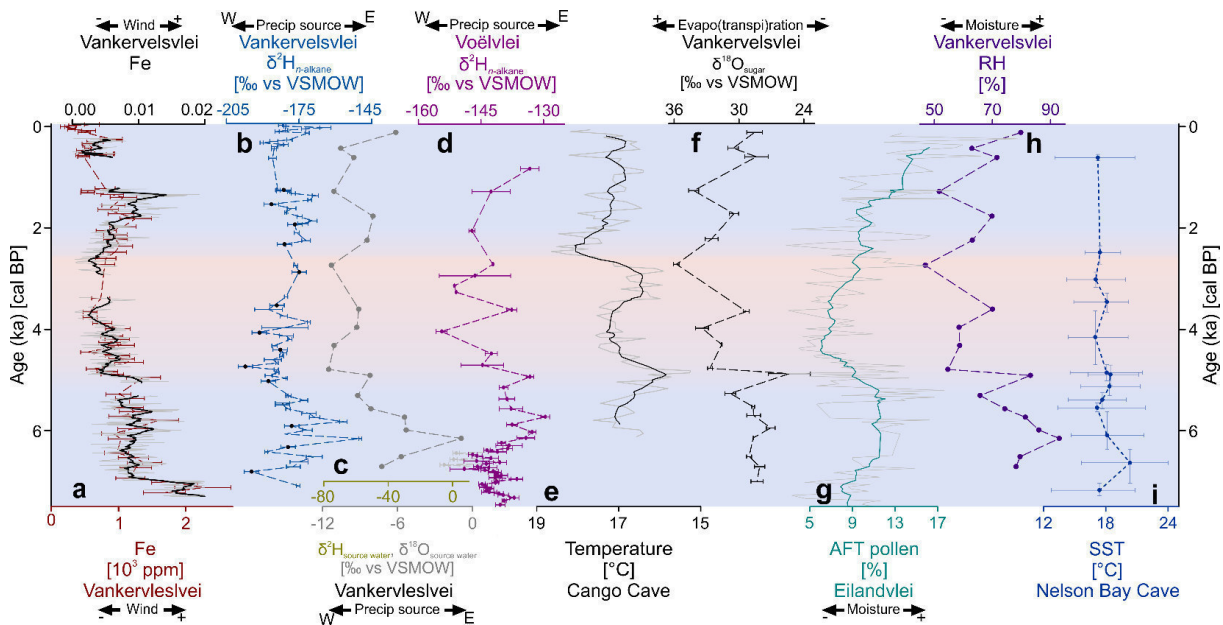


Figure 6: Inorganic and organic geochemistry of the VVV16 sediment record (a, b, c, f, h) as proxies for wind, precipitation source (W = Westerlies, E = Easterlies and/or local sources), evapotranspiration (note inverse axis) and relative humidity (moisture). Black dots in b indicate results from Strobel et al. (2019). For comparative purposes regional paleoenvironmental records are plotted on their original independent age scale: d)  $\delta^2\text{H}_{n\text{-alkane}}$  from Voëlvlei indicating precipitation source (Strobel et al., 2021), e) terrestrial paleo-temperatures at Congo Cave (note inverse axis) (Talma and Vogel, 1992), g) Afrotemperate forest (AFT) pollen from Eilandvlei indicating moisture (Quick et al., 2018), and i) sea surface temperature (SST) from Nelson Bay Cave (Cohen, 1993; Cohen and Tyson, 1995). For e), g) and h) grey line indicates original data and colour line is the running mean of seven and eleven data points, respectively. See Fig. 1 for location of the studies.

During the Holocene, the pattern of RH tracks the abundance of Afrotemperate forest (AFT) pollen recorded at neighbouring lake Eilandvlei, located ~25 km to the west of Vankervelsvlei (Fig. 1C, 6). The AFT pollen signal is an indicator for moisture availability for the surrounding Wilderness area, including Vankervelsvlei, being in line with other moisture indicators from Eilandvlei (Quick et al., 2018; Wündsche et al., 2018). The correspondence between RH and AFT pollen suggests a consistent moisture signal in the Wilderness area during the Holocene. Plant-source water and  $\delta^2\text{H}_{n\text{-alkane}}$  suggest that these moist conditions are related to increased precipitation contributed during summer (Easterlies) and/or from local sources. Conversely, dry conditions are associated with less precipitation contribution during summer (Easterlies) and/or from local sources.

At Voëlvlei, ~80 km west of Vankervelsvlei, the  $\delta^2\text{H}_{n\text{-alkane}}$  record also mirrors changes in the precipitation source (Strobel et al., 2021) (Fig. 6d). The overall pattern at this site suggested a contribution of i) both Westerly- and Easterly/locally-derived precipitation (8,230<sup>+250</sup>/<sub>-260</sub> to 6,410<sup>+140</sup>/<sub>-440</sub> cal BP), ii) dominant Easterly/local precipitation (6,410<sup>+140</sup>/<sub>-440</sub> to 4,700<sup>+500</sup>/<sub>-230</sub> cal BP), is followed by iii) variable precipitation contribution but a trend from Westerly- to Easterly-dominance (4,700<sup>+500</sup>/<sub>-230</sub> cal BP to present day) (Strobel et al., 2021). This pattern is consistent with the findings from Vankervelsvlei and Eilandvlei providing a consistent climate picture of the coastal sites at South Africa's southern Cape coast.

Holocene terrestrial temperature and sea surface temperature (SST) records are hitherto very rare at South Africa's southern Cape coast. Overall, the pattern of the  $\delta^{18}\text{O}_{\text{sugar}}$  at Vankervelsvlei resembles the terrestrial temperature record from Cango Cave (Talma and Vogel, 1992) likely indicating high (low) evapotranspiration at Vankervelsvlei contemporaneous with high (low) temperatures at Cango Cave during the Middle- and Late-Holocene (Fig. 6). Additionally, two minor trends towards more Westerly-derived winter precipitation ( $\delta^2\text{H}_{n\text{-alkane}}$  and source water) at Vankervelsvlei (at  $4,710^{+310}/_{-290}$  and  $2,710^{+590}/_{-310}$  cal BP) are accompanied by distinctly decreased temperatures at Cango Cave, while during phases of increased precipitation contribution from Easterlies and/or local sources at Vankervelsvlei temperatures are increased at Cango Cave (Fig. 6). While the variable trend in evapotranspiration at Vankervelsvlei from  $\sim 3$  cal ka BP until present day is also mirrored in variable temperatures at Cango Cave, the increasing trend towards moister conditions cannot be related to changes in temperature during this period (Fig. 6). Although the SST-record from Nelson Bay Cave (NBC, (Cohen and Tyson, 1995), Fig. 1C) indicates higher SST at  $\sim 6,640^{+400}/_{-270}$  cal BP and  $\sim 4,900^{+220}/_{-190}$  cal BP, which might be related to high RH and high precipitation contribution from Easterlies and/or local sources at Vankervelsvlei, analytical and chronological uncertainties as well as low temporal resolution all limit the comparability of this record to our study. However, both temperature records from Cango Cave and Nelson Bay Cave indicate that terrestrial temperatures and SST might be a driver of moisture at Vankervelsvlei during the Holocene. High temperatures might yield distinct land-sea gradients fostering onshore flows of moist air masses from local sources to the coastal areas during the Holocene and thus underlining the aforementioned pattern in moisture and precipitation sources at Vankervelsvlei and surrounding coastal areas. While the presence of onshore flows was previously postulated at Vankervelsvlei by increased strontium (Sr) contents which origin from sea spray (Strobel et al., 2019), based on the results of this study, we suggest that precipitation contribution from local sources distinctly contributes to moisture at the southern Capes coastal sites. Sites located further inland are at higher elevation due to the southern Cape's morphology, and precipitation from local sources is therefore likely limited to the coastal sites. This indicates that moisture at coastal and further inland located sites, e.g. Seweweekspoort (Chase et al., 2017), might be independent. Therefore, our data add further weight to the proposed steep climate response gradient between coastal sites and the adjacent uplands in the southern Cape (Chase et al., 2020; Chase and Quick, 2018). However, to provide more detailed information about those land-sea interactions, there is a need for more continuous high-resolution quantitative sea-surface and terrestrial temperatures at South Africa's southern Cape coast.

**600 cal BP until present**

There is a significant correlation between minerogenic input (Fe contents) from our study and aquatic/riparian pollen percentages ( $r = 0.68$ ,  $\alpha = 0.05$ , Fig. 6) derived from the uppermost section of the same Vankervelsvlei sediment sequence (1.96 to 0 m composite depth; 595<sup>+120</sup>/<sub>-65</sub> cal BP to present day) by du Plessis et al. (2021). The aquatic/riparian pollen are dominated by local Haloragaceae pollen (most likely *Myriophyllum*, a freshwater aquatic plant (du Plessis et al., 2021)). Based on pollen analyses only, du Plessis et al. (2021) previously argued that low Haloragaceae pollen might indicate high water levels at Vankervelsvlei. This interpretation was largely based on this taxon's relation to variations in Cyperaceae pollen. In light of the fact that wind-induced minerogenic input (Fe) had been associated with high precipitation from Easterlies and/or local sources contributing to moist conditions year-round during the Holocene (Strobel et al., 2019), we apply the same interpretation for the past 595<sup>+120</sup>/<sub>-65</sub> cal BP here. We therefore suggest that high Haloragaceae pollen indicate higher water levels at Vankervelsvlei. This is in line with previous assertions that increases in the presence of Haloragaceae is associated with high water stands in other South African lakes (e.g. Howard-Williams, 1979; Neumann et al., 2008). The pattern of minerogenic input (Fe) and aquatic/riparian pollen is mirrored by the trends in the Afrotropical forest (AFT) pollen sum, which has previously been interpreted to indicate increased year-round and less seasonal moisture conditions at Vankervelsvlei (du Plessis et al., 2021) and the surrounding Wilderness area (Quick et al., 2018). According to this interpretation moister conditions peak at ~595<sup>+120</sup>/<sub>-65</sub>, ~530<sup>+70</sup>/<sub>-100</sub> and ~260<sup>+85</sup>/<sub>-160</sub> cal BP. In general, our parameters lack the resolution (due to core loss) to characterise the Medieval Climate Anomaly (~950-700 cal BP), but they do show a trend towards drier conditions during the Little Ice Age (~650-300 cal BP) (Figs. 6 and 7). Anthropogenic impacts, i.e. forestry (Pinaceae pollen), began to alter the landscape (and site) after 60<sup>+130</sup>/<sub>-90</sub> cal BP, which explains the fading similarities in proxies in the uppermost parts of the record (Fig. 7).



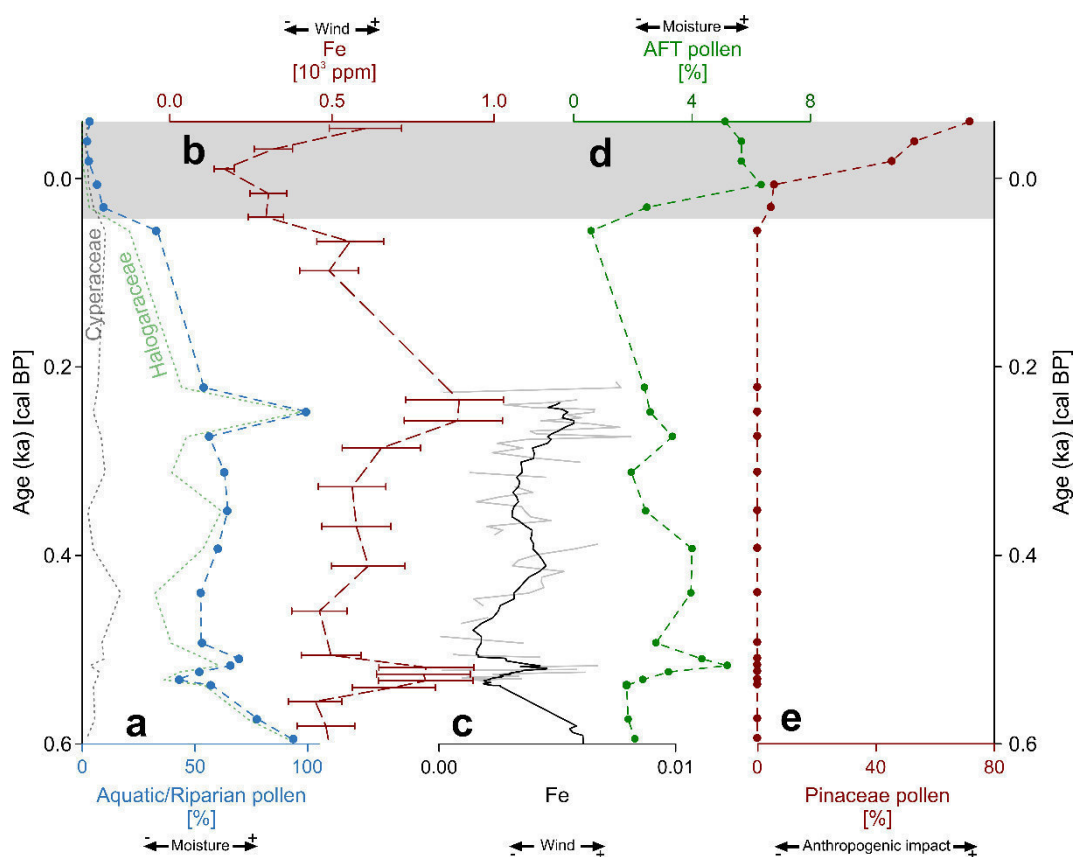


Figure 7: a) Aquatic/riparian pollen indicative for water table variations (du Plessis et al., 2021), b) and c) Fe contents and counts as local wind indicators, d) Afrotemperate forest (AFT) pollen indicative for moisture and e) Pinaceae and pollen representing anthropogenic impact (du Plessis et al., 2021). The grey shaded area marks the presence of anthropogenic impact at Vankervelsvlei indicated by increasing Pinaceae pollen, which explains fading similarities between a, b and d.

## 6 Conclusions

Our multi-proxy record from Vankervelsvlei provides new insights into the paleoclimate history at South Africa's southern Cape Coast during the Late Quaternary. In this region Vankervelsvlei represents a scarce terrestrial archive that was not influenced by the intrusion of marine water enabling robust paleoclimate reconstructing. The OSL and  $^{14}\text{C}$ -based chronology of the record has a basal age of  $263 \pm 19$  ka, and dry conditions likely prevailed from this time to  $136^{+16}_{-16}$  ka at Vankervelsvlei, contemporaneous with a major phase of barrier dune construction in the surrounding areas, particularly during MIS 5e. Even drier conditions and low geomorphic activity at the site occurred from  $136^{+16}_{-16}$  to  $112^{+12}_{-11}$  ka. From  $112^{+12}_{-11}$  to  $103^{+7}_{-7}$  ka, from  $88^{+8}_{-8}$  to  $82^{+10}_{-12}$  ka and from  $42^{+2}_{-2}$  to  $39^{+4}_{-5}$  ka  $\delta^{13}\text{C}_{n\text{-alkane}}$  values indicate the contribution largely from plants using C3 photosynthesis, with an increased contribution of plants using CAM and/or C4 photosynthesis present from  $82^{+10}_{-12}$  to  $42^{+2}_{-2}$  ka and from  $39^{+4}_{-5}$  to  $20^{+5}_{-12}$  ka.

An increased Westerly-derived winter precipitation contribution is suggested by more negative  $\delta^2\text{H}_{n\text{-alkane}}$  values from  $120^{+15}_{-14}$  to  $105^{+9}_{-8}$  ka, from  $79^{+11}_{-13}$  to  $76^{+11}_{-12}$  ka and

## Chapter 4

from 68 <sup>+13</sup>/<sub>-12</sub> to 66 <sup>+14</sup>/<sub>-11</sub> ka. Greater contributions of Easterly-derived summer precipitation are implied by more positive  $\delta^2\text{H}_{n\text{-alkane}}$  values from 74 <sup>+12</sup>/<sub>-13</sub> to 71 <sup>+13</sup>/<sub>-13</sub> ka and 64 <sup>+13</sup>/<sub>-11</sub> to 37 <sup>+5</sup>/<sub>-5</sub> ka. Variable contributions of both Westerly- and Easterly-derived precipitation are evident from 37 <sup>+5</sup>/<sub>-5</sub> to 20 <sup>+5</sup>/<sub>-12</sub> ka.

High-resolution analyses of the Middle- and Late-Holocene parts of the record show three distinct phases. The first phase from 7,230 <sup>+160</sup>/<sub>-210</sub> to 4,890 <sup>+280</sup>/<sub>-180</sub> cal BP is characterised by moist conditions and rainfall year-round, including a distinct contribution from mainly locally-derived summer-precipitation. From 4,890 <sup>+280</sup>/<sub>-180</sub> to 2,840 <sup>+350</sup>/<sub>-330</sub> cal BP, dry conditions and high seasonality, with largely Westerly-derived winter precipitation occurred. After 2,840 <sup>+350</sup>/<sub>-330</sub> cal BP, moisture has been variable but overall increasing accompanied by increasing locally-derived summer-precipitation leading to a year-round rainfall regime again.

Results of our record are in line with previous investigations at Vankervelsvlei and closely located stalagmite records providing a coherent regional climate signal at the southern Cape coast of South Africa. Due to distinct sea-level variations during the Late Quaternary, the coastline likely migrated up to 100 km south of its present position during glacial periods leading to increased continentality and dry conditions at Vankervelsvlei identifying sea-level as a distinct driver of climate variability at the site on orbital time scales. During the Middle- and Late-Holocene, Vankervelsvlei provides consistent climate signals compared to coastal archives along South Africa's southern Cape coast. While there are still discrepancies of coastal and inland climate pattern, possibly due to the application of indirect hydrological proxies at the latter and thus limited proxy comparability. Local sources are hypothesised to distinctly contribute to the precipitation and moisture pattern coupled to distinct (sea-surface) temperature driven onshore winds at the coastal sites. Further studies are needed to more fully explore the validity of this hypothesis. Additionally, our study highlights that future studies should focus on the investigation of both water isotopes, i.e.  $\delta^{18}\text{O}$  and  $\delta^2\text{H}$ , to i) enable proxy comparability and ii) overcome distinct uncertainties related to single-water-isotope studies, and therefore allow more robust paleohydrological reconstructions.

## Data availability statement

Data used in this study is available will be made available with acceptance of the paper on PANGAEA.

## Author contribution

**Paul Strobel:** Conceptualization, Investigation, Writing - Original Draft, Project administration, Funding acquisition **Marcel Bliedtner:** Investigation, Writing - Review & Editing **Andrew S. Carr:** Investigation, Writing - Review & Editing **Julian Struck:** Investigation, Writing - Review

& Editing **Nadia du Plessis**: Writing - Review & Editing **Bruno Glaser**: Methodology, Writing - Review & Editing **Michael E. Meadows**: Writing - Review & Editing **Lynne J. Quick**: Writing - Review & Editing **Michael Zech**: Methodology, Writing - Review & Editing **Roland Zech**: Conceptualization, Methodology, Writing - Review & Editing, Supervision, Project administration, Funding acquisition **Torsten Haberzettl**: Conceptualization, Methodology, Writing - Review & Editing, Supervision, Project administration, Funding acquisition

## Acknowledgements

This study was funded by the German Research Foundation (DFG) (HA 5089/11-1; ZE 860/6-1). Sediment cores were recovered within the RAIN project. PS gratefully acknowledges the support by a fellowship from the state of Thuringia (Landesgraduierstipendium). Particularly acknowledged are Lucas Bittner, Nico Blaubach, Tobias Bromm, Christian David Gregori, Corinna Heinrich, Jana Löhrlin, Heike Maennicke, Carla May, Mike Steinich, Magdalena Wagner and Marianne Zech for assistance in the lab.

## References

- Amelung, W., Cheshire, M.V., Guggenberger, G., 1996. Determination of neutral and acidic sugars in soil by capillary gas-liquid chromatography after trifluoroacetic acid hydrolysis. *Soil Biology and Biochemistry* 28, 1631-1639.
- Bar-Matthews, M., Marean, C.W., Jacobs, Z., Karkanas, P., Fisher, E.C., Herries, A.I.R., Brown, K., Williams, H.M., Bernatchez, J., Ayalon, A., Nilssen, P.J., 2010. A high resolution and continuous isotopic speleothem record of paleoclimate and paleoenvironment from 90 to 53 ka from Pinnacle Point on the south coast of South Africa. *Quaternary Science Reviews* 29, 2131-2145.
- Bateman, M.D., Carr, A.S., Dunajko, A.C., Holmes, P.J., Roberts, D.L., McLaren, S.J., Bryant, R.G., Marker, M.E., Murray-Wallace, C.V., 2011. The evolution of coastal barrier systems: a case study of the Middle-Late Pleistocene Wilderness barriers, South Africa. *Quaternary Science Reviews* 30, 63-81.
- Blaauw, M., Christen, J.A., 2011. Flexible Paleoclimate Age-Depth Models Using an Autoregressive Gamma Process. *Bayesian Analysis* 6, 457-474.
- Bowen, G.J., 2020. The Online Isotopes in Precipitation Calculator, version 3.1. URL: <http://www.waterisotopes.org>.
- Bowen, G.J., Revenaugh, J., 2003. Interpolating the isotopic composition of modern meteoric precipitation. *Water Resources Research* 39, 1-10.
- Bowen, G.J., Wassenaar, L.I., Hobson, K.A., 2005. Global application of stable hydrogen and oxygen isotopes to wildlife forensics. *Oecologia* 143, 337-348.
- Braun, K., Bar-Matthews, M., Ayalon, A., Zilberman, T., Matthews, A., 2017. Rainfall isotopic variability at the intersection between winter and summer rainfall regimes in coastal South Africa (Mossel Bay, Western Cape Province). *South African Journal of Geology* 120, 323-340.
- Braun, K., Bar-Matthews, M., Matthews, A., Ayalon, A., Cowling, R.M., Karkanas, P., Fisher, E.C., Dyez, K., Zilberman, T., Marean, C.W., 2019. Late Pleistocene records of speleothem stable isotopic compositions from Pinnacle Point on the South African south coast. *Quaternary Research* 91, 265-288.
- Braun, K., Bar-Matthews, M., Matthews, A., Ayalon, A., Zilberman, T., Cowling, R.M., Fisher, E.C., Herries, A.I.R., Brink, J.S., Marean, C.W., 2020. Comparison of climate and environment on the

## Chapter 4

- edge of the Palaeo-Agulhas Plain to the Little Karoo (South Africa) in Marine Isotope Stages 5–3 as indicated by speleothems. *Quaternary Science Reviews* 235, 105803.
- Briant, R.M., Bateman, M.D., 2009. Luminescence dating indicates radiocarbon age underestimation in late Pleistocene fluvial deposits from eastern England. *Journal of Quaternary Science* 24, 916-927.
- Briant, R.M., Brock, F., Demarchi, B., Langford, H.E., Penkman, K.E.H., Schreve, D.C., Schwenninger, J.-L., Taylor, S., 2018. Improving chronological control for environmental sequences from the last glacial period. *Quaternary Geochronology* 43, 40-49.
- British Oceanographic data centre (BODC), 2014. GEBCO's gridded bathymetric data sets (GEBCO\_2014 Grid), 30 Arc Second resolution. National Oceanographic Centre, Liverpool.
- Carr, A.S., Boom, A., Dunajko, A., Bateman, M.D., Holmes, P.J., Berrío, J.-C., 2010. New evidence for the age and palaeoecology of the Knysna Formation, South Africa. *South African Journal of Geology* 113, 241-256.
- Cawthra, H.C., Bateman, M.D., Carr, A.S., Compton, J.S., Holmes, P.J., 2014. Understanding Late Quaternary change at the land–ocean interface: a synthesis of the evolution of the Wilderness coastline, South Africa. *Quaternary Science Reviews* 99, 210-223.
- Cawthra, H.C., Bergh, E.W., Wiles, E.A., Compton, J.S., 2021. Late Quaternary deep marine sediment records off southern Africa. *South African Journal of Geology*.
- Cernusak, L.A., Wong, S.C., Farquhar, G.D., 2003. Oxygen isotope composition of phloem sap in relation to leaf water in *Ricinus communis*. *Functional Plant Biology* 30, 1059-1070.
- Chase, B.M., Boom, A., Carr, A.S., Quick, L.J., Reimer, P.J., 2020. High-resolution record of Holocene climate change dynamics from southern Africa's temperate-tropical boundary, Baviaanskloof, South Africa. *Palaeogeography, Palaeoclimatology, Palaeoecology* 539, 109518.
- Chase, B.M., Chevalier, M., Boom, A., Carr, A.S., 2017. The dynamic relationship between temperate and tropical circulation systems across South Africa since the last glacial maximum. *Quaternary Science Reviews* 174, 54-62.
- Chase, B.M., Meadows, M.E., 2007. Late Quaternary dynamics of southern Africa's winter rainfall zone. *Earth-Science Reviews* 84, 103-138.
- Chase, B.M., Quick, L.J., 2018. Influence of Agulhas forcing of Holocene climate change in South Africa's southern Cape. *Quaternary Research* 90, 303-309.
- Cockcroft, M.J., Wilkinson, M.J., Tyson, P.D., 1987. The application of a present-day climatic model to the late quaternary in southern Africa. *Climatic Change* 10, 161-181.
- Cohen, A.L., 1993. A holocene sea surface temperature record in mollusc shells from the South African coast, PhD thesis. University of Cape Town, Cape Town.
- Cohen, A.L., Tyson, P.D., 1995. Sea-surface temperature fluctuations during the Holocene off the south coast of Africa: implications for terrestrial climate and rainfall. *The Holocene* 5, 304-312.
- Colarossi, D., Duller, G.A.T., Roberts, H.M., Tooth, S., Botha, G.A., 2020. A comparison of multiple luminescence chronometers at Voordrag, South Africa. *Quaternary Geochronology* 60, 101094.
- Croudace, I.W., Rindby, A., Rothwell, R.G., 2006. ITRAX: description and evaluation of a new multi-function X-ray core scanner. Geological Society, London, Special Publications 267, 51-63.
- Dansgaard, W., 1964. Stable isotopes in precipitation. *Tellus* 16, 436-468.
- Diefendorf, A.F., Freimuth, E.J., 2017. Extracting the most from terrestrial plant-derived *n*-alkyl lipids and their carbon isotopes from the sedimentary record: A review. *Organic Geochemistry* 103, 1-21.
- du Plessis, N., Chase, B.M., Quick, L.J., Strobel, P., Haberzettl, T., Meadows, M.E., 2021. A c. 650 year pollen and microcharcoal record from Vankervelsvlei, South Africa, in: Runge, J., Gosling, W.D., Lézine, A.-M., Scott, L. (Eds.), *Quaternary Vegetation Dynamics – The African Pollen Database*. CRC Press, London, pp. 301-308.
- DWD Climate Data Center, 2020. Recent and historical dataset: Monthly mean air temperature for station George Airport (CDC-ID 68828) worldwide, version recent, last accessed: 2020-07-01. [https://opendata.dwd.de/climate\\_environment/CDC/observations\\_global/CLIMAT/](https://opendata.dwd.de/climate_environment/CDC/observations_global/CLIMAT/).

- Eglinton, T.I., Eglinton, G., 2008. Molecular proxies for paleoclimatology. *Earth and Planetary Science Letters* 275, 1-16.
- Engelbrecht, C.J., Landman, W.A., 2016. Interannual variability of seasonal rainfall over the Cape south coast of South Africa and synoptic type association. *Climate Dynamics* 47, 295-313.
- Engelbrecht, C.J., Landman, W.A., Engelbrecht, F.A., Malherbe, J., 2015. A synoptic decomposition of rainfall over the Cape south coast of South Africa. *Climate Dynamics* 44, 2589-2607.
- Engelbrecht, F.A., Marean, C.W., Cowling, R.M., Engelbrecht, C.J., Neumann, F.H., Scott, L., Nkoana, R., O'Neal, D., Fisher, E., Shook, E., Franklin, J., Thatcher, M., McGregor, J.L., Van der Merwe, J., Dedekind, Z., Difford, M., 2019. Downscaling Last Glacial Maximum climate over southern Africa. *Quaternary Science Reviews* 226, 105879.
- ESRI Inc., 2020. World Imagery Online Basemap. Esri, DigitalGlobe, GeoEye, Earthstar Geographics, CNES/Airbus DS, USDA, USGS, AeroGRID, IGN, and the GIS User Community.
- Farquhar, G.D., Ehleringer, J.R., Hubick, K.T., 1989. Carbon Isotope Discrimination and Photosynthesis. *Annual Review of Plant Physiology and Plant Molecular Biology* 40, 503-537.
- Fick, S.E., Hijmans, R.J., 2017. WorldClim 2: new 1-km spatial resolution climate surfaces for global land areas. *International Journal of Climatology* 37, 4302-4315.
- Friedman, I., Redfield, A.C., Schoen, B., Harris, J., 1964. The variation of the deuterium content of natural waters in the hydrologic cycle. *Reviews of Geophysics* 2, 177-224.
- Geldenhuis, C.J., 1988. Phytogeography of the southern Cape forest flora. *FRD Occasional report* 45, 158-181.
- Gessler, A., Brandes, E., Buchmann, N., Helle, G., Rennenberg, H., Barnard, R.L., 2009. Tracing carbon and oxygen isotope signals from newly assimilated sugars in the leaves to the tree-ring archive. *Plant, Cell & Environment* 32, 780-795.
- Haberzettl, T., Baade, J., Compton, J., Daut, G., Dupont, L., Finch, J., Frenzel, P., Green, A., Hahn, A., Hebbeln, D., Helmschrot, J., Humphries, M., Kasper, T., Kirsten, K., Mäusbacher, R., Meadows, M., Meschner, S., Quick, L., Schefuß, E., Wündsche, M., Zabel, M., 2014. Paleoenvironmental investigations using a combination of terrestrial and marine sediments from South Africa - The RAIN (Regional Archives for Integrated iNvestigations) approach. *Zentralblatt für Geologie und Paläontologie, Teil I* 2014, 55-73.
- Hahn, A., Schefuß, E., Andò, S., Cawthra, H.C., Frenzel, P., Kugel, M., Meschner, S., Mollenhauer, G., Zabel, M., 2017. Southern Hemisphere anticyclonic circulation drives oceanic and climatic conditions in late Holocene southernmost Africa. *Climate of the Past* 13, 649-665.
- Hahn, A., Schefuß, E., Groeneveld, J., Miller, C., Zabel, M., 2021. Glacial to interglacial climate variability in the southeastern African subtropics (25–20° S). *Climate of the Past* 17, 345-360.
- Harris, C., Burgers, C., Miller, J., Rawoot, F., 2010. O- and H-isotope record of Cape Town rainfall from 1996 to 2008, and its application to recharge studies of Table Mountain groundwater, South Africa. *South African Journal of Geology* 113, 33-56.
- Hepp, J., Mayr, C., Rozanski, K., Schäfer, I.K., Tuthorn, M., Glaser, B., Juchelka, D., Stichler, W., Zech, R., Zech, M., 2021. Validation of a coupled  $\delta^2\text{H}_{\text{alkane}}-\delta^{18}\text{O}_{\text{sugar}}$  paleohygrometer approach based on a climate chamber experiment. *Biogeosciences* 18, 5363–5380.
- Hepp, J., Schäfer, I.K., Lanny, V., Franke, J., Bliedtner, M., Rozanski, K., Glaser, B., Zech, M., Eglinton, T.I., Zech, R., 2020. Evaluation of bacterial glycerol dialkyl glycerol tetraether and  $^2\text{H}-^{18}\text{O}$  biomarker proxies along a central European topsoil transect. *Biogeosciences* 17, 741-756.
- Hepp, J., Tuthorn, M., Zech, R., Mügler, I., Schlütz, F., Zech, W., Zech, M., 2015. Reconstructing lake evaporation history and the isotopic composition of precipitation by a coupled  $\delta^{18}\text{O}-\delta^2\text{H}$  biomarker approach. *Journal of Hydrology* 529, 622-631.
- Hepp, J., Wüthrich, L., Bromm, T., Bliedtner, M., Schäfer, I.K., Glaser, B., Rozanski, K., Sirocko, F., Zech, R., Zech, M., 2019. How dry was the Younger Dryas? Evidence from a coupled  $\delta^2\text{H}-\delta^{18}\text{O}$  biomarker paleohygrometer applied to the Gemündener Maar sediments, Western Eifel, Germany. *Clim. Past* 15, 713-733.
- Hepp, J., Zech, R., Rozanski, K., Tuthorn, M., Glaser, B., Greule, M., Keppler, F., Huang, Y., Zech, W., Zech, M., 2017. Late Quaternary relative humidity changes from Mt. Kilimanjaro, based on a

## Chapter 4

- coupled  $^2\text{H}$ - $^{18}\text{O}$  biomarker paleohygrometer approach. *Quaternary International* 438, Part B, 116-130.
- Herrmann, N., Boom, A., Carr, A.S., Chase, B.M., West, A.G., Zabel, M., Schefuß, E., 2017. Hydrogen isotope fractionation of leaf wax n-alkanes in southern African soils. *Organic Geochemistry* 109, 1-13.
- Heyng, A.M., Mayr, C., Lücke, A., Wissel, H., Striewski, B., 2014. Late Holocene hydrologic changes in northern New Zealand inferred from stable isotope values of aquatic cellulose in sediments from Lake Pupuke. *Journal of Paleolimnology* 51, 485-497.
- Hogg, A.G., Heaton, T.J., Hua, Q., Palmer, J.G., Turney, C.S.M., Southon, J., Bayliss, A., Blackwell, P.G., Boswijk, G., Bronk Ramsey, C., Pearson, C., Petchey, F., Reimer, P., Reimer, R., Wacker, L., 2020. SHCal20 Southern Hemisphere calibration, 0–55,000 years cal BP. *Radiocarbon*, 1-20.
- Horita, J., Wesolowski, D.J., 1994. Liquid-vapor fractionation of oxygen and hydrogen isotopes of water from the freezing to the critical temperature. *Geochimica et Cosmochimica Acta* 58, 3425-3437.
- Hou, J., D'Andrea, W.J., MacDonald, D., Huang, Y., 2007. Evidence for water use efficiency as an important factor in determining the  $\delta\text{D}$  values of tree leaf waxes. *Organic Geochemistry* 38, 1251-1255.
- Howard-Williams, C., 1979. Distribution, biomass and role of aquatic macrophytes in Lake Sibaya., in: Allanson, B.R. (Ed.), *Lake Sibaya*,. Dr W Junk Publishers, Boston, pp. 88–107.
- Illenberger, W.K., 1996. The geomorphologic evolution of the Wilderness dune cordons, South Africa. *Quaternary International* 33, 11-20.
- Irving, S.J.E., 1998. Late quaternary palaeoenvironments at Vankervelsvlei, near Knysna, South Africa, Master thesis. University of Cape Town, Rondebosch.
- Irving, S.J.E., Meadows, M.E., 1997. Radiocarbon chronology and organic matter accumulation at Vankervelsvlei, near Knysna, South Africa. *South African Geographical Journal* 79, 101-105.
- Johnson, M.R., Anhausser, C.R., Thomas, R.J., 2006. *The geology of South Africa*. Geological Society of South Africa, Johannesburg/Council for Geoscience, Pretoria.
- Lemma, B., Bittner, L., Glaser, B., Kebede, S., Nemomissa, S., Zech, W., Zech, M., 2021.  $\delta^2\text{H}_{n\text{-alkane}}$  and  $\delta^{18}\text{O}_{\text{sugar}}$  biomarker proxies from leaves and topsoils of the Bale Mountains, Ethiopia, and implications for paleoclimate reconstructions. *Biogeochemistry* 153, 135-153.
- Lisiecki, L.E., Raymo, M.E., 2005. A Pliocene-Pleistocene stack of 57 globally distributed benthic  $\delta^{18}\text{O}$  records. *Paleoceanography* 20.
- Mandiola, S.R., Grundling, A.T., Grundling, P.-L., van der Plicht, J., van der Waal, B.C.W., Grootjans, A.P., 2021. Ecohydrological analysis of a South African through-flow mire: Vankervelsvlei revisited. *Mires and Peat* 27.
- Merlivat, L., 1978. Molecular diffusivities of  $\text{H}_2$   $^{16}\text{O}$ ,  $\text{HD}^{16}\text{O}$ , and  $\text{H}_2$   $^{18}\text{O}$  in gases. *The Journal of Chemical Physics* 69, 2864-2871.
- Miller, C., Hahn, A., Liebrand, D., Zabel, M., Schefuß, E., 2020. Mid- and low latitude effects on eastern South African rainfall over the Holocene. *Quaternary Science Reviews* 229, 106088.
- Mucina, L., Rutherford, M.C., 2006. *The vegetation of South Africa, Lesotho and Swaziland*. SANBI, Pretoria.
- NASA JPL, 2013. NASA Shuttle Radar Topography Mission Global 1 arc second [Data set]. NASA EOSDIS Land Processes DAAC. Accessed 2020-12-29 from <https://doi.org/10.5067/MEaSURES/SRTM/SRTMGL1.003>.
- Neumann, F.H., Stager, J.C., Scott, L., Venter, H.J.T., Weyhenmeyer, C., 2008. Holocene vegetation and climate records from Lake Sibaya, KwaZulu-Natal (South Africa). *Review of Palaeobotany and Palynology* 152, 113-128.
- Palstra, S.W.L., Wallinga, J., Viveen, W., Schoorl, J.M., van den Berg, M., van der Plicht, J., 2021. Cross-comparison of last glacial radiocarbon and OSL ages using periglacial fan deposits. *Quaternary Geochronology* 61, 101128.

- Quick, L.J., Carr, A.S., Meadows, M.E., Boom, A., Bateman, M.D., Roberts, D.L., Reimer, P.J., Chase, B.M., 2015. A late Pleistocene–Holocene multi-proxy record of palaeoenvironmental change from Still Bay, southern Cape Coast, South Africa. *Journal of Quaternary Science* 30, 870-885.
- Quick, L.J., Chase, B.M., Wündsche, M., Kirsten, K., Chevalier, M., Mäusbacher, R., Meadows, M., Haberzettl, T., 2018. A high-resolution record of Holocene climate and vegetation dynamics from the southern Cape coast of South Africa: pollen and microcharcoal evidence from Eilandvlei. *Journal of Quaternary Science*, 1-14.
- Quick, L.J., Meadows, M.E., Bateman, M.D., Kirsten, K.L., Mäusbacher, R., Haberzettl, T., Chase, B.M., 2016. Vegetation and climate dynamics during the last glacial period in the fynbos-afrotropical forest ecotone, southern Cape, South Africa. *Quaternary International* 404, Part B, 136-149.
- Reinwarth, B., Franz, S., Baade, J., Haberzettl, T., Kasper, T., Daut, G., Helmschrot, J., Kirsten, K.L., Quick, L.J., Meadows, M.E., Mäusbacher, R., 2013. A 700-Year Record on the Effects of Climate and Human Impact on the Southern Cape Coast Inferred from Lake Sediments of Eilandvlei, Wilderness Embayment, South Africa. *Geografiska Annaler Series A - Physical Geography* 95, 345-360.
- Sachse, D., Billault, I., Bowen, G.J., Chikaraishi, Y., Dawson, T.E., Feakins, S.J., Freeman, K.H., Magill, C.R., McInerney, F.A., van der Meer, M.T.J., Polissar, P., Robins, R.J., Sachs, J.P., Schmidt, H.L., Sessions, A.L., White, J.W.C., West, J.B., Kahmen, A., 2012. Molecular Paleohydrology: Interpreting the Hydrogen- Isotopic Composition of Lipid Biomarkers from Photosynthesizing Organisms. *Annual Review of Earth and Planetary Sciences* 40, 221-249.
- Schäfer, I.K., Bliedtner, M., Wolf, D., Kolb, T., Zech, J., Faust, D., Zech, R., 2018. A  $\delta^{13}\text{C}$  and  $\delta^2\text{H}$  leaf wax record from the Late Quaternary loess-paleosol sequence El Paraíso, Central Spain. *Palaeogeography, Palaeoclimatology, Palaeoecology* 507, 52-59.
- Schmidt, H.-L., Werner, R.A., Roßmann, A., 2001.  $^{18}\text{O}$  Pattern and biosynthesis of natural plant products. *Phytochemistry* 58, 9-32.
- Scott, L., Lee-Thorp, J.A., 2004. Holocene climatic trends and rhythms in southern Africa, in: Battarbee, R.W., Gasse, F., Stickley, C.E. (Eds.), *Past Climate Variability through Europe and Africa*. Springer, Dordrecht, pp. 69-91.
- Sessions, A.L., 2016. Factors controlling the deuterium contents of sedimentary hydrocarbons. *Organic Geochemistry* 96, 43-64.
- Sessions, A.L., Burgoyne, T.W., Schimmelmann, A., Hayes, J.M., 1999. Fractionation of hydrogen isotopes in lipid biosynthesis. *Organic Geochemistry* 30, 1193-1200.
- Shi, F., Rao, Z., Cao, J., Huang, C., Wu, D., Yang, W., Sun, W., 2019a. Meltwater is the dominant water source controlling  $\alpha$ -cellulose  $\delta^{18}\text{O}$  in a vascular-plant-dominated alpine peatland in the Altai Mountains, Central Asia. *Journal of Hydrology* 572, 192-205.
- Shi, F., Rao, Z., Li, Y., Cao, J., Shi, X., Li, C., Sun, W., 2019b. Precipitation  $\delta^{18}\text{O}$  Recorded by the  $\alpha$ -Cellulose  $\delta^{18}\text{O}$  of Plant Residues in Surface Soils: Evidence From a Broad Environmental Gradient in Inland China. *Global Biogeochemical Cycles* 33, 1440-1468.
- Singarayer, J.S., Burrough, S.L., 2015. Interhemispheric dynamics of the African rainbelt during the late Quaternary. *Quaternary Science Reviews* 124, 48-67.
- Sternberg, L., DeNiro, M.J., 1983. Isotopic Composition of Cellulose from C3, C4 and CAM Plants Growing Near One Another. *Science* 220, 947-949.
- Sternberg, L., Deniro, M.J., Savidge, R.A., 1986. Oxygen Isotope Exchange between Metabolites and Water during Biochemical Reactions Leading to Cellulose Synthesis. *Plant Physiology* 82, 423-427.
- Strobel, P., Bliedtner, M., Carr, A.S., Frenzel, P., Klaes, B., Salazar, G., Struck, J., Szidat, S., Zech, R., Haberzettl, T., 2021. Holocene sea level and environmental change at the southern Cape - an 8.5 kyr multi-proxy paleoclimate record from lake Voëlvlei, South Africa. *Climate of the Past* 17, 1567-1586.
- Strobel, P., Haberzettl, T., Bliedtner, M., Struck, J., Glaser, B., Zech, M., Zech, R., 2020. The potential of  $\delta^2\text{H}_{n\text{-alkanes}}$  and  $\delta^{18}\text{O}_{\text{sugar}}$  for paleoclimate reconstruction – A regional calibration study for South Africa. *Science of The Total Environment* 716, 137045.

## Chapter 4

- Strobel, P., Kasper, T., Frenzel, P., Schitteck, K., Quick, L.J., Meadows, M.E., Mäusbacher, R., Haberzettl, T., 2019. Late Quaternary palaeoenvironmental change in the year-round rainfall zone of South Africa derived from peat sediments from Vankervelsvlei. *Quaternary Science Reviews* 218, 200-214.
- Struck, J., Bliedtner, M., Strobel, P., Bittner, L., Bazarradnaa, E., Andreeva, D., Zech, W., Glaser, B., Zech, M., Zech, R., 2020. Leaf Waxes and Hemicelluloses in Topsoils Reflect the  $\delta^2\text{H}$  and  $\delta^{18}\text{O}$  Isotopic Composition of Precipitation in Mongolia. *Frontiers in Earth Science* 8.
- Stuiver, M., Reimer, P.J., Reimer, R.W., 2020. CALIB 8.2 [WWW program] at <http://calib.org> (Accessed: 2020-8-20).
- Talma, A.S., Vogel, J.C., 1992. Late Quaternary paleotemperatures derived from a speleothem from Cango Caves, Cape Province, South Africa. *Quaternary Research* 37, 203-213.
- Trabucco, A., Zomer, R., 2019. Global Aridity Index and Potential Evapotranspiration (ET0) Climate Database v2. figshare. Fileset.
- Tuthorn, M., Zech, M., Ruppenthal, M., Oelmann, Y., Kahmen, A., Valle, H.F.d., Wilcke, W., Glaser, B., 2014. Oxygen isotope ratios ( $^{18}\text{O}/^{16}\text{O}$ ) of hemicellulose-derived sugar biomarkers in plants, soils and sediments as paleoclimate proxy II: Insight from a climate transect study. *Geochimica et Cosmochimica Acta* 126, 624-634.
- Tuthorn, M., Zech, R., Ruppenthal, M., Oelmann, Y., Kahmen, A., del Valle, H.F., Eglinton, T., Rozanski, K., Zech, M., 2015. Coupling  $\delta^2\text{H}$  and  $\delta^{18}\text{O}$  biomarker results yields information on relative humidity and isotopic composition of precipitation - a climate transect validation study. *Biogeosciences* 12, 3913-3924.
- Tyson, P.D., Preston-Whyte, R.A., 2000. *The Weather and Climate of Southern Africa*. Oxford University Press, Cape Town.
- van Zinderen Bakker, E.M., 1976. The evolution of late Quaternary paleoclimates of Southern Africa. *Palaeoecology Africa* 9 9, 160-202.
- Voelker, S.L., Brooks, J.R., Meinzer, F.C., Roden, J., Pazdur, A., Pawelczyk, S., Hartsough, P., Snyder, K., Plavcová, L., Šantrůček, J., 2014. Reconstructing relative humidity from plant  $\delta^{18}\text{O}$  and  $\delta\text{D}$  as deuterium deviations from the global meteoric water line. *Ecological Applications* 24, 960-975.
- Voelker, S.L., Stambaugh, M.C., Guyette, R.P., Feng, X., Grimley, D.A., Leavitt, S.W., Panyushkina, I., Grimm, E.C., Marsicek, J.P., Shuman, B., Brandon Curry, B., 2015. Deglacial Hydroclimate of Midcontinental North America. *Quaternary Research* 83, 336-344.
- Waelbroeck, C., Labeyrie, L., Michel, E., Duplessy, J.C., McManus, J.F., Lambeck, K., Balbon, E., Labracherie, M., 2002. Sea-level and deep water temperature changes derived from benthic foraminifera isotopic records. *Quaternary Science Reviews* 21, 295-305.
- Weldon, D., Reason, C.J.C., 2014. Variability of rainfall characteristics over the South Coast region of South Africa. *Theoretical and Applied Climatology* 115, 177-185.
- Wirth, S.B., Sessions, A.L., 2016. Plant-wax D/H ratios in the southern European Alps record multiple aspects of climate variability. *Quaternary Science Reviews* 148, 176-191.
- Wissel, H., Mayr, C., Lücke, A., 2008. A new approach for the isolation of cellulose from aquatic plant tissue and freshwater sediments for stable isotope analysis. *Organic Geochemistry* 39, 1545-1561.
- Wündsche, M., Haberzettl, T., Cawthra, H.C., Kirsten, K.L., Quick, L.J., Zabel, M., Frenzel, P., Hahn, A., Baade, J., Daut, G., Kasper, T., Meadows, M.E., Mäusbacher, R., 2018. Holocene environmental change along the southern Cape coast of South Africa – Insights from the Eilandvlei sediment record spanning the last 8.9 kyr. *Global and Planetary Change* 163, 51-66.
- Wündsche, M., Haberzettl, T., Kirsten, K.L., Kasper, T., Zabel, M., Dietze, E., Baade, J., Daut, G., Meschner, S., Meadows, M.E., Mäusbacher, R., 2016. Sea level and climate change at the southern Cape coast, South Africa, during the past 4.2 kyr. *Palaeogeography Palaeoclimatology Palaeoecology* 446, 295-307.
- Yakir, D., DeNiro, M.J., 1990. Oxygen and Hydrogen Isotope Fractionation during Cellulose Metabolism in *Lemna gibba* L. *Plant Physiology* 93, 325-332.



- Zech, M., Glaser, B., 2009. Compound-specific  $\delta^{18}\text{O}$  analyses of neutral sugars in soils using gas chromatography–pyrolysis–isotope ratio mass spectrometry: problems, possible solutions and a first application. *Rapid Communications in Mass Spectrometry* 23, 3522-3532.
- Zech, M., Mayr, C., Tuthorn, M., Leiber-Sauheitl, K., Glaser, B., 2014. Oxygen isotope ratios ( $^{18}\text{O}/^{16}\text{O}$ ) of hemicellulose-derived sugar biomarkers in plants, soils and sediments as paleoclimate proxy I: Insight from a climate chamber experiment. *Geochimica et Cosmochimica Acta* 126, 614-623.
- Zech, M., Tuthorn, M., Detsch, F., Rozanski, K., Zech, R., Zöller, L., Zech, W., Glaser, B., 2013. A 220ka terrestrial  $\delta^{18}\text{O}$  and deuterium excess biomarker record from an eolian permafrost paleosol sequence, NE-Siberia. *Chemical Geology* 360-361, 220-230.
- Zech, M., Werner, R.A., Juchelka, D., Kalbitz, K., Buggle, B., Glaser, B., 2012. Absence of oxygen isotope fractionation/exchange of (hemi-) cellulose derived sugars during litter decomposition. *Organic Geochemistry* 42, 1470-1475.
- Zech, M., Zech, R., Rozanski, K., Gleixner, G., Zech, W., 2015. Do *n*-alkane biomarkers in soils/sediments reflect the  $\delta^2\text{H}$  isotopic composition of precipitation? A case study from Mt. Kilimanjaro and implications for paleoaltimetry and paleoclimate research. *Isotopes in Environmental and Health Studies* 51, 508-524.
- Zhao, X., Dupont, L., Schefuß, E., Meadows, M.E., Hahn, A., Wefer, G., 2016. Holocene vegetation and climate variability in the winter and summer rainfall zones of South Africa. *The Holocene* 26, 843-857.

## Chapter 5

---

### Synthesis and discussion

---

Author: Paul Strobel

## 5 Synthesis and discussion

---

During the past decades, several studies aimed to reconstruct Late Quaternary dynamics of the two major atmospheric circulation systems, i.e., the temperate mid-latitude Westerlies and the tropical Easterlies, providing precipitation to South Africa today. Special focus has been on South Africa's southern Cape coast, because it is currently situated in the Year-round Rainfall Zone (YRZ) and receives precipitation from both Westerlies and Easterlies (Haberzettl et al., 2014; Neumann and Scott, 2018; van Zinderen Bakker, 1976). However, existing records often lack proper chronological control and temporal resolution or use rather indirect hydrological proxies to reconstruct past environmental and climate changes.

To overcome this situation, the hydrogen isotopic composition of leaf wax-derived *n*-alkanes ( $\delta^2\text{H}_{n\text{-alkane}}$ ) and the oxygen isotopic composition of hemicellulose-derived sugars ( $\delta^{18}\text{O}_{\text{sugar}}$ ) were analyzed on modern reference material (i.e., topsoils) to evaluate their potential to serve as direct hydrological proxies (Chapter 2; Strobel et al., 2020). Additionally, coupling both isotopes into a coupled  $\delta^2\text{H}_{n\text{-alkane}}-\delta^{18}\text{O}_{\text{sugar}}$  (paleohygrometer) approach possibly enables to quantitatively reconstruct the isotopic composition of precipitation and relative humidity in South Africa (Chapter 2). The results from the regionally calibrated biomarker isotopes from South Africa (Chapter 2) are further discussed in context with existing studies on modern reference material from South Africa to contribute to a comprehensive understanding of potentials and limitations of biomarker analyzes for paleoclimate reconstructions in the country (Section 5.1).

To reconstruct paleoenvironmental and paleoclimatic changes in South Africa, and in particular paleohydrological changes along the southern Cape coast, two suitable sediment archives have been identified. Those are Lake Voëlvlei (Chapter 3; Strobel et al., 2021) and Vankervelsvlei (Chapter 4; Strobel et al., submitted). Vankervelsvlei was target for the application of a broad multi-proxy approach including the coupled  $\delta^2\text{H}_{n\text{-alkane}}-\delta^{18}\text{O}_{\text{sugar}}$  (paleohygrometer) approach, which was applied for the first time in South Africa and therefore likely enables most robust reconstruction of paleohydrological dynamics in South Africa. The reconstructed paleohydrological conditions from Vankervelsvlei are compared to the record from Lake Voëlvlei, where a similar multi-proxy approach with biomarker  $\delta^2\text{H}_{n\text{-alkane}}$  was applied, and further regional records, to draw a comprehensive picture of past hydrological changes along South Africa's southern Cape coast during major parts of the Holocene (Section 5.2.1). Additionally, potential drivers of the reconstructed paleohydrological changes are discussed (Section 5.2.2). Vankervelsvlei also provides sediments of Late Quaternary age (Chapter 4) and past environmental and hydrological dynamics at the site as well as their potential driving forces are discussed in context of further regional records to draw a comprehensive climate picture also on longer timescales.

### 5.1 Regional evaluation of $\delta^2\text{H}_{n\text{-alkane}}$ , $\delta^{18}\text{O}_{\text{sugar}}$ and the coupled isotope approach for reconstructing precipitation and relative humidity in South Africa

The compound-specific hydrogen isotope signature of leaf wax-derived  $n$ -alkanes ( $\delta^2\text{H}_{n\text{-alkane}}$ ) and compound-specific oxygen isotope signature of hemicellulose-derived sugars ( $\delta^{18}\text{O}_{\text{sugar}}$ ) are valuable proxies to better understand past environmental, climatic and particularly hydrological conditions (Chapter 2). Generally,  $\delta^2\text{H}_{n\text{-alkane}}$  and  $\delta^{18}\text{O}_{\text{sugar}}$  incorporate the isotopic signature of precipitation ( $\delta^2\text{H}_p$  and  $\delta^{18}\text{O}_p$ ) but can be modified by soil and leaf water evapotranspirative enrichment as well as variations in biosynthetic fractionation. Thus, considered alone,  $\delta^2\text{H}_{n\text{-alkane}}$  and  $\delta^{18}\text{O}_{\text{sugar}}$  signals have to be carefully interpreted. However, they are very powerful when considered together into a coupled  $\delta^2\text{H}_{n\text{-alkane}}-\delta^{18}\text{O}_{\text{sugar}}$  approach, because then they allow quantitative reconstruction of the isotopic composition of precipitation and relative humidity. However, for robust paleoclimatic and paleohydrological interpretations, the environmental drivers of the isotopic signal in both biomarkers have to be regionally evaluated. To do so, results from Chapter 2 are discussed in the context of existing regional calibration studies from South Africa in the following.

So far, three studies investigated  $\delta^2\text{H}_{n\text{-alkane}}$  on modern reference material (i.e., topsoils) in South Africa (Fig. 5.1) focusing on different parts of the country. Topsoils from southern parts of the WRZ and YRZ (Strobel et al., 2020) as well as SRZ (Hahn et al., 2018) were discussed in Chapter 2, while Herrmann et al. (2017) focused on samples from the northern parts of the WRZ, YRZ and SRZ (Fig. 5.1). The  $n$ -alkane chain-lengths used for  $\delta^2\text{H}_{n\text{-alkane}}$  analyzes in those studies differ. Strobel et al., (2020; Chapter 2) and Herrmann et al. (2017) used an amount weighted mean of the most abundant  $n$ -alkanes ( $\text{C}_{31}$  and  $\text{C}_{33}$  as well as  $\text{C}_{29}$  and  $\text{C}_{31}$ , respectively) for  $\delta^2\text{H}_{n\text{-alkane}}$  while Hahn et al. (2018) only provide  $\delta^2\text{H}_{n\text{-alkane}}$  data for the  $\text{C}_{29}$   $n$ -alkane. For hemicellulose-derived sugars, only the study by Strobel et al. (2020; Chapter 2) provides  $\delta^{18}\text{O}_{\text{sugar}}$  from the most abundant compound (Arabinose) in modern reference material from South Africa.

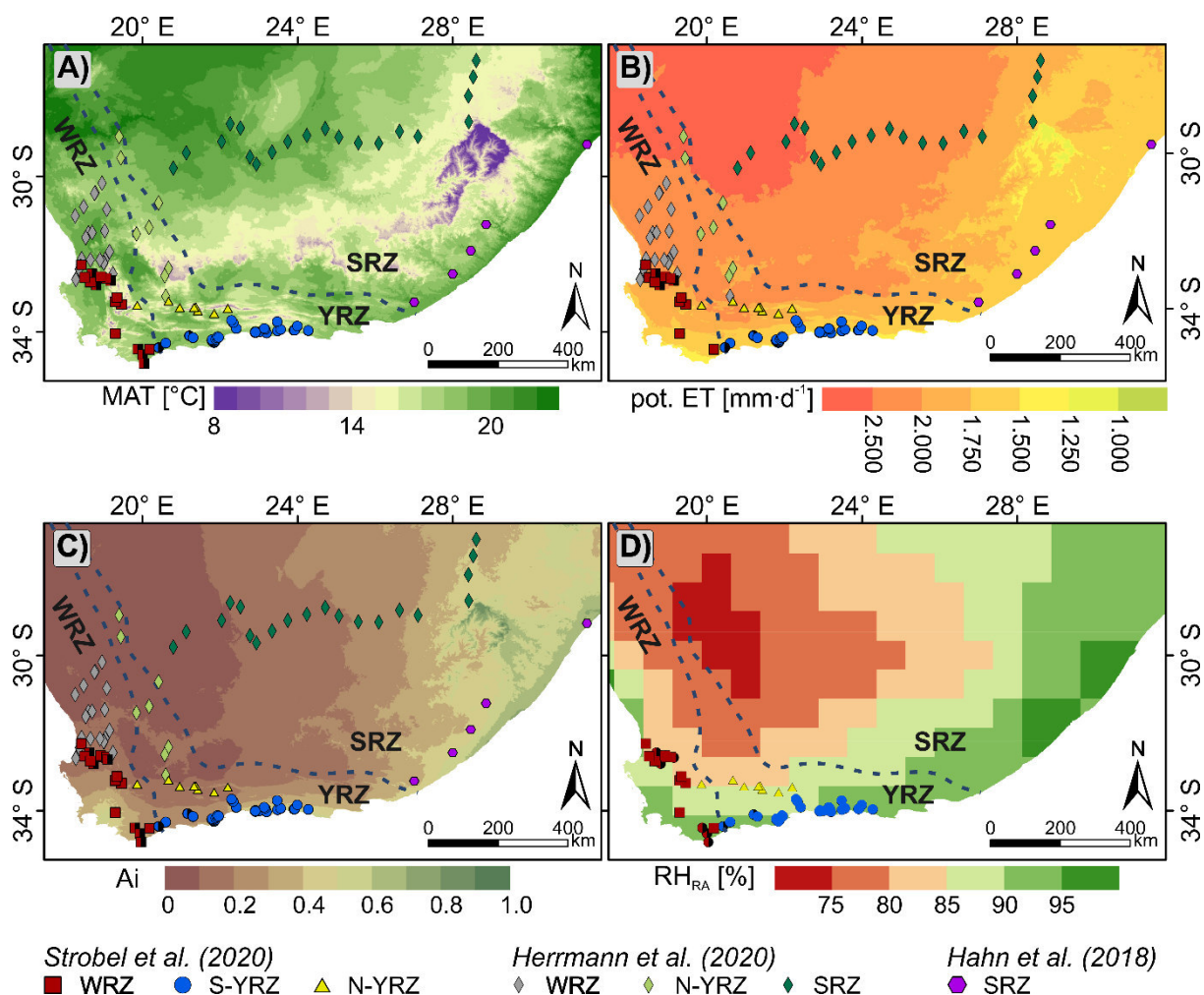


Figure 5.1: Location of topsoil samples from studies discussed in Chapter 2 (Strobel et al., 2020; Hahn et al., 2018) and Herrmann et al. (2017), compared to selected environmental parameters in southern Africa. A) Mean annual temperature (MAT) (Fick and Hijmans, 2017); B) potential evapotranspiration (pot. ET) (Trabucco and Zomer, 2019), C) Aridity index (Ai: <0.03 hyper arid; 0.03–0.2 arid; 0.2–0.5 semi-arid; 0.5–0.65 dry sub-humid; >0.65 humid) (Trabucco and Zomer, 2019) and D) relative humidity based on *ERA-Interim* reanalysis data (RH<sub>RA</sub>; Dee et al., 2011; see Chapter 2 for calculation). Samples from Strobel et al. (2020) were analyzed for  $\delta^2\text{H}_{n\text{-alkane}}$  and  $\delta^{18}\text{O}_{\text{sugar}}$  while those from Herrmann et al. (2017) and Hahn et al. (2018) were only analyzed for  $\delta^2\text{H}_{n\text{-alkane}}$ . This explains that RH is only plotted for data from Strobel et al. (2020). Abbreviations: WRZ – winter rainfall Zone; S-YRZ – southern year-round rainfall zone; N-YRZ – northern year-round rainfall zone; SRZ – summer rainfall zone.

In the regional compilation of  $\delta^2\text{H}_{n\text{-alkane}}$  from South African topsoils, the data by Strobel et al. (2020), Hahn et al. (2018) and Herrmann et al. (2017) show significant correlation between  $\delta^2\text{H}_{n\text{-alkane}}$  and  $\delta^2\text{H}_p$  (Strobel et al., 2020, Fig. 5.2). However, when combining these data sets,  $\delta^2\text{H}_{n\text{-alkane}}$  values from the northern parts of SRZ, WRZ and YRZ investigated by Herrmann et al. (2017) cause a wider scatter in  $\delta^2\text{H}_{n\text{-alkane}}$  compared to the compilation discussed in Chapter 2. In contrast,  $\delta^{18}\text{O}_{\text{sugar}}$  has been analyzed in South Africa within this thesis for the first time (Chapter 2; Strobel et al., 2020) and no correlation could be found between  $\delta^{18}\text{O}_{\text{sugar}}$  and  $\delta^{18}\text{O}_p$  (Fig. 5.2).

## Chapter 5

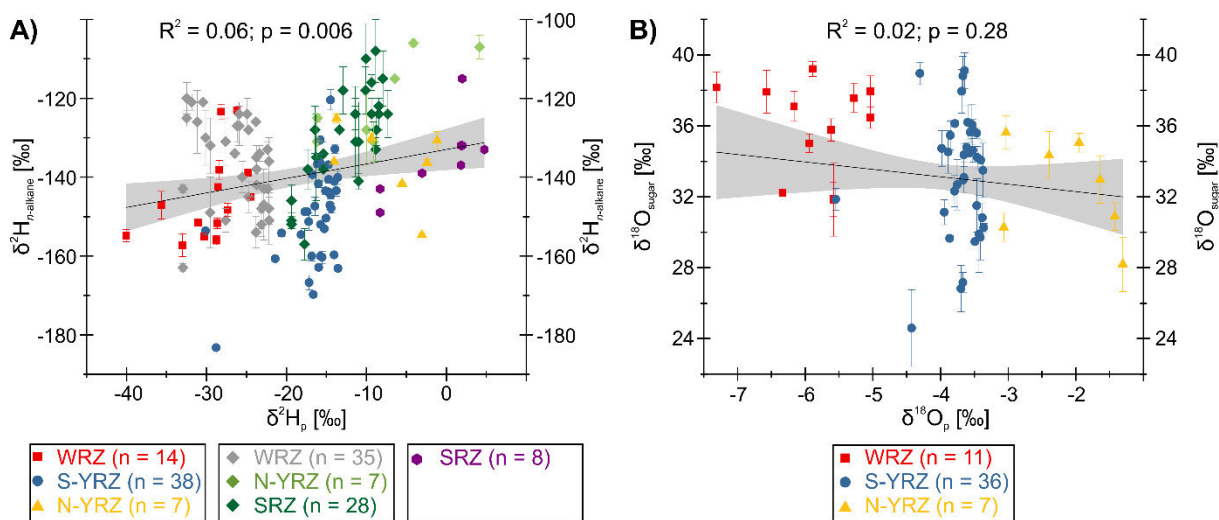


Figure 5.2: Correlation of A)  $\delta^2\text{H}_{n\text{-alkane}}$  with  $\delta^2\text{H}_p$  and B)  $\delta^{18}\text{O}_{\text{sugar}}$  with  $\delta^{18}\text{O}_p$  related to the seasonal precipitation of the sampling sites (WRZ: JJA; S-YRZ: mean annual; N-YRZ and SRZ: DJF) derived from the *Online Isotope Precipitation Calculator* (Bowen, 2020; Bowen et al., 2005) and weighted by monthly precipitation data by Fick and Hijmans (2017). The overall linear fit (black line) including  $R^2$ , 95% confidence interval (grey area) and p-value were calculated. The figure was modified after Strobel et al. (2020) (Chapter 2); data derive from the following studies: red, blue and yellow data points (Chapter 2; Strobel et al., 2020); grey, light green and dark green data points (Herrmann et al., 2017); pink data points (Chapter 2; Hahn et al., 2018).

To test  $\delta^2\text{H}_{n\text{-alkane}}$  and  $\delta^{18}\text{O}_{\text{sugar}}$  for potential environmental control, the apparent fractionation ( $\epsilon_{\text{app } 2\text{H}}$  and  $\epsilon_{\text{app } 18\text{O}}$ ) was calculated, which is the difference of the isotopic composition of the biomarker signals ( $\delta^2\text{H}_{n\text{-alkane}}$  and  $\delta^{18}\text{O}_{\text{sugar}}$ ) and precipitation ( $\delta^2\text{H}_p$  and  $\delta^{18}\text{O}_p$ ). Apparent fractionation was then correlated against the environmental parameters mean annual temperature, potential evapotranspiration and an aridity index. The compilation of the data discussed in Chapter 2 (Strobel et al., 2020; Hahn et al., 2018) shows no correlation of  $\epsilon_{\text{app } 2\text{H}}$  with the aforementioned environmental parameters on regional scale along the southern coast. Adding the samples investigated by Herrmann et al. (2017),  $\epsilon_{\text{app } 2\text{H}}$  significantly correlates with potential evapotranspiration and an aridity index while there is still no correlation with mean annual temperature (Fig. 5.3). The environmental gradients covered by the topsoil samples discussed in Chapter 2 (Hahn et al., 2018; Strobel et al., 2020) are extended by those from Herrmann et al. (2017) and the number of samples located in the arid parts of the SRZ, WRZ and YRZ become distinctly increased. However, there is still a lack of samples in the humid parts of the SRZ (Fig. 5.1), which limit the final evaluation of  $\epsilon_{\text{app } 2\text{H}}$  providing potential for misinterpretation of the available and still incomplete dataset.

On a regional scale, several previous studies suggest dependencies of  $\epsilon_{\text{app } 2\text{H}}$  on aridity (Li et al., 2019), precipitation (Aichner et al., 2010; Hou et al., 2018) or relative humidity (Hou et al., 2008; Hou et al., 2018). Additionally, a wide range in  $\epsilon_{\text{app } 2\text{H}}$  has been reported with substantially smaller values for arid than humid climates (Feakins and Sessions, 2010; Li et al., 2019; Polissar and Freeman, 2010; Smith and Freeman, 2006). Moreover,  $\epsilon_{\text{app } 2\text{H}}$  values depend on

the plants growth form with monocotyledonous plants (grasses) showing more negative  $\epsilon_{\text{app } 2\text{H}}$  values compared to dicotyledonous plants (shrubs, deciduous trees) (Hepp et al., 2021; Hepp et al., 2020; Lemma et al., 2021; Struck et al., 2020). Conversely, Struck et al. (2020) found no climate dependency on  $\epsilon_{\text{app } 2\text{H}}$  in Mongolia and Struck (2022) suggests apparent fractionation to range from  $-173$  to  $78\text{‰}$  with a mean value of  $-132 \pm 15\text{‰}$  on global scale, but also noted a substantially larger scatter in humid than in arid climates.

For  $\epsilon_{\text{app } 18\text{O}}$ , significant correlations with potential evapotranspiration and an aridity index occur while no correlation exists to mean annual temperature (Fig. 5.3, Chapter 2). These findings highlight that the  $\delta^{18}\text{O}_{\text{sugar}}$  signal is a valuable proxy for evapotranspirative enrichment, but  $\delta^{18}\text{O}_{\text{sugar}}$  signals alone cannot be used to infer past changes in  $\delta^{18}\text{O}_p$  in South Africa (Chapter 2; Strobel et al., 2020).

These findings are in good agreement with previous studies from Argentina (Tuthorn et al., 2014; Tuthorn et al., 2015) and Ethiopia (Lemma et al., 2021), which also show no significant relationship between  $\delta^{18}\text{O}_{\text{sugar}}$  and  $\delta^{18}\text{O}_p$ .  $\epsilon_{\text{app } 18\text{O}}$  in these studies highlights a distinct climate-related evapotranspirative enrichment on the biomarker signal which ranges from  $29.5\text{‰}$  in humid to  $53.6\text{‰}$  in arid regions as compiled in Struck (2022). Conversely, Struck et al. (2022) found no climate dependency on  $\epsilon_{\text{app } 18\text{O}}$  and thus  $\delta^{18}\text{O}_{\text{sugar}}$  to reflect  $\delta^{18}\text{O}_p$  in Mongolia. Like  $\epsilon_{\text{app } 2\text{H}}$ ,  $\epsilon_{\text{app } 18\text{O}}$  shows dependency on the plant's growth form with monocotyledonous plants (grasses) showing smaller  $\epsilon_{\text{app } 18\text{O}}$  values compared to dicotyledonous plants (shrubs, deciduous trees), which was also found in studies from Europe (Hepp et al., 2020), Ethiopia (Lemma et al., 2021) and a climate chamber experiment (Hepp et al., 2021).

Overall,  $\delta^2\text{H}_{n\text{-alkane}}$  shows potential to serve as a proxy to reconstruct  $\delta^2\text{H}_p$  in certain areas but might be limited to small environmental gradients. Therefore,  $\delta^2\text{H}_{n\text{-alkane}}$  signals have to be carefully interpreted in paleoclimate studies when considered alone because past changes in  $\delta^2\text{H}_p$  have to be disentangled from other factors which potentially altered the  $\delta^2\text{H}_{n\text{-alkane}}$  signals. Conversely,  $\delta^{18}\text{O}_{\text{sugar}}$  is distinctly modulated by climate dependent evapotranspirative enrichment and cannot be used to infer changes in  $\delta^{18}\text{O}_p$  in most areas when considered alone. However, considered together both biomarkers have shown the potential to overcome these limitations.

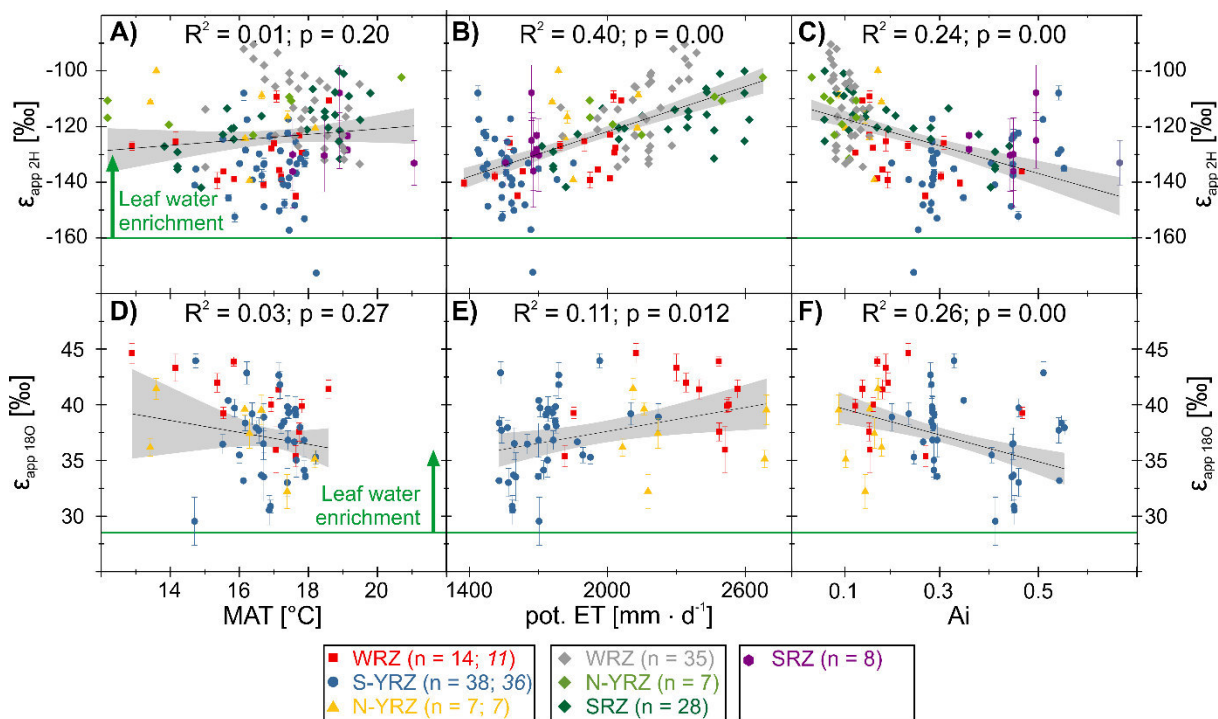


Figure 5.3: Correlation of  $\epsilon_{app\ 2H}$  and  $\epsilon_{app\ 18O}$  with A), D) mean annual temperature (MAT), B), E) potential evapotranspiration (pot. ET) and C), F) Aridity index (Ai) (Fick and Hijmans, 2017; Trabucco and Zomer, 2019). The number of samples used for correlation is indicated by non-italic ( $\epsilon_{app\ 2H}$ ) and italic ( $\epsilon_{app\ 18O}$ ) numbers. The overall linear fit (black line) including  $R^2$ , 95% confidence interval (grey area) and p-values were calculated. The vertical distance between the green line and the sample points indicates leaf water enrichment. The figure was modified after Strobel et al. (2020); data derive from the following studies: red, blue and yellow data points (Strobel et al., 2020); grey, light green and dark green data points (Herrmann et al., 2017); pink data points (Hahn et al., 2018). Please note that for  $\epsilon_{app\ 18O}$  data points reflecting prevailing CAM plants (N-YRZ) were not included in the trendline calculations (see Strobel et al., 2020).

To disentangle changes of the isotopic composition of precipitation and the effect of evapotranspirative soil and leaf water enrichment,  $\delta^2H_{n-alkane}$  and  $\delta^{18O}_{sugar}$  are considered together into the coupled  $\delta^2H_{n-alkane}-\delta^{18O}_{sugar}$  approach (paleohygrometer), which enables to calculate the plants-source water ( $\delta^2H_{source\ water}$  and  $\delta^{18O}_{source\ water}$ ) as well as relative humidity (Section 1.3; Chapter 2). The regional applicability of the coupled  $\delta^2H_{n-alkane}-\delta^{18O}_{sugar}$  approach in South Africa has been tested by correlating reconstructed plant-source water and the modelled isotopic composition of precipitation as well as reconstructed relative humidity and relative humidity derived from reanalysis data (Fig. 5.4; Chapter 2).

$\delta^2H_{source\ water}$  and  $\delta^{18O}_{source\ water}$  significantly correlate with  $\delta^2H_p$  and  $\delta^{18O}_p$ , respectively (Fig. 5.4; Chapter 2; Strobel et al., 2020). Samples located in the WRZ show generally more negative values for  $\delta^2H_{source\ water}$  and  $\delta^{18O}_{source\ water}$  compared to samples in the S-YRZ, which agrees well with  $\delta^2H_p$  and  $\delta^{18O}_p$ . However, samples located in the N-YRZ show a distinct offset to  $\delta^2H_p$  and  $\delta^{18O}_p$ . In the N-YRZ, plants using CAM metabolism dominate the local vegetation. In this (semi-)arid region of South Africa, plant-specific (phenological) adaptations and/or post-photosynthetic exchange reactions as well as the potential use of additional water sources



(e.g., fog) are suggested to lead to an overestimation of  $\delta^2\text{H}_{\text{source water}}$  and  $\delta^{18}\text{O}_{\text{source water}}$  (Chapter 2; Strobel et al., 2020).

Reconstructed relative humidity from the coupled  $\delta^2\text{H}_{n\text{-alkane}}-\delta^{18}\text{O}_{\text{sugar}}$  approach significantly correlates with relative humidity derived from reanalysis data (Fig. 5.4; Chapter 2; Strobel et al., 2020). Samples located in the WRZ show lower values compared to those in the S-YRZ, which agrees well with recent environmental conditions. For samples located in the N-YRZ, values of relative humidity are too high compared to the recent environmental conditions in this area underlining the aforementioned uncertainties related to sites dominated by plants using CAM metabolism (Chapter 2; Strobel et al., 2020). Overall, results obtained from the coupled  $\delta^2\text{H}_{n\text{-alkane}}-\delta^{18}\text{O}_{\text{sugar}}$  approach show potential to robustly reconstruct the isotopic composition of precipitation and relative humidity in South Africa. However, changes in the vegetation composition have to be considered when the coupled  $\delta^2\text{H}_{n\text{-alkane}}-\delta^{18}\text{O}_{\text{sugar}}$  approach is applied.

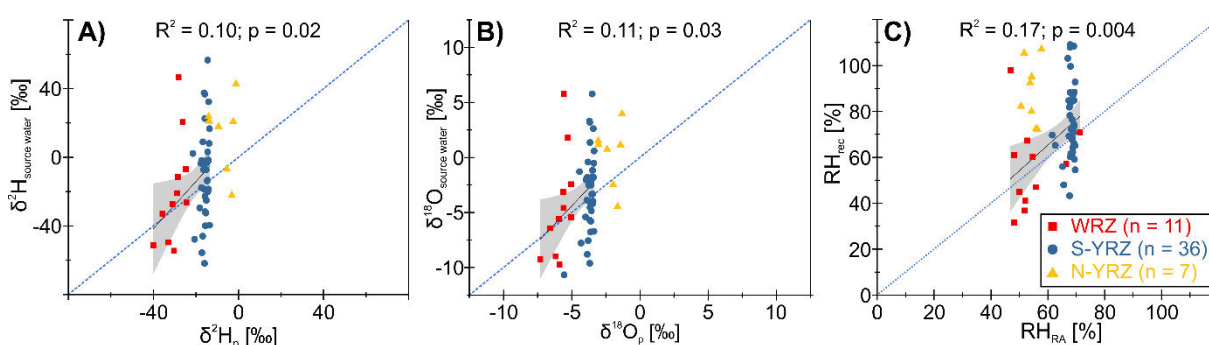


Figure 5.4: Correlation between A)  $\delta^2\text{H}_{\text{source water}}$  and  $\delta^2\text{H}_p$  as well as B)  $\delta^{18}\text{O}_{\text{source water}}$  and  $\delta^{18}\text{O}_p$  related to the seasonal precipitation of the samples (WRZ: JJA; S-YRZ: mean annual; N-YRZ and SRZ: DJF) derived from OIPC data (Bowen et al., 2005; Bowen, 2020) and weighted by monthly precipitation data by Fick and Hijmans (2017). C) Correlation between reconstructed relative humidity ( $\text{RH}_{\text{rec}}$ ) and sample-specific calculated relative humidity based on *ERA-Interim* reanalyzes data ( $\text{RH}_{\text{RA}}$ ; Dee et al., 2011). The overall linear fit excluding the N-YRZ data (black line),  $R^2$ , 95% confidence interval (grey area) and p-values were calculated as well and a 1:1 relationship was integrated in each diagram (light blue dashed line). The figure was modified after Strobel et al. (2020).

Regional calibration studies from Argentina (Tuthorn et al., 2015), Europe (Hepp et al., 2020) and Ethiopia (Lemma et al., 2021) as well as a climate chamber experiment (Hepp et al., 2021) also found correlations of reconstructed plant-source water ( $\delta^2\text{H}_{\text{source water}}$  and  $\delta^{18}\text{O}_{\text{source water}}$ ) with  $\delta^2\text{H}_p$  and  $\delta^{18}\text{O}_p$ , respectively. In the same studies, reconstructed relative humidity correlates with modern observed/modelled (mean day time) relative humidity. However, reconstructed plant-source water ( $\delta^2\text{H}_{\text{source water}}$  and  $\delta^{18}\text{O}_{\text{source water}}$ ) and relative humidity show systematic offsets to the modern observed/modelled data used for comparison. This can be described as  $\Delta^2\text{H}_{\text{source water}}$ ,  $\Delta^{18}\text{O}_{\text{source water}}$  and  $\Delta$ -relative humidity. A compilation of the offsets from the transect studies using modern reference material (i.e., topsoils) is summarized in Table 5.1. For example, variations in the plants growth form (monocot vs. dicot) and signal dampening might bias the results of the coupled  $\delta^2\text{H}_{n\text{-alkane}}-\delta^{18}\text{O}_{\text{sugar}}$  approach leading to an

## Chapter 5

underestimation of the modern isotopic composition of precipitation. In contrast, uncertainties in the data used for comparison also might contribute to the observed scatter in the data (Hepp et al., 2020; Lemma et al., 2021; Strobel et al., 2020; Tuthorn et al., 2015).

Table 5.1: Compilation of the offsets ( $\Delta$ ) of reconstructed plant-source water ( $\delta^2\text{H}_{\text{source water}}$  and  $\delta^{18}\text{O}_{\text{source water}}$ ) and relative humidity compared to the modern isotopic composition of precipitation and relative humidity, respectively. The table comprises studies based on modern reference material from Argentina (Tuthorn et al., 2015), Europe (Hepp et al., 2020), Ethiopia (Lemma et al., 2021) and South Africa (Strobel et al., 2020).

Study	$\Delta^2\text{H}_{\text{source water}}$ [‰]	$\Delta^{18}\text{O}_{\text{source water}}$ [‰]	$\Delta$ -relative humidity [%]
Argentina	$-34 \pm 20$	$-4.5 \pm 2.5$	$-20 \pm 9$
Europe	$-21 \pm 22$	$-2.9 \pm 2.8$	$-17 \pm 12$
Ethiopia	11.3	2.6	$2 \pm 18$
South Africa	$6 \pm 27$	$0.8 \pm 3.7$	$6 \pm 17$

In almost all scatter-plots discussed in this section, a large intra-zonal (within the rainfall zones) variability of the data occurs, i.e.,  $\delta^2\text{H}_{n\text{-alkane}}$  and  $\delta^{18}\text{O}_{\text{sugar}}$ ,  $\epsilon_{\text{app } 2\text{H}}$  and  $\epsilon_{\text{app } 18\text{O}}$ ,  $\delta^2\text{H}_{\text{source water}}$  and  $\delta^{18}\text{O}_{\text{source water}}$  as well as  $\text{RH}_{\text{rec}}$  (Figs. 5.2, 5.3, 5.4). For calculation and correlation of those proxies, environmental and climatic parameters were extracted from reanalysis data, i.e., the isotopic composition of precipitation (Bowen, 2020; Bowen et al., 2005), monthly precipitation and temperature from the WorldClim 2.0 dataset (Fick and Hijmans, 2017), potential evapotranspiration and an aridity index (Trabucco and Zomer, 2019) as well as relative humidity (Dee et al., 2011). Unfortunately, long-term instrumental data are very scarce for the studied area and all reanalysis data only provide an average  $\sim 30$  year signal with the spatial resolution ranging from  $\sim 1$  to  $>5500$  km<sup>2</sup> (Fig. 5.1). As a result, closely located sampling sites have almost identical values and the spatial resolution of the raster cells is not sufficient to account for small-scale micro-climatic variations especially in areas with greater topographic/microclimatic variability (Bowen, 2020; Bowen et al., 2005; Dee et al., 2011; Fick and Hijmans, 2017; Trabucco and Zomer, 2019). Additionally, the determination of the growing season is not trivial in South Africa due to distinct precipitation seasonality, water availability and drought anomalies, which can regionally strongly differ between years/decades (e.g., Engelbrecht and Landman, 2016; Reason and Rouault, 2005; Rouault et al., 2002; Weldon and Reason, 2014). In turn, this can largely affect the timing when precipitation is used for biomarker synthesis from the plants. Due to distinct changes in  $\delta^2\text{H}_p$  and  $\delta^{18}\text{O}_p$  throughout the year, also the calculation of  $\epsilon_{\text{app } 2\text{H}}$  and  $\epsilon_{\text{app } 18\text{O}}$  is affected. Moreover, uncertainties in the reanalysis datasets, plant-specific differences in the growing seasons and usage of water sources, age offsets between the molecular markers as well as between molecular markers and climate information all might contribute to the wide intra-zonal scatter (e.g., Araguás-

Araguás et al., 2000; Hou et al., 2018; Li et al., 2019; Liu and An, 2019; Strobel et al., 2020; Struck et al., 2020; Zongxing et al., 2016).

Summarizing, the results from the regional calibration study corroborate that  $\delta^2\text{H}_{n\text{-alkane}}$  and  $\delta^{18}\text{O}_{\text{sugar}}$  are valuable proxies for paleoclimate reconstructions in South Africa. The compilation of the data discussed in Chapter 2 (Hahn et al., 2018; Strobel et al., 2020) including the data from Herrmann et al. (2017) shows significant correlation of  $\delta^2\text{H}_{n\text{-alkane}}$  and  $\delta^2\text{H}_p$ , while no correlation exists for  $\delta^{18}\text{O}_{\text{sugar}}$  and  $\delta^{18}\text{O}_p$ . However, both biomarker signals show significant correlations with potential evapotranspiration and an aridity index, while there is no correlation with mean annual temperature. Thus, interpretations based on the biomarker signals alone have to disentangle changes in isotopic composition of precipitation and all other factors modifying the biomarker signals. The coupled  $\delta^2\text{H}_{n\text{-alkane}}-\delta^{18}\text{O}_{\text{sugar}}$  approach (paleohygrometer) is a powerful tool to quantitatively reconstruct the isotopic composition of the plants-source water (precipitation) and relative humidity. The results from the regional calibration study from South Africa show significant correlations of  $\delta^2\text{H}_{\text{source water}}$ ,  $\delta^{18}\text{O}_{\text{source water}}$  and relative humidity with modern  $\delta^2\text{H}_p$ ,  $\delta^{18}\text{O}_p$  and relative humidity, respectively. However, changes in the vegetation composition have to be considered when interpreting the results of the coupled  $\delta^2\text{H}_{n\text{-alkane}}-\delta^{18}\text{O}_{\text{sugar}}$  approach. To finally evaluate potentials and limitations of  $\delta^2\text{H}_{n\text{-alkane}}$  and  $\delta^{18}\text{O}_{\text{sugar}}$  as well as the coupled  $\delta^2\text{H}_{n\text{-alkane}}-\delta^{18}\text{O}_{\text{sugar}}$  approach in South Africa, there is still a lack of samples especially in the humid parts of the SRZ.

## 5.2 Holocene paleoclimate evolution and drivers of environmental change along South Africa's southern Cape coast

### 5.2.1 Holocene paleoclimate evolution along South Africa's southern Cape coast

There is considerable evidence that distinct climatic variations occurred throughout the Holocene along the southern Cape coast of South Africa. To reconstruct Holocene precipitation variability and relative humidity changes in this area, two promising sediment archives, i.e., Lake Voëlvlei (Chapter 3; Strobel et al, 2021) and Vankervelsvlei (Chapter 4; Strobel et al, submitted), were selected (Fig. 5.5). To derive a robust and most comprehensive understanding of paleoenvironmental and paleoclimatic conditions along South Africa's southern Cape coast, the newly obtained records are discussed in combination with other regional archives.

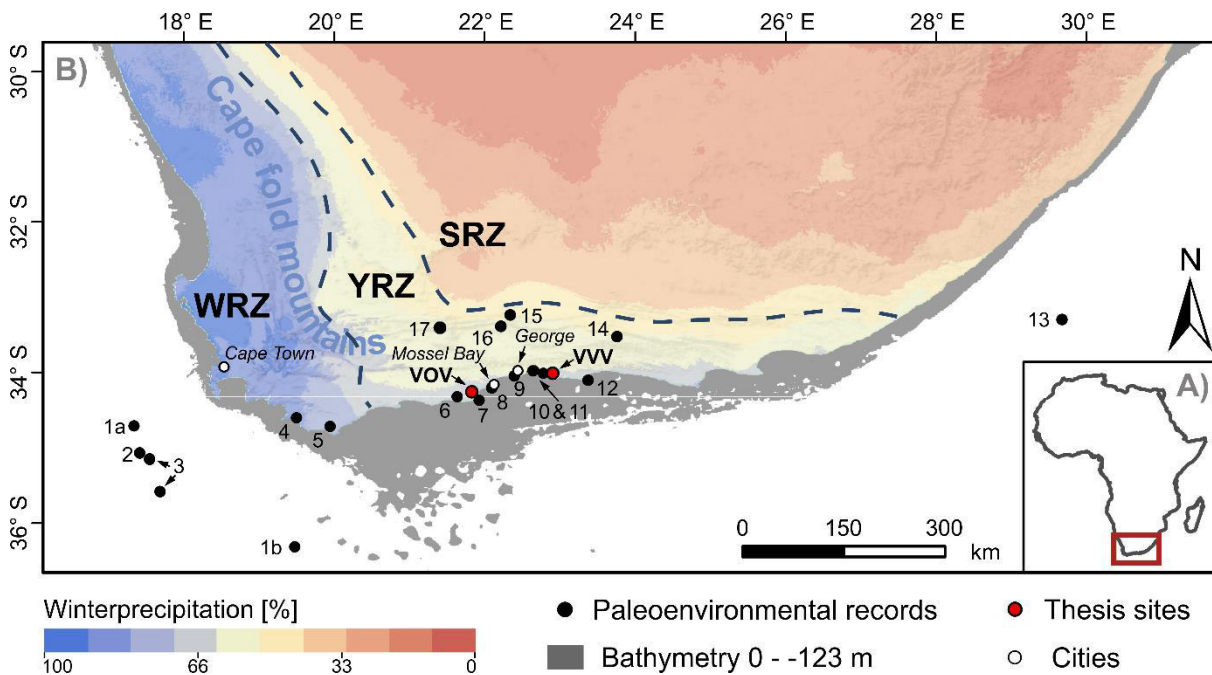


Figure 5.5: A) Simplified map of Africa and the red box highlights the area shown in B. B) The recent spatial distribution of the three major rainfall zones of southern Africa based on modern rainfall seasonality (according to Chase and Meadows, 2007). White and black dots indicate the location of cities and studies mentioned in the text, respectively: 1a & 1b, MD02-2594 & MD96-2080 (Martínez-Méndez et al., 2010); 2, U1479 (Dupont et al., 2021); 3, Cape Basin Record (Peeters et al., 2004); 4, Pearly Beach (Quick et al., 2021); 5, Agulhas Plain vleis and lunettes (Soetendalsvlei, Voëlvlei, Renosterkop, and Soutpan) (Carr et al., 2006a, 2006b); 6, Rietvlei-Still Bay (Quick et al., 2015); 7, GeoB18308-1 (Hahn et al., 2017); 8, Pinnacle Point (Bar-Matthews et al., 2010; Braun et al. 19); 9, Herolds Bay Cave (Braun et al. 2020); 10, Eilandvlei (e.g., Quick et al., 2018; Wündsche et al., 2016a, 2018); 11, Groenvlei (e.g., Martin, 1956; Wündsche et al., 2016b); 12, Nelson Bay Cave (Cohen, 1993, Cohen and Tyson, 1995); 13, CD15417-17K (Simon et al., 2013); 14, Baviaanskloof (Chase et al., 2020); 15, Efflux Cave (Braun et al. 2020); 16, Cango Cave (Talma and Vogel, 1992); 17, Seweweekspoort (e.g., Chase et al., 2017). Red dots highlight the specific sites studied in this thesis, i.e., Voëlvlei (VOV) and Vankervelsvlei (VVV). Data sources – DEM: SRTM 1 arcsec; ~30 m, (Jarvis et al. 2008).

High values of reconstructed relative humidity at Vankervelsvlei indicate overall wet conditions from ~7.5 to 5.0 ka cal BP and from ~3.0 ka cal BP until present day, while lower values from ~5.0 to ~3.0 ka cal BP indicate dry conditions at the site (Chapter 4; Strobel et al., submitted; Figs. 5.6, 5.7). This is in good agreement with palynological analyzes at Eilandvlei (Figs. 5.5, 5.6), which is located 25 km to the west of Vankervelsvlei, where changes in the abundance of Afrotropical forest (AFT) pollen were interpreted to indicate local moisture availability being in line with other moisture indicators from Eilandvlei (du Plessis et al., 2021; Quick et al., 2018; Wündsche et al., 2018; Fig. 5.7). The combination of high values of reconstructed relative humidity and high values of reconstructed plant-source water ( $\delta^2\text{H}_{\text{source water}}$  and  $\delta^{18}\text{O}_{\text{source water}}$ ) at Vankervelsvlei indicates a year-round precipitation regime from ~7.5 to ~5.0 ka cal BP and from ~3.0 ka cal BP until present day (Chapter 4; Strobel et al., submitted). In contrast, low values of reconstructed relative humidity and low values of reconstructed plant-source water ( $\delta^2\text{H}_{\text{source water}}$  and  $\delta^{18}\text{O}_{\text{source water}}$ ) indicate a shift to a winter rainfall regime from ~5.0 to

~3.0 ka cal BP (Chapter 4; Strobel et al., submitted). Therefore, the combination of reconstructed plant-source water and relative humidity suggests that moist conditions are related to increased precipitation contributed during summer (Easterlies and/or from local sources). Conversely, dry conditions are associated with less precipitation contribution during summer (Easterlies and/or from local sources) leading to a shift to a winter-rainfall regime and thus increased precipitation seasonality (Figs. 5.6, 5.7).

Recently, an additional high-resolution  $\delta^2\text{H}_{n\text{-alkane}}$  record was established at Lake Voëlvlei, located 80 km west of Vankervelsvlei, which also mirrors changes in the precipitation source (Chapter 3; Strobel et al., 2021; Figs. 5.5, 5.6). The overall pattern at this site suggests contributions of precipitation during winter and summer from ~8.2 to ~6.4 ka cal BP and increased precipitation contribution during summer from ~6.4 to 4.7 ka cal BP. From 4.7 ka cal BP until present day, the precipitation regime at Lake Voëlvlei shifts from a winter-dominated towards a year-round regime (Chapter 3; Strobel et al., 2021). This pattern is consistent with the findings at Vankervelsvlei and Eilandvlei providing a coherent climate picture of the coastal sites at South Africa's southern Cape coast (Figs. 5.6, 5.7).

The results from previous paleoenvironmental studies from South Africa's southern Cape coast roughly coincide with the findings described above. Particularly, those include dry conditions at Lake Groenvlei from ~6.8 to ~2.0 ka cal BP (Martin, 1968) and from ~4.2 to ~2.7 ka cal BP (Wündsche et al., 2016a) obtained from palynological and geochemical analyzes (Fig. 5.7). In contrast, increasing moisture from ~3.0 ka cal BP until present day was found in a marine sediment core off the Gouritz river mouth using a combination of methods such as organic, inorganic and stable geochemistry (Hahn et al., 2017; Fig. 5.7).  $\delta^2\text{H}_{n\text{-alkane}}$  from this record well matches to the records from Voëlvlei and Vankervelsvlei showing increasing contributions of Easterly-derived summer precipitation and a shift from a winter to a year-round precipitation regime from ~3 ka until present day (Fig. 5.6).

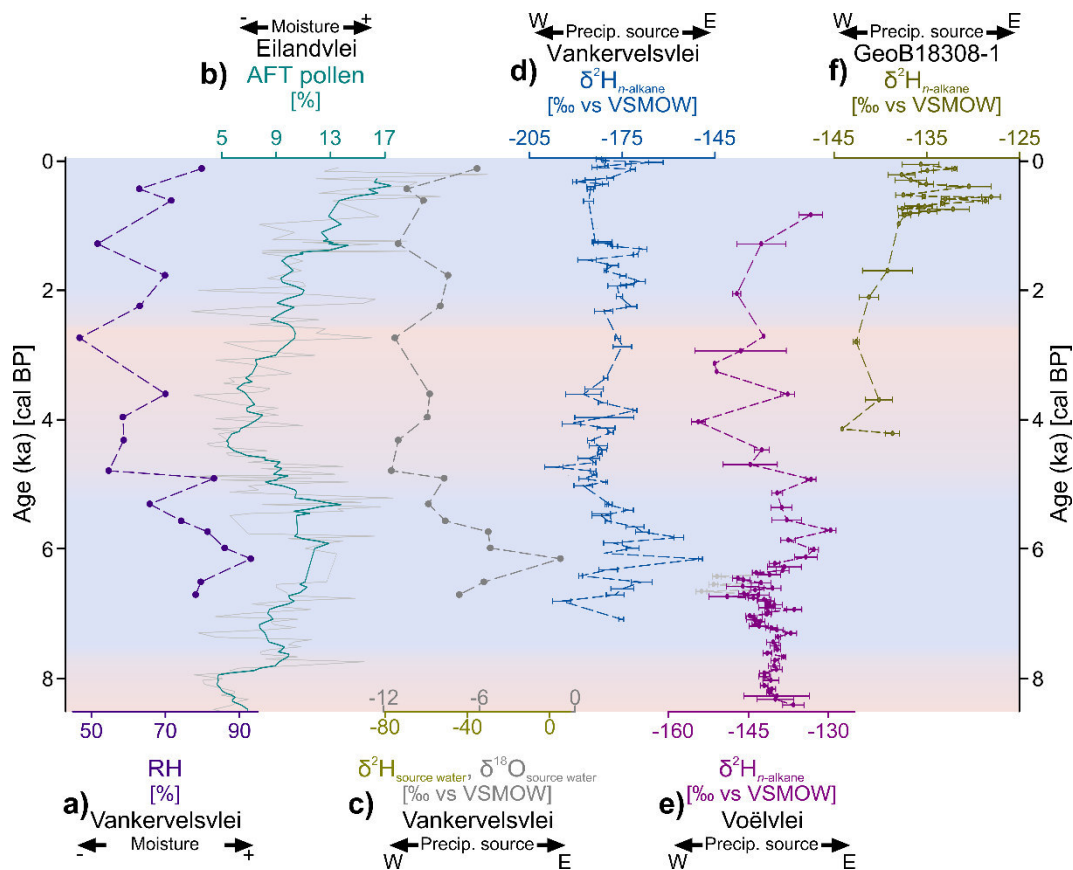


Figure 5.6: a) Reconstructed relative humidity (RH) at Vankervelsvlei (Strobel et al., submitted) compared to b) Afrotemperate forest pollen (AFT) at Eilandvlei as indicators for local moisture availability (Quick et al., 2018). c) The reconstructed isotopic composition of the plants-source water ( $\delta^2\text{H}_{\text{source water}}$ ,  $\delta^{18}\text{O}_{\text{source water}}$ ) at Vankervelsvlei compared to  $\delta^2\text{H}_{n\text{-alkane}}$  at d) Vankervelsvlei (Strobel et al., submitted; Strobel et al., 2019), e) Voëlvlei (Strobel et al., 2021) and f) GeoB18308-1 (Hahn et al., 2017), as indicators for precipitation source (W – Westerlies; E – Easterlies and/or local sources).

A further assessment of the spatial extent of the described precipitation source and moisture pattern along the southern Cape coast is limited due to a scarcity of climate records and most existing studies are rather discontinuous, confident to specific periods, lack a precise chronological control, provide only coarse temporal resolution and/or lack of direct hydrological proxies. However, in the western parts of the YRZ, pollen assemblages at Rietvlei-Still Bay indicate humid conditions from 11 to 7 ka and from 3.3 ka until present day while dry condition occurred from 7 to 3.3 ka (Quick et al., 2015; Fig. 5.7). The chronological control of the Rietvlei-Still Bay record is limited, possibly explaining temporal offsets of the moisture signals at Rietvlei-Still Bay and sites at the southern Cape coast. Unfortunately, an assessment of the spatial extent of the precipitation source and moisture signal to the east of the thesis sites (i.e., Vankervelsvlei and Voëlvlei; Chapters 3 and 4) is limited due to a general lack of terrestrial paleoclimate records in the respective areas of the YRZ (Fig. 5.5). In the adjacent interior of the YRZ, records at Baviaanskloof (Chase et al., 2020) and Seweweekspoort (Chase et al., 2017) (Figs. 5.5, 5.7) show a different moisture pattern compared to the southern Cape coast, but an in-phase pattern with records located in the SRZ. This highlights that the Cape Fold

Mountains (i.e., the Swartberge mountains), where both records are located, are an orographic barrier limiting a northward extent of the southern Cape coast precipitation source and moisture signal.

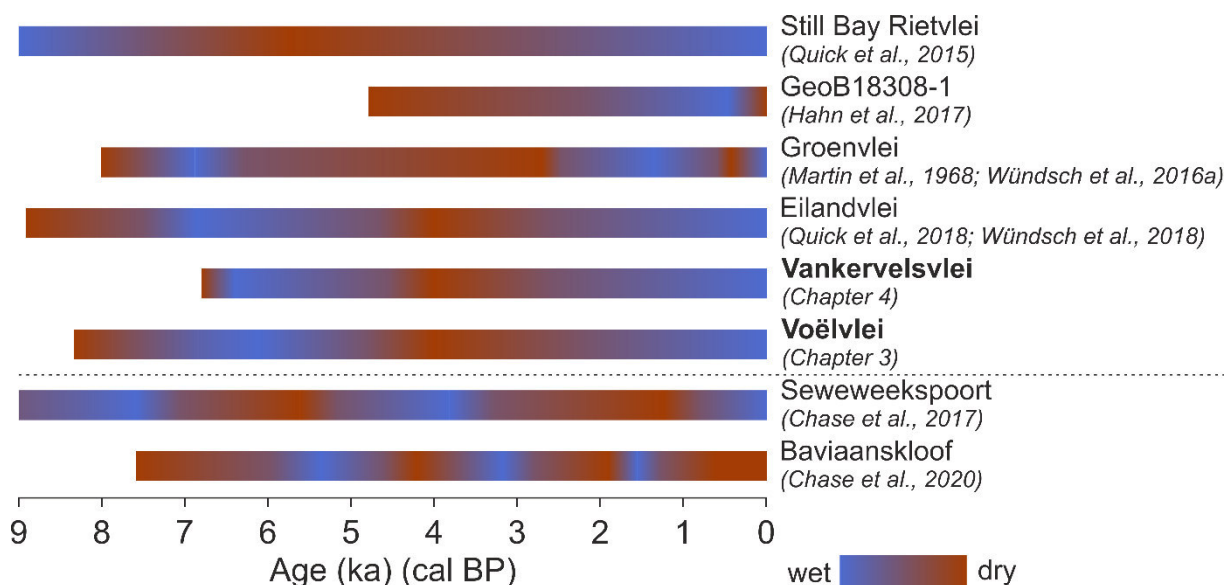


Figure 5.7: Comparison of generalized Holocene palaeoclimate trends inferred from selected marine and terrestrial records from South Africa. Bolt letters highlight studies presented in this thesis. The records below the dashed line are located in the adjacent interior of the YRZ.

## 5.2.2 Drivers of Holocene paleoclimate dynamics along South Africa's southern Cape coast

So far, the driving forces behind the climate pattern described in the previous section have been subject to considerable debate. Some studies suggest insolation, the strength and position of the mid-latitude Westerlies, El Niño-Southern Oscillation (ENSO), the extent of the Antarctic sea ice and sea surface temperatures to be drivers of Holocene climate variability in South Africa (e.g., Chase et al., 2017; Chase and Quick, 2018; Miller et al., 2020).

To better evaluate past driving forces along the southern Cape coast the understanding of recent climate factors and dynamics is crucial. However, the modern precipitation variability along South Africa's southern Cape coast was not well understood for long time (Weldon and Reason, 2014). To overcome this situation, several studies aimed to untangle the relative contributions of various weather systems to the annual precipitation in this area during the past years (e.g., Engelbrecht and Landman, 2016; Engelbrecht et al., 2015; Favre et al., 2013; Weldon and Reason, 2014). Associated with the temperate Westerlies, ridging anticyclones and cut-off lows are the main synoptic-scale weather systems (Engelbrecht et al., 2015; Ndarana et al., 2021). Precipitation of tropical origin is mainly contributed by tropical-temperate trough cloud bands (Engelbrecht et al., 2015; Hart et al., 2013; Macron et al., 2014). The

## Chapter 5

presence and frequency of some of these weather systems has been attributed to the principal climate modes of the ENSO. Higher frequency of cut-off lows affecting the southern Cape coast has been observed during La Niña compared to El Niño years (Engelbrecht and Landman, 2016; Favre et al., 2013; Weldon and Reason, 2014). Additionally, increased precipitation along South Africa's southern Cape coast has been linked to positive phases of the Southern Annular Mode (SAM) (Engelbrecht and Landman, 2016; Ibebuchi, 2021). This means that the atmospheric zonal mean pressure gradient between the mid-latitudes and Antarctica is high resulting in a poleward displacement and strengthening of the mid-latitude Westerlies (e.g., Engelbrecht and Landman, 2016; Malherbe et al., 2014; Reason and Rouault, 2005). This poleward position of the Westerlies promotes arising eddies, such as cut-off lows and ridging anticyclones, to expand equatorward favoring increased precipitation along the southern Cape coast (Hartmann and Lo, 1998; L'Heureux and Thompson, 2006). Additionally, high sea surface temperatures in the South Atlantic and southern Indian Ocean play an important role for the genesis of synoptic scale weather systems (Mason and Jury, 1997; Singleton and Reason, 2006; Washington and Preston, 2006).

Results from Voëlvlei and Vankervelsvlei are discussed in the following to identify potential drivers of the climate evolution along South Africa's southern Cape coast during the Holocene. At 34 °S, where both sites are located, mean annual insolation has generally been increasing throughout the Holocene while summer insolation has increased as well but winter insolation has decreased (Berger and Loutre, 1991; Wündsche et al., 2018; Fig. 5.8). However, moisture evolution along the southern Cape coast does not follow the aforementioned pattern indicating that local insolation is unlikely the dominant driver of climate variability during the Holocene (Fig. 5.8).

Records providing information about past ENSO variability are available, for example, from Ecuador (Moy et al., 2002), Galápagos Islands (Conroy et al., 2008; Zhang et al., 2014) and off Peru (Rein et al., 2005; Rein et al., 2004). The pattern of wet conditions from ~7.5 to ~5 ka cal BP and from ~3 ka cal BP until present day coincide with low El Niño and thus dominantly La Niña frequency off Peru during these periods (Rein et al., 2005; Rein et al., 2004; Fig. 5.8). In contrast, dry conditions along South Africa's southern Cape from ~5 to ~3 ka cal BP are in line with higher El Niño and lower La Niña frequency (Rein et al., 2005; Rein et al., 2004; Fig. 5.8). Although the overall pattern matches well, a more detailed comparison of the records from Voëlvlei and Vankervelsvlei to the record inferring El Niño frequency is challenging, which is also true for further regional high-resolution records located along South Africa's southern Cape coast (e.g., Eilandvlei; Quick et al., 2018; Wündsche et al., 2018).



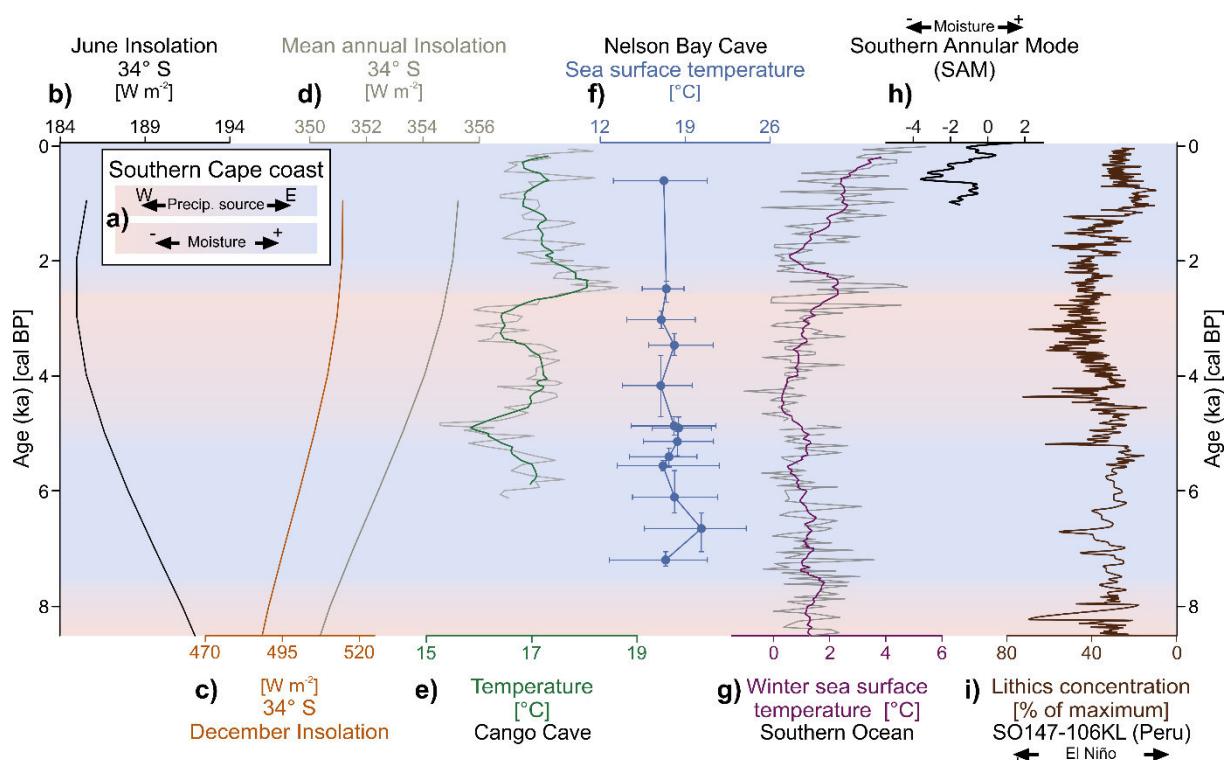


Figure 5.8: a) Generalized precipitation source and local moisture availability pattern derived for the southern Cape coast displayed in the background. Red background color indicate high Westerly-derived precipitation and low local moisture availability while blue color refers to high Easterly-derived precipitation and high local moisture availability along South Africa's southern Cape coast. For comparison b) June, c) December and d) mean annual insolation at 34° S are displayed (Berger and Loutre, 1991). Additionally depicted are, e) temperatures at Congo Cave (Talma and Vogel, 1992), f) sea surface temperatures at Nelson Bay Cave (Cohen, 1993; Cohen and Tyson, 1995) and g) winter sea surface temperatures of the Southern Ocean (Nielsen et al., 2004) as well as h) a Southern Annular Mode Index (70 year running mean) (Abram et al., 2014) and i) lithic concentration as proxy for El Niño frequency derived from the marine sediment record SO147-106KL recovered off Peru (Rein et al., 2005).

During the past years, an increasing number of SAM reconstructions for the past millennia has been developed (e.g., Abram et al., 2014; Dätwyler et al., 2020; Dätwyler et al., 2018; Fogt and Marshall, 2020). It is suggested, that SAM is currently in its most positive state, which is in good agreement with increasing moisture at Vankervelsvlei and Voëlvlei as well as along South Africa's southern Cape coast (e.g., Quick et al., 2018; Wündsche et al., 2018; Wündsche et al., 2016a; Fig. 5.8). While direct SAM reconstructions lack of data for major parts of the Holocene, southern Atlantic and Indian Ocean sea surface temperatures and the extent of the Antarctic sea ice can serve as indirect indicators for past spatial shifts of the southern hemispheric Westerlies and thus SAM. This is based on the assumption that an equatorward shift of the Westerlies is associated with the equatorward expansion of the Antarctic sea ice extent. In contrast, a poleward displacement of the Westerlies is accompanied by a poleward contraction of the Antarctic sea ice (e.g., Chase and Meadows, 2007; Fletcher and Moreno, 2012; Perren et al., 2020; Stuut et al., 2004; Stuut and Lamy, 2004). However, it is noticeable that this general assumption is still subject of debate (e.g., Fletcher and Moreno, 2012). The

sea surface temperatures in the southern Atlantic Ocean and the extent of the Antarctic sea ice have been target of several studies. For comparison with sites located along the southern Cape coast, studies located in the area south of South Africa are of particular interest due to an unequal expansion and retreat of the Antarctic sea ice (e.g., Crosta et al., 2021; Ghadi et al., 2020; Hodell et al., 2001; Nielsen et al., 2004). A retreat of the Antarctic sea ice is suggested during the early- and late-Holocene while it expands during the mid-Holocene (e.g., Hodell et al., 2001; Nielsen et al., 2004; Fig. 5.8). Wet conditions at Vankervelsvlei and Voëlvlei as well as along the southern Cape coast from ~7.5 to ~5.0 ka cal BP and from ~3.0 ka cal BP until present day broadly coincide with a poleward retreat of the Antarctic sea ice (Hodell et al., 2001; Nielsen et al., 2004; Quick et al., 2018; Wündsche et al., 2018; Wündsche et al., 2016a). In contrast, dry conditions at South Africa's southern Cape coast from ~5.0 to ~3.0 ka cal BP are roughly in line with an equatorward expansion of the Antarctic sea ice (Fig. 5.8).

Recently, the Agulhas current was attributed to be a further driver of climate variability along South Africa's southern Cape coast during the Holocene. It is proposed that energy brought by the ocean current leads the development of onshore flows of moist air (Chase and Quick, 2018). In this context, wet conditions at Vankervelsvlei and Voëlvlei from ~7.5 to ~5.0 ka cal BP and from ~3 ka cal BP until present day have been identified to be associated with distinct precipitation contribution from local sources (Chapters 3 and 4; Strobel et al., 2021; Strobel et al., submitted). The driver of this moisture evolution might be the Agulhas current. Although several records provide information about sea surface and air temperature variations during the Holocene, their significance is often limited due to analytical and dating uncertainties as well as a lack of sufficient temporal resolution, which limits the evaluation of this hypothesis (e.g., Cohen, 1993; Cohen and Tyson, 1995; Hahn et al., 2017; Martínez-Méndez et al., 2010; Peeters et al., 2004; Simon et al., 2013; Talma and Vogel, 1992; Fig. 5.8).

### **5.3 Late Quaternary paleoclimate evolution and drivers of environmental change along South Africa's southern Cape coast**

Paleoclimate records extending the Holocene are very rare along South Africa's southern Cape coast, but existing records show evidence for distinct climatic variations during the Late Quaternary. Most of these records are limited to marine sediments (e.g., Dupont et al., 2021; Martínez-Méndez et al., 2010; Peeters et al., 2004; Simon et al., 2013), but there are also records based on terrestrial deposits (e.g., Bar-Matthews et al., 2010; Braun et al., 2019; Braun et al., 2020; Chase et al., 2017; Talma and Vogel, 1992; Fig. 5.5). Additionally, one focus has been on Vankervelsvlei, where several sediment cores have been recovered from different locations during the past years (Chapter 4; Quick et al., 2016; Strobel et al., submitted; Strobel et al., 2019).

### 5.3.1 Late Quaternary paleoenvironmental and paleoclimatic reconstruction along South Africa's southern Cape coast

The new record from Vankervelsvlei discussed in Chapter 4 (Strobel et al., submitted) shows a basal age of  $256^{+19/-19}$  ka. Sediments from  $256^{+19/-19}$  ka to  $110^{+8/-8}$  ka consist almost exclusively of sand, likely indicating significant geomorphic activity at the site and within the surrounding area during this time (Chapter 4; Strobel et al., submitted). Unfortunately, further paleoenvironmental inferences for the time interval from  $256^{+19/-19}$  to  $110^{+8/-8}$  ka are limited due to the high sand contents (Chapter 4; Strobel et al. submitted). However, from  $171^{+16/-13}$  to  $136^{+16/-16}$  ka *n*-alkane amounts were insufficient for  $\delta^2\text{H}_{n\text{-alkane}}$  but sufficient for  $\delta^{13}\text{C}_{n\text{-alkane}}$  measurements, which imply a contribution from vegetation using CAM and/or C4 photosynthesis, and/or decreased moisture availability (water use efficiency; WUE) at Vankervelsvlei during this period (Fig. 5.9). From  $136^{+16/-16}$  to  $112^{+12/-11}$  ka, more positive  $\delta^{13}\text{C}_{n\text{-alkane}}$  values, in comparison to the previous period, imply drier conditions and that more plants were using CAM and/or C4 photosynthetic mode. Contemporary, negative  $\delta^2\text{H}_{n\text{-alkane}}$  values indicate high contribution of Westerly-derived winter precipitation (Chapter 4; Strobel et al. submitted). From  $112^{+12/-11}$  to  $103^{+7/-7}$  ka (MIS 5e, 5d), from  $88^{+8/-8}$  to  $82^{+10/-12}$  ka (MIS 5c, 5b) and from  $42^{+2/-2}$  to  $39^{+4/-5}$  ka (MIS 3)  $\delta^{13}\text{C}_{n\text{-alkane}}$  values clearly indicate a dominant contribution of plants using C3 photosynthetic mode. During the same periods, more positive  $\delta^2\text{H}_{n\text{-alkane}}$  values indicate high contributions of both winter (Westerly-derived) and summer (Easterly-/locally-derived) precipitation and likely a year-round rainfall regime. This is supported by the results of the coupled  $\delta^2\text{H}_{n\text{-alkane}}-\delta^{18}\text{O}_{\text{sugar}}$  (paleohygrometer) approach, although the number of samples is distinctly limited. Conversely, plants using CAM and/or C4 photosynthetic mode are present at Vankervelsvlei from  $82^{+10/-12}$  to  $42^{+2/-2}$  ka (MIS 5a to early MIS 3) and from  $39^{+4/-5}$  to  $20^{+5/-12}$  ka (transition from MIS 3 to MIS 2) (Chapter 4; Strobel et al., submitted; Fig. 5.9). Contemporary, more negative  $\delta^2\text{H}_{n\text{-alkane}}$  values indicate high Westerly-derived winter precipitation contribution and thus a shift to a winter-rainfall regime at Vankervelsvlei (Fig. 5.11), which is also supported by the results of the coupled  $\delta^2\text{H}_{n\text{-alkane}}-\delta^{18}\text{O}_{\text{sugar}}$  (paleohygrometer) approach (Fig. 5.11). A sedimentary hiatus from  $20^{+5/-12}$  ka to  $7.3^{+0.2/-0.2}$  ka likely indicates drought conditions at Vankervelsvlei, leading to desiccation and degradation of the previously accumulated peat during MIS 2 (Chapter 4; Strobel et al., submitted; Strobel et al., 2019)

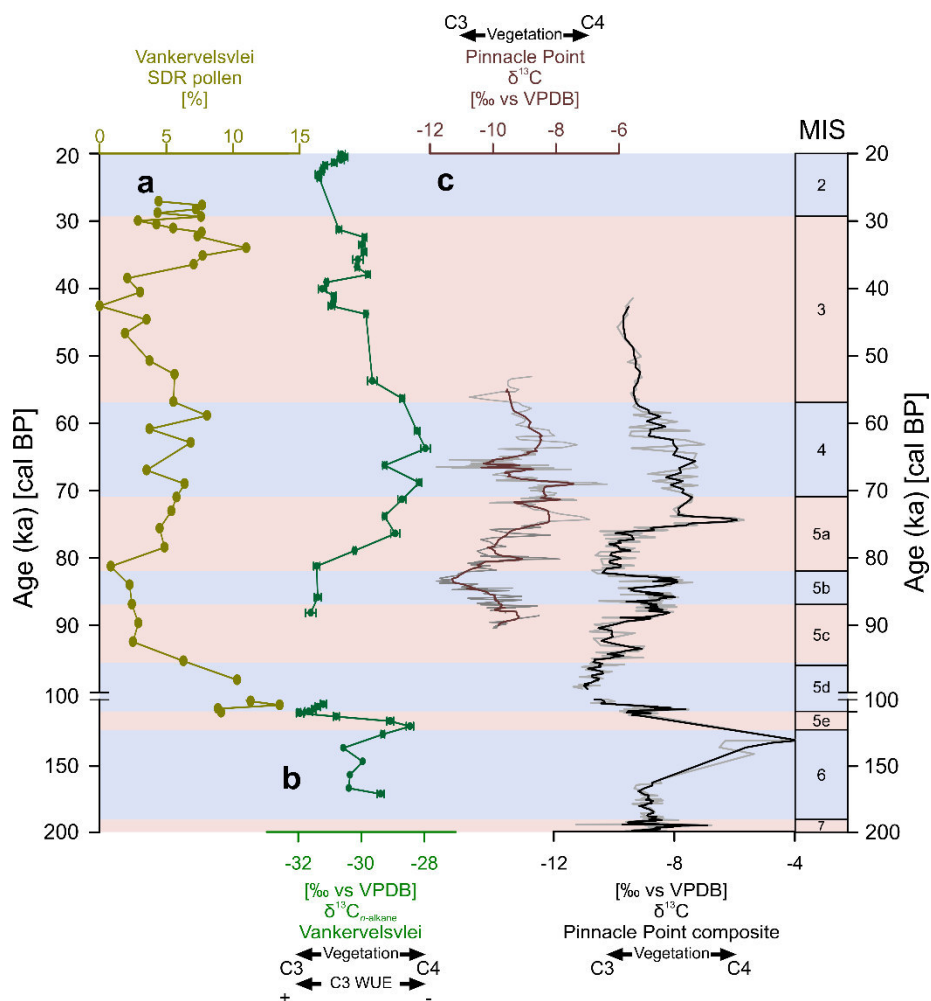


Fig. 5.9: Comparison of a) percentages of succulent/drought resistant (SDR) pollen (Quick et al., 2016) and b)  $\delta^{13}C_{n-alkane}$  from Vankervelsvlei (Strobel et al., submitted) as well as c)  $\delta^{13}C$  from Pinnacle point (grey line original data; colored line running mean of eleven data points) (Bar-Matthews et al., 2010) and d)  $\delta^{13}C$  composite record from Pinnacle point (PP29 and Staircase Cave; grey line original data; black line running mean of three data points; Braun et al., 2019). Note that pollen results are from an earlier study on Vankervelsvlei and are plotted on their original independent age scale and an axis break at 100 ka.

In a site-specific comparison, trends in  $\delta^{13}C_{n-alkane}$  (Chapter 4; Strobel et al., submitted) coincide with changes in the presence of Succulent/Drought Resistant (SDR) pollen (Fig. 5.9) from sediment core VVV10.1 recovered from Vankervelsvlei in 2010 (Quick et al., 2016). *Euphorbia* dominates the SDR pollen sum and was previously interpreted to indicate local drought at Vankervelsvlei (Quick et al., 2016) and thus the SDR pollen sum provides a coherent environmental signal at the site (Fig. 5.9).

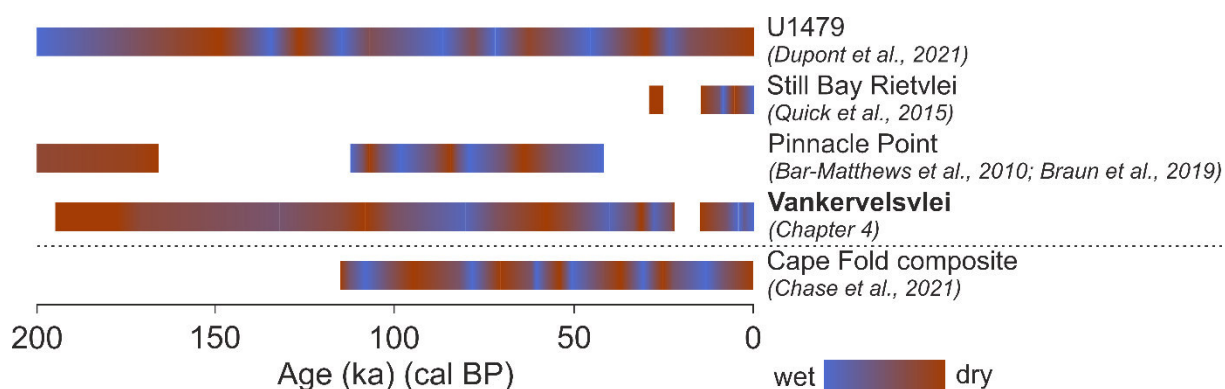


Figure 5.10: Comparison of generalized Late Quaternary palaeoclimate trends inferred from selected marine and terrestrial records from South Africa. The record below the dashed line summarizes studies located in the adjacent interior of the YRZ.

For regional comparison, speleothem records can be used to evaluate past variations in vegetation ( $\delta^{13}\text{C}$ ) and precipitation source ( $\delta^{18}\text{O}$ ) along the southern Cape coast. For example, two records from Pinnacle Point, i.e., Crevice Cave (Bar-Matthews et al., 2010) and a composite record from Staircase Cave and PP29 (Braun et al., 2019), provide  $\delta^{13}\text{C}$  in high temporal resolution and high chronological control (Fig. 5.5). Although the temporal resolution of the Vankervelsvlei record is lower than at these sites,  $\delta^{13}\text{C}$ -records from the speleothems perfectly resemble the trends and interpretation of  $\delta^{13}\text{C}_{n\text{-alkane}}$  and SDR pollen from Vankervelsvlei (Fig. 5.9) (Chapter 4; Bar-Matthews et al., 2010; Braun et al., 2019; Quick et al., 2016; Strobel et al., submitted). Additionally, the pattern of the  $\delta^{18}\text{O}$ -records from Pinnacle Point, i.e., Crevice Cave (Bar-Matthews et al., 2010) and a composite record from Staircase Cave and PP29 (Braun et al., 2019), roughly follow that of  $\delta^2\text{H}_{n\text{-alkane}}$  at Vankervelsvlei and therefore support a coherent precipitation source signal along the southern Cape coast (Chapter 4; Strobel et al., submitted; Figs. 5.10, 5.11). However, besides the isotopic composition of precipitation also local temperature drives  $\delta^{18}\text{O}$  in speleothems (McDermott, 2004), which potentially explains minor discrepancies between  $\delta^2\text{H}_{n\text{-alkane}}$  at Vankervelsvlei and  $\delta^{18}\text{O}$  of the speleothem records at Pinnacle Point.

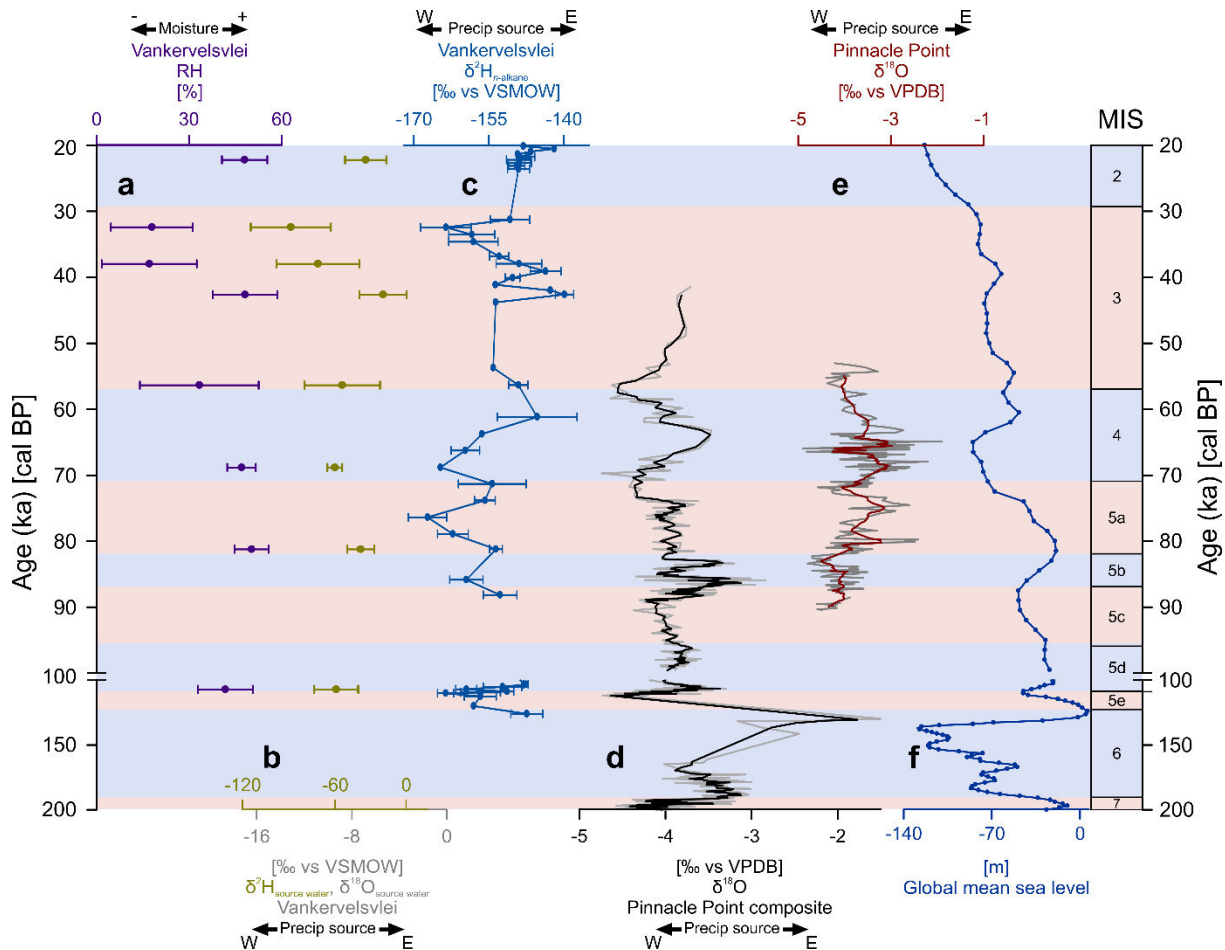


Fig. 5.11: a) Reconstructed relative humidity (RH), b) reconstructed plant-source water ( $\delta^2\text{H}_{\text{source water}}$  and  $\delta^{18}\text{O}_{\text{source water}}$ ) and c)  $\delta^2\text{H}_{n\text{-alkane}}$  from Vankervelsvlei (Strobel et al., submitted). d)  $\delta^{18}\text{O}$  composite record from Pinnacle point (PP29 and Staircase Cave; grey line original data; black line running mean of three data points; Braun et al., 2019), e)  $\delta^{18}\text{O}$  from Pinnacle point (grey line original data; colored line running mean of eleven data points; Bar-Matthews et al., 2010) and f) global mean sea level (Waelbroeck et al., 2002) are shown for comparison. Note an axis break at 100 ka.

Overall, several paleoclimate records located at or near the present day southern Cape coast show relatively coherent trends, but a detailed assessment of the longitudinal extent of the reconstructed environmental dynamics and precipitation source pattern along the southern Cape coast is limited due to a general scarcity of climate records of Late Quaternary age. However, pollen assemblages off South Africa (Dupont et al., 2021; Fig. 5.5) representative for the southwest of South Africa roughly follow the environmental and climate dynamics along the southern Cape coast. Additionally, dry conditions during MIS 2 at wetlands on the Agulhas plain (Carr et al., 2006; Quick et al., 2015), presently located in the WRZ (Fig. 5.5), support the results from the southern Cape coast. Similar to the Holocene, a divergent climate pattern occurs between the southern Cape coast and sites located in the adjacent interior of the YRZ. There, high-resolution speleothem records have been developed at Efflux Cave and Cango Cave during the past decades (Braun et al., 2020; Fig. 5.5; Talma and Vogel, 1992). Recently,

both records have been combined to a composite record together with a hyrax midden record from Seweweekspoort to a composite record (Chase et al., 2021; Chase et al., 2017). However, while a depositional hiatus at Cango Cave (from 16.7 to 6.1 ka) (Talma and Vogel, 1992) supports dry conditions during this time along the southern Cape coast, contemporary moist conditions occurred at Seweweekspoort (Chase et al., 2017), highlighting potential regional differences also in the adjacent interior of the YRZ.

### **5.3.2 Driver of Late Quaternary climate dynamics along South Africa's southern Cape coast**

Climate variability and its driving forces in South Africa during the Late Quaternary are subject to considerable debate (Chapter 1). Generally, a major driver of global glacial-interglacial cycles are variations in solar radiation (insolation), which is driven by the Earth's orbital parameters with their respective cycles, i.e., precession (19 to 23 ka), obliquity (~41 ka), eccentricity (~100 ka) (e.g., Berger and Loutre, 1991; Lisiecki and Raymo, 2005). Those orbital-scale cycles are suggested to additionally drive past variations in, for example, sea level, the strength and position of the mid-latitude Westerlies, the extent of the Antarctic sea ice, Agulhas leakage and sea surface temperatures which all have been discussed as potential drivers of Late Quaternary climate variability in South Africa to different degrees and with temporal variability and spatial heterogeneity (e.g., Caley et al., 2018; Caley et al., 2011; Chase et al., 2017; Chase and Meadows, 2007; Chase et al., 2019; Chevalier and Chase, 2015; Dupont et al., 2021; Ghadi et al., 2020; Hahn et al., 2021; Martínez-Méndez et al., 2010; Miller et al., 2019; Miller et al., 2020; Peeters et al., 2004; Simon et al., 2013; Simon et al., 2020). Particularly, the spatial extent of the major rainfall zones covering South Africa with their related atmospheric precipitation sources mainly depend on an interplay of all these drivers. However, in principle, the intensity and spatial extent of the monsoon driven tropical Easterlies rely on high sea surface temperatures and strong summer warming of the continent to create strong convection cells. These conditions are best developed during warmer interglacial periods and therefore monsoon intensity in South Africa is generally weakened during cooler glacial periods (Bowler et al., 2001; Chase and Thomas, 2007; Miller et al., 2019). The influence of the temperate Westerlies is driven by their latitudinal position. Presently, the Westerlies affect only the southern and western margins of South Africa due to their equatorward migration during austral winter (Engelbrecht and Landman, 2016; Engelbrecht et al., 2019; Tyson, 1986). However, it has been suggested that an expansion of Antarctic sea ice during glacial periods leads to an equatorward displacement of the Westerlies and more humid conditions in southwestern Africa (Chase and Thomas, 2007; Cockcroft et al., 1987; van Zinderen Bakker, 1976).

## Chapter 5

Results discussed in Chapter 4 provide evidence for distinct environmental, climate and particularly hydrological changes along South Africa's southern Cape coast, during the Late Quaternary. As mentioned previously,  $\delta^2\text{H}_{n\text{-alkane}}$  likely refers to past changes in the atmospheric source of precipitation in this area (Strobel et al., submitted; Strobel et al., 2020). The pattern of the  $\delta^2\text{H}_{n\text{-alkane}}$ -record discussed in Chapter 4 and Section 5.3.1 (Strobel et al., submitted) is resembled by changes in the global mean sea level (Waelbroeck et al., 2002; Fig. 5.11) and thus indicates changes in precipitation sources on glacial-interglacial scale. More positive  $\delta^2\text{H}_{n\text{-alkane}}$  values indicate a high contribution of Easterly- and/or locally-derived precipitation during high sea level (interglacial periods). Conversely, negative  $\delta^2\text{H}_{n\text{-alkane}}$  values occur during low sea level (glacial periods) indicating high proportions of Westerly-derived precipitation (Chapter 4; Strobel et al., submitted; Strobel et al., 2019; Waelbroeck et al., 2002; Fig. 5.11). Additionally, sea level was distinctly lower than at present during glacial periods, with the coastline south of its present position, which increased continentality at Vankervelsvlei (Chapter 4; Cawthra et al., 2014; Fig. 5.5). This was likely most pronounced during MIS 6 and MIS 2 (~90-100 km) and to a lesser degree during MIS 4 (~20-30 km) (BODC, 2014; Cawthra et al., 2014; Lisiecki and Raymo, 2005; Waelbroeck et al., 2002). Therefore, variations in the global mean sea level are suggested to distinctly drive climate variability along the southern Cape coast leading to increased continentality and drier conditions during glacial compared to interglacial periods (Chapter 4; Strobel et al., submitted; Strobel et al., 2019). During MIS 2, in particular, modelled temperatures and precipitation (seasonality) imply a lower mean annual temperature (i.e., 2 to 4°C) and reduced precipitation due to increased continentality of this area, resulting in overall dry conditions (Engelbrecht et al., 2019). This is in very good agreement with dry conditions reconstructed at wetlands on the Agulhas plain (Carr et al., 2006; Quick et al., 2015) as well as sedimentary hiatuses at Vankervelsvlei for large parts of MIS 2 (Chapter 4; Strobel et al., submitted; Strobel et al., 2019) and Cango Cave (from 16,660 to 6,110 cal BP) (Talma and Vogel, 1992). Conversely, both proxy (e.g., Chase et al., 2017; Quick et al., 2021) and modelled data (e.g., Cockcroft et al., 1987; Engelbrecht et al., 2019) indicate temporarily moister conditions in the interior and at the north-south aligned Cape Fold Mountains and the western escarpment of South Africa inter alia due to reduced temperatures leading to an increased effective ecosystem moisture availability. Unfortunately, the evaluation of drivers of Holocene climate variations along the southern Cape coast, i.e., ENSO and SAM, on longer timescale is limited due to a lack of records of Late Quaternary age and the limited temporal resolution of the proxies at Vankervelsvlei (Chapter 4; Strobel et al., submitted). Other studies in this area suggest their high-resolution proxy-data to be driven by orbital precession during the Late Quaternary (Braun et al., 2019; Braun et al., 2020). This is supported by Dupont et al. (2021) who suggest the combination of past sea level changes and orbital precession to be the main drivers for variations in the vegetation composition of South Africa's southwestern coastal region (Dupont et al., 2021). Moreover, local insolation and the latitudinal insolation



gradient during Southern Hemisphere summer and winter are suggested to be additional drivers of past changes in vegetation composition of South Africa's southwestern coastal region referring to variations in climate and hydrology (Dupont et al., 2021). The latitudinal insolation gradient describes the differences of local insolation at 30°S to that at 60°S on December 21 (summer) and June 21 (winter). It is suggested that maximum precession, high local summer insolation and weak latitudinal insolation gradient during austral winter all might increase summer precipitation along the southern coast during the Late Quaternary (Dupont et al., 2021).

Integrative works have aimed to summarize the Quaternary variability in both ocean and atmospheric circulation systems and their impact on southern African climate including a variety of forcing mechanisms (Braun et al., 2020; Chase et al., 2021; Chase et al., 2017; Chase and Meadows, 2007; Chase et al., 2019; Chevalier and Chase, 2015; Neumann and Scott, 2018). Although the number of studies reconstructing Late Quaternary climate variability in South Africa has been increasing during the past decades, a comprehensive understanding of past environmental changes and their driving forces is still limited.

## References

- Abram, N.J., Mulvaney, R., Vimeux, F., Phipps, S.J., Turner, J., England, M.H., 2014. Evolution of the Southern Annular Mode during the past millennium. *Nature Climate Change* 4, 564-569.
- Aichner, B., Herzsuh, U., Wilkes, H., Vieth, A., Böhner, J., 2010.  $\delta D$  values of *n*-alkanes in Tibetan lake sediments and aquatic macrophytes – A surface sediment study and application to a 16ka record from Lake Koucha. *Organic Geochemistry* 41, 779-790.
- Araguás-Araguás, L., Froehlich, K., Rozanski, K., 2000. Deuterium and oxygen-18 isotope composition of precipitation and atmospheric moisture. *Hydrological Processes* 14, 1341-1355.
- Bar-Matthews, M., Marean, C.W., Jacobs, Z., Karkanas, P., Fisher, E.C., Herries, A.I.R., Brown, K., Williams, H.M., Bernatchez, J., Ayalon, A., Nilssen, P.J., 2010. A high resolution and continuous isotopic speleothem record of paleoclimate and paleoenvironment from 90 to 53 ka from Pinnacle Point on the south coast of South Africa. *Quaternary Science Reviews* 29, 2131-2145.
- Berger, A., Loutre, M.F., 1991. Insolation values for the climate of the last 10 million years. *Quaternary Science Reviews* 10, 297-317.
- Bowen, G.J., 2020. The Online Isotopes in Precipitation Calculator, version 3.1. URL: <http://www.waterisotopes.org>.
- Bowen, G.J., Wassenaar, L.I., Hobson, K.A., 2005. Global application of stable hydrogen and oxygen isotopes to wildlife forensics. *Oecologia* 143, 337-348.
- Bowler, J.M., Wyrwoll, K.-H., Lu, Y., 2001. Variations of the northwest Australian summer monsoon over the last 300,000 years: the paleohydrological record of the Gregory (Mulan) Lakes System. *Quaternary International* 83-85, 63-80.
- Braun, K., Bar-Matthews, M., Matthews, A., Ayalon, A., Cowling, R.M., Karkanas, P., Fisher, E.C., Dyez, K., Zilberman, T., Marean, C.W., 2019. Late Pleistocene records of speleothem stable isotopic compositions from Pinnacle Point on the South African south coast. *Quaternary Research* 91, 265-288.
- Braun, K., Bar-Matthews, M., Matthews, A., Ayalon, A., Zilberman, T., Cowling, R.M., Fisher, E.C., Herries, A.I.R., Brink, J.S., Marean, C.W., 2020. Comparison of climate and environment on the

## Chapter 5

- edge of the Palaeo-Agulhas Plain to the Little Karoo (South Africa) in Marine Isotope Stages 5–3 as indicated by speleothems. *Quaternary Science Reviews* 235, 105803.
- British Oceanographic data centre (BODC), 2014. GEBCO's gridded bathymetric data sets (GEBCO\_2014 Grid), 30 Arc Second resolution. National Oceanographic Centre, Liverpool.
- Caley, T., Extier, T., Collins, J.A., Schefuß, E., Dupont, L., Malaizé, B., Rossignol, L., Souron, A., McClymont, E.L., Jimenez-Espejo, F.J., García-Comas, C., Eynaud, F., Martinez, P., Roche, D.M., Jorry, S.J., Charlier, K., Wary, M., Gourves, P.-Y., Billy, I., Giraudeau, J., 2018. A two-million-year-long hydroclimatic context for hominin evolution in southeastern Africa. *Nature* 560, 76-79.
- Caley, T., Kim, J.H., Malaizé, B., Giraudeau, J., Laepple, T., Caillon, N., Charlier, K., Rebaubier, H., Rossignol, L., Castañeda, I.S., Schouten, S., Sinninghe Damsté, J.S., 2011. High-latitude obliquity as a dominant forcing in the Agulhas current system. *Climate of the Past* 7, 1285-1296.
- Carr, A.S., Thomas, D.S.G., Bateman, M.D., Meadows, M.E., Chase, B., 2006. Late Quaternary palaeoenvironments of the winter-rainfall zone of southern Africa: Palynological and sedimentological evidence from the Agulhas Plain. *Palaeogeography, Palaeoclimatology, Palaeoecology* 239, 147-165.
- Cawthra, H.C., Bateman, M.D., Carr, A.S., Compton, J.S., Holmes, P.J., 2014. Understanding Late Quaternary change at the land–ocean interface: a synthesis of the evolution of the Wilderness coastline, South Africa. *Quaternary Science Reviews* 99, 210-223.
- Chase, B., Harris, C., de Wit, M.J., Kramers, J., Doel, S., Stankiewicz, J., 2021. South African speleothems reveal influence of high- and lowlatitude forcing over the past 113.5 k.y. *Geology* 49, 1353–1357.
- Chase, B.M., Boom, A., Carr, A.S., Quick, L.J., Reimer, P.J., 2020. High-resolution record of Holocene climate change dynamics from southern Africa's temperate-tropical boundary, Baviaanskloof, South Africa. *Palaeogeography, Palaeoclimatology, Palaeoecology* 539, 109518.
- Chase, B.M., Chevalier, M., Boom, A., Carr, A.S., 2017. The dynamic relationship between temperate and tropical circulation systems across South Africa since the last glacial maximum. *Quaternary Science Reviews* 174, 54-62.
- Chase, B.M., Meadows, M.E., 2007. Late Quaternary dynamics of southern Africa's winter rainfall zone. *Earth-Science Reviews* 84, 103-138.
- Chase, B.M., Niedermeyer, E.M., Boom, A., Carr, A.S., Chevalier, M., He, F., Meadows, M.E., Ogle, N., Reimer, P.J., 2019. Orbital controls on Namib Desert hydroclimate over the past 50,000 years. *Geology* 47, 867-871.
- Chase, B.M., Quick, L.J., 2018. Influence of Agulhas forcing of Holocene climate change in South Africa's southern Cape. *Quaternary Research* 90, 303-309.
- Chase, B.M., Thomas, D.S.G., 2007. Multiphase late Quaternary aeolian sediment accumulation in western South Africa: Timing and relationship to palaeoclimatic changes inferred from the marine record. *Quaternary International* 166, 29-41.
- Chevalier, M., Chase, B.M., 2015. Southeast African records reveal a coherent shift from high- to low-latitude forcing mechanisms along the east African margin across last glacial–interglacial transition. *Quaternary Science Reviews* 125, 117-130.
- Cockcroft, M.J., Wilkinson, M.J., Tyson, P.D., 1987. The application of a present-day climatic model to the late quaternary in southern Africa. *Climatic Change* 10, 161-181.
- Cohen, A.L., 1993. A holocene sea surface temperature record in mollusc shells from the South African coast, PhD thesis. University of Cape Town, Cape Town.
- Cohen, A.L., Tyson, P.D., 1995. Sea-surface temperature fluctuations during the Holocene off the south coast of Africa: implications for terrestrial climate and rainfall. *The Holocene* 5, 304-312.
- Conroy, J.L., Overpeck, J.T., Cole, J.E., Shanahan, T.M., Steinitz-Kannan, M., 2008. Holocene changes in eastern tropical Pacific climate inferred from a Galápagos lake sediment record. *Quaternary Science Reviews* 27, 1166-1180.
- Crosta, X., Etourneau, J., Orme, L.C., Dalaiden, Q., Campagne, P., Swingedouw, D., Goosse, H., Massé, G., Miettinen, A., McKay, R.M., Dunbar, R.B., Escutia, C., Ikehara, M., 2021. Multi-

- decadal trends in Antarctic sea-ice extent driven by ENSO–SAM over the last 2,000 years. *Nature Geoscience* 14, 156-160.
- Dätwyler, C., Grosjean, M., Steiger, N.J., Neukom, R., 2020. Teleconnections and relationship between the El Niño–Southern Oscillation (ENSO) and the Southern Annular Mode (SAM) in reconstructions and models over the past millennium. *Climate of the Past* 16, 743-756.
- Dätwyler, C., Neukom, R., Abram, N.J., Gallant, A.J.E., Grosjean, M., Jacques-Coper, M., Karoly, D.J., Villalba, R., 2018. Teleconnection stationarity, variability and trends of the Southern Annular Mode (SAM) during the last millennium. *Climate Dynamics* 51, 2321-2339.
- Dee, D.P., Uppala, S.M., Simmons, A.J., Berrisford, P., Poli, P., Kobayashi, S., Andrae, U., Balmaseda, M.A., Balsamo, G., Bauer, P., Bechtold, P., Beljaars, A.C.M., van de Berg, L., Bidlot, J., Bormann, N., Delsol, C., Dragani, R., Fuentes, M., Geer, A.J., Haimberger, L., Healy, S.B., Hersbach, H., Hólm, E.V., Isaksen, I., Kållberg, P., Köhler, M., Matricardi, M., McNally, A.P., Monge-Sanz, B.M., Morcrette, J.-J., Park, B.-K., Peubey, C., de Rosnay, P., Tavolato, C., Thépaut, J.-N., Vitart, F., 2011. The ERA-Interim reanalysis: configuration and performance of the data assimilation system. *Quarterly Journal of the Royal Meteorological Society* 137, 553-597.
- du Plessis, N., Chase, B.M., Quick, L.J., Meadows, M.E., 2021. A Late Holocene pollen and microcharcoal record from Eilandvlei, southern Cape coast, South Africa, in: Runge, J., Gosling, W.D., Lézine, A.-M., Scott, L. (Eds.), *Quaternary Vegetation Dynamics – The African Pollen Database*. CRC Press, London, pp. 293-300.
- Dupont, L.M., Zhao, X., Charles, C., Faith, J.T., Braun, D., 2021. Continuous vegetation record of the Greater Cape Floristic Region (South Africa) covering the past 300 thousand years (IODP U1479). *Climate of the Past Discussion*. 2021, 1-32.
- Engelbrecht, C.J., Landman, W.A., 2016. Interannual variability of seasonal rainfall over the Cape south coast of South Africa and synoptic type association. *Climate Dynamics* 47, 295-313.
- Engelbrecht, C.J., Landman, W.A., Engelbrecht, F.A., Malherbe, J., 2015. A synoptic decomposition of rainfall over the Cape south coast of South Africa. *Climate Dynamics* 44, 2589-2607.
- Engelbrecht, F.A., Marean, C.W., Cowling, R.M., Engelbrecht, C.J., Neumann, F.H., Scott, L., Nkoana, R., O'Neal, D., Fisher, E., Shook, E., Franklin, J., Thatcher, M., McGregor, J.L., Van der Merwe, J., Dedekind, Z., Difford, M., 2019. Downscaling Last Glacial Maximum climate over southern Africa. *Quaternary Science Reviews* 226, 105879.
- Favre, A., Hewitson, B., Lennard, C., Cerezo-Mota, R., Tadross, M., 2013. Cut-off Lows in the South Africa region and their contribution to precipitation. *Climate Dynamics* 41, 2331-2351.
- Feakins, S.J., Sessions, A.L., 2010. Controls on the D/H ratios of plant leaf waxes in an arid ecosystem. *Geochimica et Cosmochimica Acta* 74, 2128-2141.
- Fick, S.E., Hijmans, R.J., 2017. WorldClim 2: new 1-km spatial resolution climate surfaces for global land areas. *International Journal of Climatology* 37, 4302-4315.
- Fletcher, M.-S., Moreno, P.I., 2012. Have the Southern Westerlies changed in a zonally symmetric manner over the last 14,000 years? A hemisphere-wide take on a controversial problem. *Quaternary International* 253, 32-46.
- Fogt, R.L., Marshall, G.J., 2020. The Southern Annular Mode: Variability, trends, and climate impacts across the Southern Hemisphere. *WIREs Climate Change* 11, e652.
- Ghadi, P., Nair, A., Crosta, X., Mohan, R., Manoj, M.C., Meloth, T., 2020. Antarctic sea-ice and palaeoproductivity variation over the last 156,000 years in the Indian sector of Southern Ocean. *Marine Micropaleontology* 160, 101894.
- Haberzettl, T., Baade, J., Compton, J., Daut, G., Dupont, L., Finch, J., Frenzel, P., Green, A., Hahn, A., Hebbeln, D., Helmschrot, J., Humphries, M., Kasper, T., Kirsten, K., Mäusbacher, R., Meadows, M., Meschner, S., Quick, L., Schefuß, E., Wündsche, M., Zabel, M., 2014. Paleoenvironmental investigations using a combination of terrestrial and marine sediments from South Africa - The RAIN (Regional Archives for Integrated iNvestigations) approach. *Zentralblatt für Geologie und Paläontologie, Teil I* 2014, 55-73.
- Hahn, A., Miller, C., Andó, S., Bouimetarhan, I., Cawthra, H.C., Garzanti, E., Green, A.N., Radeff, G., Schefuß, E., Zabel, M., 2018. The provenance of terrigenous components in marine sediments along the east coast of southern Africa. *Geochemistry, Geophysics, Geosystems* 19, 1946–1962.

## Chapter 5

- Hahn, A., Schefuß, E., Andò, S., Cawthra, H.C., Frenzel, P., Kugel, M., Meschner, S., Mollenhauer, G., Zabel, M., 2017. Southern Hemisphere anticyclonic circulation drives oceanic and climatic conditions in late Holocene southernmost Africa. *Climate of the Past* 13, 649-665.
- Hahn, A., Schefuß, E., Groeneveld, J., Miller, C., Zabel, M., 2021. Glacial to interglacial climate variability in the southeastern African subtropics (25–20° S). *Climate of the Past* 17, 345-360.
- Hart, N.C.G., Reason, C.J.C., Fauchereau, N., 2013. Cloud bands over southern Africa: seasonality, contribution to rainfall variability and modulation by the MJO. *Climate Dynamics* 41, 1199-1212.
- Hartmann, D.L., Lo, F., 1998. Wave-Driven Zonal Flow Vacillation in the Southern Hemisphere. *Journal of the Atmospheric Sciences* 55, 1303-1315.
- Hepp, J., Mayr, C., Rozanski, K., Schäfer, I.K., Tuthorn, M., Glaser, B., Juchelka, D., Stichler, W., Zech, R., Zech, M., 2021. Validation of a coupled  $\delta^2\text{H}_{n\text{-alkane}}-\delta^{18}\text{O}_{\text{sugar}}$  paleohygrometer approach based on a climate chamber experiment. *Biogeosciences* 18, 5363–5380.
- Hepp, J., Schäfer, I.K., Lanny, V., Franke, J., Bliedner, M., Rozanski, K., Glaser, B., Zech, M., Eglinton, T.I., Zech, R., 2020. Evaluation of bacterial glycerol dialkyl glycerol tetraether and  $^2\text{H}-^{18}\text{O}$  biomarker proxies along a central European topsoil transect. *Biogeosciences* 17, 741-756.
- Herrmann, N., Boom, A., Carr, A.S., Chase, B.M., West, A.G., Zabel, M., Schefuß, E., 2017. Hydrogen isotope fractionation of leaf wax *n*-alkanes in southern African soils. *Organic Geochemistry* 109, 1-13.
- Hodell, D.A., Kanfoush, S.L., Shemesh, A., Crosta, X., Charles, C.D., Guilderson, T.P., 2001. Abrupt Cooling of Antarctic Surface Waters and Sea Ice Expansion in the South Atlantic Sector of the Southern Ocean at 5000 cal yr B.P. *Quaternary Research* 56, 191-198.
- Hou, J., D'Andrea, W.J., Huang, Y., 2008. Can sedimentary leaf waxes record D/H ratios of continental precipitation? Field, model, and experimental assessments. *Geochimica et Cosmochimica Acta* 72, 3503-3517.
- Hou, J., Tian, Q., Wang, M., 2018. Variable apparent hydrogen isotopic fractionation between sedimentary *n*-alkanes and precipitation on the Tibetan Plateau. *Organic Geochemistry* 122, 78-86.
- Ibebuchi, C.C., 2021. On the Relationship between Circulation Patterns, the Southern Annular Mode, and Rainfall Variability in Western Cape. *Atmosphere* 12, 753.
- L'Heureux, M.L., Thompson, D.W.J., 2006. Observed Relationships between the El Niño–Southern Oscillation and the Extratropical Zonal-Mean Circulation. *Journal of Climate* 19, 276-287.
- Lemma, B., Bittner, L., Glaser, B., Kebede, S., Nemomissa, S., Zech, W., Zech, M., 2021.  $\delta^2\text{H}_{n\text{-alkane}}$  and  $\delta^{18}\text{O}_{\text{sugar}}$  biomarker proxies from leaves and topsoils of the Bale Mountains, Ethiopia, and implications for paleoclimate reconstructions. *Biogeochemistry* 153, 135-153.
- Li, Y., Yang, S., Luo, P., Xiong, S., 2019. Aridity-controlled hydrogen isotope fractionation between soil *n*-alkanes and precipitation in China. *Organic Geochemistry* 133, 53-64.
- Lisiecki, L.E., Raymo, M.E., 2005. A Pliocene-Pleistocene stack of 57 globally distributed benthic  $\delta^{18}\text{O}$  records. *Paleoceanography* 20.
- Liu, J., An, Z., 2019. Variations in hydrogen isotopic fractionation in higher plants and sediments across different latitudes: Implications for paleohydrological reconstruction. *Science of The Total Environment* 650, 470-478.
- Macron, C., Pohl, B., Richard, Y., Bessafi, M., 2014. How do Tropical Temperate Troughs Form and Develop over Southern Africa? *Journal of Climate* 27, 1633-1647.
- Malherbe, J., Landman, W.A., Engelbrecht, F.A., 2014. The bi-decadal rainfall cycle, Southern Annular Mode and tropical cyclones over the Limpopo River Basin, southern Africa. *Climate Dynamics* 42, 3121-3138.
- Martin, A.R.H., 1968. Pollen Analysis of Groenvlei Lake Sediments Knysna (South Africa). *Review of Palaeobotany and Palynology* 7, 107-144.
- Martínez-Méndez, G., Zahn, R., Hall, I.R., Peeters, F.J.C., Pena, L.D., Cacho, I., Negre, C., 2010. Contrasting multiproxy reconstructions of surface ocean hydrography in the Agulhas Corridor and implications for the Agulhas Leakage during the last 345,000 years. *Paleoceanography* 25, PA4227.

- Mason, S.J., Jury, M.R., 1997. Climatic variability and change over southern Africa: a reflection on underlying processes. *Progress in Physical Geography: Earth and Environment* 21, 23-50.
- McDermott, F., 2004. Palaeo-climate reconstruction from stable isotope variations in speleothems: a review. *Quaternary Science Reviews* 23, 901-918.
- Miller, C., Finch, J., Hill, T., Peterse, F., Humphries, M., Zabel, M., Schefuß, E., 2019. Late Quaternary climate variability at Mfabeni peatland, eastern South Africa. *Climate of the Past* 15, 1153-1170.
- Miller, C., Hahn, A., Liebrand, D., Zabel, M., Schefuß, E., 2020. Mid- and low latitude effects on eastern South African rainfall over the Holocene. *Quaternary Science Reviews* 229, 106088.
- Moy, C.M., Seltzer, G.O., Rodbell, D.T., Anderson, D.M., 2002. Variability of El Niño/Southern Oscillation activity at millennial timescales during the Holocene epoch. *Nature* 420, 162-165.
- Ndarana, T., Rammopo, T.S., Reason, C.J.C., Bopape, M.-J., Engelbrecht, F., Chikoore, H., 2021. Two types of ridging South Atlantic Ocean anticyclones over South Africa and the associated dynamical processes. *Atmospheric Research*, 105897.
- Neumann, F.H., Scott, L., 2018. E.M. van Zinderen Bakker (1907–2002) and the study of African Quaternary palaeoenvironments. *Quaternary International* 495, 153-168.
- Nielsen, S.H.H., Koç, N., Crosta, X., 2004. Holocene climate in the Atlantic sector of the Southern Ocean: Controlled by insolation or oceanic circulation? *Geology* 32, 317-320.
- Peeters, F.J.C., Acheson, R., Brummer, G.-J.A., de Ruijter, W.P.M., Schneider, R.R., Ganssen, G.M., Ufkes, E., Kroon, D., 2004. Vigorous exchange between the Indian and Atlantic oceans at the end of the past five glacial periods. *Nature* 430, 661-665.
- Perren, B.B., Hodgson, D.A., Roberts, S.J., Sime, L., Van Nieuwenhuyze, W., Verleyen, E., Vyverman, W., 2020. Southward migration of the Southern Hemisphere westerly winds corresponds with warming climate over centennial timescales. *Communications Earth & Environment* 1, 58.
- Polissar, P.J., Freeman, K.H., 2010. Effects of aridity and vegetation on plant-wax  $\delta D$  in modern lake sediments. *Geochimica et Cosmochimica Acta* 74, 5785-5797.
- Quick, L.J., Carr, A.S., Meadows, M.E., Boom, A., Bateman, M.D., Roberts, D.L., Reimer, P.J., Chase, B.M., 2015. A late Pleistocene–Holocene multi-proxy record of palaeoenvironmental change from Still Bay, southern Cape Coast, South Africa. *Journal of Quaternary Science* 30, 870-885.
- Quick, L.J., Chase, B.M., Carr, A.S., Chevalier, M., Grobler, B.A., Meadows, M.E., 2021. A 25,000 year record of climate and vegetation change from the southwestern Cape coast, South Africa. *Quaternary Research*, 1-18.
- Quick, L.J., Chase, B.M., Wündsche, M., Kirsten, K., Chevalier, M., Mäusbacher, R., Meadows, M., Haberzettl, T., 2018. A high-resolution record of Holocene climate and vegetation dynamics from the southern Cape coast of South Africa: pollen and microcharcoal evidence from Eilandvlei. *Journal of Quaternary Science*, 1-14.
- Quick, L.J., Meadows, M.E., Bateman, M.D., Kirsten, K.L., Mäusbacher, R., Haberzettl, T., Chase, B.M., 2016. Vegetation and climate dynamics during the last glacial period in the fynbos-afrotemperate forest ecotone, southern Cape, South Africa. *Quaternary International* 404, Part B, 136-149.
- Reason, C.J.C., Rouault, M., 2005. Links between the Antarctic Oscillation and winter rainfall over western South Africa. *Geophysical Research Letters* 32, L07705.
- Rein, B., Lückge, A., Reinhardt, L., Sirocko, F., Wolf, A., Dullo, W.-C., 2005. El Niño variability off Peru during the last 20,000 years. *Paleoceanography* 20.
- Rein, B., Lückge, A., Sirocko, F., 2004. A major Holocene ENSO anomaly during the Medieval period. *Geophysical Research Letters* 31, L17211.
- Rouault, M., White, S.A., Reason, C.J.C., Lutjeharms, J.R.E., Jobard, I., 2002. Ocean–Atmosphere Interaction in the Agulhas Current Region and a South African Extreme Weather Event. *Weather and Forecasting* 17, 655-669.
- Simon, M.H., Arthur, K.L., Hall, I.R., Peeters, F.J.C., Loveday, B.R., Barker, S., Ziegler, M., Zahn, R., 2013. Millennial-scale Agulhas Current variability and its implications for salt-leakage through the Indian–Atlantic Ocean Gateway. *Earth and Planetary Science Letters* 383, 101-112.

## Chapter 5

- Simon, M.H., Ziegler, M., Barker, S., van der Meer, M.T.J., Schouten, S., Hall, I.R., 2020. A late Pleistocene dataset of Agulhas Current variability. *Scientific Data* 7, 385.
- Singleton, A.T., Reason, C.J.C., 2006. Numerical simulations of a severe rainfall event over the Eastern Cape coast of South Africa: sensitivity to sea surface temperature and topography. *Tellus A: Dynamic Meteorology and Oceanography* 58, 335-367.
- Smith, F.A., Freeman, K.H., 2006. Influence of physiology and climate on  $\delta D$  of leaf wax *n*-alkanes from C3 and C4 grasses. *Geochimica et Cosmochimica Acta* 70, 1172-1187.
- Strobel, P., Bliedtner, M., Carr, A.S., Frenzel, P., Klaes, B., Salazar, G., Struck, J., Szidat, S., Zech, R., Haberzettl, T., 2021. Holocene sea level and environmental change at the southern Cape - an 8.5 kyr multi-proxy paleoclimate record from lake Voëlvlei, South Africa. *Climate of the Past* 17, 1567-1586.
- Strobel, P., Bliedtner, M., Carr, A.S., Struck, J., du Plessis, N., Glaser, B., meadows, M.E., Quick, L.J., Zech, M., Zech, R., Haberzettl, T., submitted. Reconstructing Late Quaternary precipitation and its source on the southern Cape coast of South Africa: A multi-proxy paleoenvironmental record from Vankervelsvlei.
- Strobel, P., Haberzettl, T., Bliedtner, M., Struck, J., Glaser, B., Zech, M., Zech, R., 2020. The potential of  $\delta^2H_{n\text{-alkanes}}$  and  $\delta^{18}O_{\text{sugar}}$  for paleoclimate reconstruction – A regional calibration study for South Africa. *Science of The Total Environment* 716, 137045.
- Strobel, P., Kasper, T., Frenzel, P., Schitteck, K., Quick, L.J., Meadows, M.E., Mäusbacher, R., Haberzettl, T., 2019. Late Quaternary palaeoenvironmental change in the year-round rainfall zone of South Africa derived from peat sediments from Vankervelsvlei. *Quaternary Science Reviews* 218, 200-214.
- Struck, J., 2022. Calibration and First Application of Biomarker and Compound-Specific Isotope Analyses in Mongolia, Physical Geography, Institute of Geography. Friedrich Schiller University Jena, Jena.
- Struck, J., Bliedtner, M., Strobel, P., Bittner, L., Bazarradnaa, E., Andreeva, D., Zech, W., Glaser, B., Zech, M., Zech, R., 2020. Leaf Waxes and Hemicelluloses in Topsoils Reflect the  $\delta^2H$  and  $\delta^{18}O$  Isotopic Composition of Precipitation in Mongolia. *Frontiers in Earth Science* 8.
- Stuut, J.-B.W., Crosta, X., van der Borg, K., Schneider, R., 2004. Relationship between Antarctic sea ice and southwest African climate during the late Quaternary. *Geology* 32, 909-912.
- Stuut, J.-B.W., Lamy, F., 2004. Climate variability at the southern boundaries of the Namib (southwestern Africa) and Atacama (northern Chile) coastal deserts during the last 120,000 yr. *Quaternary Research* 62, 301-309.
- Talma, A.S., Vogel, J.C., 1992. Late Quaternary paleotemperatures derived from a speleothem from Cango Caves, Cape Province, South Africa. *Quaternary Research* 37, 203-213.
- Trabucco, A., Zomer, R., 2019. Global Aridity Index and Potential Evapotranspiration (ET0) Climate Database v2. figshare. Fileset.
- Tuthorn, M., Zech, M., Ruppenthal, M., Oelmann, Y., Kahmen, A., Valle, H.F.d., Wilcke, W., Glaser, B., 2014. Oxygen isotope ratios ( $^{18}O/^{16}O$ ) of hemicellulose-derived sugar biomarkers in plants, soils and sediments as paleoclimate proxy II: Insight from a climate transect study. *Geochimica et Cosmochimica Acta* 126, 624-634.
- Tuthorn, M., Zech, R., Ruppenthal, M., Oelmann, Y., Kahmen, A., del Valle, H.F., Eglinton, T., Rozanski, K., Zech, M., 2015. Coupling  $\delta^2H$  and  $\delta^{18}O$  biomarker results yields information on relative humidity and isotopic composition of precipitation - a climate transect validation study. *Biogeosciences* 12, 3913-3924.
- Tyson, P.D., 1986. Climatic change and variability in southern Africa. Oxford University Press, Cape Town.
- van Zinderen Bakker, E.M., 1976. The evolution of late Quaternary paleoclimates of Southern Africa. *Palaeoecology Africa* 9 9, 160-202.
- Waelbroeck, C., Labeyrie, L., Michel, E., Duplessy, J.C., McManus, J.F., Lambeck, K., Balbon, E., Labracherie, M., 2002. Sea-level and deep water temperature changes derived from benthic foraminifera isotopic records. *Quaternary Science Reviews* 21, 295-305.

- Washington, R., Preston, A., 2006. Extreme wet years over southern Africa: Role of Indian Ocean sea surface temperatures. *Journal of Geophysical Research: Atmospheres* 111, D15104.
- Weldon, D., Reason, C.J.C., 2014. Variability of rainfall characteristics over the South Coast region of South Africa. *Theoretical and Applied Climatology* 115, 177-185.
- Wündsche, M., Haberzettl, T., Cawthra, H.C., Kirsten, K.L., Quick, L.J., Zabel, M., Frenzel, P., Hahn, A., Baade, J., Daut, G., Kasper, T., Meadows, M.E., Mäusbacher, R., 2018. Holocene environmental change along the southern Cape coast of South Africa – Insights from the Eilandvlei sediment record spanning the last 8.9 kyr. *Global and Planetary Change* 163, 51-66.
- Wündsche, M., Haberzettl, T., Kirsten, K.L., Kasper, T., Zabel, M., Dietze, E., Baade, J., Daut, G., Meschner, S., Meadows, M.E., Mäusbacher, R., 2016a. Sea level and climate change at the southern Cape coast, South Africa, during the past 4.2 kyr. *Palaeogeography Palaeoclimatology Palaeoecology* 446, 295-307.
- Wündsche, M., Haberzettl, T., Meadows, M.E., Kirsten, K.L., Kasper, T., Baade, J., Daut, G., Stoner, J.S., Mäusbacher, R., 2016b. The impact of changing reservoir effects on the C-14 chronology of a Holocene sediment record from South Africa. *Quaternary Geochronology* 36, 148-160.
- Zhang, Z., Leduc, G., Sachs, J.P., 2014. El Niño evolution during the Holocene revealed by a biomarker rain gauge in the Galápagos Islands. *Earth and Planetary Science Letters* 404, 420-434.
- Zongxing, L., Qi, F., Song, Y., Wang, Q.J., Yang, J., Yongge, L., Jianguo, L., Xiaoyan, G., 2016. Stable isotope composition of precipitation in the south and north slopes of Wushaoling Mountain, northwestern China. *Atmospheric Research* 182, 87-101.

## Chapter 6

---

### Conclusions and Outlook

---

Author: Paul Strobel



## 6 Conclusions and Outlook

---

### 6.1 Conclusions

This thesis focuses on the reconstruction of paleoenvironmental and paleoclimatic changes, and in particular paleohydrological variations, along South Africa's southern Cape coast during the Late Quaternary using direct hydrological proxies. In this context, biomarkers and their compound-specific isotopes show great potential to serve as direct hydrological proxies in paleoenvironmental research in South Africa. However, for robust interpretation of the proxy signals, they need to be regionally calibrated in a first step on modern reference material (i.e., topsoils). Subsequently, they can be applied to sediments together with well-established methods such as granulometry and palynology as well as organic and inorganic geochemistry to robustly reconstruct paleoenvironmental, paleoclimatic and particularly paleohydrological changes in South Africa during the Holocene and Late Quaternary.

The hydrogen isotopic composition of leaf wax-derived *n*-alkanes ( $\delta^2\text{H}_{n\text{-alkane}}$ ) and the oxygen isotopic composition of hemicellulose-derived sugars ( $\delta^{18}\text{O}_{\text{sugar}}$ ) are such valuable direct hydrological proxies. However, factors such as evapotranspiration and the plants growth form and photosynthetic mode potentially influence the proxy-signal and can complicate the interpretation when analyzed in a single-water isotope approach. Coupling both isotopes into a coupled  $\delta^2\text{H}_{n\text{-alkane}}-\delta^{18}\text{O}_{\text{sugar}}$  approach (paleohygrometer) shows great potential to quantitatively reconstruct the isotopic composition of precipitation and relative humidity. Within this thesis, the potential of  $\delta^2\text{H}_{n\text{-alkane}}$  and  $\delta^{18}\text{O}_{\text{sugar}}$  as well as coupling both isotopes for climate reconstruction in South Africa could be shown. More detailed, the newly obtained proxies show the great potential to robustly reconstruct the isotopic composition of precipitation and relative humidity in South Africa. The reconstructed isotopic composition of precipitation refers to the atmospheric source of moisture and thus enables to disentangle precipitation contributions from the major atmospheric circulation systems in South Africa. Reconstructed relative humidity reflects local moisture availability. However, (past) changes of the dominant plants growth form and photosynthetic mode have to be considered prior to interpretation, because they possibly bias the results of the coupled  $\delta^2\text{H}_{n\text{-alkane}}-\delta^{18}\text{O}_{\text{sugar}}$  approach. This highlights that compound-specific isotope analyzes and the application of the coupled  $\delta^2\text{H}_{n\text{-alkane}}-\delta^{18}\text{O}_{\text{sugar}}$  approach provide an enormous added value in paleoenvironmental and paleoclimatic, and in particular paleohydrological studies, when applied in sediment archives.

The regionally evaluated biomarker isotopes and the coupled  $\delta^2\text{H}_{n\text{-alkane}}-\delta^{18}\text{O}_{\text{sugar}}$  approach are the foundation for robust reconstruction of past environmental and climate changes and their respective variations of the atmospheric circulation patterns contributing precipitation along the southern Cape coast of South Africa. The sediment records from Voëlvllei and Vankervelsvllei provide evidence for distinct environmental and climate changes during major parts of the

## Chapter 6

Holocene. Both records provide robust chronological control and the combination of the newly evaluated biomarker proxies together with well-established sedimentological and geochemical proxies in a multi-proxy approach in high temporal resolution helps to draw a coherent picture of moisture availability and precipitation source along South Africa's southern Cape coast. During the Holocene, hydroclimate variability is driven by contributions from Easterly- and locally-derived precipitation leading to moist conditions and a year-round precipitation regime from ~7.5 to ~5.0 ka cal BP and from ~3.0 ka cal BP until present day, while drier conditions accompanied by a shift to a winter rainfall regime occurred from ~5.0 to ~3.0 ka cal BP. Comparison with other regional records support these results, but the driving forces of the reconstructed climate variability are still subject of considerable debate. To some extent, this is due to a lack of studies providing robust records which can be used for comparison.

Besides providing Holocene sediments, Vankervelsvlei is one of the scarce terrestrial sediment archives along the southern Cape coast also providing sediments of Late Quaternary age. Proxy-data indicate distinct environmental and climatic changes at the site during the past. During glacial periods, distinct sea level variations made the coastline migrate up to 100 km south of its present position. This led to increased continentality and dry conditions at Vankervelsvlei and the southern Cape coast. Conversely, during interglacial periods, the coastline was roughly at its present position and more humid conditions have been recorded at Vankervelsvlei. This identifies sea-level changes as a main driver of climate variability at the site on orbital time scales. The results are supported by previous investigations at Vankervelsvlei as well as stalagmite records from the surrounding area therefore providing a coherent regional climate signal along South Africa's southern Cape coast.

Overall, this thesis demonstrates the benefit of analyzing and coupling compound-specific oxygen and hydrogen isotopes from plant-derived biomarkers for paleohydrological studies. Using the combination of these methods in a multi-proxy approach enables to draw a comprehensive and coherent picture of past environmental changes along South Africa's southern Cape coast and, to a first time in this region, enables to reliably reconstruct the atmospheric source of precipitation and relative humidity.

## 6.2 Outlook

Future climate scenarios given by the Intergovernmental Panel on Climate Change predict distinct environmental and climatic changes in South Africa such as increasing temperatures and decreasing amounts of precipitation in large parts of the country. For the humid parts of the country, including the southern Cape coast, a much greater unpredictability and more extreme events such as floods are predicted. The reliability of predicting future scenarios distinctly depends on robust reconstructions of past environmental, climatic and particularly hydrological variations. While water is a fundamental resources for all levels of socio-economic activities, reliable predictions of future changes of the amount and seasonality of precipitation are of great interest for the society.

This thesis shows the great potential of plant-derived biomarkers and their compound-specific isotopic signatures for paleohydrological studies. However, samples of modern reference material used to evaluate the potential of compound-specific hydrogen from leaf wax-derived *n*-alkanes and compound-specific oxygen isotopes from hemicellulose-derived sugars are unequally distributed in South Africa, with the latter being distinctly underrepresented. Therefore, there is a need to increase the understanding of regional drivers of the isotopic signature of compound-specific oxygen isotopes from hemicellulose-derived sugars in South Africa, especially by analyzing samples from the summer rainfall zone as well as the more arid parts of the winter and year-round rainfall zones of the country.

Within this thesis, two sediment archives are used to reconstruct the paleoenvironmental, paleoclimatic and particularly paleohydrological history of South Africa's southern Cape coast during the Holocene and the Late Quaternary. Studies at both sites, Voëlvlei and Vankervelsvlei, highlight the need and value of a robust understanding about the depositional settings in the sediment archives to establish a reliable chronology, which is the foundation to robustly reconstruct paleoenvironmental and paleoclimatic changes. It is additionally highlighted, that the signal interpretation in near-coastal terrestrial sediment archives is more straight forward when marine water intrusions are absent during the past. To avoid erroneous interpretations and to derive the most comprehensive understanding of past environmental, climatic and hydrological changes, sediment archives should always focus on a multi-proxy approach including methods from disciplines such as sedimentology, palynology, paleontology, mineralogy as well as organic, inorganic and stable isotope geochemistry and avoid estuarine sediment basins.

The enormous potential of the coupled  $\delta^2\text{H}_{n\text{-alkane}}-\delta^{18}\text{O}_{\text{sugar}}$  approach (paleohygrometer) is demonstrated, but the existing record from Vankervelsvlei unfortunately provides only coarse temporal resolution. Therefore, there is potential to distinctly increase the number of samples and thus temporal resolution at the site for both the Holocene and the Late Quaternary. This potentially enables to disentangle past drivers of hydroclimate variability such as ENSO, SAM,

## Chapter 6

sea surface temperature and the extent of the Antarctic sea ice at South Africa's southern Cape coast, which are still subject of considerable debate. To evaluate the spatial extent of past environmental and climatic dynamics in South Africa and to enable proxy comparability, there is a need for further studies investigating terrestrial sediment records using the coupled  $\delta^2\text{H}_{n\text{-alkane}}-\delta^{18}\text{O}_{\text{sugar}}$  approach (paleohygrometer) in multi proxy-approaches. This is especially the case for the winter rainfall zone and the summer rainfall zone to more comprehensively decipher past variations of the temperate Westerlies and tropical Easterlies directly in that regions where each system dominates the precipitation season in South Africa. Moreover, the coupled  $\delta^2\text{H}_{n\text{-alkane}}-\delta^{18}\text{O}_{\text{sugar}}$  approach (paleohygrometer) potentially sheds light on a proposed steep environmental gradient of coastal and further inland located regions in the year-round rainfall zone, which possibly exists due to the application of rather indirect hydrological proxies and discrepancies in their interpretations. Due to proxy comparability and nature as direct hydrological proxies, the results of the coupled  $\delta^2\text{H}_{n\text{-alkane}}-\delta^{18}\text{O}_{\text{sugar}}$  approach (paleohygrometer) could contribute to a better understanding of regional hydrological variability also in the year-round rainfall zone.

The identification of archives providing sediments of Late Quaternary age and their analyzes using direct hydrological proxies in a multi-proxy approach should also be focus of future research. This is because besides a robust and comprehensive understanding of Holocene environmental and climate variability also Late Quaternary climate dynamics and their driving forces are of great interest for future climate predictions.

Besides reliable reconstruction of past environmental, climatic and particularly hydrological changes in South Africa, their connection to ecosystem hazards is of great interest for our society. For example, wildfires are recently very prominent and are predicted to increase at South Africa's southern Cape coast. Well-established and innovative proxies, such as the abundances and distributions of charcoal, polyaromatic hydrocarbons and monosaccharide anhydrates, could be analyzed in sediment archives and compared to robust paleohydrological proxies. For that purpose, for example, Vankervelsvlei would be well-suited and shows great potential to reconstruct past fire history at the Southern Cape coast during the Holocene in high temporal resolution with outstanding chronological control.

# Appendix

## Supplementary data

### Appendix 1: The potential of $\delta^2\text{H}_{\text{r-alkanes}}$ and $\delta^{18}\text{O}_{\text{sugar}}$ for paleoclimate reconstruction – A regional calibration study for South Africa

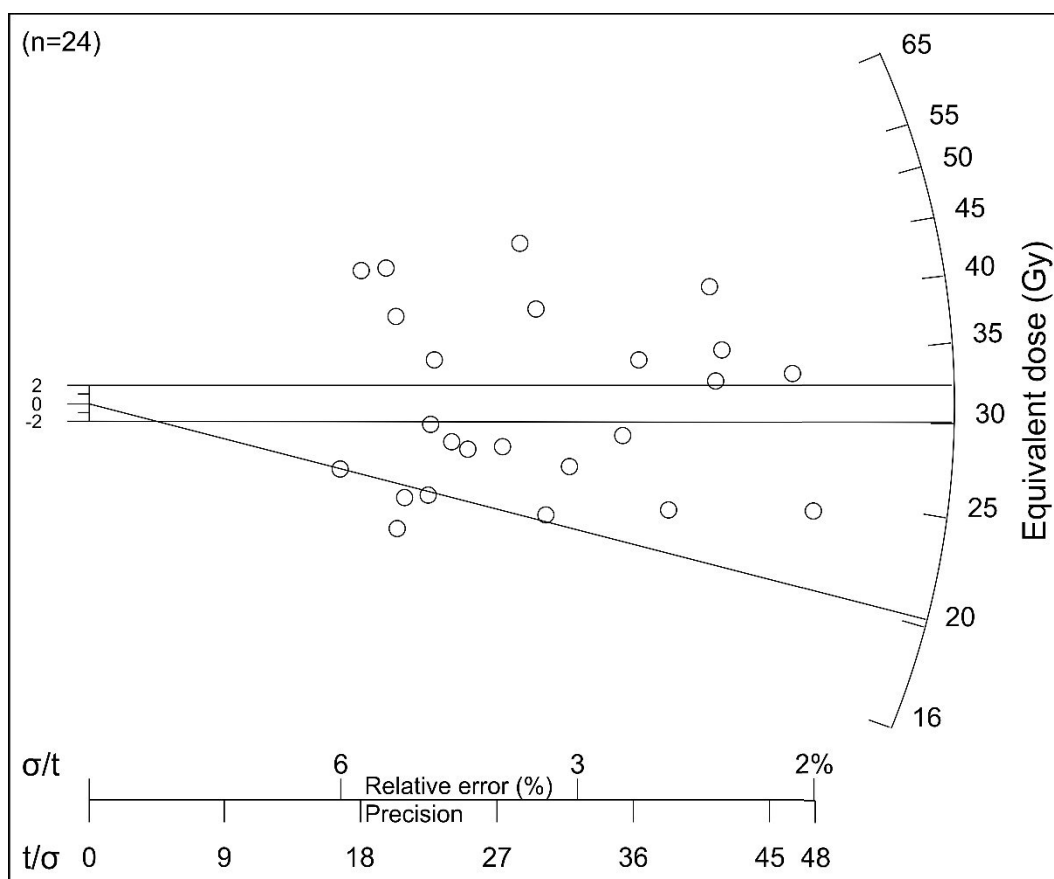
The research data shown in Chapter 2 is available online at Pangaea:  
<https://doi.pangaea.de/10.1594/PANGAEA.935599>

### Appendix 2: Holocene sea level and environmental change at the southern Cape - an 8.5 kyr multi-proxy paleoclimate record from lake Voëlvlei, South Africa

The research data shown in Chapter 3 is available online at Pangaea:  
<https://doi.pangaea.de/10.1594/PANGAEA.935616>

The supplementary information of the article presented in Chapter 3 is shown below and available online at:

<https://cp.copernicus.org/articles/17/1567/2021/cp-17-1567-2021-supplement.pdf>



S1: Radial plot showing the De distribution of the OSL sample.

**Appendix 3: Reconstructing Late Quaternary precipitation and its source on the southern Cape coast of South Africa: A multi-proxy paleoenvironmental record from Vankervelsvlei**

The study shown in Chapter 4 has been published in *Quaternary Science reviews*:

Strobel, P., Bliedtner, M., Carr, A.S., Struck, J., du Plessis, N., Glaser, B., Meadows, M.E., Quick, L.J., Zech, M., Zech, R., Haberzettl, T., 2022. Reconstructing Late Quaternary precipitation and its source on the southern Cape coast of South Africa: A multi-proxy paleoenvironmental record from Vankervelsvlei. *Quaternary Science Reviews* 284, 107467. <https://doi.org/10.1016/j.quascirev.2022.107467>.

The research data shown in Chapter 4 is available online at Pangaea:  
<https://doi.pangaea.de/10.1594/PANGAEA.940148>

The supplementary information of the article presented in Chapter 4 is shown below and available online at:

<https://ars.els-cdn.com/content/image/1-s2.0-S0277379122000981-mmc1.docx>

**Supplementary Information for**

**Reconstructing Late Quaternary precipitation and its source on the southern Cape coast of South Africa: A multi-proxy paleoenvironmental record from Vankervelsvlei**

Strobel, P.\*<sup>1</sup>, Bliedtner, M.<sup>1</sup>, Carr, A. S.<sup>2</sup>, Struck, J.<sup>1</sup>, du Plessis, N.<sup>3,4</sup>, Glaser, B.<sup>5</sup>, Meadows, M.E.<sup>3,6</sup>, Quick, L.J.<sup>4</sup>, Zech, M.<sup>7</sup>, Zech, R.<sup>1</sup>, Haberzettl, T.<sup>8</sup>

\* Corresponding author: Physical Geography, Institute of Geography, Friedrich Schiller University Jena, Loebdergraben 32, 07743 Jena, Germany, [paul.strobel@uni-jena.de](mailto:paul.strobel@uni-jena.de), +49 (0)3641 9 48807

<sup>1</sup> Physical Geography, Institute of Geography, Friedrich Schiller University Jena, Jena, Germany

<sup>2</sup> School of Geography, Geology and the Environment, University of Leicester, Leicester, UK

<sup>3</sup> Department of Environmental and Geographical Science, University of Cape Town, Rondebosch, South Africa

<sup>4</sup> African Centre for Coastal Palaeoscience, Nelson Mandela University, Port Elizabeth, South Africa

<sup>5</sup> Institute of Agricultural and Nutritional Sciences, Soil Biogeochemistry, Martin-Luther University Halle-Wittenberg, Halle (Saale), Germany

<sup>6</sup> School of Geographic Sciences, East China Normal University, Shanghai, People's Republic of China

<sup>7</sup> Heisenberg Chair of Physical Geography with Focus on Paleoenvironmental Research, Institute of Geography, Technische Universität Dresden, Dresden, Germany

<sup>8</sup> Physical Geography, Institute for Geography and Geology, University of Greifswald, Greifswald, Germany

## 1 Radiocarbon ages

Table S1: Conventional radiocarbon ages as well as  $2\sigma$  calibrated age ranges and median calibrated ages (Calib 8.20) (Stuiver et al., 2020) using the SHcal20 calibration curve (Hogg et al., 2020) of dated bulk TOC and organic macro particle (OMP) samples from the composite VVV16 record. \* and # mark recalibrated ages published by Strobel et al. (2019) and du Plessis et al. (2021), respectively.

Composite depth [m]	Lab ID	$1\sigma$ conventional $^{14}\text{C}$ age [BP]	Dated material	Median age and $2\sigma$ error [cal BP]
0.83	Poz-92269	$10\pm 30$	OMP	$50^{+40/-40}$ #
1.43	Poz-92270	$545\pm 30$	OMP	$525^{+25/-25}$ #
1.82	Poz-102442	$560\pm 30$	OMP	$530^{+30/-30}$ #
4.26	Poz-86757	$1,385\pm 30$	OMP	$1,270^{+40/-10}$ *
5.42	Poz-86758	$2,385\pm 35$	OMP	$2,360^{+30/-60}$ *
6.48	Poz-86759	$3,765\pm 35$	OMP	$4,080^{+80/-90}$ *
7.65	Poz-86760	$4,420\pm 40$	OMP	$4,960^{+90/-110}$ *
8.69	Poz-86761	$5,350\pm 40$	bulk	$6,090^{+110/-100}$ *
9.59	Poz-86762	$6,300\pm 50$	bulk	$7,190^{+120/-40}$ *
10.12	Poz-86763	$7,070\pm 40$	bulk	$7,870^{+95/-120}$ *
11.11	Poz-86764	$6,560\pm 40$	bulk	$7,440^{+70/-110}$ *
11.21	Poz-86765	$24,530\pm 180$	bulk	$28,750^{+400/-480}$ *
11.65	Poz-87258	$24,650\pm 150$	bulk	$28,310^{+400/-460}$ *
11.75	Poz-86767	$24,180\pm 180$	bulk	$28,880^{+280/-270}$ *
12.00	Poz-87259	$27,700\pm 180$	bulk	$31,570^{+340/-360}$ *
12.82	Poz-87260	$33,500\pm 400$	bulk	$38,300^{+1,100/-1,200}$ *

## 2 Optically Stimulated Luminescence dating (OSL)

Samples for OSL dating were taken from short sections of core tubing. The ends of the tubes were opened under subdued red light at the University of Leicester. Sediment was extracted from the interior of the core tubes over typical depth ranges of ~5 cm. Two sub-samples were taken from the core tube of sample 16-1-10, with 16-1-10a taken over a depth range of 4-9 cm and the subjacent 16-1-10b over a depth range of 9-15 cm. In all cases, material in contact with the core tube surfaces was not sampled for equivalent dose ( $D_e$ ) determination, but a representative sub-set of this sediment was used to estimate the sample water contents and radionuclide contents (for dose rate analyses). Coarse quartz and K-feldspar grains were then isolated from these samples following standard methods, including HCl treatment to remove carbonates,  $\text{H}_2\text{O}_2$  treatment to remove organics and wet sieving to isolate a size fraction for analysis (between 90 and 250  $\mu\text{m}$ ). In most cases this was the 180-212  $\mu\text{m}$  fraction, but for fine grained material (VVV16-27 and VVV16-2-8) it was necessary to use a wider and finer

## Appendix

grained fraction (**Table S5**). The sieve fractions were density separated to isolate the fractions  $<2.58 \text{ g}\cdot\text{cm}^{-3}$  and  $>2.58 <2.7 \text{ g}\cdot\text{cm}^{-3}$ . The quartz-rich fraction was etched for 45 minutes in 48% hydrofluoric acid, washed in HCl for one hour, rinsed, dried and then re-sieved. The  $<2.58 \text{ g}\cdot\text{cm}^{-3}$  (K-feldspar) fractions were not etched.

All luminescence measurements were performed on a Risoe DA20 TL/OSL reader. For quartz analyses, stimulation (40 s at 125 °C) was provided by blue LEDs (wavelength 470 nm) at 70% power (delivering  $\sim 72 \text{ mW}\cdot\text{cm}^{-2}$  to the sample). OSL signals were detected with an EMI 9235QA photomultiplier tube with a U-340 detection filter. For K-feldspar measurements stimulation was provided by IR diodes (wavelength 870 nm) with detection of the resulting (blue-violet) IRSL through a combination of Schott BG39 filters and Corning 7-59 filters (detection range 320-450 nm). Laboratory irradiations were delivered by a  $^{90}\text{Sr}$  beta source with a dose rate (at the time of measurement) of  $8.08\text{-}7.98 \text{ Gy}\cdot\text{min}^{-1}$ . This beta source has been calibrated against the Risoe calibration quartz and validated via comparison with an external luminescence dating laboratory.

Sample equivalent doses ( $D_e$ ) for quartz were estimated using the Single Aliquot Regeneration (SAR) protocol (Murray and Wintle, 2000, 2003; Wintle and Murray, 2006). All SAR analyses comprised a 6 or 7 regeneration point sequence, and included a (repeat) recycling dose, a zero dose and a feldspar detection (IR depletion test) dose point (Duller, 2003). Appropriate measurement (preheating) conditions were determined using dose recovery preheat experiments (Murray and Wintle, 2003). The K-feldspar extracts were analysed using the post-IR IRSL single aliquot regeneration method (Buylaert et al., 2009; Thomsen et al., 2008), which comprises an initial IRSL measurement at 50°C followed immediately by a post-IR IRSL measurement at 225°C (pIRIR<sub>225</sub>). All measurements were carried out on small (2 mm) aliquots, which in most cases (except VVV16-2-7 and the two VVV16-2-8 samples) contained  $\sim 100\text{-}200$  grains. For quartz, the signal integration windows comprised the first 0.8 seconds of stimulation with a subtracted background signal derived from the last 1.6 seconds. For K-feldspar the integration windows (300 second stimulation for the pIRIR<sub>225</sub>) were the first 8 seconds and the last 20 seconds. In both cases, aliquots with recycling values outside 10% of unity, recuperation  $>5\%$  of the natural signal, or (for quartz) IR-depletion ratios  $<0.9$  were removed prior to any averaging of the  $D_e$  distributions. Analyses were carried out in the Analyst software. Dose response curves were fitted with saturating exponential or saturating exponential plus linear curves and  $D_e$  uncertainties incorporate counting statistics, curve fitting uncertainties and a 1.5% systematic uncertainty (Duller, 2007) (all calculated within the Risoe Analyst software). The uncertainty in final  $D_e$  estimate also incorporates a beta source calibration uncertainty (3%).

### ***Dose recovery experiments and sample properties***



A group of samples underwent dose recovery (DR) experiments to assess the suitability of the quartz SAR protocol (Murray and Wintle, 2003). Each sample was bleached twice (with a 10,000 second pause between) at room temperature with blue LEDs and then given a known beta dose. Preheating temperatures within the SAR protocol were varied to assess sample properties and to optimise measurement conditions. Data from these measurements are summarised in **Table S2**, along with indicative data on sample behaviour, including the key aliquot rejection criteria of: 1) average recycling ratio (ratios of repeat point regeneration points) and 2) average the recuperation measurement (% of natural signal). All samples exhibited good responses to the SAR protocol and equivalent doses were recovered across a range of preheat temperatures (with perhaps the exception the very lowest (160°C) temperature preheat combinations). This response is quite typical of quartz from the southern Cape of South Africa. On this basis, preheating temperatures of 220 or 240 °C, all with a 160 °C (cut) test dose preheat, were selected. An additional dose recovery experiment was conducted for the pIRIR<sub>225</sub> protocol using material from VVV16-6-11. Here small aliquots were exposed to (UK) daylight for 7 days. They were then given a 302 Gy beta dose and analysed using the same pIRIR<sub>225</sub> protocol. The results (dose recovery ratio of 0.93±0.02, n=3) suggest acceptable performance of this sample/protocol combination.

*Table S2: Results of quartz SAR dose recovery experiments for selected samples. These data comprise the results from a range of preheating combinations (from 180-260°C for the preheat and 160 or 220°C cut heats for the test dose preheat with three aliquots for each combination). The administered beta doses are shown in parentheses in the sample column.*

Sample	Average dose recovery ratio all temperatures	Average recycling ratio	Average recuperation (%)	DR ratio for chosen preheat combination
VVV16-2-7 (16 Gy)	0.99±0.06 (n=27)	1.03±0.04	0.3±0.2	1.01±0.01 (n=3)
VVV16-1-9 (47 Gy)	1.06±0.09 (n=27)	0.99±0.03	0.5±0.2	1.01±0.02 (n=3)
VVV16-1-10a (40 Gy)	1.03±0.07 (n=22)	0.97±0.03	0.3±0.1	1.01±0.01 (n=3)

### ***Equivalent dose determination***

Between 17 and 24 aliquots were used to estimate the sample quartz equivalent doses (**Table S3**). For quartz, the data were derived using saturating exponential plus linear fits applied to the dose response curves, although the fits using single saturating exponential equations were also checked. The former generally provided a slightly better fit to the data. Three samples have mean D<sub>e</sub>s greater than 120 Gy and may be close to saturation point of quartz dose

## Appendix

response curve (**Table S3**). For these samples the ratio to  $D_0$  parameter (from the saturating exponential fit) was in some cases close to or more than twice the  $D_0$ , which is normally considered indicative of samples close to saturation (Wintle and Murray, 2006), and certainly is indicative of a natural luminescence signal that intercepts on the low gradient part of a dose response curve. In particular, the sample VVV16-1-11 had an average ratio to  $D_0$  well in excess of two, and indeed 6 of 19 measured aliquots did not produce a finite  $D_e$  regardless of the choice of curve fitting. To address this the K feldspar fraction was analysed for the deepest samples. The yield of K-rich feldspar in these samples was very low, but sufficient material was recovered for analysis of samples VVV16-6-10 and VVV16-6-11. Both the low temperature (IR50) and post-IR (pIRIR<sub>225</sub>) analyses produced ages significantly higher than the minimum age obtained for the quartz fraction, supporting the interpretation that the quartz signal for VVV16-6-11 was in saturation. The measured K-Feldspar fading rates (g-value<sub>2days</sub> = % signal loss per decade) were obtained following Auclair et al. (2003) and are estimated at  $3.1 \pm 0.5$  % (IR50) and  $1.5 \pm 0.5$  % (pIRIR<sub>225</sub>).

The equivalent dose distributions are plotted in radial diagrams **Figure S1**. The OD parameter is the relative spread of equivalent doses after measurement uncertainties are excluded (Galbraith et al., 1999). For the quartz measurements, for small (2 mm) aliquots most samples display moderate, but not excessive amounts of scatter (OD ranging from 6-28%). In several cases, individual outliers (identified following Medialdea et al., 2014 and marked with black boxes in figure S1) account for a significant amount of the OD, and these were removed prior to averaging and age calculation (the change in mean and OD value resulting from this is also shown in **Figure S1**). An exception to these observations is the rather broad, albeit unskewed,  $D_e$  distribution observed for VVV16-2-8(49) (28% OD). Given the finer grain size range analysed in this case, one might expect more signal averaging (and perhaps less inter-aliquot scatter), and the source of the observed scatter (particularly in comparison to adjacent less scattered sample VVV16-2-8) is not entirely clear. Overall, however, this largely moderate level of OD, along with an absence of significant positive skew in any of the  $D_e$  distributions, in conjunction with the supporting radiocarbon dating for the younger samples, suggests incomplete bleaching or mixing are not major issues for most samples. Final age calculations are therefore based on the central age model (Galbraith et al., 1999) equivalent dose.

The ages for the K-feldspar analyses (VVV16-6-10 and VVV16-6-11) are markedly older than the quartz samples, but are consistent with the wider core stratigraphy with each other's relative positions. The K-feldspar IRSL signal bleaches substantially slower than quartz OSL (Godfrey-Smith et al., 1988), and even more so for post-IR signals (Buylaert et al., 2009), implying a greater risk of incomplete bleaching prior to deposition (**Figure S1**). Although the post-IR signals for both samples show moderate amounts of inter-aliquot scatter, the amount of scatter for the pIRIR<sub>225</sub> measurements is not markedly higher than the lower

temperature (more easily bleached) IR50 signals (Table S3). Estimation of the IR50 age following fading correction allows a partial check of the compatibility of the ages from these more or less rapidly bleached signals, although the additional uncertainty added by the fading correction is in this instance quite large. Fading correction following the Huntley and Lian (2006) / Kars et al. (2008) approach (implemented in the R package Luminescence) produced a fading-corrected IR50 age of  $286 \pm 36$  ka for VVV16-6-11, which despite the wide uncertainties provides some evidence this sample is indeed substantially older than those overlying it. For the purpose of age-depth modelling, the fading uncorrected pIRIR<sub>225</sub> age (obtained following removal of a single high  $D_e$  outlier) for VVV16-6-11 is considered preferable (i.e.  $256 \pm 19$  ka).

# Appendix

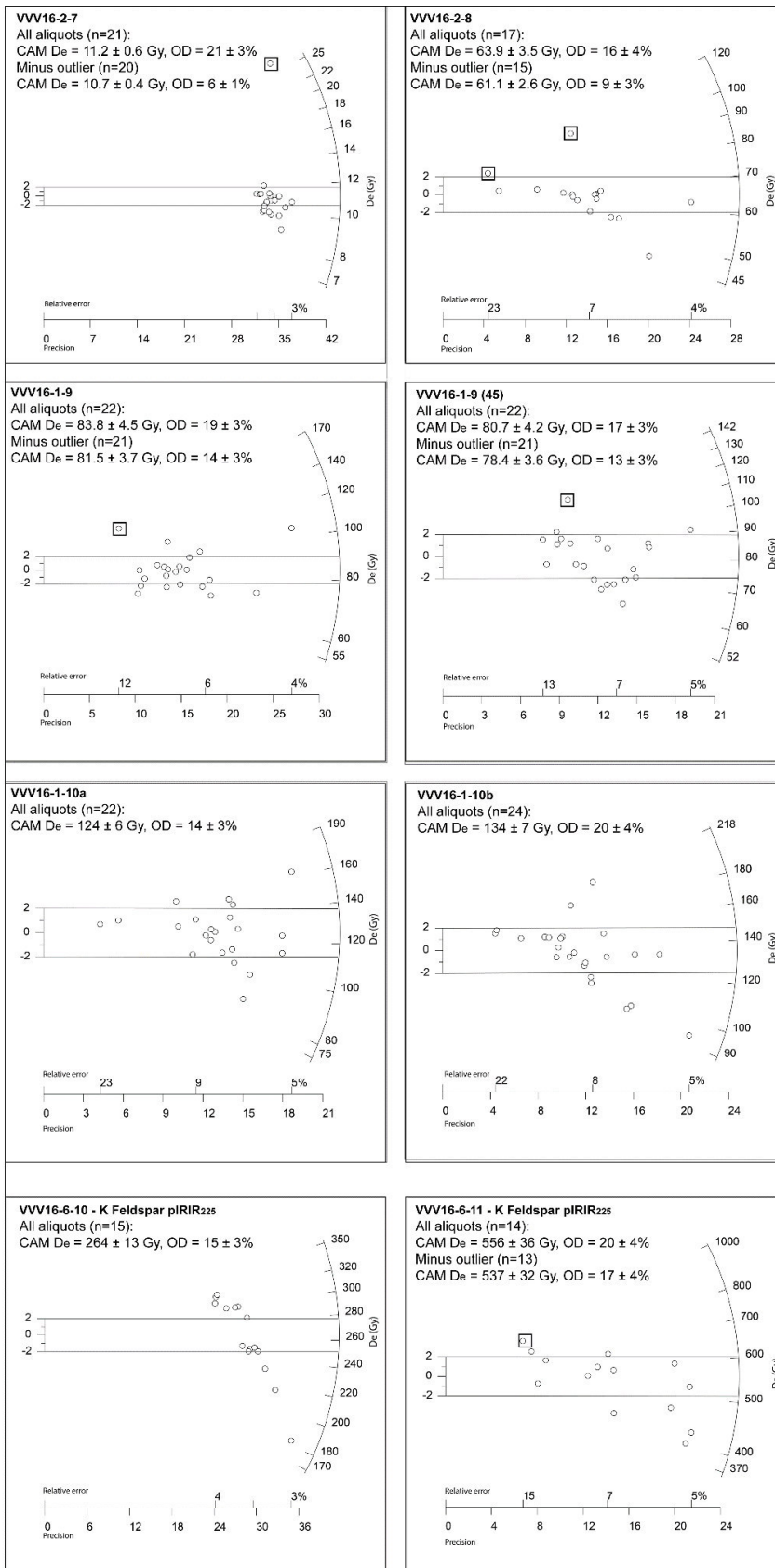


**Figure S1:** Radial plots showing the equivalent dose ( $D_e$ ) distributions for the quartz and K-feldspar SAR analyses used to construct the VVV core chronology. Black boxes around data points indicate formal outlier aliquots removed before averaging and age calculation, with the text box indicating the central age model (CAM)  $D_e$  and OD values before and after outlier removal. Radial plots were made in Radial Plotter 9.5 (Vermeesch, 2009).

**Table S3:** Summary of measured sample equivalent doses, based on the central age model (Galbraith et al, 1999) estimates, along with the estimated sample overdispersion and equivalent dose distribution skewness.

Sample	Acceptable aliquots (# rejected)	Equivalent dose (Gy)	OD (%)	Skew	Average ratio to D <sub>0</sub> ~
16-2-7	21 (1)	10.7±0.4	6±1	-0.5±0.6	0.6±0.1
16-2-8	16 (1)	61±3*	9±3	0.9±0.6	1.4±0.5
16-1-9 (45)	22 (2)	78±4^	13±3	-0.1±0.5	1.4±0.3
16-1-9	22 (0)	82±4^	14±3	0.8±0.5	1.4±0.3
16-1-10(a)	22 (0)	124±6	14±3	-0.05±0.5	2.3±0.6
16-1-10 (b)	24 (0)	134±7	20±4	0.3±0.5	2.3±0.9
16-6-10 IR50	15 (0)	224±13	18±3	0.0±0.6	0.4±0.1
16-6-10 (pIRIR <sub>225</sub> )	15 (0)	264±13	15±3	-0.5±0.6	0.7±0.2
16-6-11 (Quartz)	13 (6)	239±13 <sup>§</sup>	11±4	-0.2±0.7	3.2±0.7
16-6-11 IR50	14 (0)	352±20	18±3	-1.1±0.6	0.8±0.2
16-6-11 pIRIR <sub>225</sub>	14 (0)	537±32^	17±4	0.2±0.6	1.6±0.4

^One outlier removed prior to averaging; \*Two high outliers removed prior to averaging; ~Ratio to D<sub>0</sub> based on fitting single saturating exponential to dose-response. <sup>§</sup>Potentially minimum D<sub>e</sub> based on aliquots fitted with saturating exponential plus linear fit.

### Dose rate estimation

Dose rates (Table S4) were determined from elemental contents obtained using inductively coupled plasma mass spectrometry (ICP-MS) for U and Th and ICP-OES for K. The U, Th and K contents were converted to annual dose rates following Guérin et al. (2011) with corrections for grain size (Mejdahl, 1979), water content (Aitken, 1985) and HF etching (Bell, 1979). Additional verification of the resulting dose rate determinations was provided assessment of the external beta dose rates using GM-Beta Counting (Bøtter-Jensen and Mejdahl, 1988; Jacobs and Roberts, 2015; Table S4). For K-feldspar, the internal K and Rb dose rates for were based on the assumption of grain K and Rb contents of 12.5±0.5% and 400±100 ppm respectively (Huntley and Baril, 1997; Huntley and Hancock, 2001). The K-feldspar fractions were not etched, and the dose rates for these measurements include external alpha contributions using an “a-value” of 0.1 (Balescu and Lamothe, 1993). Cosmic dose rates were determined based on the measured core depth following Prescott and Hutton (1994). Final age uncertainties incorporate 3% relative uncertainties for the dose rate conversion factors, grain size attenuation factor, water attenuation and HF etching, propagated via standard methods.

## Appendix

HF etching is assumed to have entirely removed the  $\alpha$ -irradiated outer portion of the quartz grains.

The as-measured water content is quite varied and very high in some cases (**Table S5**). It is also possible that the modern water contents are relatively high compared the burial average. As these past variations are poorly constrained, we have used the measured sample water contents with a 5% (absolute water content) uncertainty, which was propagated into the final dose rate uncertainties. As a measure of sensitivity to varying water content, reducing the absolute water content by 10%, will result in age that is ~9% younger. Thus, we anticipate that this 5% uncertainty incorporates the majority of water content variation at this site. This issue is somewhat mitigated for the K-feldspar samples, where the internal beta dose rate contributes ~40% of the total dose to the sample.

**Table S4:** External beta dose rate estimates obtained using ICP-MS elemental data and GM Beta Counting. In each case the dose rate has been corrected for the grain size fraction analysed for the equivalent dose and for the sample water content. The mean ratio for the two methods is  $1.01 \pm 0.08$

Sample	External beta dose rate via GM-Beta Counting (Gy ka <sup>-1</sup> )	External beta dose rate via ICP-MS analysis (Gy ka <sup>-1</sup> )
VVV16-2-7	0.60±0.05	0.61±0.04
VVV16-2-8 (2017)	1.08±0.06	1.17±0.07
VVV16-1-9 (2017)	0.86±0.05	0.93±0.06
VVV16-1-9 (2021)	0.89±0.05	0.91±0.06
VVV16-1-10 (a)	0.69±0.07	0.66±0.04
VVV16-1-10 (b)	0.62±0.04	0.57±0.04
VVV16-6-10 (2021)	0.33±0.03	0.29±0.02

**Table S5:** Age estimates using equivalent dose estimates derived from central age model estimates. K-feldspar dose rates contain an additional external alpha dose of  $0.06 \pm 0.01$  Gy ka<sup>-1</sup> as these samples were not HF etched.

Sample	Size fraction (µm)	Water (%)	Depth (m)	U (ppm)	Th (ppm)	K (%)	External Alpha dose (Gy ka <sup>-1</sup> )	External Beta dose (Gy ka <sup>-1</sup> )	Internal Beta dose (Gy ka <sup>-1</sup> )	Gamma (Gy ka <sup>-1</sup> )	Cosmic (Gy ka <sup>-1</sup> )	Total dose rate (Gy ka <sup>-1</sup> )	Age (ka)
16-2-7	90-150	57±5	10.4	2.21	11.1	0.80	na	0.605±0.014	na	0.591±0.041	0.064±0.003	1.26±0.06	8.5±0.5
16-2-8	90-250	45±5	11.3	4.27	17.1	1.43	na	1.117±0.074	na	1.092±0.074	0.058±0.003	2.32±0.11	26.3±1.6
16-1-9 (45)	150-250	37±5	11.9	3.00	11.9	1.10	na	0.889±0.056	na	0.832±0.056	0.055±0.003	1.78±0.08	44±3
16-1-9	180-212	34±5	12.1	2.79	13.8	1.09	na	0.932±0.059	na	0.898±0.063	0.054±0.003	1.88±0.09	43±3
16-1-10a	180-212	17±5	12.9	1.95	9.02	0.60	na	0.662±0.043	na	0.668±0.049	0.050±0.003	1.38±0.07	90±6
16-1-10b	180-212	16±5	12.9	1.46	8.58	0.52	na	0.573±0.037	na	0.597±0.046	0.050±0.003	1.22±0.06	110±8
16-6-10 (70) (K-feldspar pIRIR <sub>225</sub> )	180-212	15±5	13.8	1.25	3.60	0.19	0.102±0.025	0.316±0.021	0.848±0.059	0.309±0.023	0.046±0.003	1.62±0.07	163±11
16-6-11 (Quartz)	180-212	14±5	14.5	1.28	7.41	0.41	na	0.486±0.032	na	0.519±0.040	0.044±0.003	1.05±0.05	>166
16-6-11 (K-feldspar pIRIR <sub>225</sub> )	180-212	14±5	14.5	1.28	7.41	0.41	0.102±0.025	0.532±0.033	0.848±0.059	0.519±0.040	0.044±0.003	2.10±0.09	256±19

### 3 Physical as well as inorganic and organic geochemical analyses

#### **Methods**

For grain size analyses, sample aliquots were treated with H<sub>2</sub>O<sub>2</sub> (15%, 30%) to remove organic matter and subsequently treated with HCl (15%) to remove carbonates. As a dispersant, 5 ml Sodium-Pyrophosphate (Na<sub>4</sub>P<sub>2</sub>O<sub>7</sub> · 10 H<sub>2</sub>O) were added to each sample and shaken for >2 h. The grain-size distribution was determined with a Laser Diffraction Particle Size Analyzer (LS 13320, Beckman Coulter, California, USA). Samples were measured with the Aqueous Liquid Module in several 60 second cycles until a reproducible signal was obtained. The 'Fraunhofer' optical model of light scattering was used for computing grain size distribution. The median grain size as well as fractions of clay, silt and sand of each sample were calculated from the first constant measurement. Granulometric parameters were calculated with a modified version of the Software Gradistat 4.2 (Blott and Pye, 2001).

Sample aliquots were dried at 105 °C for >24 h and water content was calculated as the difference between moist and dried samples. To determine loss on ignition (LOI), dried samples were combusted at 550 °C for 4 h and LOI was calculated as the difference between dried and combusted sample weight (e.g. Heiri et al., 2001).

Carbon and nitrogen contents and their stable isotopes were analysed from freeze dried sample aliquots (-50 °C; >72 h) with an Elementar Analyzer (vario EL cube) coupled to an isotope ratio mass spectrometer (Isoprime precision). ~30 mg of untreated sediment samples was weighted into tin boats (Elementar, 6 x 6 x 12) and measured for total carbon (TC), total nitrogen (TN) and the nitrogen isotopic composition ( $\delta^{15}\text{N}$ ). Prior to the analyses of total organic carbon (TOC) and the bulk organic carbon isotopic composition ( $\delta^{13}\text{C}_{\text{TOC}}$ ), carbonates were removed from the samples with 1N HCl at 60 °C for 8 h. Samples were subsequently washed with ultrapure water to pH neutrality and ~30 mg were weighted into tin boats. The analytical precision of the  $\delta^{15}\text{N}$  and  $\delta^{13}\text{C}$  analyses was checked against certified standards (L-Proline, EDTA and USGS65), and gave an analytical error <0.19‰, <0.17‰ and <0.30‰, respectively.  $\delta^{15}\text{N}$  and  $\delta^{13}\text{C}$  are given in their delta notation against Air and the Vienna Pee Dee Belemnite (VPDB). The molar ratio of TOC and TN was calculated based on their respective molecular weights. Relative errors were calculated based on triplicate measurements (N: <1.7%, TOC: <0.5%).

Lipid extraction is described in section 3.4 (main manuscript) and subsequently *n*-alkane amounts were calculated as the sum of C<sub>21</sub> to C<sub>35</sub>, and are given in  $\mu\text{g} \cdot \text{g}^{-1}$  dry weight. Odd-over-even predominance (OEP) values (eq. 1) were determined following Hoefs et al. (2002). Low values (<5) indicate an enhanced state of degradation (Bugge et al., 2010; Zech et al., 2010). The Average Chain Length (ACL) (eq. 2) was calculated from the odd-numbered *n*-alkanes (Poynter et al., 1989).



$$\text{OEP} = \left( \frac{nC_{27} + nC_{29} + nC_{31} + nC_{33}}{nC_{26} + nC_{28} + nC_{30} + nC_{32}} \right) \quad (1)$$

$$\text{ACL} = \frac{27 \cdot nC_{27} + 29 \cdot nC_{29} + 31 \cdot nC_{31} + 33 \cdot nC_{33}}{nC_{27} + nC_{29} + nC_{31} + nC_{33}} \quad (2)$$

### **Data description**

The sediments in Unit A consist nearly exclusively of sand (55 to 98 %) and median grain size ranges from 79.9 to 282.7  $\mu\text{m}$  (Fig. S2). Unit B is dominated by silt (45 to 90 %), clay and sand range from 6 to 23 % and 1 to 55 %, respectively, and median grain size ranges from 6.2 to 79.9  $\mu\text{m}$  (**Figure S2**).

Physical properties as well as inorganic and organic geochemical proxies support the subdivision of the sediment sequence in five units. LOI of the sediment sequence shows low values in Units A and B (0.15 to 7.1 %) and distinctly higher values in Units D and E (80 to 98 %) (Fig. S3). Water content was determined for Unit D and E exclusively and ranges from 84 to 95 % with distinctly lower values in E than in D. TOC and N contents are lowest in Unit A (0.05 $\pm$ 0.01 to 0.64 $\pm$ 0.07 % and 0.02 $\pm$ 0.00 to 0.07 $\pm$ 0.00 %, respectively), slightly higher in Unit B (1.25 $\pm$ 0.14 to 7.10 $\pm$ 0.77 % and 0.10 $\pm$ 0.00 to 0.34 $\pm$ 0.00 %, respectively) and highest in Unit D and E (45.8 $\pm$ 0.2 to 54.1 $\pm$ 0.3 % and 0.54 $\pm$ 0.01 to 1.70 $\pm$ 0.03 %, respectively) (Fig. S3). Molar C/N-ratios follow this pattern and show lowest values in Unit A, higher values in Unit B and highest values in Unit D and especially E (2.6 to 14.9, 13.2 to 34.4 and 33.2 to 102.3, respectively).  $\delta^{13}\text{C}_{\text{TOC}}$  and  $\delta^{15}\text{N}$  values are more positive in Unit A ( $-26.9\pm 0.02$  to  $-20.1\pm 0.1$  ‰ and 1.23 $\pm$ 0.04 to 4.1 $\pm$ 0.13 ‰, respectively).  $\delta^{13}\text{C}_{\text{TOC}}$  values are more negative in Unit B whereas  $\delta^{15}\text{N}$  values stay positive in  $^{15}\text{N}$  ( $-27.0\pm 0.2$  to  $-24.7\pm 0.2$  ‰ and 0.31 $\pm$ 0.04 to 4.08 $\pm$ 0.13 ‰, respectively). In Unit D and E both  $\delta^{13}\text{C}_{\text{TOC}}$  and  $\delta^{15}\text{N}$  values are distinctly more negative than in the lower units ( $-28.5\pm 0.0$  to  $-21.5\pm 0.0$  ‰ and  $-3.78\pm 0.44$  to  $-0.06 \pm 0.01$  ‰, respectively) (Fig. S3).

*n*-Alkane amounts and OEP show low values in Units A and B (0.005 – 0.05  $\mu\text{g}\cdot\text{g}^{-1}$  and 2.7 – 13.3, respectively) and distinctly increase in Units D and E (0.76 – 87.0  $\mu\text{g}\cdot\text{g}^{-1}$  and 1.4 – 23.9, respectively) (Fig. S3). ACL values are higher in Units A and B (30.1 – 30.9 and 0.10 – 0.47, respectively) compared to Units D and E (29.4 – 30.7 and 0.02 – 0.35, respectively).

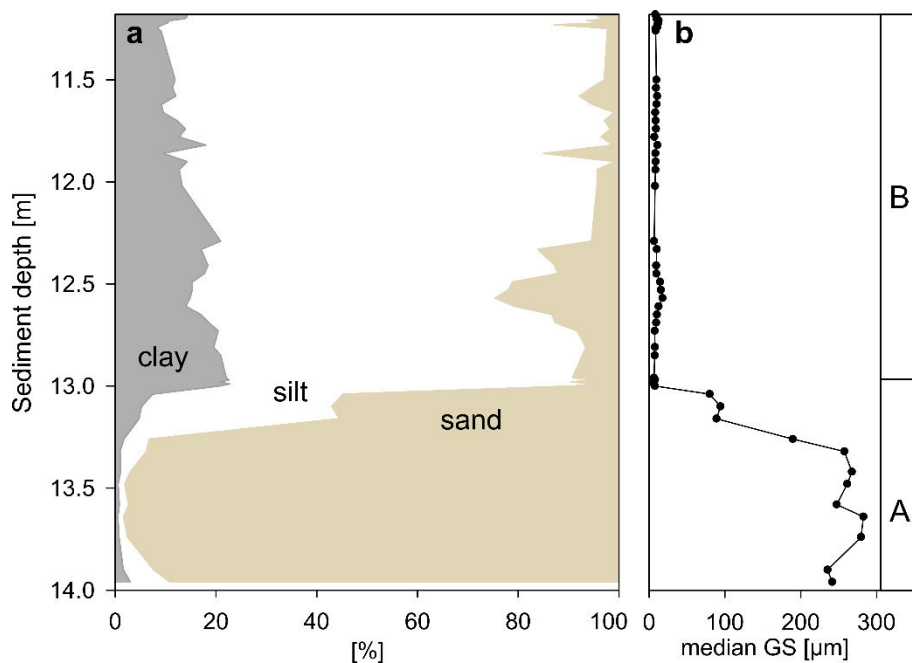


Figure S2: Percentages of clay, silt and sand (a) as well as median grain size (b) from the VVV16 sediment sequence. Lithological units are depicted at the right.

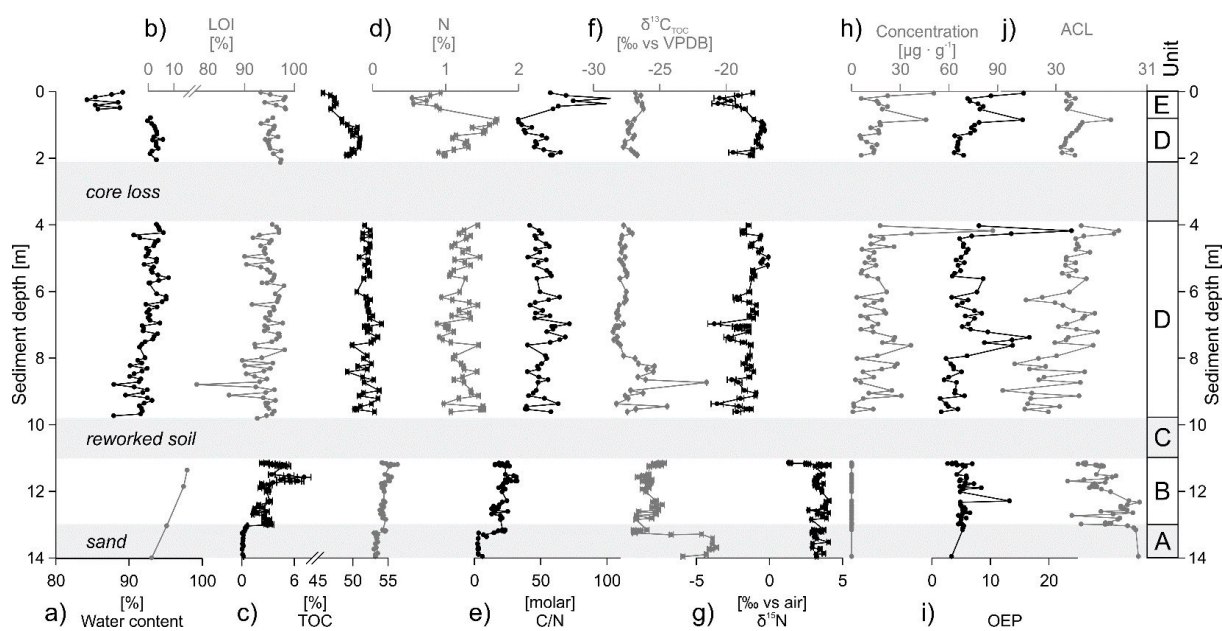


Figure S3: a) Water content, b) loss on ignition at 550°C (LOI, note axis break), c) total organic carbon (TOC, note axis break), d) nitrogen, f)  $\delta^{13}\text{C}_{\text{TOC}}$ , g)  $\delta^{15}\text{N}$ , e) molar C/N ratio, h) n-alkane amounts, i) Odd-over-even predominance (OEP) and c) Average chain length (ACL) from the VVV16 sediment sequence. Lithological units are depicted at the right.

## References

- Aitken, M.J., 1985. Thermoluminescence Dating. Academic Press, London.
- Auclair, M., Lamothe, M., Huot, S., 2003. Measurement of anomalous fading for feldspar IRSL using SAR. *Radiation Measurements* 37, 487-492.
- Balescu, S., Lamothe, M., 1993. Thermoluminescence dating of the holsteinian marine formation of Herzelee, northern France. *Journal of Quaternary Science* 8, 117-124.
- Bell, W.T., 1979. Thermoluminescence dating: radiation dose rate data. *Archaeometry* 21, 243-245.
- Blott, S.J., Pye, K., 2001. GRADISTAT: a grain size distribution and statistics package for the analysis of unconsolidated sediments. *Earth Surface Processes and Landforms* 26, 1237-1248.
- Bøtter-Jensen, L., Mejdahl, V., 1988. Assessment of beta dose-rate using a GM multicounter system. *International Journal of Radiation Applications and Instrumentation. Part D. Nuclear Tracks and Radiation Measurements* 14, 187-191.
- Buggle, B., Wiesenberg, G.L.B., Glaser, B., 2010. Is there a possibility to correct fossil n-alkane data for postsedimentary alteration effects? *Applied Geochemistry* 25, 947-957.
- Buylaert, J.P., Murray, A.S., Thomsen, K.J., Jain, M., 2009. Testing the potential of an elevated temperature IRSL signal from K-feldspar. *Radiation Measurements* 44, 560-565.
- du Plessis, N., Chase, B.M., Quick, L.J., Strobel, P., Haberzettl, T., Meadows, M.E., 2021. A c. 650 year pollen and microcharcoal record from Vankervelsvlei, South Africa, in: Runge, J., Gosling, W.D., Lézine, A.-M., Scott, L. (Eds.), *Quaternary Vegetation Dynamics – The African Pollen Database*. CRC Press, London, pp. 301-308.
- Duller, G.A.T., 2003. Distinguishing quartz and feldspar in single grain luminescence measurements. *Radiation Measurements* 37, 161-165.
- Duller, G.A.T., 2007. Assessing the error on equivalent dose estimates derived from single aliquot regenerative dose measurements. *Ancient TL* 25, 15-24.
- Galbraith, R.F., Roberts, R.G., Laslett, G.M., H., Y., Olley, J.M., 1999. Optical dating of single and multiple grains of quartz from Jinmium rock shelter, northern Australia: part I, Experimental design and statistical models. *Archaeometry* 41, 339-364.
- Godfrey-Smith, D.I., Huntley, D.J., Chen, W.H., 1988. Optical dating studies of quartz and feldspar sediment extracts. *Quaternary Science Reviews* 7, 373-380.
- Guérin, G., Mercier, N., Adamiec, G., 2011. Dose-rate conversion factors: update. *Ancient TL* 29, 5-8.
- Heiri, O., Lotter, A.F., Lemcke, G., 2001. Loss on ignition as a method for estimating organic and carbonate content in sediments: reproducibility and comparability of results. *Journal of Paleolimnology* 25, 101-110.
- Hoefs, M.J.L., Rijpstra, W.I.C., Sinninghe Damsté, J.S., 2002. The influence of oxic degradation on the sedimentary biomarker record I: evidence from Madeira Abyssal Plain turbidites. *Geochimica et Cosmochimica Acta* 66, 2719-2735.
- Hogg, A.G., Heaton, T.J., Hua, Q., Palmer, J.G., Turney, C.S.M., Southon, J., Bayliss, A., Blackwell, P.G., Boswijk, G., Bronk Ramsey, C., Pearson, C., Petchey, F., Reimer, P., Reimer, R., Wacker, L., 2020. SHCal20 Southern Hemisphere calibration, 0–55,000 years cal BP. *Radiocarbon*, 1-20.
- Huntley, D.J., Baril, M.R., 1997. The K content of K-feldspars being measured in optical dating or in thermoluminescence dating. *Ancient TL* 15, 11-13.
- Huntley, D.J., Hancock, R.G.V., 2001. The Rb contents of the K-feldspar grains being measured in optical dating. *Ancient TL* 19, 43–46.
- Huntley, D.J., Lian, O.B., 2006. Some observations on tunnelling of trapped electrons in feldspars and their implications for optical dating. *Quaternary Science Reviews* 25, 2503-2512.

- Jacobs, Z., Roberts, R.G., 2015. An improved single grain OSL chronology for the sedimentary deposits from Diepkloof Rockshelter, Western Cape, South Africa. *Journal of Archaeological Science* 63, 175-192.
- Kars, R.H., Wallinga, J., Cohen, K.M., 2008. A new approach towards anomalous fading correction for feldspar IRSL dating — tests on samples in field saturation. *Radiation Measurements* 43, 786-790.
- Medialdea, A., Thomsen, K.J., Murray, A.S., Benito, G., 2014. Reliability of equivalent-dose determination and age-models in the OSL dating of historical and modern palaeoflood sediments. *Quaternary Geochronology* 22, 11-24.
- Mejdahl, V., 1979. Thermoluminescence dating: Beta-dose attenuation in quartz grains. *Archaeometry* 21, 61-72.
- Murray, A.S., Wintle, A.G., 2000. Luminescence dating of quartz using an improved single-aliquot regenerative-dose protocol. *Radiation Measurements* 32, 57-73.
- Murray, A.S., Wintle, A.G., 2003. The single aliquot regenerative dose protocol: potential for improvements in reliability. *Radiation Measurements* 37, 377-381.
- Poynter, J.G., Farrimond, P., Robinson, N., Eglinton, G., 1989. Aeolian-Derived Higher Plant Lipids in the Marine Sedimentary Record: Links with Palaeoclimate, in: Leinen, M., Sarnthein, M. (Eds.), *Paleoclimatology and Paleometeorology: Modern and Past Patterns of Global Atmospheric Transport*. Springer Netherlands, Dordrecht, pp. 435-462.
- Prescott, J.R., Hutton, J.T., 1994. Cosmic ray contributions to dose rates for luminescence and ESR dating: Large depths and long-term time variations. *Radiation Measurements* 23, 497-500.
- Strobel, P., Kasper, T., Frenzel, P., Schitteck, K., Quick, L.J., Meadows, M.E., Mäusbacher, R., Habertzettl, T., 2019. Late Quaternary palaeoenvironmental change in the year-round rainfall zone of South Africa derived from peat sediments from Vankervelsvlei. *Quaternary Science Reviews* 218, 200-214.
- Stuiver, M., Reimer, P.J., Reimer, R.W., 2020. CALIB 8.2 [WWW program] at <http://calib.org> (Accessed: 2020-8-20).
- Thomsen, K.J., Murray, A.S., Jain, M., Bøtter-Jensen, L., 2008. Laboratory fading rates of various luminescence signals from feldspar-rich sediment extracts. *Radiation Measurements* 43, 1474-1486.
- Vermeesch, P., 2009. RadialPlotter: A Java application for fission track, luminescence and other radial plots. *Radiation Measurements* 44, 409-410.
- Wintle, A.G., Murray, A.S., 2006. A review of quartz optically stimulated luminescence characteristics and their relevance in single-aliquot regeneration dating protocols. *Radiation Measurements* 41, 369-391.
- Zech, M., Buggle, B., Leiber, K., Marković, S., Glaser, B., Hambach, U., Huwe, B., Stevens, T., Sümegi, P., Wiesenberger, G., Zöller, L., 2010. Reconstructing Quaternary vegetation history in the Carpathian Basin, SE-Europe, using *n*-alkane biomarkers as molecular fossils. *E&G – Quaternary Science Journal* 58.